EFFECTS OF NEUROMODULATION ON NEUROVASCULAR COUPLING

Dissertation

zur Erlangung des Grades eines
Doktors der Naturwissenschaften

der Mathematisch-Naturwissenschaftlichen Fakultät
und
der Medizinischen Fakultät
der Eberhard-Karls-Universität Tübingen

vorgelegt
von

Jose Daniel Zaldivar Perez
aus Mexiko Stadt, Mexiko

June 2016

Tag der mündlichen Prüfung:	June 2nd, 2017
Dekan der Math.-Nat. Fakultät:	Prof. Dr. W. Rosenstiel
Dekan der Medizinischen Fakultät:	Prof. Dr. I. B. Autenrieth
1. Berichterstatter:	Prof. Dr. Nikos Logothetis
2. Berichterstatter:	Prof. Dr. Uwe Ilg
Prüfungskommission:	Prof. Dr. Nikos Logothetis
	Prof. Dr. Uwe Ilg
	Prof. Dr. Andreas Bartels
	Dr. Jozien Goense

Erklärung / Declaration:

Ich erkläre, dass ich die zur Promotion eingereichte Arbeit mit dem Titel:

„ **EFFECTS OF NEUROMODULATION ON NEUROVASCULAR COUPLING** “

selbständig verfasst, nur die angegebenen Quellen und Hilfsmittel benutzt und wörtlich oder inhaltlich übernommene Stellen als solche gekennzeichnet habe. Ich versichere an Eides statt, dass diese Angaben wahr sind und dass ich nichts verschwiegen habe. Mir ist bekannt, dass die falsche Abgabe einer Versicherung an Eides statt mit Freiheitsstrafe bis zu drei Jahren oder mit Geldstrafe bestraft wird.

I hereby declare that I have produced the work entitled " EFFECTS OF NEUROMODULATION ON NEUROVASCULAR COUPLING ", submitted for the award of a doctorate, on my own (without external help), have used only the sources and aids indicated and have marked passages included from other works, whether verbatim or in content, as such. I swear upon oath that these statements are true and that I have not concealed anything. I am aware that making a false declaration under oath is punishable by a term of imprisonment of up to three years or by a fine.

Tübingen, den .....

.....

Datum / Date Unterschrift /Signature

This work is dedicated to my
loving and caring daughter, ***Daniela***

Remember!
When writing the story of your life,
Do not let anyone else hold the pen.

TABLE OF CONTENTS

Acknowledgements

I would like to first thank my mentors, Nikos Logothetis and Jozien Goense, for introducing me to the wonders and frustrations of a scientific career. I thank them for their guidance, their never ending support and encouragement, as well as for their intellectual contributions to my development as a scientist. Both have taught all about self-discipline as well as to be creative during the design of experiments, and the presentation of scientific communications. They created an environment of unwavering support and independent thinking while fostering a strong sense of lab camaraderie. Without their wisdom and guidance, I doubt I would have lasted this long. I sincerely hope I continue to have opportunities to interact with them..

I am sincerely grateful to all the members of my dissertation committee for their time and extreme patience while understanding my work: thanks to Stefan Laufer for being a supportive, strong guiding force. To Uwe Ilg, whom I am most appreciative for agreeing to serve on the committee on short notice, and knowing he would probably have less time than the others to comprehend my research. To Andreas Bartels for his help and for agreeing being part of my Ph.D. committee defense. Although, Stefano Panzeri is not officially a member on my committee, I am thankful to him for encouraging me to find different ways to answer one question and for showing me the paths towards computational neuroscience. I also want thank to Kevin Whittingstall and Alexander Rauch. In the one hand, Kevin introduced me to the neurophysiology in the visual system. Alexander Rauch for appreciating my research strengths and patiently encouraging me to improve in my weaker areas, but more importantly, for giving that shot that let me start my projects.

To my lab-mates, thanks for the fun and support. Especially thanks to my friends Jozien Goense, Cesare Magri, Timothy Melano and Veronika von Pfoestl, for their friendship and companionship, and for not let me fall during the difficult times. To Pedro Douay, for his never ending support and advise, not only to me, but to my family. I am indebted and thankful to Joachim Werner for helping me during my experiments and answering all of my questions. To Axel Olterman for teaching me about electronics and the basis of the neurophysiology signal. To Yusuke Murayama for his patience and for being the silent friend I always trusted. To Mirko Lindig, for all the fun during the experiments and the trust deposited on me. To Thomas Steudel, for his patience, his trust and his German-made quality at doing what he does. To Deniz Ipek, for all of her time devoted to assisting during experiments. To Michael Beyerlein for his hard work and his patience. To Conchy Moya for helping me from the first day I visited Tuebingen. To the amazing people in the

electronic and machine workshops. To Andre Marreiros for sharing office space and trusting me. To the latino-community, Juan, Mario and Marlon for all of the fun.

There are many more people I could thank, but time, space, and modesty compel me to stop here and continue with family before I run out of space. My parents (Tere and Oscar) imbued in me a love of science; they taught me to be curious and always encouraged my questions; and most importantly, they have loved me and supported me throughout my entire life. I would like to also thank my grandmother who has given me nothing more than just love and wise guidance, her efforts and her constant way of loving me have showed that family should always be a priority in life. My grandfather for his wisdom and for showing me to never give up. Of course, I will never forget my brother, Oscar thanks for being there for me, for sharing your first moments of life and recharging my battery after long working hours. Thanks for everything that helped me get to this day.

Lastly, I am thankful for the love and support of my beautiful family. Words cannot express how grateful I am to my girls. My daughter Daniela is a constant reminder of the joy and wonder in life. Her sweet smiles, hugs and kisses showed me to ***never be afraid of storms, they just teach you how to sail your ship***. Finally, I am eternally grateful for the love and support of my wife, Erika Lara. She has taught me more than anyone, has been a better fiend that I have ever deserved, and has loved me more than I thought possible. Without her none of this would have been possible and so it is only fitting that this thesis be devoted to her, as is all of my life.

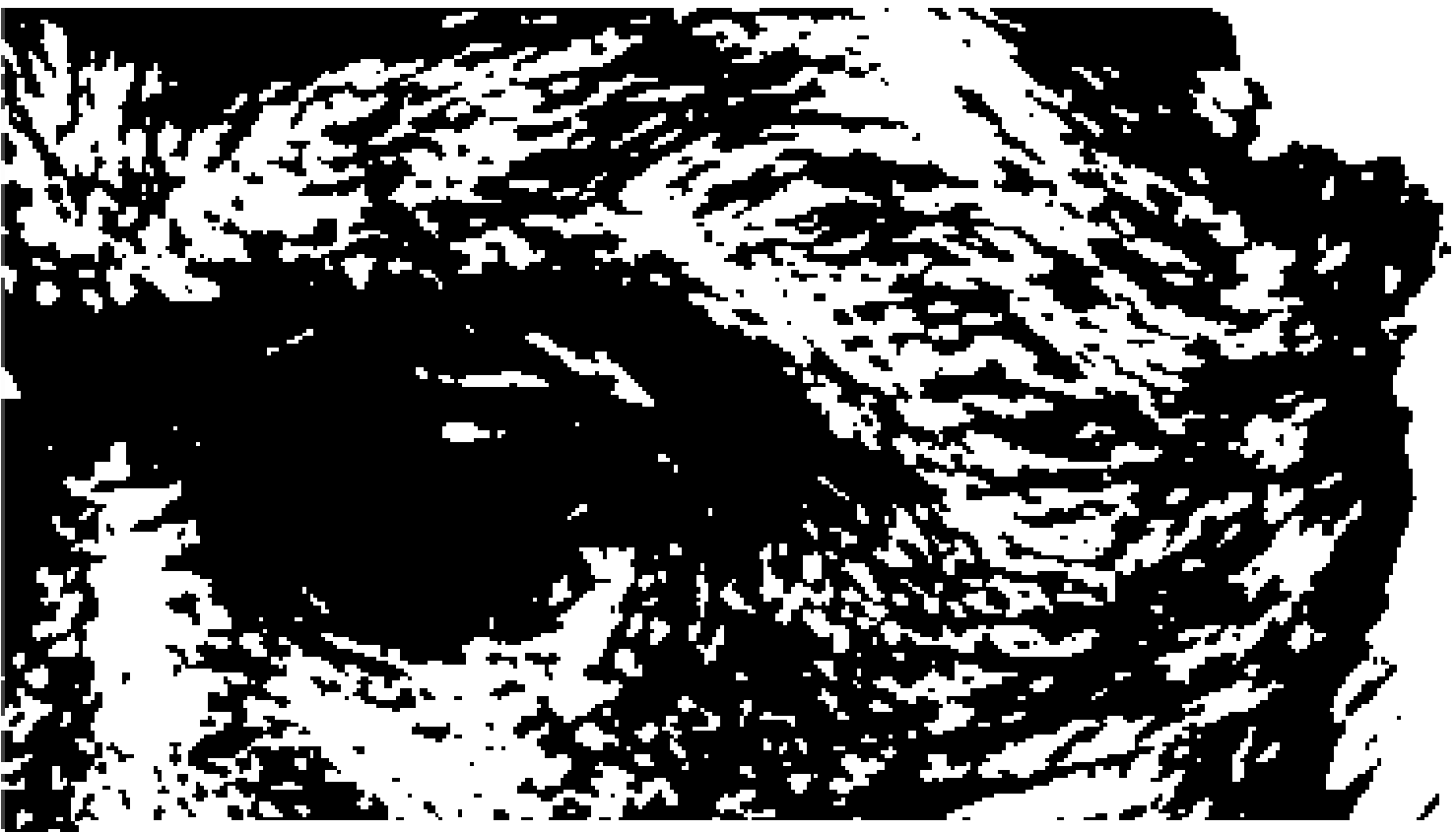

1. Summary

1. Summary

The communication between neurons within neural circuits relies on neurotransmitters (glutamate, γ-aminobutyric acid (GABA)) and neuromodulators (acetylcholine, dopamine, serotonin, etc.). However, despite sharing similar molecular elements, neurotransmitters and neuromodulators are distinct classes of molecules and mediate different aspects of neural activity and metabolism. Neurotransmitters on one hand are responsible for synaptic signal transmission (classical transmission) while neuromodulators exert their functions by mediating different postsynaptic events that result in changes to the balance between excitation and inhibition.

Neuromodulation, while essential to nervous system function, has been significantly more difficult to study than neurotransmission. This is principally due to the fact that effects elicited by neuromodulators are usually of slow onset, long lasting, and are not simply excitation or inhibition. In contrast to the effects of neurotransmitters, neuromodulators enable neurons to be more flexible in their ability to encode different sorts of information (e.g. sensory information) on a variety of time scales. However, it is important to appreciate that one of the challenges in the study of neuromodulation is to understand the extent to which neuromodulators' actions are coordinated at all levels of brain function. That is, from the cellular and metabolic level to network and cognitive control.

Therefore, understanding the molecules that mediate brain networks interactions is essential to understanding the brain dynamic, and also helps to put the cellular and molecular processes in perspective. Functional magnetic resonance imaging (fMRI) is a technique that allows access to various cellular and metabolic aspects of network communication that are difficult to access when studying one neuron at the time. Its non-

invasiveness nature allows the comparison of data and hypotheses of the primate brain to that of the human brain. Hence, understanding the effects of neuromodulation on local microcircuits is needed. Furthermore, given the massive projections of the neuromodulatory diffuse ascending systems, fMRI combined with pharmacological and neurophysiological methods may provide true insight into their organization and dynamics. However, little is known about how to interpret the effects of neuromodulation in fMRI and neurophysiological data, for instance, how to disentangle blood oxygenation level dependent (BOLD) signal changes relating to cognitive changes (presumably neuromodulatory influences) from stimulus-driven or perceptual effects.

The purpose of this dissertation is to understand the causal relationship between neural activity and hemodynamic responses under the influence of neuromodulation. To this end we present the results of six studies. In the first study, we aimed to establish a mass-spectrometry-based technique to uncover the distribution of different metabolites, neurotransmitters and neuromodulators in the macaque brain. We simultaneously measured the concentrations of these biomolecules in brain and in blood. In a second study, we developed a multimodal approach consisting of fMRI (BOLD and cerebral blood flow or CBF), electrophysiological recording with a laminar probe and pharmacology to assess the effects of neuromodulation on neurovascular coupling. We developed a pharmacological injection delivery system using pressure-operated pumps to reliably apply drugs either systemically or intracortically in the NMR scanner. In our third study, we systemically injected lactate and pyruvate to explore whether the plasma concentration of either of these metabolites affects the BOLD responses. This is important given that both metabolites are in a metabolic equilibrium; if this equilibrium is disrupted, changes in the NAD and NADH concentrations would elicit changes in the CBF. In a fourth study, we explored the influence of dopaminergic (DAergic) neuromodulation in the BOLD, CBF and neurophysiological activity. Here we found that DAergic neuromodulation dissociated the BOLD responses from the underlying neural activity. Interestingly, the changes in the

neural activity were tightly coupled to the effects seen in the CBF responses. In a subsequent study, we explored whether the effects of dopamine (DA) on the electrophysiological responses are cortical layer dependent and whether specific patterns of neural activity can be used to infer the effects of neuromodulation on the neural activity. This is important, given that different types of neural activity provide independent information about the amplitude and dynamics from BOLD responses, and studies have shown that these bands originate from different cortical layers. What this study revealed, is that local field potentials (LFPs) in the midrange frequencies can indeed provide indications about the sustained effects of neuromodulation on cortical sensory processing. Given the results from the previous study, in our sixth study, we aimed at understanding how different cortical layers may process incoming and outgoing information in the different LFP bands.

These findings provide evidence that neuromodulation has profound effects on neurovascular coupling. By changing the excitation-inhibition balance of neural circuits, neuromodulators not only mediate the neural activity, but also adjust the metabolic demands. Therefore, understanding how the different types of neuromodulators affect the BOLD response is essential for an effective interpretation of fMRI-data, not only in tasks involving attentional and reward-related processes, but also for future diagnostic use of fMRI, since many psychiatric disorders are the result of alterations in neuromodulatory systems.

1. Zusammenfassung

Die Kommunikation zwischen den Neuronen innerhalb neuronalen Schaltkreise beruht auf Neurotransmitter (Glutamat, γ-Aminobuttersäure (GABA)) und Neuromodulatoren (Acetylcholin, Dopamin, Serotonin, etc.). Neurotransmitter und Neuromodulatoren sind jedoch unterschiedliche Klassen von Molekülen und verschiedenen Aspekte der neuronalen Aktivität und den Stoffwechsel vermitteln. Neurotransmitters sind einerseits verantwortlich für die synaptische Signalübertragung (klassische Übertragung), während ihre Funktionen ausüben, Neuromodulatoren durch verschiedene postsynaptischen Ereignisse zu vermitteln, die in Änderungen an der Balance zwischen Erregung und Hemmung führen.

Neuromodulation , während wesentlich Funktion des Nervensystems hat sich als Neurotransmission wesentlich schwieriger gewesen, zu studieren. Dies ist hauptsächlich auf die Tatsache zurückzuführen, die durch Neuromodulatoren sind in der Regel von langsamen Beginn, langlebig, und sind nicht einfach Anregung oder Hemmung ausgelöst beeinflusst. Im Gegensatz zu den Wirkungen von Neurotransmittern, Neuromodulatoren ermöglichen Neuronen flexibler zu sein in ihrer Fähigkeit, verschiedene Arten von Informationen (beispielsweise sensorische Informationen) auf einer Vielzahl von Zeitskalen zu kodieren. Im Gegensatz zu den Wirkungen von Neurotransmittern, Neuromodulatoren ermöglichen Neuronen flexibler zu sein in ihrer Fähigkeit, verschiedene Arten von Informationen (beispielsweise sensorische Informationen) auf einer Vielzahl von Zeitskalen zu kodieren. Im Gegensatz zu den Wirkungen von Neurotransmittern, Neuromodulatoren ermöglichen Neuronen flexibler zu sein in ihrer Fähigkeit, verschiedene Arten von Informationen (beispielsweise sensorische Informationen) auf einer Vielzahl von Zeitskalen zu kodieren. Jedoch ist es wichtig, dass

eine der Herausforderungen bei der Untersuchung von Neuromodulations zu schätzen ist, das Ausmaß, in dem Neuromodulatoren Aktionen koordiniert sind auf allen Ebenen der Gehirnfunktion zu verstehen. Das heißt, von der zellulären und metabolischen Ebene zu vernetzen und kognitive Kontrolle.

Daher die Moleküle zu verstehen, die Gehirn Netzwerke Interaktionen vermitteln ist wesentlich für das Verständnis des Gehirns dynamisch, und hilft auch, die zellulären und molekularen Prozesse in Perspektive zu setzen. Funktionellen Kernspintomographie (fMRI) ist eine Technik, die Zugang zu verschiedenen zellulären und metabolischen Aspekte der Netzwerk-Kommunikation ermöglicht, die schwer zugänglich sind, wenn zu der Zeit eines Neurons zu studieren. Seine nicht-Invasivität Natur ermöglicht den Vergleich von Daten und Hypothesen des Primatengehirn zu der des menschlichen Gehirns. Somit wurde das Verständnis der Auswirkungen der Neuromodulation auf lokale Mikro benötigt. Darüber hinaus sind die massiven Projektionen der neuromodulatorischen diffuse Aufstiegsanlagen gegeben, kombiniert fMRI mit pharmakologischen und neurophysiologischen Methoden wahren Einblick in ihre Organisation und Dynamik liefern. Allerdings ist nur wenig darüber bekannt, wie die Auswirkungen der Neuromodulations in fMRI und neurophysiologische Daten zu interpretieren, zum Beispiel, wie Blutoxydation pegelabhängig (BOLD) Signaländerungen in Bezug auf kognitive Veränderungen (vermutlich neuromodulatorischen Einflüsse) von Stimulus-driven oder Wahrnehmungseffekte zu entwirren.

Der Zweck dieser Arbeit ist es, die kausale Beziehung zwischen neuronaler Aktivität und hämodynamischen Reaktionen unter dem Einfluss der Neuromodulations zu verstehen. Zu diesem Zweck stellen wir die Ergebnisse von sechs Studien. In der ersten Studie wollten wir eine auf Massenspektrometrie basierende Technik einzurichten, um die Verteilung von verschiedenen Metaboliten, Neurotransmittern und Neuromodulatoren in Makakengehirn aufzudeckenWir maßen gleichzeitig die Konzentrationen dieser Biomoleküle im Gehirn und im Blut. In einer zweiten Studie entwickelten wir einen

multimodalen Ansatz, bestehend aus fMRI (BOLD und zerebralen Blutflusses oder CBF), elektrophysiologische Aufzeichnung mit einer laminaren Sonde und Pharmakologie, die Auswirkungen der Neuromodulation auf neurovaskulären Kopplung zu beurteilen. Wir entwickelten eine pharmakologische Injektionsverabreichungssystem druckbetriebenen Pumpen mit zuverlässiger Medikamente gelten entweder systemisch oder intrakortikale im NMR-Scanner. In unserer dritten Studie injizierten wir systemisch Laktat und Pyruvat zu untersuchen, ob die Plasmakonzentration von entweder dieser Metaboliten die BOLD-Antworten beeinflusst. Dies ist wichtig, dass beide gegeben Metaboliten in einem Stoffwechselgleichgewicht sind; wenn dieses Gleichgewicht gestört ist, Veränderungen in den NAD und NADH-Konzentrationen würden Veränderungen in der CBF entlocken. In einer vierten Studie untersuchten wir den Einfluss von dopaminergen (DA-erge) -Neuromodulation im BOLD, CBF und neurophysiologische Aktivität. Hier fanden wir, dass DAerge -Neuromodulation die BOLD-Antworten von der zugrunde liegenden neuronalen Aktivität distanzierte. Interessanterweise waren verbunden, um die Veränderungen in der neuronalen Aktivität eng auf die in den CBF Reaktionen gesehen Wirkungen. In einer nachfolgenden Studie untersuchten wir, ob die Wirkungen von Dopamin (DA) auf die elektrophysiologischen Reaktionen sind Rindenschicht abhängig, und ob bestimmte Muster der neuronalen Aktivität verwendet werden kann, die Wirkungen von Neuromodulations auf die neurale Aktivität zu schließen. Dies ist wichtig, da verschiedene Arten von neuralen Aktivität liefern unabhängige Informationen über die Amplitude und die Dynamik von BOLD-Antworten, und Studien haben gezeigt, dass diese Bands aus verschiedenen kortikalen Schichten stammen. Was diese Studie ergab, dass lokale Feldpotentiale (LFP) in den mittleren Frequenzen in der Tat Hinweise über die nachhaltige Wirkung der Neuromodulation auf die kortikale sensorische Verarbeitung zur Verfügung stellen kann. In Anbetracht der Ergebnisse der früheren Studie, in unserer sechsten Studie wollten wir auf das Verständnis, wie die verschiedenen kortikalen Schichten verarbeiten kann ein- und ausgehenden Informationen in den verschiedenen LFP-Bands.

Diese Ergebnisse belegen, dass -Neuromodulation profunde Auswirkungen auf die neurovaskulären Kopplung hat. Durch die Veränderung der Erregungs Hemmung Gleichgewicht neuronaler Schaltkreise vermitteln Neuromodulatoren nicht nur die neurale Aktivität, sondern auch die metabolischen Anforderungen anzupassen. Daher verstehen, wie die verschiedenen Arten von Neuromodulatoren beeinflussen die BOLD-Antwort für eine effektive Interpretation von fMRI-Daten notwendig ist, nicht nur in Aufgaben attentional und Belohnung bezogenen Prozessen mit, sondern auch für zukünftige diagnostische Verwendung von fMRI, da viele psychiatrische Störungen sind das Ergebnis von Veränderungen in neuromodulatorischen Systemen.

1. Resumen

La comunicación de las neuronas en los circuitos neuronales depende de los neurotransmisores (glutamato, acido γ-amino-butírico o GABA) y los neuromoduladores (acetilcolina, dopamina, serotonina, etc.). Sin embargo, tanto neurotransmisores como neuromoduladores son diferentes clases de moléculas y median diferentes aspectos de la actividad neuronal y del metabolismo, a pesar de compartir elementos moleculares muy similares. Los neurotransmisores, por una lado, son responsables de la transmisión sináptica de la información mientras que los neuromoduladores median diferentes eventos pos-sinápticos que resultan en cambios en el balance de la excitación e inhibición.

La influencia de la neuromodulación es esencial para la función del sistema nerviosos, sin embargo es más difícil de estudiar que neurotransmisión. Esto se debe a que los efectos de los neuromoduladores suelen ser de un inicio lento, de larga duración, y no reflejan excitación o inhibición. En contraste a los efectos de los neurotransmisores, los neuromoduladores permiten que las neuronas sean más flexibles en su habilidad de codificar diferentes tipos de información (por ejemplo, información sensorial) en varias escalas temporales. Sin embargo, es importante darse cuenta que uno de objetivos primordiales en el estudio de neuromodulación es el de entender el grado en que la acción de los neuromoduladores está coordinada a todos los niveles de la función cerebral. Es decir, desde los aspectos celulares y metabólicos hasta los niveles de redes neuronales y control cognitivo.

Por lo tanto, comprender los forma en la que diferentes moléculas median la interacción entre redes neuronal es esencial para el entendimiento de la dinámica cerebral, y también nos ayudara a comprender los procesos celulares y moleculares asociados a la percepción. La resonancia magnética funcional (fMRI, por sus siglas en inglés) es una

técnica que permite acceder a varios aspectos celulares y metabólicos de la comunicación entre redes neuronales que suele ser de difícil acceso. Al mismo tiempo y debido que la fMRI es de naturaleza no invasiva, también permite comparar resultados e hipótesis entre humanos y primates. Por lo tanto, entender los efectos de la neuromodulación en la actividad de los circuitos neuronales es de alta relevancia. Dado que las proyecciones anatómicas de los sistemas de neuromoduladores, el uso de fMRI en combinación con farmacología y neurofisiología puede incrementar nuestro conocimiento sobre la estructura y dinámica de los sistemas de neuromoduladores. Sin embargo, poco se sabe sobre cómo interpretar los efectos de neuromodulation usando fMRI y neurofisiología, por ejemplo, como diferenciar los cambios en la señal BOLD que están relacionados a diferentes estados cognitivos (presumiblemente reflejando la influencia de neuromodulation).

El propósito de esta disertación es la de comprender la relación causal que existe entre la actividad neural y la respuesta hemodinámica bajo la influencia de neuromodulación. Para tal fin presentamos los resultados de seis estudios que fueron producto de esta disertacion. En el primer estudio, desarrollamos una técnica basada en espectrometría de masa para detectar y medir la concentración de diferente metabolitos, neurotransmisores y neuromoduladores en el cerebro de primates. Dicha cuantificación se desarrollo simultáneamente tanto in sangre y cerebro. En un segundo estudio, utilizamos varias técnicas de fMRI (BOLD y flujo cerebral sanguíneo, CBF por sus siglas en ingles), registros electrofisiológicos con electrodos laminares y farmacología para acceder a los efectos de neuromodulation en el acople neurovascular. Para este fin, desarrollamos un sistema de inyecciones, basada en cambios de presión, para aplicar substancias sistémicamente o intracorticalmente dentro de un escáner de resonancia magnética. En nuestro tercer estudio, comparamos los efectos de lactato y piruvato para explorar como el desequilibrio metabólico de estas dos substancias afecta la respuesta BOLD. Esto es de gran importancia ya que ambas substancias metabólicas usualmente están en

equilibrio. Sin embargo, cuando dicho equilibrio es interrumpido, los procesos metabólicos que acontecen en la mitocondria afectan las concentraciones de NAD y NADH causado cambios en el CBF. En un cuarto estudio, exploramos los efectos de las modulación dopaminergica (DAergic) en las señales BOLD, CBF y en la actividad neuronal. Encontramos que la modulación DAergic disocia las respuesta BOLD de la respuesta neuronal. Interesalmente, los cambios que observamos en la actividad de las neuronas estaba altamente acoplados a los efectos que observamos en la señal de CBF. En un estudio subsecuente, exploramos si los efectos de dopamina en la actividad neuronal es diferentes en las distintas capas de la corteza cerebral. Al mismo tiempo y ya que los neuromoduladores afectan la actividad de circuitos neuronales, exploramos si dichos efectos pueden usados como marcadores de la influencia de la neuromodulación . Esto es importante, ya que diferentes tipos de actividad neuronal brinda información sobre la amplitud y dinámica de la repuesta BOLD, y estudies han demostrado que estas bandas se originan de diferentes capas cortical. Este estudio revelo, que los potenciales de capo (LFPs, por sus siglas en ingles) en frecuencias intermedias puede ser indicativos sobre los efectos de neuromodulation en el procesamiento cortical. Dado los resultados en el estudio previo, en un sexto estudio, nos enfocamos a entender que tan diferentes las capas de la corteza procesan información entrante y saliente en diferentes frecuencias de los LFPs.

Estos descubrimientos demuestran que los efectos de los neuromoduladores tiene una fuerte influencia en el acople neurovascular. Los neuromoduladores cambian el balance de excitación e inhibición de los circuitos neuronal, pero también median las demandas metabólicas. De esta manera, entender cómo interpretar los efectos de los neuromoduladores en la respuesta BOLD es esencial para una interpretación veraz y efectiva de los datos generados con fMRI. Estos resultados, no solo nos permiten comprender los procesos que están relacionados a la atención o de varios procesos cognitivos, sino que a su vez, nos permite comprender la señal de fMRI para su futuro uso

en la medicina diagnostica, ya que muchas enfermedades psiquiátricas están asociadas a trastornos en el sistemas neuromoduladores.

2. Synopsis

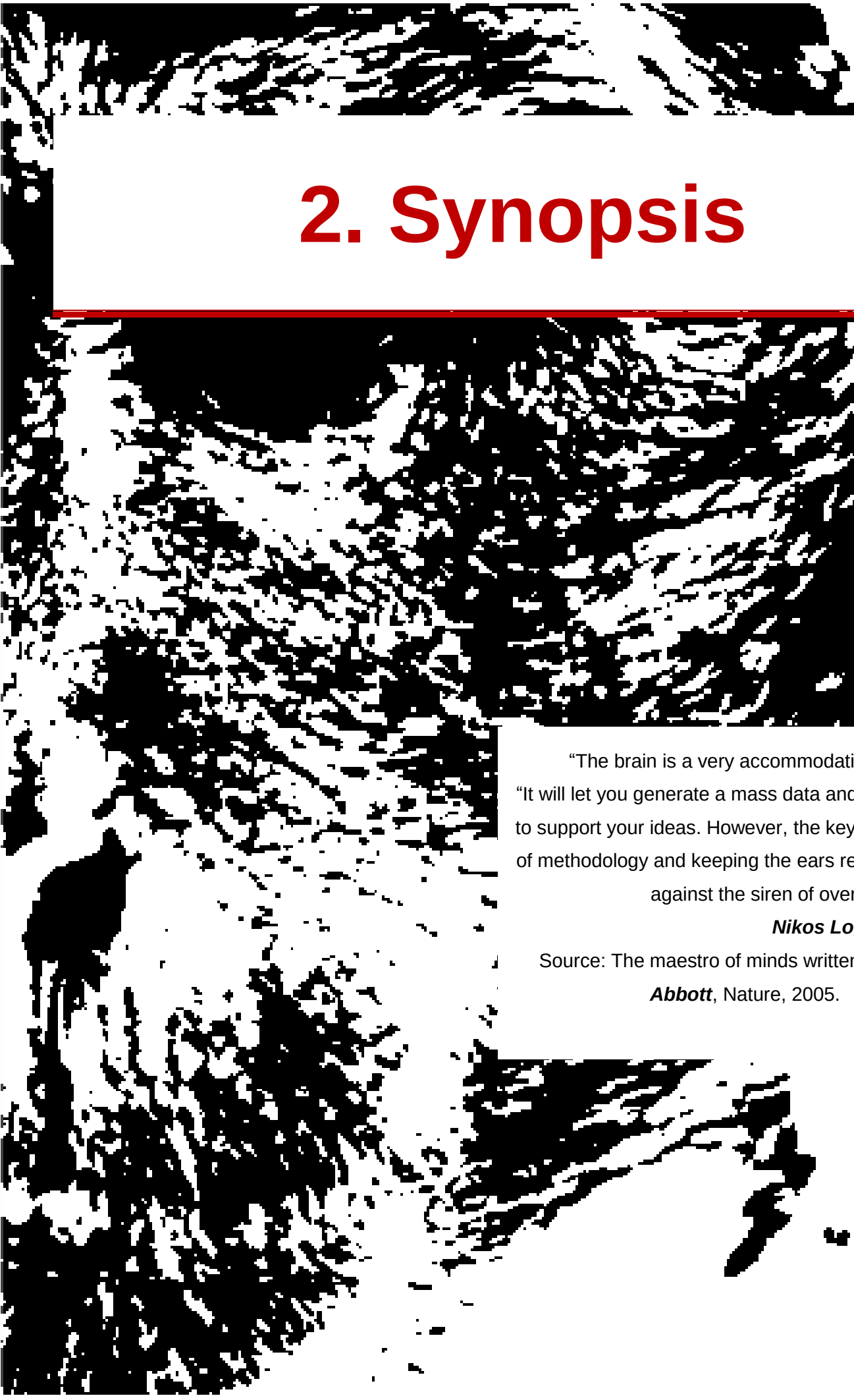

"The brain is a very accommodating structure"… "It will let you generate a mass data and interpret them to support your ideas. However, the key is strict quality of methodology and keeping the ears resolute plugged against the siren of over-interpretation"

Nikos Logothetis, 2005

Source: The maestro of minds written by ***Alison Abbott***, Nature, 2005.

2.1 Introduction

2.1.1 General Remarks

The communication between neurons within neural circuits relies on neurotransmitters (glutamate, γ-aminobutyric acid (GABA)) and neuromodulators (acetylcholine, dopamine, serotonin, etc.), which are usually released subsequent to presynaptic action potentials (Marder, 2012; Marder et al., 2014). However, despite sharing similar molecular elements, neurotransmitters and neuromodulators are distinct classes of molecules and they mediate different aspects of the neural computation and metabolism (Dayan, 2012; Disney et al., 2007; Fellous and Linster, 1998; Gil et al., 1997; Gu, 2002; Hasselmo, 1995; Yu and Dayan, 2005). Neurotransmitters on one hand are responsible for synaptic signal transmission (classical transmission) while neuromodulators exert their functions by mediating different postsynaptic events that result in changes to the balance between excitation and inhibition (Logothetis, 2008).

Neuromodulation, while essential to nervous system function, has been significantly more difficult to study than neurotransmission. In principle, because the effects elicited by neuromodulators are usually of slow onset, long duration, and are not simple excitation or inhibition (Hamood and Marder, 2014; Harris-Warrick and Marder, 1991; Marder et al., 2014). Neuromodulators, in contrast to neurotransmitters, give to neurons the opportunity to be more flexible in their ability to encode different sorts of information (e.g. sensory information) on a variety of time scales, and adjust their metabolic demands. However, it is important to appreciate that the main challenge in the study of neuromodulation, is to understand the extent to which neuromodulators action is coordinated at all levels of brain function (Dayan, 2012; Herrero et al., 2008; Yu and Dayan, 2005). That is, from the cellular and metabolic level, to network and cognitive control.

For instance, understanding the molecular basis by which brain networks interact and communicate between each other is essential for the comprehension of the brain dynamics, and also helps to put the cellular and molecular processes in perspective. However, although a great deal has been learned from characterizing the responses of single neurons involve in sensory-, motor- as well as in cognitive function. Functional magnetic resonance imaging (fMRI) is an example par excellence of a method allowing non-invasive investigation of groups of neurons and neural networks involve in behavior and sensory processing. Therefore, given the massive projection patterns of the neuromodulatory diffuse ascending systems, fMRI potentially combined with pharmacology and neurophysiology may provide insight into how neural networks dynamics is alerted by neuromodulation.

An important aspect about fMRI signals, is that it can measure a broad variety of neural events, even if they are brief since most have metabolic consequences (Logothetis et al., 2012; Russ and Leopold, 2015). However, it is worth noting that fMRI does not measure electrical or neurochemical activity directly, but it relies on a combination of changes in blood deoxygenation and blood flow that are induced by neural activity (Ogawa et al., 1990; Ogawa et al., 1992). Nonetheless, whether all aspects of neural activity drive the blood-oxygen level dependent (BOLD) responses equally, and if not, which ones are more important: for instance the input versus the output from an area, or inhibition versus excitation, stimulus driven or neuromodulation activity. Answer to such questions will directly affect our interpretation of fMRI results and thus help us to understand results obtained with fMRI.

In my PhD work I set out to investigate the influence of neuromodulation on neural and neurovascular coupling activity. To guide the reader into the intriguing world of fMRI and the neural, as well as the metabolic, events associated to the dynamics of this signal, I will summarize the knowledge regarding the technique. First, I will briefly discuss the known physical principles about fMRI signals as well as the metabolic and neural mechanisms

that give rise to the BOLD responses. Additionally, given the difference between neurotransmission and neuromodulation and that they mediate different aspects of neural computation and metabolism, we extensively discuss their similarities and the different processes they mediate. I also present the multimodal approach used for elucidating the causal relationship of neuromodulation into neural and haemodynamic activity. This approach consists of fMRI (BOLD and CBF), electrophysiological recording with a laminar probe and pharmacology which is extensively discussed in our manuscripts. Subsequently, I will briefly introduce the manuscripts and extensively discuss their findings. Based on our finding, I also formulate a number of new but ripe predictions for testing, and we also present possible clinical application relevant to the studies in this dissertation. I aim to give a comprehensive outline of this fascinating field and highlight the need of a novel approach to reach deeper insight into the unsettled mechanisms mediated by neuromodulation.

2.1.2 Basic principles underlying fMRI signals

fMRI techniques relay on set of physical principles and to properly understand them we should begin by looking at a single nucleus. Quantum particles such as the proton and the electron possess an important quantum mechanical property called spin. In the particular case of the protons as hydrogen atoms (^{1}H), the most abundant element in the human body, Spin is a purely quantum mechanical property and has no macroscopic equivalent, but it can be thought of as spheres that are spinning about their axis. This gives rise to a net magnetic moment along the direction of the axis of the spins, which is the source of the signal we seek to measure. When placed in a strong magnetic field (B_0), the nuclei align with the field, creating a net longitudinal magnetization in the direction of the field. While the aligned nuclei precess about the B_0 axis at an angular frequency determined by the Larmor frequency, but at a random phase with respect to one another. The Larmor frequency is specific to the nucleus and depends on the field strength of B_0. The application of a radiofrequency (RF) electromagnetic field pulse causes the nuclei to absorb the

energy at a particular frequency band, and become “excited”. We can imagine this process as the RF pulse aligning the phase of the precessing nuclei and tipping them over into the transverse plane, driving the net longitudinal magnetization M_0 to zero, and establish phase-coherence in the x,y-plane, the transversal magnetization. The transverse component of the spins oscillates in the xy-plane (the so called free induction decay, FID) that can be measured by the RF-coil, which is the key signal measured in MRI and fMRI experiments. After the RF pulse is removed, the system gradually returns to equilibrium. Now the nuclei emit the absorbed energy as they “relax”. Net transverse magnetization disappear due to loss of phase-coherence, in a process known as transversal relaxation, while the longitudinal magnetization grows back to its original size in a process referred to as longitudinal relaxation. During this time a signal is created that can be measured using a receiver coil. Longitudinal relaxation represents the restoration of net magnetization along the B_0 direction as the nuclei return to their original aligned state. It is seen as an exponential recovery in magnetization described by a time constant T_1. Transverse relaxation is the loss of net magnetization in the transverse plane due to loss of phase coherence. Since the net magnetization depends upon the combined contribution of a large number of nuclei, its value is largest when all the nuclei are in phase. However, the removal of the RF pulse causes the nuclei to de-phase, causing an exponential decay in magnetization described by a time constant T_2. Both the T_1 and T_2 values depend on tissue type and it is this property that allows for the creation of structural MR images that can be used to differentiate between different tissue types. The term T_2^* is similar to T_2, but also depends on local inhomogeneities in the magnetic field caused by changes in blood flow and oxygenation. These inhomogeneities cause the nuclei to dephase quicker than they normally would. Certain pulse sequences are able to eliminate the effects of these inhomogeneities, while others seek to emphasize them. The T_2^* signal provides the basis for fMRI, as it is sensitive to neurovascular changes that accompany psychological and behavioral function.

One important aspect of magnetic resonance imaging is its ability to create a spatial map of signals non-invasively, based on a variety of different contrasts that are sensitive to both the number and properties of the nuclei being imaged. The basic principle of most of the commonly used sequences is fairly simple: assume the initial value of the net magnetization is given by M0. By altering how often we excite the nuclei (TR) and how soon after the excitation we begin data collection (TE) we can control which characteristics of the tissues is emphasized. The flip angle (FA) indicates the angle by which the net magnetization was tilted away from its alignment with B1.

The MRI scanner is ultimately provides us with an image that is represented by a matrix of numbers corresponding to spatial locations. These images generally show the spatial distribution of some property of the nuclei, such as the density of the specific nuclei, their mobility, or the relaxation time, within a tissue or area. Therefore, the different pulse sequences define particular aspects of RF pulses and the shape of the magnetic field, that allow us to the acquired data into a map of the underlying signal sources.

2.1.3 The tight neurovascular and neurometabolic coupling

Individual neurons are surrounded by complex interaction with capillaries, glial cells and adjacent neurons (Hillman, 2014; Kasthuri et al., 2015). This coupling, so-called neurovascular and neurometabolic coupling, serves as medium for the cell-to-cell communication, metabolite transport and ensure adequate supply of oxygen and glucose to neurons when needed (Andreone et al., 2015; Leithner and Royl, 2014). The average width of the space between brain cells is ~ 20 nm, that is, three times smaller than the diameter of a neuron or a glial cell body (Kasthuri et al., 2015). Despite the small space between neurons, the diffusion of ions and other solutes within this thin brain-extracellular-space is reasonably high, thus, providing the elements for the resting and action potential of cells, and acting as a volume-conductor (Logothetis et al., 2007).

The brain extracellular fluid (BECF) contains a large range of molecules involved in the communication within brain cells and in the maintenance of the brain's high metabolic demands (Ivanisevic et al., 2014; Magistretti and Allaman, 2015). Additionally, the BECF is the route for which molecules such as O_2, glucose and amino acids are delivered to the brain, and products of metabolism, including CO_2 and catabolized neurotransmitters leave the brain (Leybaert, 2005).

The composition and the concentration of solutes in the BECF are continuously changing with neural activity, and variations in the composition of the BECF can also affect the neural activity (Cauli and Hamel, 2010; Ding et al., 2016; von Pfostl et al., 2012; Zaldivar et al., 2014; Zhang et al., 2008). However, different and multiple mechanism are carefully deployed by the brain to control the composition of the BECF: *i)* the blood-brain-barrier (BBB) prevents that changes in the blood chemical composition affects the BECF (Hawkins and Davis, 2005; Rapoport, 1996; Weber et al., 2008); *ii)* the BECF and the cerebral-spinal-fluid (CSF; see Zhang et al., 2008) are in slow diffusional equilibrium, therefore self- and mutually-regulating their composition; and *iii)* the surrounding glial cells provide structural and metabolic support neurons, and they also condition the BECF composition (Amzica and Steriade, 2000).

Following the activation of neural activity, the neurovascular coupling increases the cerebral blood flow (CBF) in order to match the supply of blood and nutrients (Logothetis, 2008; Sokoloff, 1977b). Under normal circumstances, glucose is the only useful energy substrate for the brain but its metabolism differs in neurons and astrocytes (Chih and Roberts Jr, 2003; Magistretti and Allaman, 2015). For instance, neurons are preferentially oxidative while astrocytes prefer glycolysis (Bouzier-Sore et al., 2006). That is, neurons prefer to fully oxidized glucose and metabolites, such as pyruvate and lactate, for the production of end-stage fuel in the form of adenosine-triphosphate (36 ATP per glucose molecule or 17 if the substrate is lactate/pyruvate). All of these metabolic processes taking place in the mitochondria, involve the tricarboxylic acid (TCA) cycle and electro transfer in

the respiratory chain, O_2 consumption, and the production of CO_2 and H_2O (Magistretti and Allaman, 2015; Pellerin and Magistretti, 2004). The glycolysis, however, involves the production of two molecules of ATP as glucose is processed into pyruvate. Lactate is also formed by glycolysis: under low oxygen tension (Hertz et al., 2007), pyruvate is converted to lactate in a process that regenerated NAD+, and essential cofactor to sustain a glycolytic flux (Belanger et al., 2011).

However, lactate can also be produced under normal O_2 conditions (Samuelsson et al., 2007; von Pfostl et al., 2012; Yao et al., 2003) and when it is fully oxidized, it provides up to 10 % of the brain energy requirement (Boumezbeur et al., 2010; Gallagher et al., 2009). Usually lactate is transported out of the astrocytes, and into neurons, where it fuels the neural-activity-related energy needs, and studies have shown that neurons preferentially oxidizes lactate over glucose when both substrates are present in the BECF (Bouzier-Sore et al., 2006; Itoh et al., 2003). Nonetheless, the reasons for the increase in lactate production during neuronal activity is not entirely clear. Studies have suggested that lactate production increases when the glycolytic activity transiently exceeds ongoing oxidative metabolism. This is usually observed when the NADH shuttles are not activated as quickly as needed (Clarke et al., 1989a, b).

Energy utilization is related to the activity of ionic pumps and metabolic transporters that help to reestablish the electrochemical gradient and the composition of the BECF. Several experimental evidence have suggested that the restoration of ion gradients occurs in parallel with the glutamate/glutamine cycling (Attwell and Laughlin, 2001a; Bak et al., 2006). As a consequence of glutamatergic neurotransmission 80% of the glucose entering the brain is oxidized (Petroff et al., 2002). The same can be said for γ-aminobutyric acid (GABA), which can be included in the glutamate/glutamine cycle, because GABA is partly recycled in astrocytes via glutamine synthesis (McKenna, 2007). However, this process of GABA would not account for more than 8 – 10% of the total glutamine flux in the human cortex (Shen et al., 1999). The essential point is that the majority of the energy

consumption is directly reflecting the level of glutamatergic neurotransmission and its associated recycling.

From an anatomical perspective, astrocytes are ideally positioned to guide information in a bidirectional manner between neurons and blood vessels (Belanger et al., 2011; Cauli and Hamel, 2010; Dienel et al., 2007). The endfeet of an astrocyte, usually contacts hundreds of synapses and covers about ~ 98 % of the alblumical surface of cerebral vessels (Mathiisen et al., 2010; Simard and Nedergaard, 2004). At the same time, astrocytes are also coupled via gap junctions, thus, establishing an electrical syncytium that allows localized signals to be spread across broad regions (Parys et al., 2010). This structural coupling provides an efficient means to spread and amplify metabolic signals across neural networks (Hertz et al., 2007). Moreover, gap junctions also provide a route for information to be conducted to the upstream pial circulation (Figueroa and Duling, 2009). A variety of vasoactive molecules, such as H^+, K^+, adenosine nitric oxide, etc., increase the CBF in a activity-dependent manner (Attwell et al., 2010; Hamilton et al., 2010), which entails that glutamate signaling on astrocytes causes/triggers vasomotor responses, either vasoconstriction and vasodilation (Attwell et al., 2010; Attwell and Laughlin, 2001a; Iadecola and Nedergaard, 2007). Not to mention, that these molecules have the capability to diffuse to smooth muscle cells and cause vascular effects influencing the hemodynamic signals (Iadecola and Nedergaard, 2007; Mathiisen et al., 2010).

2.1.4 What we know about the mechanisms behind the BOLD

The blood oxygenation-level dependent (BOLD) signal, takes advantage of differences in the magnetic properties of oxygenated- (OHb) and deoxygenated-hemoglobin (dHB; Ogawa et al., 1990). When the neuronal activity increases in a certain area, it triggers an increase in the metabolic demands for O_2 and nutrients (Belanger et al., 2011; Magistretti and Allaman, 2015). It can also be seen, as the neural firing signaling the extraction of O_2 from OHb causing the hemoglobin to become paramagnetic as iron atoms are more exposed to the surrounding water (Buxton, 2013). This creates small distortions in the

magnetic field that cause a decrease in T_{2^*}, leading to a faster decay of the signal and a local decrease in BOLD signal (Logothetis and Wandell, 2004). Subsequently, overcompensation in blood flow increases the amount of OHb and a decrease in the dHb concentration which increases the T_{2^*} and leads to a signal increase in the gradient-echo (GE) images (Kim, 1995; Ogawa et al., 1992).

Moreover, the BOLD signal represents a complex response controlled by several parameters (Kim and Ogawa, 2012; Ogawa et al., 1990) and its magnitude is determine by the CBF, the cerebral-metabolic consumption of oxygen ($CMRO_2$) and the cerebral blood volume (CBV; Buxton, 2013; Leontiev et al., 2007). The BOLD signals has both negative and positive components reflecting different neuronal (Logothetis et al., 2001; Shmuel et al., 2006) and metabolic processes (Goense et al., 2012; Sokoloff, 1977a, b). For instance, positive BOLD corresponds to the hyperoxygenated following an increased in the CBF, as the haemoglobin in capillaries and post-capillary vessels shifts toward OHb. This reduces the magnetic field gradients surrounding capillaries and veins and increases the signal intensity in BOLD images (Logothetis and Wandell, 2004; Ogawa et al., 1990; Ogawa et al., 1992). Following stimulation, CBV, which increases during elevated activity, returns to its basal value more slowly than CBF and $CMRO_2$, resulting in a post-stimulus undershoot in signal intensity (Attwell and Laughlin, 2001a). On the other hand, negative BOLD occurs because the local increase in CMRO2 that accompanies neural activity precedes the elevation of CBF in the activated region, causing an early transient in dHb concentration.

It is worth noting that, the BOLD signal only provides an indirect measure of neural activity. It is therefore important to understand how well the BOLD signal reflects actual increases in neuronal firing and whether all the types of neural activity drive the BOLD responses equally, and if not, which ones are more important: for instance the input versus the output from an area, or inhibition versus excitation, stimulus driven or neuromodulatory activity. In short, the work by Logothetis et al., (2001) showed that the BOLD signal corresponds

closely to the local electrical field potentials (LFPs) surrounding a group of cells, which is likely to reflect changes in post-synaptic activity under many conditions. In good agreement with these observations, several studies using the deoxyglucose (2-DG) autoradiographic techniques demonstrated that regional glucose utilization is directly related to neuronal synaptic activity (Sokoloff, 1977b; Sokoloff et al., 1977). In this view, the greatest 2-DG uptake was found to be in the neuropil, i.e. in areas rich in synapses, dendrites, and axons, rather than in cell bodies. Moreover, studies that compared orthodromic (activation of both pre- and postsynaptic terminals) and antidromic electrical stimulation (activating postsynaptic terminals only) demonstrated that glucose utilization increases only at presynaptic terminals (Kadekaro et al., 1985; Kadekaro et al., 1987). Along with these line of evidence, the highest density of cytochrome oxidase (enzyme of the respiratory chain) is found in somato dendritic regions adjacent to axon (Di Rocco et al., 1989; Kageyama and Wong-Riley, 1986).

However, to better understand the relationship between BOLD signal and the underlying cellular activity it is of obvious importance to understand what type of neural activity drives the hemodynamic responses and how this relationship is mediated by the different neuromodulators (Logothetis, 2008).

2.1.5 Neural correlates of the BOLD-fMRI signal

Electrophysiological studies at the systems and behavioral level typically record extracellular signals, which reflect synaptic and spiking activity (Belitski et al., 2008; Belitski et al., 2010; Einevoll et al., 2013). As we discussed earlier, neurons are embedded in the BECF, which acts as a volume conductor, allowing the passive spread of electrical signal (Logothetis, 2008; Oeltermann et al., 2007): when excitatory postsynaptic potentials occur in one part of a neuron its membrane potential will momentarily be depolarized due to current flowing into the cell (inward currents). This causes an outward flow of current along the core of the cell (Einevoll et al., 2013; 2007). This current is, subsequently, matched by a return current flowing through the extracellular space. The active region of

the membrane together form a current sink, while the inactive region act collectively as a current source (current-source analysis, or CSD, is used for the source and sink detections). In other words, the current sink is localized at the site of synaptic excitation, where there is a net influx of positive ions.

Given the resistive nature of the ECF these current generate the so-called extracellular field potentials (EFP; see Destexhe et al., 1999; Logothetis, 2008). The signals detected by an electrode placed at neural site represents the mean-EFP from the spatially weighted sum of sinks and sources along multiple cells at this particular point (Buzsaki et al., 2012; Buzsaki and Wang, 2012). Three different signals are usually extracted from the extracellular microelectrode recordings, each covering a different frequency region of the acquired signals: *(i)* the multiple-unit-activity (MUA) is characterized as compound electrical signals in a frequency range around 900 to 3500 Hz. This signal has been shown to reflect population spiking activity of neurons (seems to incorporate signals from a sphere of 150–300 μm radius; (Buchwald et al., 1966; Gray et al., 1989; Legatt et al., 1980; Logothetis, 2008)) and vary systematically with stimulus properties in the same way as the activity of single neurons (Kayser et al., 2007; Whittingstall and Logothetis, 2009); *(ii)* covering the same frequency range as MUA, the single-unit activity (SUA) reports mainly on the activity of the principal neurons that form the major output of a cortical area; and *(iii)* the local field potentials (LFPs, low-pass filter cutoff of approximately 250 Hz) is defined as the low-frequency components of the EFP and represents the weighted average of synchronized dendro-somatic components of the synaptic signals (input of a given cortical area as well as its local intracortical processing) of a neuronal population within 0.5–3 mm of the electrode tip (Logothetis, 2008; Mitzdorf, 1985, 1987).

The LFP-power modulation is traditionally decomposed and interpreted in the frequency domains initially introduced in the electroencephalography (EEG) literature (Coenen, 1995; Nunez, 1981): delta (0.5 – 4 Hz), theta (4 – 8 Hz), alpha (9 – 15 Hz), beta/nMOD (18 – 38 Hz), gamma (50 – 100 Hz) and high-gamma (100 – 150/250 Hz). However, there

are inconsistencies in the exact definition of frequency bands, given that their frequency definition are associated to distinct behavioral states or sensory inputs (Steriade, 2006; Whittingstall and Logothetis, 2009). An alternative and powerful approach to separate functionally meaningful LFP-bands, is to quantify co-variation in amplitude across frequencies (Belitski et al., 2008). This procedure consists in computing correlation among LFP-bands to detect whether or not the amplitude variations in one band are dependent or independent from the amplitude variations in another (Belitski et al., 2008; Magri et al., 2012a). Accordingly, to identify the boundaries between statistically independent bands two types of correlations among frequency have been used: (*i*) signal correlations reflect similarities between different frequency bands in their tuning to external conditions; (*ii*) noise correlations reflect the trial-by-trial variability between different bands after discounting their similarities in tuning (Belitski et al., 2008).

The signal and noise correlations approach in combination with mutual information have provided powerful means to quantify both the amount and the nature of information carried by each frequency band (Belitski et al., 2008; 2010; Brunel, 2016; Brunel and Wang, 2001, 2003; Panzeri et al., 2010). What these studies found, is that in visual cortex frequencies above 50 Hz and frequencies bellow 20 Hz shared neither signal correlation nor noise correlations, indicating that they act as independent visual information channels and probably originate from separate neural process. These studies, interestingly, also revealed that frequencies between 18 – 30 Hz exhibited high noise correlations but low signal correlations, and carry little stimulus information (Belitski et al., 2008). This profile of information and correlations have led to suggest that the signals in this frequency range are generated by common processes that are unrelated to the visual stimuli, perhaps, the influence of neuromodulation (Einevoll et al., 2013; Magri et al., 2012b).

Given the distinction of the different signals that can be obtained from the extracellular recordings and due that they can be decomposed depending on the amount and nature of information they carry, one can ask which signals best explains the activity reflected in the

fMRI experiments?. Simultaneous measurements of intracortical neuronal activity and fMRI in the behaving and anesthetized non-human primates have characterized the relationship between the activity of each LFP and BOLD, as well as MUA and BOLD responses (Goense and Logothetis, 2008; Magri et al., 2012b; Rauch et al., 2008a; Rauch et al., 2008b; Zaldivar et al., 2014). In view of these studies, the correlation coefficients are higher between LFP and BOLD that between MUA and the BOLD signals (Logothetis et al., 2001; Viswanathan and Freeman, 2007). This implies that the overall synaptic activity or the input of an area is a strong generator of BOLD signal than its output (Logothetis, 2008; Logothetis et al., 2010; Viswanathan and Freeman, 2007). Furthermore, these findings also revealed that BOLD signals and LFP are preferentially correlated at specific frequency bands of the LFP (Magri et al., 2012b). This is not surprising giving that different LFP bands correlate with distinct behavioral states and reflect to a large extent the activity of different neural processing pathways (Belitski et al., 2008).

Studies combining fMRI with neurophysiology, either simultaneously or consecutively, have found frequency-dependent match between the fMRI signals and the different LFP-bands (Goense and Logothetis, 2008; Logothetis et al., 2001; Magri et al., 2012b). For instance, frequency bands bellow 12 Hz showed negative correlation with the imaging signals. In other words, reduced field potential during increased blood flow response (Magri et al., 2012b). However, high frequencies, in particular bands between 50 and 100 Hz, showed good correlation with the imaging signal and, importantly, stronger correlations than the observed for the MUA (Logothetis et al., 2001; Rauch et al., 2008b).

Another aspect worth to consider is that frequencies in the gamma range (50 – 100 Hz) and frequencies bellow 20Hz are strongly modulated by the sensory stimulus, which has been used to assess the correlations to the BOLD-responses (Belitski et al., 2008; Magri et al., 2012b). Moreover, as discussed ealier, the activity reflected in frequencies between 18 to 38 Hz dissociates from the activity in the low and high-frequency bands. However, it appears that the activity in this frequency band is highly informative about how fast

changes in the BOLD signal occur following changes in the gamma power (Magri et al., 2012b). That is, when the power in this band is high, BOLD responses would increase fast and decrease slowly (sustained decrease). On the other hand, when the power in this band is low, the BOLD responses would raise slowly but return to baseline activity faster. Release of neuromodulators such as acetylcholine, dopamine, noradrenaline, and serotonin has been shown to affect cortical excitability (Steriade, 1993). Neuromodulators are known to alter the relationship between the BOLD signal and neural activity in multiple and different ways (Dayan, 2012), for example, by affecting key neural parameters such as the balance between excitation and inhibition (Rauch et al., 2008b; Zaldivar et al., 2014), or they may be involved in the regulation of cerebral blood flow and neurovascular coupling (Dayan, 2012; Iadecola, 2004), therefore allowing faster or slower hemodynamic responses.

2.1.6 Neurotransmission and Neuromodulation

Chemically mediated transmission is the major means by which signals are communicated between neurons within neural circuits. These transmitters of information can be conceptualized as an endogenous substance being released by neurons, acts on receptors typically located on the membranes of postsynaptic cells and produces functional changes in the biophysical properties of the target cells (Miledi, 1973). However, it is worth noting that not all of these molecules behave similarly (Dayan, 2012; Gil et al., 1997) and given their difference in dynamics, transmitters can be divided in two basic types: *(i)* neurotransmitters which are release from sources intrinsic to a local circuit (classical neurotransmitters, such as glutamate, GABA and glycine); and (*ii)* neuromodulators, those that arise from extrinsic sources (such as dopamine, serotonin, etc.).

The molecular elements that mediate neurotransmission and neuromodulation are similar but they have different temporal scales and dynamics, which can be explained by differences in the structure and function of their receptors (Clapham, 1994; Geppetti et al.,

2015; Herguedas et al., 2016; Rao and Finkbeiner, 2007). For instance, when neurotransmitters are released by a presynaptic neuron, they directly, and immediately, influence its postsynaptic target. Such influence of the neurotransmitters, is usually fast given that their receptors are harnessed to ion-channels that open, to increase ion conductance, once the neurotransmitter binds its receptor (Rao and Finkbeiner, 2007). On the other hand, the effects elicited by neuromodulators, tend to be of slow onset and long duration since their receptors are coupled via second messenger pathways (also known as metabotropic receptors), which do not directly open ion-channels but modulate their opening and closing time, as wells as their affinity to specific ions (Clapham, 1994; Geppetti et al., 2015).

Furthermore, neuromodulators and neurotransmitters alter the regional metabolic demands, whether they modulate global activity of microcircuits or differentially affect a small subset of neurons (Dayan, 2012; Harris-Warrick and Marder, 1991; Logothetis, 2008). However, both classes of transmitters differ in their mechanisms mediating brain metabolism (Attwell and Laughlin, 2001a; Gibson et al., 1981; Gsell et al., 2006; Hawkins, 2009; Leybaert, 2005). In principle, neurotransmitters are usually reabsorbed by presynaptic neurons or by glia, and/or broken down into a metabolite that can either be used to produce energy or to generate more neurotransmitter (Bak et al., 2006; Magistretti and Allaman, 2015). For example, glutamate and γ-aminobutyric acid (GABA), the major excitatory and inhibitory neurotransmitters (Gil et al., 1997; Hasselmo, 1995), are recycled by the presynaptic neurons to replenish the glutamate or GABA vesicular pool (Bak et al., 2006; McKenna, 2007; Stobart and Anderson, 2013). In addition, the remaining glutamate/GABA in the synaptic cleft can, to some extent, be catabolized within the TCA-cycle in astrocytes, thereby directly mediating the metabolic demands (Bak et al., 2006).

Neuromodulators, in contrast to neurotransmitters, end up spending a significant amount of time in the BECF, influencing (or modulating) the activity from several other neurons and mediating the CBF (Dayan, 2012). Such influence in neural activity and CBF can either

be direct or indirect, and is highly dependent on receptors' location and density. Hence, the effects of neuromodulators can be the result of various mechanisms: *(i)* given that the receptors of neuromodulators are usually expresses on the vasculature surface, they can directly mediate the vascular tone bypassing the glia-cells.. However, as mentioned earlier, such influence would highly depend on whether or not the receptors are expressed in a defined brain region (Krimer et al., 1998); *(ii)* the activation of neuromodulator receptors on the target cells results in a cascade of biochemical reactions that modulate the response properties of neurons and can either increase or decrease the synthesis of ion channels, metabolic transporter and enzymes (Froemke, 2015; Gil et al., 1997; Marder, 2012; Marder and Thirumalai, 2002). Hence, resulting increased/decreased inflow/outflow of ions and metabolites which eventually changes the composition of the BECF and influence the vascular tone (Amzica and Steriade, 2000; Simard and Nedergaard, 2004); *(iii)* adenosine, which mediates the vascular tone directly, is usually produced as a consequence of activating second-messengers signaling cascades which yields to increased, or decreased, ATP-utilization and the release of adenosine to the BECF; and *(iv)* neuromodulators also mediate the responses of neurons via long-range interactions with other brain regions (Jbabdi et al., 2015; Knosche and Tittgemeyer, 2011). In other words, a neuromodulator can affect the activity from region A directly, but can also modulate the activity from the region B indirectly. That is, because region A and B are interconnected and their activity are dependent of each other. Therefore, if the activity from region A is highly influence by a certain class of neuromodulator, this would either increase or decrease the neural activity in region B following by changes in its metabolic demands (Logothetis et al., 2010; Tolias et al., 2005; Zaldivar et al., 2014).

Overall, neuromodulators alter the input/output properties of neural circuits and optimize their energy expenditure (Attwell and Laughlin, 2001b; Marder et al., 2014; Sengupta et al., 2014). The anatomy and physiology of neuromodulator systems have been well described (Gu, 2002). For instance, cortical innervation by axons containing the

neuromodulators, acetylcholine (Ach), dopamine (DA), noradrenaline (NE), serotonin (5HT) or histamine, arises mostly from cell groups located in the nucleus basalis of Meynert in the basal fore brain (Mesulam et al., 1983), ventral tegmental area of the midbrain (VTA), locus coeruleous (LC in the midbrain), raphe nuclei in the brain stem and tuberomammillary nucleus in the posterior hypothalamus (Matthews et al., 2016), respectively. Axon terminals of these neuromodulator systems build up a network occupying the entire cerebral cortex and mediating different aspects of neural computation (Gu, 2002). More interestingly, each of the neuromodulatory pathway tends to show a distinct laminar distribution patterns and densities of axon fibers, (Eickhoff et al., 2007a; 2007b) and within a cortical region, the laminar distribution of a given neuromodulators is usually different across species (Gu, 2002). Furthermore, neuromodulators can form symmetric and asymmetric synapses with cortical neurons which include both pyramidal neurons (glutamatergic) and interneurons (GABAergic). Responses to each of the neuromodulator transmitters are mediated by numerous receptor subtypes which are linked to multiple signal transduction mechanism.

2.1.7 Pharmacology: pharmaco-MRI (phMRI)

The most direct way to test the *"causal"* role of the neurovascular coupling- and neurophysiology-related responses is to directly perturb that neural activity and measure its effects on fMRI activity (Logothetis et al., 2010; Rauch et al., 2008a; Rauch et al., 2008b; von Pfostl et al., 2012; Zaldivar et al., 2014). Optogenetics strategies to control genetically distinct populations of neurons with light have been rapidly evolve and widely adopted in neuroscience (Lee et al., 2010). Although this technic have already reshaped neuroscience by allowing for more precise control of circuit function, current limitations of these approaches should be considered. For instance, it is unlikely that all neurons sharing the same genetic marker have the same function or project to the same sites. At the same time, given the diversity of neuron types, there is a lack of genetic tools for cell-type specific targeting of proteins in the primate brain (Izpisua Belmonte et al., 2015; Miller et al., 2016).

Lastly, but not least, photostimulation is not able to produce patterns of neural fluctuations that are above 80 Hz (Malyshev et al., 2015)

Pharmacology has been used to investigate how neurotransmitter- and neuromodulatory-systems influence neural activity, providing the means to study the neurochemical basis of brain modulation. It is through pharmacology that the characterizations of the neurotransmitters involve in excitation and inhibition was made possible (Hayashi, 1952, 1959). For example, the excitatory and inhibitory nature of glutamate and GABA, respectively, was first motivated by pharmacology experiments carried by Takashi Hayashi. His studies revealed that the injections of glutamate into the cerebral ventricles of dogs caused generalized seizures (Hayashi, 1952) which were inhibited by subsequent intraventricular injections of GABA (Hayashi, 1959). This generalized seizures were the result of changing the composition in the CSF which affects the composition in the BECF (Amzica and Steriade, 2000; Hawkins and Davis, 2005; Hawkins, 2009; Hayashi, 1952, 1959; McKenna, 2007). This resulted in a coordinated and generalized activation of glutamatergic receptors which caused the seizures.

The neurotransmitters GABA and glutamate are important mediators of many critical physiological and metabolic, as well as pathophysiological, events underlying brain function and dysfunction. Pharmacological studies using drugs that selectively block or augment the action of GABA or glutamate support the notion that these two neurotransmitters, despite their opposing excitatory and inhibitory action, control the overall excitability in the brain (Armstrong-James et al., 1993; Bak et al., 2006; Chen et al., 2005; Gsell et al., 2006; Herguedas et al., 2016; Herrero et al., 2013). For instance, the excitatory actions of glutamate are mediated by AMPA (α-amino-3-hydroxy-5-methyl-4-isoxazolepropionic acid) and NMDA (N-methyl-D-aspartate) receptors located in postsynaptic neurons (Hirsch et al., 2015; Rao and Finkbeiner, 2007; Self et al., 2012; Siegelbaum and Tsien, 1983). Local excitation, perhaps induced by sensory stimulation or by a cognitive task, is strongly affected by recurrent inhibition mediated by GABAergic

interneurons (Douglas and Martin, 2004; Kujala et al., 2015). Together, glutamate and GABA are not only re responsible for a major part of neurotransmission but also mediate changes in the regional CBF (Goense and Logothetis, 2008; Logothetis, 2008).

Despite their seemingly ubiquitous projections, neuromodulatory systems have strikingly specific activity-modulation through multiple neurochemicals and layer-specific projection profiles (Gu, 2002). It follows that each system likely modulates different aspects of neural activity and behavior (Dayan, 2012). Hence, it is expected that different neuromodulators exert different effects on the hemodynamic signals, because they have different projection patterns and receptor types (Rauch et al., 2008b; Zaldivar et al., 2014). These receptors are located in all neuronal compartments, influencing every aspect of neural computation and metabolism (Dayan, 2012; Sengupta et al., 2014) and their effects highly depend on their location, density and distribution (Gu, 2002; Krimer et al., 1998). Further, the effects of neuromodulators cannot be simply viewed as increases or decreases in neural excitability, but rather, having divergent actions on multiple ion conductances, and consequently on the metabolism of a neural network (Attwell and Laughlin, 2001a; Dayan, 2012; Sengupta et al., 2014).

Understanding how neuromodulators affect the BOLD response is evidently essential for an effective interpretation of fMRI-data, not only in task-related fMRI but may also aid diagnostic use of fMRI, since many psychiatric disorders are associated with alterations in neuromodulatory systems (Dayan, 2012; Mitterschiffthaler et al., 2006). Thus, the combination of fMRI and pharmacology can help understanding neuromodulatory mechanisms, and the further combination with electrophysiology become a powerful tool to test the coupling between fMRI signals, neural signals, and the different neuromodulators (Rauch et al., 2008b; Zaldivar et al., 2014).

Pharmacological-fMRI (phMRI) was initially used to map spatiotemporal patterns of brain activity elicited by acute pharmacological challenges (Honey and Bullmore, 2004; Schwarz

et al., 2007). For example, studies in humans using scopolamine (a selective acetylcholine-muscarinic receptor antagonist) to pharmacologically induce memory impairment, showed substantially reduced activation in the hippocampus, fusiform gyrus and prefrontal cortex (Honey and Bullmore, 2004; Sperling et al., 2002). Other studies found that cortical activation increased while subcortical activation decreased with the use of serotoninergic agonists (Loubinoux et al., 2002).

It is worth noting that the effects of drugs on neural responses, vascular reactivity and neurovascular coupling are complex, and judicious interpretation of data is often hampered by the indirect nature of the fMRI signals (Dayan, 2012; Noudoost and Moore, 2011; Zaldivar et al., 2014). Hence, studies that cross-validate BOLD measures of drug action with behavior, electrophysiological measures and/or with other neuroimaging techniques, are invaluable in resolving these important issues. For instance, the use of a GABA-antagonist induced a sustained increase in brain activation, likely due to reduced inhibition, whereas GABA-releasing agents correlated with decreased hemodynamic responses (Chen et al., 2005; Kalisch et al., 2004; Reese et al., 2000). Moreover, reduced tissue perfusion was accompanied by an increased tissue oxygen tension, demonstrating an overall reduction of oxidative metabolism due to GABAergic neurotransmission (Chen et al., 2005).

Similarly, studies have shown that when presynaptic glutamate release is blocked (Kida et al., 2001; Kida et al., 2006) or when selective antagonists either for AMPA- or NMDA-receptors are used (Rao and Finkbeiner, 2007), BOLD and CBF responses are reduced. Furthermore, Gsell, et al. (Gsell et al., 2006) showed a differential contribution of the two major ionotropic glutamate receptors to the hemodynamic response. The reductions in BOLD and CBF were dose-dependent and stronger when using AMPA-receptor antagonists than when blocking NMDA-receptors (Gsell et al., 2006). This difference may reflect the different roles of the receptors. For instance, blockade of AMPA-receptors disturbs the thalamocortical input (feedforward), decreasing all neural responses and

consequently the blood flow (Logothetis, 2008; Rao and Finkbeiner, 2007). NMDA-receptor antagonists reduce the postsynaptic currents (feedback) without affecting the feedforward responses (Gsell et al., 2006; Rao and Finkbeiner, 2007). Another possible reason may be that NMDA-receptors exert an indirect vasomotor role via the release of nitric oxide (Faraci and Breese, 1993). Overall, different studies have shown that the effects mediated by GABAergic and glutamatergic neurotransmission (Chen et al., 2005; Gozzi et al., 2008; Gozzi et al., 2005; Zonta et al., 2003) are reflected in the fMRI signals.

Yet, despite the tight correlation between neural activity and the hemodynamic responses, it is difficult to make inferences about particular brain functions by only using phMRI. For instance, Rauch et al. (2008b) showed how complex the relationship between neural activity and the hemodynamic response can be under the influence of neuromodulation. Using a selective serotonin (5HT1A-receptor) agonist in V1, which causes persistent hyperpolarization of pyramidal neurons, they found that despite the decreased spiking activity, both the local processing reflected in the LFP and the BOLD responses were unaffected. Thus, the output of a neural network poses relative little metabolic demands compared with the overall presynaptic and postsynaptic processing of the incoming afferent activity (Goense and Logothetis, 2008; Logothetis, 2008; Rauch et al., 2008b).

Hence, combining fMRI, neurophysiology and pharmacology may help us to disentangle the relationships between the hemodynamic signal and the neural activity. Although in some cases the interpretation of the signals is straightforward (Rauch et al., 2008a), in other cases the effects of neuromodulators will strongly depend on receptor type, location and density, as well as on the particular functions they modulate (Dayan, 2012; Rauch et al., 2008b; Zaldivar et al., 2014).

2.1.8 Primary Visual Cortex and Neuromodulation in Non-human Primates

The primary visual cortex (V1) is the principal telencephalic recipient of visual input in humans and non-human primates (NHP; Callaway, 1998; Izpisua Belmonte et al., 2015),

and electrophysiological and neuroimaging mapping have revealed, that the visual field layout and basic neural selectivity of V1 are similar in humans and NHP (Papanikolaou et al., 2014; Self et al., 2016).

V1 is the earliest cortical visual area and highly specialized for processing information about static and moving objects (DiCarlo et al., 2012; Leopold, 2012; Rajalingham et al., 2015). This is principally due to the well-organized maps about the visual space that V1 keeps (Douglas and Martin, 2004, 2007; Hubel and Wiesel, 1962). It is worth noting that nearly all lateral geniculate nucleus (LGN) projections are directed to V1. Such projections can be subdivided in different pathway: *(i)* magnocellular (M), *(ii)* parvocellular (P), and *(iii)* koniocellular (K). Each of these pathway receives inputs from different types of retina cells and projects to distinct zones in V1 (Callaway, 1998; Nassi and Callaway, 2009). In principle, neurons from the LGN-layers M and P project to separate subcompartments of layers 4C and 6 (Callaway, 1998). Moreover, neurons from the M-pathway have relatively large receptive fields and respond transiently to visual stimuli. In contrast, cell originating from the P-pathway have small receptive fields and convey more detailed fine spatial information (Nassi and Callaway, 2009).

Another notable specialization of V1, is the high density and cellular morphology of neurons located in the granular layer (G-layer; Douglas and Martin, 2004; Roelfsema and Treue, 2014) which has been attributed to specialized class of thalamo-recipient neurons with dendritic spines with an unusually compact stellate morphology (Lewis and Lund, 1990). This characteristic is also present in humans and in other primates (such as New World Primates; see Mitchell and Leopold, 2015), and it is totally absent among rodent (Takahata et al., 2006; Takahata et al., 2012). In the extragranular layers of primate V1 (supragranular layers, SG; infragranular layers, IG), the information from the P, M and K pathways becomes less segregated and is, to some extent, reorganized to meet the requirements of dorsal and ventral processing streams (Callaway, 1998; Douglas and Martin, 2004; Nassi and Callaway, 2009). For example, information is segregated between

the “blobs” and “interblobs” in the SG (Horton, 1984) which have different visual response properties and projection targets (Federer et al., 2009). For instance, the primate interblob regions are organized into columns and are sensitive to a particular orientation. Such orientation columns are present in certain mammalian species such as cats (Hubel and Wiesel, 1962) and tree shrews (Humphrey and Norton, 1980) but they are, however, absent in rodents (Metin et al., 1988), including highly visual rodents such as squirrels (Van Hooser et al.,2005).

Furthermore, the organization of the vasculature in the macaque V1 is highly specialized as well. It has a marked gradient in the microvascular density along the cortical layers, with the highest density in the G-layer (Logothetis, 2008; Weber et al., 2008). Moreover, this appears to be consistent across all monkey species and humans (Blinder et al., 2013; Duvernoy et al., 1981; Zheng et al., 1991) and it seems to be developed in parallel to the COX activity (Fonta and Imbert, 2002). Interestingly, the vascular density in other visual areas appears to be lower compared to the V1 (Duvernoy et al., 1981; Zheng et al., 1991) and the laminar differences also appear to be less pronounce (Weber et al., 2008)

Therefore, V1 offers great advantages over other cortical structures for the study of neuromodulation and neurotransmission on the neurovascular coupling. First, the activity of the neurons in V1 is strongly but selectively influence by the stimulus and it offers the means to study event-related hemodynamic and neurophysiological responses and their causal relationship (Logothetis et al., 2001). This visual-induced modulation, can easily be separated into two stages of information processing: *(i)* an initial peak immediately after the stimulus onset (50 – 100 ms) which provides a measure for the feedforward input and the rapid local processing taking place within V1 (Maier et al., 2011; Xing et al., 2012); and *(ii)* a later sustained period of neural activity (100 ms and onwards) which provides a measure of recurrence modulation in V1 (Self et al., 2012; Self et al., 2013). Third, multiple studies have demonstrated that the neuromodulatory and neurotransmitter receptors are expressed in different cortical layer.

The laminar distribution of neuromodulator receptors and neurons are remarkably important, given that the population of neurons in different cortical layers employ different coding strategies (Hansen et al., 2012) which can be, in principle, differentially modulated by neuromodulators (Dayan, 2012). For example; the influence of the cholinergic system in V1, centrally involve in attention (Herrero et al., 2008), is mediated by two distinct types of cholinergic receptors, muscarinic and nicotinic, both located in different cortical layers (Disney and Aoki, 2008; Disney et al., 2007; Gu, 2002). The nicotinic receptors, located in the G-layers, enhances the sensory driven-activity while the muscarinic receptors, preferentially located in the SG-layer, suppress the lateral connectivity to prevent distracting signals (Disney et al., 2007). In addition, dopaminergic (DAergic) neuromodulation appears to have strong influence in the visual cortex, and anatomical studies have shown that dopamine receptors (DARs) are neither expressed in V1 nor in the LGN (Ding et al., 2016; Krimer et al., 1998; Lidow et al., 1991; Lidow et al., 1990). However, neurophysiological studies have demonstrated that DAergic neuromodulation increases the readout of information in the V1 via long-range connection with higher-order areas (Arsenault et al., 2013; Noudoost and Moore, 2011; Shuler and Bear, 2006; Zaldivar et al., 2014). This is particularly interesting, giving that long range projections to V1 are mostly located in the SG-layers (Chatterjee and Callaway, 2003).

In the following sections, I present six studies conducted to address the various questions regarding the effects of neuromodulation on the neurovascular coupling. These studies were carried out by using a multimodal approach consisting of fMRI (BOLD and CBF), multisite neurophysiological recordings (multiple laminar probes), chemical sampling (brain and blood sampling) and pharmacological methods (local and systemic injections of chemical substances) in the anesthetized NHPs. We presented various types of visual sensory stimulation in all the studies presented here, with the exception of the neurochemical study (Manuscript Nr. 1). The visual stimuli were delivered using a gamma corrected custom-built projector and a SVGA fiber-optic system (see details in Manuscript

Nr. 2). The visual stimuli that we used were: *(i)* black-and-white rotating checkerboard stimulus alternating with uniform black-background, to efficient elicit robust retinotopic maps in V1 (Slotnick et al., 2005); and *(ii)* naturalistic and colorful movies with no soundtrack also alternating with a uniform black-background. The importance of using naturalistic stimulus, are due to the fact that is not an static but varies on time scales allowing us to compute power and information changes associated to all of the existing visual features in the movie (Russ and Leopold, 2015).

First, we present a mass-spectrometry-based method that we developed, to successfully uncover the distribution of different metabolites, neurotransmitters and neuromodulators in the brain and blood from the NHPs (Manuscript Nr. 1). After having stablished the relative distribution of multiple biomolecules in brain and blood, we developed a multimodal approach, consisting of fMRI (BOLD, CBF), electrophysiological recording and pharmacology, to investigate the influence of neuromodulation in neurovascular coupling (Manuscript Nr. 2). Third, giving that changes haemodynamic signals are highly dependent on the influence of metabolites supplying energy, we investigated how changes in the ratio of lactate/pyruvate levels affects the fMRI signals (Manuscript Nr. 3). In a fourth study, we showed dissociation of BOLD-signals from neural activity and CBF under the influence of DAergic neuromodulation (Manuscript Nr. 4). We then explored if the effects elicited DA are layer dependent and if any of the LFP-frequency bands can be used to predict neuromoulation influence (Manuscript Nr. 5). Subsequently, we investigated how distinct features in the visual scene are encoded by the different cortical layers and which LFP-frequency bands can be informative about such features (Manuscript Nr. 6). Lastly, we discuss how our findings may relate to cognitive effects on the fMRI signals, given that certain cognitive modalities are mediated by distinct types of neuromodulators. Based on our finding, we also formulate a number of new but ripe predictions for testing, and we also present possible clinical application relevant to the studies in this dissertation. Together

the findings reported here provide new insights of neuromodulatory effects on the haemodynamic responses and neural activity.

2.3 Introduction to Manuscripts

Manuscript Nr. 1.

Measuring multiple neurochemicals and related metabolites in blood and brain in the rhesus monkey by using dual microdialysis sampling and capillary hydrophilic interaction chromatography-mass spectrometry.

Motivation

An appropriate information processing and a prompt response of neurons to the animal's cognitive demands, highly depends on the interactions between multiple molecules and their effectors (e.g. receptors). Accordingly, more than 99% of the communication between and within neuronal networks completely relies on the maintenance of concentration balance among different molecules (Magistretti and Allaman, 2015). Therefore, changes in the excitation-inhibition balance and/or in the brain metabolic demands inevitably affect the composition of the BECF, the neural and hemodynamic responses (Logothetis, 2008). Interestingly, to keep a constancy of neural function, the brain carefully controls the composition from the BECF by: (*i*) protecting the BECF from fluctuations in the blood composition using the BBB; (*ii*) the slow diffusional equilibrium between the CSF and BECF helps stabilizing the composition of the neural microenvironment; and (*iii*) the surrounding glial cells "condition' the BECF. Thereby, the assessment of intraneural and interneural communications and complex interactions among brain regions and subregions, will ultimately define how metabolites mediate neural function. Hence, it is important to first stablish experimental techniques that allows to simultaneously quantify fluctuation from multiple neurochemicals BECF, as well as to estimate their relative distribution with respect to other compartments.

Methods

Microdialysis has been widely used in the field of neuroscience, because it measures free, unbound neurotransmitters, and various other biomolecules, from the BECF (Shackman et al., 2007; Zhang et al., 2007). This technique requires the insertion of probes, containing a semipermeable membrane at the tip, into the tissue of interest (brain and blood). This

dialysis probe is connected to an inlet and an outlet tubing which are continuously perfused with a solution (carrier solution) that resembles the composition of the surrounding tissue fluid (artificial cerebral-spinal-fluid, ACSF; or PBS (Lee et al., 2016)). Once the probe is positioned in the tissue, compounds in the extracellular fluid diffuse into the carrier solution and the concentration of the different compounds can be measure using various analytical techniques. It is worth noting, that microdialysis can easily be coupled with mass-spectrometry (MS), allowing to selectively separate molecules according to their molecular mass and to quantify them with extremely high accuracy, even if their concentration is small (Zhang et al., 2007). However, the interpretation of the mass spectra is commonly difficult and it becomes progressively more of an issue when multiple, and different, molecular species are present within a sample. One approach for simplifying this situation involves coupling the mass spectrometer with another instrumental techniques to remove many of the unwanted components to be detected. For instance, high-performance-liquid-chromatography (HPLC) has been widely used to separate, identify and quantitate compounds. However, the performance of this methodology would highly depend on the nature of the chemical sample and the HPLC modality used.

Results

In this study, we developed an alternative HPLC method for the detection of multiple functional and metabolically related molecules in brain and blood. This technique consists in coupling the MS with the hydrophilic-interaction-chromatography (HILIC-MS) modality, which allows to separate molecules through differences in polarity and hydrophilicity. This is of great importance, given that many of the cellular metabolites and neurotransmitters are highly polar in nature. Hence, we used HILIC-MS to measure the concentrations from multiple compounds that derivate from glucose and citrate cycles. In particular, we quantified acetylcholine, lactate, pyruvate, glutamate and glutamine levels form the BECF and blood. This dual microdialysis sampling in brain and blood helped us to determine concentration-time profiles to fully characterized the influx and efflux of molecules from brain and blood.

Manuscript Nr. 2.

Pharmaco-based fMRI and neurophysiology in non-human primates

Motivation

As extensively described in the above sections, the activation of neuromodulator receptors changes the neural activity followed by changes in the regional brain metabolism and the regional-CBF, both reflected in the BOLD responses (Dayan, 2012). Nonetheless, despite the importance of neuromodulators on the neurovascular coupling dynamics, we still lack a clear understanding about their role and their possible mechanisms.

Multiple studies have addressed these questions using new methodologies in combination with fMRI (Lee et al., 2010). For instance, optogenetics and fMRI (so called ofMRI) offers to possibility to investigate genetically specified networks in the living brain as well as to test their local and global impact in their projecting targets (Lee et al., 2010; Matthews et al., 2016). Although the enthusiasm for optogenetics is well deserved, these methods have some inherent limitations that are worth to consider: first, this combination is limited to the rodent brain due to the complexity of the primate brain and its diversity of neuron types (Logothetis, 2010). Similarly, given this diversity of neuron types, the lack of genetic tools for cell-type specific targeting of proteins in the primate brain (Izpisua Belmonte et al., 2015) and the invasiveness of local injection of viral vectors combined with laser stimulation. Moreover, this combination also have the limitation to reproduce certain patterns of neural activity. For example, photo-stimulation is not able to reproduce neuronal fluctuations up to 100 Hz, while higher frequency components of the input are severely attenuated (Malyshev et al., 2015). Therefore, fMRI-optogenetics cannot really elucidate details onto the relationships between stimulus or task-selective neuronal activity and fMRI yet.

Methods

The combination of pharmacology and fMRI (phMRI) is a multimodal methodology that has already provided important evidence pertaining the neural events underlying the hemodynamic changes seen with fMRI and optical imaging (Gozzi et al., 2008; Gsell et

al., 2006; Hamel et al., 2015; Hillman, 2014; Rauch et al., 2008a; Rauch et al., 2008b; von Pfostl et al., 2012; Zaldivar et al., 2014). The importance of these techniques lies in their non-invasiveness, allowing us to test the same hypotheses in humans and in monkeys (Honey and Bullmore, 2004). However, it is worth noting that many pharmacological agents do not only affect neuronal activity, but also affect the blood flow directly, thereby complicating the interpretation of the signal. Hence, the combination of phMRI with concomitant invasive electrophysiology offers the possibility to better test the relationships between neural and fMRI signals under the influence of different neuromodulators. Hence, identifying the behaviorally relevant microcircuitry on which a given modulators acts, and demonstrating that such modulation is required for an specific stat-dependent influence on a specific behavior in vivo, is relevant for our understanding of the normal and diseased brain (Dayan, 2012).

Results

Hence, in this study we developed a multimodal approach consisting of fMRI, pharmacology and neurophysiology that help us understanding the causal relationship between neuromodulation and the neurovascular coupling in the visual cortex of anesthetized non-human primates. In this study we present an overview about the pressure-operated pumps that we developed to accurately deliver drugs, either locally or systemically. At the same time, we also showed how different aspects of the fMRI signal can be affect by neuromodulators and how they are associated to the neural activity.

Manuscript Nr. 3.

Effects of lactate on the early visual cortex of non-human primates, investigated by pharmaco-MRI and neurochemical analysis.

Motivation

The O_2 consumption supports the near-complete oxidation of the glucose entering the brain, and it is widely accepted that glucose and O_2 are the main source of energy for the brain (Sokoloff, 1977a). Nonetheless, despite an apparent abundance of O_2, neurons and glial cells maintain an elevated production of lactate, and intense stimulations increase glucose uptake out of proportion to O_2 consumption (Fox and Raichle, 1986) resulting in substantial lactate build-up. Yet, why does brain metabolism need the "***apparent***" less efficient glycolytic pathway during enhanced activity and energy demand?.

Multiple hypothesis have addressed this question with the well-known phenomenon of muscle physiology. During moderate-to-vigorous exercise, resulting in blood lactate concentrations of up to 10mM, the human brain takes up and oxidizes lactate to a considerably larger extent than under normal conditions, supplying up to 20 – 25 % of total brain energy demands (Hurley et al., 1984; Oyono-Enguelle et al., 1990; Quistorff et al., 2008). This is remarkable, given that the lactate oxidation occurs at the expense of blood glucose utilization and has led to suggest that the lactate in plasma is an efficient energy substrate for the adult human brain.

In this study we systematically increased the levels of lactate and pyruvate given that studies have observed that changes in the plasma level of lactate/pyruvate ratio increases the CBF. It is worth noting, that both lactate and pyruvate are in the near equilibrium, and changes in their concentrations affects the oxidization/glycolysis balance. Hence, we were interested to measure whether BOLD-signal is sensitive to detect changes in the concentrations of lactate and pyruvate (Hurley et al., 1984).

Methods

We monitored the BOLD signal in primary visual cortex of anaesthetized macaques during systemic infusion of lactate and pyruvate, while we animals view a rotating checkerboard that was continuously changing in direction, followed by an isoluminant black-gray screen.

Results

We observed reliable lactate-induced BOLD responses, which could be confirmed at population and individual level by their strong correlation with systemic lactate concentrations. Comparable BOLD effects where observed after a slow infusion of pyruvate. We show here that physiological changes in lactate and pyruvate levels are indeed reflected in the BOLD signal, and describe the technical prerequisites to reliably trace a lactate challenge using BOLD-fMRI.

Manuscript Nr. 4.

Dopamine-induced dissociation of BOLD and neural activity in macaque visual cortex

Motivation

Neuromodulators allow for a flexible reconfiguration of hard-wired connectivity to adapt neural circuits to the behavioral needs of the animal (Harris-Warrick and Marder, 1991). By altering the input-output properties of neural circuits, neuromodulation can also alter their energy expenditure, with concomitant effects on the hemodynamic responses, and thereby neuromodulators can affect fMRI signals as well (Arsenault et al., 2013; Pessiglione et al., 2006). Yet, it is still unclear how to interpret the effects of neuromodulation in fMRI signals, for instance, how to disentangle BOLD signal changes relating to task and reward (presumably neuromodulatory influences) from stimulus-driven or perceptual effects (Boynton, 2011; Dayan, 2012). Understanding how neuromodulators affect the BOLD response is essential for an effective interpretation of fMRI-data, not only in tasks involving attentional and reward-related processes, but also for diagnostic use of fMRI, since many psychiatric disorders lead to alterations in neuromodulatory systems (Mitterschiffthaler et al., 2006).

DAergic neuromodulation is centrally involved in many cognitive processes, most notably those underlying reward and addiction (Redish, 2004; Schultz, 2007), learning and working-memory (Ljungberg et al., 1992; Puig and Miller, 2012), motivation, attention (Stanisor et al., 2013) and decision making (de Lafuente and Romo, 2011) and it also plays a role in perceptual processes (Algaze et al., 2005; Happel et al., 2014; Noudoost and Moore, 2011; Rogers, 2003). Furthermore, diseases such as Parkinson's disease (PD) and schizophrenia show alterations in dopamine (DA) kinetics (Winterer and Weinberger, 2004). Visual processing is affected in PD (Holroyd and Wooten, 2006), and L-DOPA (metabolic precursor of DA) is effective in treating amblyopia (Algaze et al., 2005; Rogers, 2003) indicating a role of DA in early visual processing.

DA has been extensively studied in the prefrontal cortex (PFC) and striatum (Puig and Miller, 2012; Schultz, 2007), but how it affects processing in V1 is still relatively unexplored (Arsenault et al., 2013). It has been shown that DA improves the signal-to-noise ratio (SNR) in PFC and sensory areas, including V1 (Happel et al., 2014; Jacob et al., 2013; Servan-Schreiber et al., 1990), and thereby changes the signal detection performance at the behavioral level (Puig and Miller, 2012; Shuler and Bear, 2006). Recent work has also provided insights into the effects of DA on the BOLD signal, highlighting the complexity of interpreting the relationship between neural activity and fMRI signals under neuromodulation: increases as well as decreases were seen depending on area, paradigm and methodology (Arsenault et al., 2013; Linville et al., 1993; Pessiglione et al., 2006; Serences, 2008; Watanabe et al., 2011). However, there often seems to be a mismatch between the BOLD and neurophysiological responses in V1 (Boynton, 2011), as the expectation of reward tends to increase neural spiking (Shuler and Bear, 2006) but reduce fMRI responses (Arsenault et al., 2013; Serences, 2008).

Another factor affecting the interpretation of the effect of neuromodulators on the BOLD response is that many neuromodulators exert a direct influence on the vasculature (Dayan, 2012; Krimer et al., 1998; Linville et al., 1993; Yamada et al., 2001), as well as through their effects on neural activity. In the case of DA, both vasodilation (Esaki et al., 2002; Mandeville et al., 2013; Marota et al., 2000) and vasoconstriction (Krimer et al., 1998) have been reported. These effects, however, are highly dependent on the distribution and density of DA-receptors (DARs) (Mandeville et al., 2013). In V1, the dopamine receptor density is low to almost undetectable (Lidow et al., 1991), which allows for study of dopamine's neuromodulatory effects without the confound of direct vascular effects in V1.

Methods

Summarizing, the effects of DA neuromodulation on fMRI signals remain seemingly contradictory, because of variations in task, reward and attentional state, and DA's involvement in all these processes. To resolve some of these issues, in this study we

combined systemic- and intracortical injections of DA with pharmaco-MRI (BOLD and cerebral blood flow, CBF) and electrophysiology, to investigate the impact of DAergic neuromodulation on neurovascular coupling in macaque V1. Applying DA in anesthetized animals allowed us to investigate the mechanisms by which DA affects the neural and BOLD signals, without the effects of behavioral processes like reward expectation or value and attention, which can be difficult to disentangle (Arsenault et al., 2013; Stanisor et al., 2013).

Results

We found that systemic application of L-DOPA+Carbidopa (LDC) increased the neural responses, while decreasing the BOLD-response and increasing the CBF-response, suggesting that energy consumption increases by a disproportionate amount relative to the hemodynamic response. DA increases the fidelity of the neural network at a high metabolic price, which was more faithfully reflected in the CBF than in the BOLD-responses. However, it also implies that especially in the case of neuromodulation, increases or decreases in the BOLD signal may not necessarily be interpreted as decreases or increases in neural responses or metabolic demands.

Manuscript Nr. 5.

Lamina and frequency specificity of information in primary visual cortex.

Motivation

One of the primary goals of systems neuroscience is to understand the neural mechanisms underlying behavior. Although a great deal of knowledge has been learnt from characterizing the responses of single neurons involve in sensory, motor and cognitive function (Romo and Salinas, 2003), we still lack a clear understanding about the collective interaction between neural networks. The LFP activity, generated by transmembrane current originating from cells near to the intracortical electrode tip (Haider et al., 2016; Logothetis and Wandell, 2004; Mitzdorf, 1985) is an important marker for neural cooperation as it reflects several local perisynaptic integrative processes (Haider et al., 2016; Whittingstall and Logothetis, 2009). The activity reflected in the LFPs is traditional decomposed and interpreted in different frequency bands reflecting diverse aspects of neural activity (Magri et al., 2012a; Whittingstall and Logothetis, 2009).

In the macaque V1, single-channel LFP analysis revealed two distinct frequency bands that carry independent information about the sensory stimuli: a low frequency band (1 – 24 Hz), and a high frequency (50 – 100 Hz) gamma oscillation range (Belitski et al., 2008; Belitski et al., 2010). However, it is worth noting that LFP-dynamic patterns and associated mechanisms are highly dependent on the detailed local properties of the networks, including the recurrent local organization and synaptic inputs from other brain structures. Therefore, one would expect that differences in the source and strength of inputs to neurons in different cortical layers would change the nature and amount of information on each frequency band. For instance, one important distinction between cortical networks in the middle-, superficial- and deep-layers (G-, SG- and IG- layers, respectively) is the spatial spread of intracortical connections. In the G-layers, which receives inputs from LGN, the spatial spread of connections is small (Briggs and Callaway, 2005), whereas in

SG- and IG-layers neurons receive recurrent import from larger distances via long-range interactions (Callaway, 1998; Nassi and Callaway, 2009).

Methods

In this study, we explored whether the nature and the amount of information in each LFP-bands differ across cortical layers. Here we used laminar electrodes with fine spacing spanning the whole cortical depth. We acquired LFP in V1 under anesthesia while presenting a 2 minute long Hollywood color movie clip. We then computed the Current Source Density (CSD) for each trial. From the time-resolved power of the CSD in each trial, we estimated the mutual information that the power at each frequency carries about which section of the movie is being presented, and how much information there is in frequency bands about different spatial resolutions of changes in luminance.

Results

We found, across depth and frequency, two distinct regions carrying large amounts of independent information about the movie stimulus: the low frequency (4-16 Hz) band had high information at depths corresponding to layers 4-6, whereas the high frequency (64-250 Hz) band had high information in layers 1-3. This suggests that different laminae of cortical circuits generate independent information channels that code information in separate frequency ranges. Furthermore, we found the low frequency band contained information about low spatial frequencies changes in luminance (<1 cycle per degree), whilst the high frequency band contained information about finer spatial details (1-6 cycles per degree). This suggests information about these two spatial frequency components arises through two different cortical mechanisms within V1, and information about them is encoded separately in two different frequency bands.

Manuscript Nr. 6.

Dopamine elicits lamina and frequency specific increase of information in the macaque primary visual cortex.

Motivation

The LFP are generally used to investigate cortical network mechanism involve in sensory processing (Belitski et al., 2008), motor planning and higher cognitive processes (de Lafuente and Romo, 2011; Puig and Miller, 2012), including attention, memory and perception. The LFP are also signals that are highly used for steering neuroprosthetic devices and for monitoring neural activity in human recordings because they are more easily and stably recorded in chronic settings than are spikes.

The oscillatory activity patterns reflected in the LFPs are crucial for the engagement and disengagement of functional neural circuits as animals engage into different cognitive operations (Haegens et al., 2011a; Haegens et al., 2011b; Nacher et al., 2013). That is, because they provide an effective means to control the timing of neuronal firing to coordinate the cooperation and communication between functionally active neural circuits (Buzsaki et al., 2012; Buzsaki et al., 2007). Therefore, the activity measured with the LFPs generally reflects different aspects of neural activity, which are generated by distinct neural mechanism's and expressed in different frequency ranges. The relative strength of these components thus determine a so-called specific spectral fingerprint. However, previous studies in the macaque V1 showed that these frequency bands not only vary in the amplitude but also the tuning to sensory features, the type and amount of sensory information vary across the LFP's frequency bands (Belitski et al., 2008; Magri et al., 2012b). However, a stricking discrepancy between the activity reflected in the low- (< 20 H) and high- frequency bands (> 50 Hz) dissociate from the activity reflected in the middle-frequency band (18 - 38). It has been proposed, based on statistical considerations, that this middle frequency band reflectes the influence of neuromodulation.

Methods

Here in this study, we used laminar electrodes with fine spacing spanning the whole cortical depth of V1 and investigated the whether the middle frequency bands can be an indicative for neuromodulation influence and whether it relates to stimulus encoding. Given that the different cortical layers generate independent information channels that code information in separate frequency ranges, we explored whether this information is disrupted or improved under the influence of DAergic neuromodulation.

Results

DAergic neuromodulation elicited frequency- and stimulus dependent power changes in the recorded LFPs. During spontaneous activity, we observed a remarkable increase specific to the middle-frequency (18 – 38 Hz) band power accompanied by a decrease of gamma (50 – 150 Hz) power. In contrast, during visual stimulation with movie clips DA increased both the power of gamma and of the middle frequency band. Moreover, DA increased the information in LFP power, particularly superficial and deep layers and in the gamma (50 – 100 Hz) frequency band. Overall, our results show that the middle-frequency band captures endogenous non-stimulus driven oscillations that are modulated by dopamine, and that dopamine regulates gamma-range information coding in visual cortex.

.

2.4 General Discussions

The communication between neurons highly depends on the interaction and cooperation between multiple neurotransmitters and neuromodulators. They provide to neurons within neural circuits the flexibility of adjusting their activity and metabolic demands depending on the animal's cognitive demands. However, to better understand the relationship of neuromodulation on functional imaging, the relationship between neural activity, metabolism, and their association to the different classes of neuromodulator receptors must be explored. Furthermore, the cell types of the brain, the mechanisms that supply nutriments for energy production, and mechanisms that link neural activity to energy production and consumption, likely play important roles in the relationship between neuromodulation and functional imaging and, therefore, also require study.

The pharmacological approach that we developed Manuscript Nr. 2, offered us great advantages over iontophoresis. In principle, because the pharmacological agents available for iontophoresis should be ionized and in aqueous solutions, therefore limiting the selection of the drugs, which in most cases, lack selectivity. Therefore, by using pressure-operated systems any substance can be injected either intracortically and/or systemically (Figure 4.4 and Figure 4.5). Another important aspect about our system, is that it provided us with the flexibility to easily adjust flow-rates and volumes. This is remarkable, given that high volume and flow rates for intracortical injections can disturb the neural microenvironment and change the neural activity independent of the pharmacological challenge.

2.4.1 The metabolic profile in the brain and blood of the non-human primates

In this dissertation, we first aimed to gain comprehensive insight into the metabolic processes that mediate neural function. We developed a targeted mass spectrometry-based approach capable of measuring a broad range of metabolites, neurotransmitters and neuromodulators (Manuscript Nr.1; Li et al., 2011). The development of this HILIC-

MS method (Manuscript Nr. 2) was applied to quantify five biomolecules in the BECF from the macaque's brain (Manuscript Nr. 1; Manuscript Nr. 2; and Manuscript Nr. 3). In Figure 3.2, we show classical chromatograms from all of the detected molecules in the brain, as well as for the compounds that were used for characterizing the spectrometry profiles of each of the detected molecules. It is worth noting that the chromatograms are usually characterized by a series of peaks, each one representing a compound passing throughout the HPLC detector (Schlichtherle-Cerny et al., 2003). Each of the peaks are two-dimensional plots with the ordinate axis giving concentration in terms of detector response (intensity) and the abscissa representing the time taken to detect a particular compound (retention time). The combination of these two factors, allowed us to identify a specific molecule, and thereby helped to determine a concentration of molecules. In view of the results depicted in the Figure 3.2, one can clearly see that each of the molecules have different chromatogram profiles, i.e., different retention times and different intensities, that allows us to understand the selectivity and sensitivity of our method. More importantly, this method demonstrated that biomolecules of interest were, indeed, simultaneously detected and were consistent across different animals from which we collected data.

The average concentration of each neurotransmitter and metabolite is listed in the Table 3.3. The concentration of acetylcholine was measured at the low nanomolar (nM) level, whereas the concentration from the lactate, pyruvate, glutamate and glutamine were in the micromolar (µM) range. This is remarkably important, given that the levels of glutamate and acetylcholine appear to be similar to those obtained from human cerebral spinal fluid (CSF; Parrot et al., 2004) whose chemical composition is highly dependent on the composition of the BECF (Cauli and Hamel, 2010; Ding et al., 2016). However, the concentrations from lactate, pyruvate and glutamine are slightly different to those reported in humans (Quistorff et al., 2008; van Hall et al., 2009). This is not surprising given that the levels of these molecules are highly dependent of multiple factors, such as the subject's gender, weight, diet and physical condition (Zhang et al., 2007).

We also considered factors related to the methodology itself, that could be a confound in the detection and interpretation of this data. For instance, it has been shown that the pH, and the concentration of solutes and water in the buffer solutions seem to strongly affect the chromatographic behavior of the analytes (Schlichtherle-Cerny et al., 2003; Uutela et al., 2005; Zhang et al., 2007). In order to avoid such interference and to achieve an optimal detectability of the five molecules, we also examined how each of these factors affects the HILIC's detection performance of each molecule. It is remarkable that the results in Figure 3.1 provided us with the suitable conditions for an optimal HILIC-MS separation.

Another advantage of the combined microdialysis and HILIC-MS, is that it continuously monitors molecules over time, which allows kinetic analysis within the same animal (Zhang et al., 2008). This is important for two reasons: *(i)* because it avoids the inter animal variability that confounds the data from single-time point, therefore helping to construct a single concentration time profile; *(ii)* because it helps to determine changes in the concentration that could be associated to fluctuations in the influx and efflux of the brain.

Therefore, taking into account the advantages mentioned above, we simultaneously measured the concentrations of the biomolecules in the brain and blood to quantitatively estimate the transport process in the BBB. These results are shown in the Figure 3.2; the concentration of each of the molecules in the blood are depicted in the Table 3.1. Here we found that the concentration levels of each molecule are substantially different between brain and blood. For instance, higher concentrations for all of the molecules were found in blood and are in good agreement with the values reported in healthy humans (Hawkins, 2009). This highlights the importance of the neuronal microenvironment and its different mechanisms to control the composition of the BECF, given that they restrict the movement of solutes, despite their higher concentrations in the blood, in order to provide constancy for neuronal function (Magistretti and Allaman, 2015; Viswanathan and Freeman, 2007).

The neuromodulators, neurotransmitters and metabolites identified so far, are rather simple chemicals that are either available as the products of normal metabolism or from common food. Indeed, some neurotransmitters and neuromodulators are simply amino acids, as part of the proteins in food. Once neurotransmitters and neuromodulators have been synthetized or eaten, they must be transported to the axon terminals (unless they are synthetized there) and stored in vesicles ready for release (Ivanisevic et al., 2014). Thereby, the reported concentrations in the brain and blood are the net result of all transport (transporter-mediated and/or diffusion) and metabolic processes that contribute to the formation and removal of metabolites (Zhang et al., 2008). At steady state, and during anesthesia, the overall concentration of a metabolite is stable even though individual molecules are continuously entering and leaving the BECF/blood (Ivanisevic et al., 2014; Kaddurah-Daouk and Krishnan, 2009; Li and Freeman, 2015).

The molecules reported above (Manuscript Nr. 1) have important implications in the regulation of neural and hemodynamic responses (Belanger et al., 2011; Dayan, 2012; Magistretti and Allaman, 2015)., Any fluctuations in their levels (reflecting changes in the flux due to normal brain activity or dysfunction) would inevitably affect the fMRI signals (Magistretti and Allaman, 2015). In the normal brain, there are multiple factors that can change the flux of a metabolite, for example; the availably of the enzymes and coenzymes controlling the reactions (activation or inactivation of biochemical reactions), metabolite concentrations and transport, diffusion and tissue pH (Wishart, 2016). One critical step or factor in the synthesis and storage of the neurotransmitter, neuromodulators and metabolites, and perhaps the stability of the haemodynamic signals, is the rate-limiting factor. For instance, multiple studies have estimated the rate-limiting factor by calculating the ratios between the "***immediate metabolite***" and the "***molecule of interest***" to assess the dynamic state of metabolic pathways (Bellander et al., 2004; Petroff et al., 2002; Richards et al., 2003; Zlotnik et al., 2011). For example, an increase in the ratio of lactate/pyruvate in brain has been used as an indicator of a deficient metabolic supply in

brain, such as what is observed in Alzheimer's disease (Iadecola, 2004). In addition, a decreased glutamine/glutamate ratio has been suggested as indicative of a traumatic injury in brain (Richards et al., 2003), hypoxia (Raman et al., 2005; Samuelsson et al., 2007) and epilepsy (Petroff et al., 2002).

We also calculated the ratios in blood and brain for the lactate/pyruvate and glutamine/glutamate, and found that in both cases the ratios are higher in brain than in blood (Figure 3.3). The striking difference in the ratio of glutamine/glutamate in brain and blood are possibly reflect the higher turnover rate of glutamate in brain than in blood, resulting in the high levels of glutamine and low levels of glutamate in the brain (Petroff et al., 2002; Shen et al., 1999). We also found that the ratio of lactate/pyruvate was slightly higher in brain than in the blood (Figure 3.3), which lead us to suggest than lactate and pyruvate are in the near equilibrium in both compartments (Hertz et al., 2007; Mintun et al., 2004). Indeed, changes in the ratio of lactate/pyruvate in blood also affects the lactate/pyruvate ratio in brain, and conversely (Iadecola, 2004; Mintun et al., 2004).

2.4.2 Glycolytic alterations and BOLD-CBF regulation

It is worth noting that in the normal brain, lactate and pyruvate are known to serve as equivalent substrates for the production of metabolic energy, and their equilibrium highly depend on each other. That is, if the lactate concentrations increase, the pyruvate levels also increase (Belanger et al., 2011; Li and Freeman, 2015; Magistretti and Allaman, 2015; Pellerin and Magistretti, 2004). More importantly, any change in their concentrations, either in brain or blood, would inevitably affect the CBF given that they are in near equilibrium with the NADH/NAD+ (Mintun et al., 2004). This is supported by the evidence reported in our Manuscript Nr. 3, in which we increased the plasma levels of both lactate and pyruvate.

The results in the Manuscript Nr. 3 clearly show that the BOLD and CBF responses increased due to the injections of lactate (BOLD results in Figure 5.1D and Figure 5.2A and CBF results in Figure 5.4) and pyruvate (BOLD results in Figure 5.7A and CBF results

not shown). More interestingly, the profiling induced by both substances were similar and highly correlated to their respective plasma levels (blood sampling results Figure 5.1D and Figure 5.2B). In both cases, we observed a positive baseline increase in the intensity of the BOLD and CBF signals, with minor and non-significant effects in visually-induced neural activity (Figure 5.2A, Figure 5.7A-B).

However, the effects of lactate appear to be delayed relative to the injection onset (Figure 5.1D). This might be due to the lactate influx into the red-blood cells (Skelton et al., 1998; Smith et al., 1997) which is, indeed, supported by our blood chemistry sampling showing delayed changes in the concentration of lactate relative to the start of the injections (Figure 5.1D, Figure 5.2B). Technical issues related to the pressure-operated pumps that we developed are discharged (Figure 4.1; see details in Manuscript Nr. 2) given that our system reliably and accurately delivers substances systemically and intracortically in non-human primate, placed inside an NMR scanner (Manuscript Nr. 2; Manuscript Nr. 3; Manuscript Nr. 4). In addition, our data also suggests that the strength of lactate/pyruvate effects on the BOLD response varies depending on the physical condition of the animal (Figure 5.3; see Freund et al., 1990; Oyono-Enguelle et al., 1990; Voytko and Tinkler, 2004). These differences are actually reflected in the different onset and dynamics of the BOLD responses and in our blood-chemical sampling (Figure 5.3A-B).

Evidence from *in vitro* and *in vivo* biochemical and imaging studies converge to indicate that: *(i)* the major energetic load in the brain is localized at the synapse; and *(ii)* synaptic activity and local energy demand is balance by multiple molecular mechanisms. Hence, astrocytes are the key cells for coupling synaptic activity and energy metabolism (Attwell et al., 2010; Belanger et al., 2011; Gordon et al., 2008; Hertz et al., 2007; Hillman, 2014; Magistretti and Allaman, 2015). In principle, after crossing the BBB, the glucose in blood that enters the brain, first encounters the astrocytic endfoot. Although at this point glucose can diffuse directly to neurons, it is preferentially taken up by astrocytes and metabolized

to lactate via astrocytic-glycolysis. Most of this lactate is excreted into the BECF surrounding neurons.

Multiple studies have demonstrated that astrocytes transport substances between the blood and neurons by providing fuel to neurons in the form of lactate (Attwell et al., 2010; Belanger et al., 2011; Chih and Roberts Jr, 2003; Dienel et al., 2007; Iadecola and Nedergaard, 2007). Therefore, the observed changes in the BOLD and CBF after lactate and pyruvate injections most likely originates from the interaction of neuronal and vascular effects (lactate Figure 5.5A-B and pyruvate Figure 5.6A-B). Hence, the advantage of using lactate for neuronal function is that it provides a form of substrate buffering, as second energy reservoir that is available to neurons (Magistretti and Allaman, 2015). It is worth noting that the availability of glucose in the neuronal microenvironment highly depends on the moment-to-moment supply provided by blood and it varies with neural activity (Li and Freeman, 2015). The concentration of extracellular lactate, however, is buffered against such variability by the surrounding astrocytes, which continuously shuttle lactate to the BECF through the metabolism of glucose or by breaking down glycogen stored in the astrocytes (Magistretti and Allaman, 2015). What determines this exchange between astrocytes and neurons? The answer to this question lies in the redox state of cells; neurons are predominantly oxidative (glucose mostly oxidized in neurons) whereas astrocytes are highly glycolytic (Magistretti and Allaman, 2015; Pellerin and Magistretti, 2004). Hence, according to the redox switch model, the inhibition of glucose transport induced by glutamate in neurons increases the favorable condition for the use of lactate as an energy substrate in this cell type as these two processes compete for intracellular NAD+ (Cerdan et al., 2006).

2.4.3 Effects of neuromodulation on BOLD and neural activity

Glucose is the primary energy source for the neurons, it is transported from the bloodstream across the BBB according to need, and its metabolism usually occurs in two stages: an anaerobic or non-oxidative stage, (glycolysis) followed by an aerobic stage

(oxidative phosphorilazation). The balance between these two stages has consequences for both the amount of O_2 consumed and the energy produced. However, such balance depends on the multiple factors, such as: *(i)* vasoactive substances that either dilate or constrict vessels, such as the vasoactive intestinal poly-peptide (VIP; Magistretti et al., 1981); *(ii)* the concentrations of K^+ which increase the glycolytic rate of astrocytes (Bittner et al., 2011); and *(iii)* neuromodulators (Dayan, 2012).

Most of the neuromodulators and their receptors have been extensively studied because they have been recognized as an essential element for the function or dysfunction of the central nervous system (Dayan, 2012; Yu and Dayan, 2005). As we have extensively discussed during the course of this dissertation, neuromodulators change the excitation/inhibition balance which can inevitably affect brain metabolism, CBF and the oxygenation of the tissue, all impacting the BOLD-responses (Goense and Logothetis, 2008; Logothetis, 2008). However, studying the effects of neuromodulators on the neurovascular coupling is not simple, given that multiple factors can affect the interpretation of the effects of neuromodulation on the BOLD responses (Logothetis, 2008). For instance, many neuromodulator receptors exert direct influence on the vasculature, as well as through their effects on neural activity (Krimer et al., 1998; Linville et al., 1993; Yamada et al., 2001). The effects of neuromodulators ultimately depend on the expression and distribution of their receptor types (Dayan, 2012; Gil et al., 1997; Krimer et al., 1998; Lidow et al., 1991).

In the Manuscript Nr. 4, we took advantage of the anatomical organization of dopaminergic (DAergic) system in the early visual cortex. In V1, for instance, the density of dopamine-(DA-) receptors (DARs) is low to almost undetectable (Lidow et al., 1991; Lidow et al., 1990), which allowed to study DA's neuromodulatory effects without the cofound of direct vascular effects in V1 (Zaldivar et al., 2014). It is worth noting that the effects of DA have been extensively addressed by using different pharmacological approaches in rats and monkeys, for example, the blocking of the DA-transporter (DAT) to enhance the levels of

DA in the synaptic cleft (e.g. amphetamines; Esaki et al., 2002; Mandeville et al., 2013). However, these substances are not usually selective to the DAT and can also alter the kinetics of other neurochemicals (such as norepinephrine, serotonin, etc) and change the CBV (Leonard and Shallice, 1971). Hence, we mimicked DAergic neuromodulation by systemically applying L-DOPA+Carbidopa (LDC; Black et al., 2003; Dadeya et al., 2009). L-DOPA and Carbidopa increases the bioavailability of L-DOPA (which is the DA's metabolic precursor) by inhibiting its breakdown in the periphery, before it crosses into the brain, and preventing increased cardiovascular output, which could affect the haemodynamic responses in the brain. Carbidopa inhibits DOPA-decarboxylase (DDC), the enzyme responsible for the conversion of L-DOPA to DA. It is worth noting that LDC is the first line of medication in Parkinson's disease where levels of DA are usually depleted (Black et al., 2003; Gordon et al., 2007).

Our results revealed that LDC strongly dissociated the BOLD and neural activity in V1. We found, that the injections of LDC reduced the visual-induced modulation in the BOLD responses (Figure 6.1C-D) while increased the power and the signal-to-noise ratio (SNR) from the gamma and MUA bands (Figure 6.2 gamma shown in dark blue and MUA in red). These results extend previous observation in humans and macaques in which fMRI responses decreased with cues that predict and anticipate reward (Arsenault et al., 2013; Serences, 2008). However, our findings further revealed that fluctuations in the neural activity were not faithfully followed by the BOLD responses, and were not compatible with the idea of decreased metabolic consumption to explain the BOLD reduction (Arsenault et al., 2013). Interestingly, a decrease in BOLD-responses in V1 during an improvement in behavioral performance was also seen in studies of amblyopia, after an acute dose of L-DOPA (Algaze et al., 2005; Rogers, 2003), agreeing with our findings.

Furthermore, we measured CBF to resolve this apparent contradiction (BOLD and neural activity dissociation). It is remarkable that both fMRI techniques are sensitive to different aspects of the hemodynamic response and their combination allows to better assess the

effects of DA on O_2 consumption ($CMRO_2$) and metabolism (Leontiev and Buxton, 2007; Leontiev et al., 2007; Sicard and Duong, 2005). Interestingly, we found that the baseline and the visually-induced modulation increased during the LDC injections (Figure 6.4).

The increase in neural activity and CBF, and the decrease in BOLD-signal can be best explained as a disproportionate increase in $CMRO_2$ triggered by DA. The BOLD signal reflects the concentration of dHb, and is affected by CBF, CBV and $CMRO_2$. Given that the stimulus-evoked CBF increased and the stimulus-evoked BOLD decreased upon DA injection, this indicated the stimulus-evoked dHb is higher after dopamine application. Since the CBF increased, this is most likely due to an increased dHb production, i.e. an increase in $CMRO_2$. In other words, an increase in CBF modulation and a decrease in BOLD-response can occur when the O_2-consumption increases by a proportionally larger amount than the inflow of fresh blood, leading to a relative increase in concentration of dHb and a decrease in the BOLD signal compared to the pre-injection response to the stimulus.

Effects of DA on the neuronal or astrocytic oxygen metabolism are unlikely to explain our results, in principle, because local applications of DA did not have any effect on the neural responses (Figure 6.6). If L-DOPA acted on neural or astrocytic oxygen metabolism, we would have expected changes under local DA application, which we did not observe in any of the concentrations tested. It can also be argued that the lack of neural responses to DA could be due to a failure of delivering the drugs intracortically. However, we ruled out this possibility by performing local application of GABA in V1 (Figure 4.5B). Multiple concentrations were tested to determine the performance of our injection system. As expected, the V1 responses to GABA injection were concentration dependent and demonstrate that our intracortical DA results are not due to incorrect pharmacological technique (Figure 4.5B).

Therefore, we suggest that the findings in the Manuscript Nr. 4 are the result of long-range interactions with higher order regions, for instance prefrontal cortex (PFC; Jacob et al., 2013; Noudoost and Moore, 2011). Indeed, various studies have shown that this interaction with the PFC enhances states of high persistent activity in sensory cortex, thereby improving the stimulus detection performance (Happel et al., 2014; Jacob et al., 2013). These effects are the result of DAergic modulation acting on different cell-types in the PFC by: *(i)* increasing the excitability from cells that gate sensory inputs to PFC by an enhancing their SNR; and *(ii)* by strengthening persistent representations of sensory signals which may allow to adapt behavior in response to changes in the sensory environment (Ott et al., 2014).

It is important to appreciate that different neuromodulators are likely to cause differential effects on BOLD, CBF and neural activity (Dayan, 2012). This is not only because neuromodulators are distinct classes of molecules, but because their effects are mediated by diverse types of receptors that can either be located in distinct subsets of neurons or activate different signaling pathways (Billimoria et al., 2006; Brunel and Wang, 2001; Constantinople and Bruno, 2011; Dayan, 2012; Fellous and Linster, 1998; Hamood and Marder, 2014; Hasselmo, 1995; Zaldivar et al., 2014). For example, the application of serotonin receptor agonist, which causes persistent hyperpolarization of pyramidal neurons, leads to a ceasing of the MUA response (Rauch et al., 2008b). However, at the very same time, both the LFP and the BOLD signal still respond to visual stimulation with no alterations in their amplitude and their SNR. The results from this study not only showed that BOLD signal is coupled to the synaptic activity instead of neural spiking response, but it also supports the notion that different types of neuromodulatory pathways can elicit differential effects in BOLD and neural activity (Rauch et al., 2008b; Zaldivar et al., 2014).

2.4.4 Lamina specific effects of dopamine in V1

The results in Manuscript Nr. 4, can also be interpreted as DA enhancing the excitatory recurrence through interaction with higher cortical areas and promoting the cortical

representation of sensory information (Noudoost and Moore, 2011). Accordingly, given that the different layers in V1 encode different aspects of the sensory information one should expect that DA indirectly exerts differential effects in each cortical layer. For instance, an important distinction between cortical networks in the middle (G-layers), superficial (SG-layers) and deep layers (IG-layers) is the spatial spread of their intracortical connections. In G-layer, for example, neurons receive inputs from the LGN and the spatial spread of connections is small (Adesnik et al., 2012; Briggs and Callaway, 2001, 2005; Callaway, 1998; Gilbert, 1977). On the other hand, SG- and IG-layers receive recurrent input from larger distances (up to several mm) via long horizontal circuitry (Callaway, 1998; Gilbert, 1977). Therefore, it was important to determine if the effects described in the Manuscript Nr. 4 are similar of different in all cortical depths.

We first characterized how changes in power and information are reflected in the distinct frequency bands and layers. In the Manuscript Nr. 5 we found that LFP power is smooth and its depth profile is close to flat (Figure 7.2A, B). We found that there are two cortical regions at which oscillations in these frequency ranges are more informative. Namely 4 – 16 Hz at G- and IG-layers, and 50 – 60 Hz at SG. Previous work has shown that in the macaque Vq information is codded in two frequency bands (< 20 Hz and > 50 Hz) containing independent information about the sensory stimulus. Having stablishes that there are two cortical regions at which oscillation in these frequency range are much informative (Manuscript Nr. 5), hence we investigated how these profiles of information and power are affected by the influence of DAergic neuromodulation. Given that the results from Manuscript Nr. 4 are compatible with the idea that DA indirectly mediates recurrence, we expected that neurons from the SG-layers, and possibly IG-layers, would be mostly affected by the LDC injections. In the Manuscript Nr. 6, we investigated the effects of LDC on the different LFP bands. As discussed earlier, the LFPs reflect several components of neural activity generated by different neural mechanisms and expressed in different frequency regimes (Figure 4.3). These distinct frequencies are associated to different

aspects of the sensory stimulus and convey independent information about the sensory stimulus (Belitski et al., 2008; Einevoll et al., 2013; Magri et al., 2012a).

Our results revealed that depending on the stimulus condition LDC increases the LFP-power from certain frequencies. For instance, during spontaneous activity, LDC increases the power in the intermediate frequencies (18 – 38 Hz) while decreasing the power in the gamma (50 – 150 Hz). In contrast, during the stimulus presentation the power from both gamma and intermediate bands increase (Figure 8.2).

Interestingly, previous neurophysiology studies in the macaque showed that low (<20 Hz) and high frequencies (> 40 Hz) dissociate from the activity from the intermediate bands (18 – 38 Hz), and given their high noise- and low signal-correlations it has been proposed that they reflect neuromodulation influence (Figure 4.3; see Belitski et al., 2008; Einevoll et al., 2013; Magri et al., 2012b).

Our results, thus, support the notion that intermediate frequencies reflect the influence of neuromodulation; therefore we named this frequency band as the neuromodulation band (nMOD-band). Basic circuit function and internal brain states directly depend on neuromodulator actions (Dayan, 2012; Herrero et al., 2008; Yu and Dayan, 2005). Our data suggests that the power modulation in the nMOD band is linked to ongoing mechanisms that help the system to maintain the current cognitive status which can, in principle, be instantiated by neuromodulators (Engel and Fries, 2010; Gray et al., 1989). Therefore, increases in power in this frequency band might be because the system has to maintain the current cognitive set (a decrease in power is associated to unexpected or novel events; see Buschman and Miller, 2007; Engel and Fries, 2010; Lundqvist et al., 2016). It is therefore remarkable that the nature of our manipulation in this study consisted of continuous infusions of the immediate DA metabolic precursor which allows maintaining the concentrations of DA constant while assessing the effects on the neural activity (Black et al., 2003; Zaldivar et al., 2014). Thus, the fact that nMOD power increases during the

stimulus presentation highlights the efficiency of our manipulations to keep DAergic systems in a continuous operating mode. Furthermore, the increased DA-levels, and the subsequent activation of DA-receptors (DARs), results in an elevated and sustained neural activity due to strong recurrent excitation and enhance SNR mediated by DARs, as observed in the Manuscript Nr. 4.

To test whether the observed changes in power have any significance in the stimulus encoding, we computed the mutual information that each frequency band carry about the sensory stimulus (Figure 7.2 and Figure 8.3). Interestingly, we found that LDC increases the information from alpha, nMOD and gamma bands, in particular in the SG- and IG-layers (Figure 8.3). Second, we also found that alpha information increases in all layers. Interestingly, recent studies have indicated that alpha and gamma bands are important for feedback and feedforward activity respectively (van Kerkoerle et al., 2014). What these studies show, is that gamma oscillations initiate at the G-layer and propagate further to the SG and IG layers while alpha propagates in the opposite directions. Our results further suggest that these oscillations are generated at one cortical depth without too much stimulus dependency (low information and signal-CV in the G), but as the oscillations propagate to further layers (SG and IG) these are amplified or suppressed in a stimulus dependent manner. Hence, the fact that DA increases the gamma information in the top and deep layers, supports the theory that DA provide with mechanism for an efficient propagation of sensory information towards higher areas and for communication back to the thalamus for efficient processing of incoming sensory inputs (Swadlow and Gusev, 2001; Timofeev and Steriade, 1996, 1998).

The multimodal approach described in this dissertation allowed us to better understand the effects of neuromodulation on hemodynamics, neurometabolism and neurophysiology responses. These findings support the notion that neuromodulators determine how neural circuits process information during sensory stimulation. In this dissertation, we showed that neuromodulators can have strong influence on the BOLD and CBF responses, and

combining fMRI with pharmacological and neurophysiological techniques can aid understanding the effects of neuromodulation on neural circuits and neurovascular coupling. If we are able to identify signatures of individual neuromodulators in the fMRI and neurophysiological signals, we may also be able to detect chemical imbalances associated with brain diseases.

2.4.5 Limitations

The set of studies used in this dissertation provide reliable knowledge about the effects of neuromodulation on neurovascular coupling and the concomitant effects on neural activity (Manuscript Nr. 2; Manuscript Nr. 4; Manuscript Nr. 5). We also showed that such effects of neuromodulators can disturb the stimulus encoding from the different cortical layers (Manuscript Nr. 5 and 6) and that neuromodulation effects can be inferred by looking at the power modulation of the midrange frequency bands (Manuscript Nr. 6). Nonetheless, one possible concern in the interpretation of these results is that the data was collected under anesthetized conditions.

Several studies have reported layer dependent changes in neural activity associated to anesthesia (Alkire and Miller, 2005; Sellers et al., 2013; Sellers et al., 2015; Wanger et al., 2013). What these studies have revealed is that sensory evoked activity and the cortico-cortical interactions with higher areas are usually disrupted in the top layers (SG) using isoflurane (Sellers et al., 2015), while concentration-dependent difference in power across layers are usually observed with urethane (Wanger et al., 2013). These studies suggest that the effects of anesthesia on cortical layers would highly depend on the class of anesthetic and their mechanisms of action. For instance, the anesthesia protocol used in our current study has been extensively used to investigate the neurovascular coupling in sensory areas (Goense and Logothetis, 2008; Magri et al., 2012b; Zaldivar et al., 2014). These studies have revealed that neural responses and hemodynamic signals under this anesthesia regime are very similar to those in the awake state (Goense and Logothetis, 2008). Indeed, no differences on the activation of the neural networks associated to face

recognition have been observed between anesthetized and awake monkeys (Ku et al., 2011). Also, LFP-power modulation, signal and noise correlations, as well as the information spectrum look very similar in the awake and the anesthetized condition (Belitski et al., 2010). Another important aspect to consider is that μ-opioid receptors are usually located at high densities in basal ganglia and thalamus, especially in regions associated to motor commands, while regions associated with cognition, ventral tegmental area, substantia nigra and frontal regions, have low densities of μ-opioid receptors.

Therefore, the advantage of using anesthetized monkeys is that we can assess the effects of different neuromodulators on neural and hemodynamic properties without needing to take behavioral parameters, like reward- and attentional effects, into account. However, differences in regional CBF under the effects of neuromodulation have also been observed between awake and anesthetized animals (Hershey et al., 2000; Hershey et al., 2004). Furthermore, differences depending on the type of anesthesia are expected. Given that neuromodulatory properties are strongly dependent on behavioural state of the animal, or its level of alertness, fMRI studies on neuromodulatory effects are complex. Ideally it would be interesting to compare many of the neuromodulators effects in awake and anesthetized animals under the same protocol. Further comparative studies are needed to address cortical versus neuromodulatory contributions to neural processing, and their relation to haemodynamic responses.

2.4.6 Outlook

In this dissertation we have made great strides in delineating the effects of neuromodulation on the neurovascular coupling of the macaque V1 using pharmacology, laminar neurophysiology, fMRI (BOLD and CBF) and chemistry sampling. While the results presented here have provided valuable insights into the effects of neuromodulation in these signals, they also raise a number of interesting questions and hypotheses.

For instance, we showed that we are able to simultaneously measure multiple neurochemicals in the BECF and blood, which helped us to define regional metabolic process that contribute to the homeostasis in the normal monkeys brain (Manuscript Nr. 1). However, these experiments were mostly collected while the monkeys were anesthetized and with no sensory stimulation. Yet, how these chemical profiles may change under the influence of sensory stimulation and how these profiles can vary during sensory- and/or cognitive tasks, are questions that will ultimately define how metabolites and neuro-transmitters/modulators mediate neural function. To answer this question, one needs to first complement the neurochemistry analysis with other techniques, such as electrophysiology and fMRI (BOLD, CBF, CBV or $CMRO_2$), to better characterize the signaling molecules associated to the different neuronal events. In addition, given that the data for the Manuscript Nr. 1 was mostly collected in V1, it will be interesting to assess differences in a broad array of metabolites across different anatomical regions during resting state and during cognitive tasks. This will increase our knowledge about the distribution of metabolites in the brain, given that the knowledgebase for regional distribution of brain metabolites appears to be contradictory and limited to a small set of molecules in the brain of rodents (Minati et al., 2010; Pouwels and Frahm, 1998).

Moreover, in our Manuscript Nr. 3, we combined pharmaco-MRI and neurophysiology (approach developed in the Manuscript Nr. 2) with blood-chemistry sampling. Although in this study we found that lactate and pyruvate exerted similar effects in the BOLD and CBF responses, associated to increased lactate and pyruvate levels, the neurophysiology experiments were slightly different (Figure 5.5 and Figure 5.6). Here we found that lactate elicits stronger and long-lasting effects in the LFPs than pyruvate (Figure 5.5 and Figure 5.6). This is surprising, giving that lactate and pyruvate are in near-equilibrium and their metabolism equally depends of the presence of the lactate dehydrogenase (LDH; Magistretti and Allaman, 2015; Pellerin and Magistretti, 2004). Hence, these results raise the question of whether different cell types have distinct metabolic profiles and/or

preferences (Belanger et al., 2011; Pellerin and Magistretti, 2004; Simard and Nedergaard, 2004). In particular it is not known if such a difference can also be found between interneurons and pyramidal cells. If such difference existed, this will imply the existence of rich and coordinated cell signaling mechanisms in the regulation of metabolic processes for the overall balance of excitation and inhibition. Therefore, the development of novel techniques, with even higher spatial and temporal resolution, will provide new tools to refine our understanding of intracellular metabolic exchanges and possibly reveal a higher level of regulation in subcellular compartments (Belanger et al., 2011; Magistretti and Allaman, 2015). This is important given that neuromodulators acts through different intracellular signal pathways which result in changes in the metabolism as well as in the synthesis of different molecules that subserve different aspects of intracellular communication.

In our Manuscript Nr. 2 and Manuscript Nr. 4, we explored the effects DA into the neurovascular coupling. Briefly, we found that DA dissociated the BOLD signal from the underlying neural activity. A phenomena that is not locally mediated by DARs in V1 (Zaldivar et al., 2014). Multiple studies have suggested that the effects of DA in the sensory information are the result of long-range interactions with higher order areas, possibly via prefrontal cortex (PFC; Happel et al., 2014; Jacob et al., 2013; Noudoost and Moore, 2011). However, little is known about how this interaction between V1 and PFC may evolve. Therefore, it will be interesting to conduct experiments that mimic DAergic neuromodulation, either pharmacologically or by a cognitive task, while simultaneously recording BOLD, CBF and neurophysiology activity in V1 and PFC. This is also relevant for the Manuscript Nr. 6, given that we found that SG-layer increased their information capabilities under the influence of DA. Therefore, it will remarkable to explore the effects of DA using high-resolution fMRI and investigate laminar difference in neurovascular coupling under the influence of DA. Given that DAergic neuromodulation in V1 increases the information capabilities from SG- and IG-layers, but not in the G-layers, it is expected

that the profile that we observed in the Manuscript Nr. 4 would likely change in different layers.

In the Manuscript Nr. 5 and Manuscript Nr. 6, we investigated differences in power and information-content from the cortical layers in V1, either with and without the influence of neuromodulation. These findings, allows us to separate the effects of feedforwards signals from feedback signals and to identify the neural activity associated to neuromodulatory processes. However, it will be interesting to investigate how different can these profiles be under the effects of other neuromodulators. This will probably require the exploration about their effects using CSD analysis to better understand their effects in the propagation of oscillatory activity. This will imply that different neuromodulators are likely to generated different CSD profiles.

2.4.7 Outlook for clinical applications

Multiple studies in the clinical neuroscience, have been focused at targeting structural changes associated to different brain disorders (Cahn et al., 2002; Clark and Sahakian, 2008; DeLisi et al., 2006; Karlsgodt et al., 2010). Although a great deal of information has been learnt about the anatomical abnormalities associated to brain dysfunction, much of the reported structural changes usually reflect the post-onset period of a certain disease (Karlsgodt et al., 2010). An important new challenge for clinical neuroimaging, in particular fMRI, is being set with the availability of therapies that could delay the onset or expression of chronic neurological diseases (Iadecola, 2004). However, the clinical obstacle is to identify early disease specifically and with confidence, in order to assist clinical decisions (Bartsch et al., 2006; Jezzard and Buxton, 2006).

One of the essential problems for such clinical aids is that we need to understand the magnitude of the BOLD signal in a meaningful way. That is, rather than a mapping study, where the central goal is simply to detect where activation is happening, the goal in many disease studies is to detect differences in the level of the response (Jezzard and Buxton,

2006). Many studies are applying fMRI techniques to try to shed light on disease mechanisms or to provide a means to assess the progression of disease or the response to treatment (Karlsgodt et al., 2010; Rashid et al., 2015). Yet there is a fundamental ambiguity underlying these studies: if a disease group shows a different BOLD response to that of a healthy group in response to a standard task, how should this be interpreted? It could represent a difference in the neural activity associated with the task, but it could also be an effect of the disease on vascular responsiveness, or the coupling of neural activity with CBF, or chronic changes in the baseline state. Unfortunately, from the BOLD responses alone, we cannot distinguish any of these possibilities.

To move forward, an important step is to determine the specific molecular basis associated to the brain disorders, such as changes in neurotransmitter systems and cellular signaling, as well the associated metabolic and neural changes. However, we must first gain insights into the aspects that better reflected in the fMRI-BOLD responses. The findings presented in this dissertation provided us with a concise idea about the complexity of the mechanisms modulating the neurovascular coupling. We showed that neuromodulators can have profound effects in the BOLD responses that not necessarily correspond to the neural activity, therefore implying that that caution is necessary in interpreting BOLD signals. Thus, combining BOLD with PET, EEG and MEG can deepen our understanding of physiological function and pathologies involving neuromodulatory systems.

2.5 References

Adesnik, H., Bruns, W., Taniguchi, H., Huang, Z.J., and Scanziani, M. (2012). A neural circuit for spatial summation in visual cortex. Nature *490*, 226-231.

Algaze, A., Leguire, L.E., Roberts, C., Ibinson, J.W., Lewis, J.R., and Rogers, G. (2005). The effects of L-dopa on the functional magnetic resonance imaging response of patients with amblyopia: a pilot study. J AAPOS *9*, 216-223.

Alkire, M.T., and Miller, J. (2005). General anesthesia and the neural correlates of consciousness. Prog Brain Res *150*, 229-244.

Amzica, F., and Steriade, M. (2000). Neuronal and glial membrane potentials during sleep and paroxysmal oscillations in the neocortex. J Neurosci *20*, 6648-6665.

Andreone, B.J., Lacoste, B., and Gu, C. (2015). Neuronal and Vascular Interactions. Annu Rev Neurosci.

Armstrong-James, M., Welker, E., and Callahan, C.A. (1993). The contribution of NMDA and non-NMDA receptors to fast and slow transmission of sensory information in the rat SI barrel cortex. J Neurosci *13*, 2149-2160.

Arsenault, J.T., Nelissen, K., Jarraya, B., and Vanduffel, W. (2013). Dopaminergic reward signals selectively decrease fMRI activity in primate visual cortex. Neuron *77*, 1174-1186.

Attwell, D., Buchan, A.M., Charpak, S., Lauritzen, M., Macvicar, B.A., and Newman, E.A. (2010). Glial and neuronal control of brain blood flow. Nature *468*, 232-243.

Attwell, D., and Laughlin, S.B. (2001a). An energy budget for signaling in the grey matter of the brain. J Cerebr Blood F Met *21*, 1133-1145.

Attwell, D., and Laughlin, S.B. (2001b). An energy budget for signaling in the grey matter of the brain. J Cereb Blood Flow Metab *21*, 1133-1145.

Bak, L.K., Schousboe, A., and Waagepetersen, H.S. (2006). The glutamate/GABA-glutamine cycle: aspects of transport, neurotransmitter homeostasis and ammonia transfer. Journal of Neurochemistry *98*, 641-653.

Bartsch, A.J., Homola, G., Biller, A., Solymosi, L., and Bendszus, M. (2006). Diagnostic functional MRI: illustrated clinical applications and decision-making. J Magn Reson Imaging *23*, 921-932.

Belanger, M., Allaman, I., and Magistretti, P.J. (2011). Brain energy metabolism: focus on astrocyte-neuron metabolic cooperation. Cell Metab *14*, 724-738.

Belitski, A., Gretton, A., Magri, C., Murayama, Y., Montemurro, M.A., Logothetis, N.K., and Panzeri, S. (2008). Low-frequency local field potentials and spikes in primary visual cortex convey independent visual information. J Neurosci *28*, 5696-5709.

Belitski, A., Panzeri, S., Magri, C., Logothetis, N.K., and Kayser, C. (2010). Sensory information in local field potentials and spikes from visual and auditory cortices: time scales and frequency bands. J Comput Neurosci *29*, 533-545.

Bellander, B.M., Cantais, E., Enblad, P., Hutchinson, P., Nordstrom, C.H., Robertson, C., Sahuquillo, J., Smith, M., Stocchetti, N., Ungerstedt, U*., et al.* (2004). Consensus meeting on microdialysis in neurointensive care. Intensive Care Med *30*, 2166-2169.

Billimoria, C.P., DiCaprio, R.A., Birmingham, J.T., Abbott, L.F., and Marder, E. (2006). Neuromodulation of spike-timing precision in sensory neurons. J Neurosci *26*, 5910-5919.

Bittner, C.X., Valdebenito, R., Ruminot, I., Loaiza, A., Larenas, V., Sotelo-Hitschfeld, T., Moldenhauer, H., San Martin, A., Gutierrez, R., Zambrano, M*., et al.* (2011). Fast and reversible stimulation of astrocytic glycolysis by K+ and a delayed and persistent effect of glutamate. J Neurosci *31*, 4709-4713.

Black, K.J., Carl, J.L., Hartlein, J.M., Warren, S.L., Hershey, T., and Perlmutter, J.S. (2003). Rapid intravenous loading of levodopa for human research: clinical results. J Neurosci Methods *127*, 19-29.

Blinder, P., Tsai, P.S., Kaufhold, J.P., Knutsen, P.M., Suhl, H., and Kleinfeld, D. (2013). The cortical angiome: an interconnected vascular network with noncolumnar patterns of blood flow. Nat Neurosci *16*, 889-897.

Boumezbeur, F., Petersen, K.F., Cline, G.W., Mason, G.F., Behar, K.L., Shulman, G.I., and Rothman, D.L. (2010). The contribution of blood lactate to brain energy metabolism in humans measured by dynamic 13C nuclear magnetic resonance spectroscopy. J Neurosci *30*, 13983-13991.

Bouzier-Sore, A.K., Voisin, P., Bouchaud, V., Bezancon, E., Franconi, J.M., and Pellerin, L. (2006). Competition between glucose and lactate as oxidative energy substrates in both neurons and astrocytes: a comparative NMR study. Eur J Neurosci *24*, 1687-1694.

Boynton, G.M. (2011). Spikes, BOLD, attention, and awareness: a comparison of electrophysiological and fMRI signals in V1. J Vis *11*, 12.

Briggs, F., and Callaway, E.M. (2001). Layer-specific input to distinct cell types in layer 6 of monkey primary visual cortex. Journal of Neuroscience *21*, 3600-3608.

Briggs, F., and Callaway, E.M. (2005). Laminar patterns of local excitatory input to layer 5 neurons in macaque primary visual cortex. Cereb Cortex *15*, 479-488.

Brunel, N. (2016). Is cortical connectivity optimized for storing information? Nat Neurosci *19*, 749-755.

Brunel, N., and Wang, X.J. (2001). Effects of neuromodulation in a cortical network model of object working memory dominated by recurrent inhibition. J Comput Neurosci *11*, 63-85.

Brunel, N., and Wang, X.J. (2003). What determines the frequency of fast network oscillations with irregular neural discharges? I. Synaptic dynamics and excitation-inhibition balance. Journal of Neurophysiology *90*, 415-430.

Buchwald, J.S., Halas, E.S., and Schramm, S. (1966). Relationships of Neuronal Spike Populations and Eeg Activity in Chronic Cats. Electroen Clin Neuro *21*, 227-&.

Buschman, T.J., and Miller, E.K. (2007). Top-down versus bottom-up control of attention in the prefrontal and posterior parietal cortices. Science *315*, 1860-1862.

Buxton, R.B. (2013). The physics of functional magnetic resonance imaging (fMRI). Rep Prog Phys *76*.

Buzsaki, G., Anastassiou, C.A., and Koch, C. (2012). The origin of extracellular fields and currents--EEG, ECoG, LFP and spikes. Nat Rev Neurosci *13*, 407-420.

Buzsaki, G., Kaila, K., and Raichle, M. (2007). Inhibition and brain work. Neuron *56*, 771-783.

Buzsaki, G., and Wang, X.J. (2012). Mechanisms of Gamma Oscillations. Annual Review of Neuroscience, Vol 35 *35*, 203-225.

Cahn, W., Hulshoff Pol, H.E., Lems, E.B., van Haren, N.E., Schnack, H.G., van der Linden, J.A., Schothorst, P.F., van Engeland, H., and Kahn, R.S. (2002). Brain volume changes in first-episode schizophrenia: a 1-year follow-up study. Arch Gen Psychiatry *59*, 1002-1010.

Callaway, E.M. (1998). Local circuits in primary visual cortex of the macaque monkey. Annu Rev Neurosci *21*, 47-74.

Cauli, B., and Hamel, E. (2010). Revisiting the role of neurons in neurovascular coupling. Front Neuroenergetics *2*, 9.

Cerdan, S., Rodrigues, T.B., Sierra, A., Benito, M., Fonseca, L.L., Fonseca, C.P., and Garcia-Martin, M.L. (2006). The redox switch/redox coupling hypothesis. Neurochem Int *48*, 523-530.

Chatterjee, S., and Callaway, E.M. (2003). Parallel colour-opponent pathways to primary visual cortex. Nature *426*, 668-671.

Chen, Z., Silva, A.C., Yang, J., and Shen, J. (2005). Elevated endogenous GABA level correlates with decreased fMRI signals in the rat brain during acute inhibition of GABA transaminase. J Neurosci Res *79*, 383-391.

Chih, C.P., and Roberts Jr, E.L. (2003). Energy substrates for neurons during neural activity: a critical review of the astrocyte-neuron lactate shuttle hypothesis. J Cereb Blood Flow Metab *23*, 1263-1281.

Clapham, D.E. (1994). Direct G protein activation of ion channels? Annu Rev Neurosci *17*, 441-464.

Clark, L., and Sahakian, B.J. (2008). Cognitive neuroscience and brain imaging in bipolar disorder. Dialogues Clin Neurosci *10*, 153-163.

Clarke, A.R., Atkinson, T., and Holbrook, J.J. (1989a). From analysis to synthesis: new ligand binding sites on the lactate dehydrogenase framework. Part I. Trends Biochem Sci *14*, 101-105.

Clarke, A.R., Atkinson, T., and Holbrook, J.J. (1989b). From analysis to synthesis: new ligand binding sites on the lactate dehydrogenase framework. Part II. Trends Biochem Sci *14*, 145-148.

Coenen, A.M. (1995). Neuronal activities underlying the electroencephalogram and evoked potentials of sleeping and waking: implications for information processing. Neurosci Biobehav Rev *19*, 447-463.

Constantinople, C.M., and Bruno, R.M. (2011). Effects and mechanisms of wakefulness on local cortical networks. Neuron *69*, 1061-1068.

Dadeya, S., Vats, P., and Malik, K.P. (2009). Levodopa/carbidopa in the treatment of amblyopia. J Pediatr Ophthalmol Strabismus *46*, 87-90; quiz 91-82.

Dayan, P. (2012). Twenty-five lessons from computational neuromodulation. Neuron *76*, 240-256.

de Lafuente, V., and Romo, R. (2011). Dopamine neurons code subjective sensory experience and uncertainty of perceptual decisions. PNAS *108*, 19767-19771.

DeLisi, L.E., Szulc, K.U., Bertisch, H.C., Majcher, M., and Brown, K. (2006). Understanding structural brain changes in schizophrenia. Dialogues Clin Neurosci *8*, 71-78.

Destexhe, A., Contreras, D., and Steriade, M. (1999). Spatiotemporal analysis of local field potentials and unit discharges in cat cerebral cortex during natural wake and sleep states. J Neurosci *19*, 4595-4608.

Di Rocco, R.J., Kageyama, G.H., and Wong-Riley, M.T. (1989). The relationship between CNS metabolism and cytoarchitecture: a review of 14C-deoxyglucose studies with correlation to cytochrome oxidase histochemistry. Comput Med Imaging Graph *13*, 81-92.

DiCarlo, J.J., Zoccolan, D., and Rust, N.C. (2012). How does the brain solve visual object recognition? Neuron *73*, 415-434.

Dienel, G.A., Schmidt, K.C., and Cruz, N.F. (2007). Astrocyte activation in vivo during graded photic stimulation. J Neurochem *103*, 1506-1522.

Ding, F., O'Donnell, J., Xu, Q., Kang, N., Goldman, N., and Nedergaard, M. (2016). Changes in the composition of brain interstitial ions control the sleep-wake cycle. Science *352*, 550-555.

Disney, A.A., and Aoki, C. (2008). Muscarinic acetylcholine receptors in macaque V1 are most frequently expressed by parvalbumin-immunoreactive neurons. The Journal of comparative neurology *507*, 1748-1762.

Disney, A.A., Aoki, C., and Hawken, M.J. (2007). Gain modulation by nicotine in macaque v1. Neuron *56*, 701-713.

Douglas, R.J., and Martin, K.A. (2004). Neuronal circuits of the neocortex. Annu Rev Neurosci *27*, 419-451.

Douglas, R.J., and Martin, K.A. (2007). Recurrent neuronal circuits in the neocortex. Curr Biol *17*, R496-500.

Duvernoy, H.M., Delon, S., and Vannson, J.L. (1981). Cortical blood vessels of the human brain. Brain Res Bull *7*, 519-579.

Eickhoff, S.B., Rottschy, C., and Zilles, K. (2007a). Laminar distribution and co-distribution of neurotransmitter receptors in early human visual cortex. Brain Struct Funct *212*, 255-267.

Eickhoff, S.B., Schleicher, A., Scheperjans, F., Palomero-Gallagher, N., and Zilles, K. (2007b). Analysis of neurotransmitter receptor distribution patterns in the cerebral cortex. Neuroimage *34*, 1317-1330.

Einevoll, G.T., Kayser, C., Logothetis, N.K., and Panzeri, S. (2013). Modelling and analysis of local field potentials for studying the function of cortical circuits. Nat Rev Neurosci *14*, 770-785.

Einevoll, G.T., Pettersen, K.H., Devor, A., Ulbert, I., Halgren, E., and Dale, A.M. (2007). Laminar population analysis: Estimating firing rates and evoked synaptic activity from multielectrode recordings in rat barrel cortex. Journal of Neurophysiology *97*, 2174-2190.

Engel, A.K., and Fries, P. (2010). Beta-band oscillations--signalling the status quo? Curr Opin Neurobiol *20*, 156-165.

Esaki, T., Itoh, Y., Shimoji, K., Cook, M., Jehle, J., and Sokoloff, L. (2002). Effects of dopamine receptor blockade on cerebral blood flow response to somatosensory stimulation in the unanesthetized rat. J Pharmacol Exp Ther *303*, 497-502.

Faraci, F.M., and Breese, K.R. (1993). Nitric oxide mediates vasodilatation in response to activation of N-methyl-D-aspartate receptors in brain. Circ Res *72*, 476-480.

Federer, F., Ichida, J.M., Jeffs, J., Schiessl, I., McLoughlin, N., and Angelucci, A. (2009). Four Projection Streams from Primate V1 to the Cytochrome Oxidase Stripes of V2. Journal of Neuroscience *29*, 15455-15471.

Fellous, J.M., and Linster, C. (1998). Computational models of neuromodulation. Neural Comput *10*, 771-805.

Figueroa, X.F., and Duling, B.R. (2009). Gap junctions in the control of vascular function. Antioxid Redox Signal *11*, 251-266.

Fonta, C., and Imbert, M. (2002). Vascularization in the primate visual cortex during development. Cerebral cortex *12*, 199-211.

Fox, P.T., and Raichle, M.E. (1986). Focal physiological uncoupling of cerebral blood flow and oxidative metabolism during somatosensory stimulation in human subjects. PNAS *83*, 1140-1144.

Freund, H., Oyono-Enguelle, S., Heitz, A., Ott, C., Marbach, J., Gartner, M., and Pape, A. (1990). Comparative lactate kinetics after short and prolonged submaximal exercise. Int J Sports Med *11*, 284-288.

Froemke, R.C. (2015). Plasticity of cortical excitatory-inhibitory balance. Annu Rev Neurosci *38*, 195-219.

Gallagher, C.N., Carpenter, K.L., Grice, P., Howe, D.J., Mason, A., Timofeev, I., Menon, D.K., Kirkpatrick, P.J., Pickard, J.D., Sutherland, G.R.*, et al.* (2009). The human brain utilizes lactate via the tricarboxylic acid cycle: a 13C-labelled microdialysis and high-resolution nuclear magnetic resonance study. Brain *132*, 2839-2849.

Geppetti, P., Veldhuis, N.A., Lieu, T., and Bunnett, N.W. (2015). G Protein-Coupled Receptors: Dynamic Machines for Signaling Pain and Itch. Neuron *88*, 635-649.

Gibson, G.E., Peterson, C., and Sansone, J. (1981). Neurotransmitter and carbohydrate metabolism during aging and mild hypoxia. Neurobiol Aging *2*, 165-172.

Gil, Z., Connors, B.W., and Amitai, Y. (1997). Differential regulation of neocortical synapses by neuromodulators and activity. Neuron *19*, 679-686.

Gilbert, C.D. (1977). Laminar differences in receptive field properties of cells in cat primary visual cortex. The Journal of physiology *268*, 391-421.

Goense, J., Merkle, H., and Logothetis, N.K. (2012). High-resolution fMRI reveals laminar differences in neurovascular coupling between positive and negative BOLD responses. Neuron *76*, 629-639.

Goense, J.B., and Logothetis, N.K. (2008). Neurophysiology of the BOLD fMRI signal in awake monkeys. Curr Biol *18*, 631-640.

Gordon, G.R., Choi, H.B., Rungta, R.L., Ellis-Davies, G.C., and MacVicar, B.A. (2008). Brain metabolism dictates the polarity of astrocyte control over arterioles. Nature *456*, 745-749.

Gordon, M., Markham, J., Hartlein, J.M., Koller, J.M., Loftin, S., and Black, K.J. (2007). Intravenous levodopa administration in humans based on a two-compartment kinetic model. J Neurosci Methods *159*, 300-307.

Gozzi, A., Large, C.H., Schwarz, A., Bertani, S., Crestan, V., and Bifone, A. (2008). Differential effects of antipsychotic and glutamatergic agents on the phMRI response to phencyclidine. Neuropsychopharmacol *33*, 1690-1703.

Gozzi, A., Schwarz, A.J., Reese, T., Crestan, V., Bertani, S., Turrini, G., Corsi, M., and Bifone, A. (2005). Functional magnetic resonance mapping of intracerebroventricular infusion of a neuroactive peptide in the anaesthetised rat. J Neurosci Meth *142*, 115-124.

Gray, C.M., Konig, P., Engel, A.K., and Singer, W. (1989). Oscillatory Responses in Cat Visual-Cortex Exhibit Inter-Columnar Synchronization Which Reflects Global Stimulus Properties. Nature *338*, 334-337.

Gsell, W., Burke, M., Wiedermann, D., Bonvento, G., Silva, A.C., Dauphin, F., Buhrle, C., Hoehn, M., and Schwindt, W. (2006). Differential effects of NMDA and AMPA glutamate receptors on functional magnetic resonance imaging signals and evoked neuronal activity during forepaw stimulation of the rat. J Neurosci *26*, 8409-8416.

Gu, Q. (2002). Neuromodulatory transmitter systems in the cortex and their role in cortical plasticity. Neuroscience *111*, 815-835.

Haegens, S., Nacher, V., Hernandez, A., Luna, R., Jensen, O., and Romo, R. (2011a). Beta oscillations in the monkey sensorimotor network reflect somatosensory decision making. PNAS *108*, 10708-10713.

Haegens, S., Nacher, V., Luna, R., Romo, R., and Jensen, O. (2011b). alpha-Oscillations in the monkey sensorimotor network influence discrimination performance by rhythmical inhibition of neuronal spiking. PNAS *108*, 19377-19382.

Haider, B., Schulz, D.P., Hausser, M., and Carandini, M. (2016). Millisecond Coupling of Local Field Potentials to Synaptic Currents in the Awake Visual Cortex. Neuron *90*, 35-42.

Hamel, E.J., Grewe, B.F., Parker, J.G., and Schnitzer, M.J. (2015). Cellular level brain imaging in behaving mammals: an engineering approach. Neuron *86*, 140-159.

Hamilton, N.B., Attwell, D., and Hall, C.N. (2010). Pericyte-mediated regulation of capillary diameter: a component of neurovascular coupling in health and disease. Front Neuroenergetics *2*.

Hamood, A.W., and Marder, E. (2014). Animal-to-Animal Variability in Neuromodulation and Circuit Function. Cold Spring Harb Symp Quant Biol *79*, 21-28.

Hansen, B.J., Chelaru, M.I., and Dragoi, V. (2012). Correlated variability in laminar cortical circuits. Neuron *76*, 590-602.

Happel, M.F., Deliano, M., Handschuh, J., and Ohl, F.W. (2014). Dopamine-modulated recurrent corticoefferent feedback in primary sensory cortex promotes detection of behaviorally relevant stimuli. J Neurosci *34*, 1234-1247.

Harris-Warrick, R.M., and Marder, E. (1991). Modulation of neural networks for behavior. Annu Rev Neurosci *14*, 39-57.

Hasselmo, M.E. (1995). Neuromodulation and cortical function: modeling the physiological basis of behavior. Behav Brain Res *67*, 1-27.

Hawkins, B.T., and Davis, T.P. (2005). The blood-brain barrier/neurovascular unit in health and disease. Pharmacol Rev *57*, 173-185.

Hawkins, R.A. (2009). The blood-brain barrier and glutamate. Am J Clin Nutr *90*, 867S-874S.

Hayashi, T. (1952). A physiological study of epileptic seizures following cortical stimulation in animals and its application to human clinics. Jpn J Physiol *3*, 46-64.

Hayashi, T. (1959). The inhibitory action of beta-hydroxy-gamma-aminobutyric acid upon the seizure following stimulation of the motor cortex of the dog. The Journal of physiology *145*, 570-578.

Herguedas, B., Garcia-Nafria, J., Cais, O., Fernandez-Leiro, R., Krieger, J., Ho, H., and Greger, I.H. (2016). Structure and organization of heteromeric AMPA-type glutamate receptors. Science *352*, aad3873.

Herrero, J.L., Gieselmann, M.A., Sanayei, M., and Thiele, A. (2013). Attention-induced variance and noise correlation reduction in macaque V1 is mediated by NMDA receptors. Neuron *78*, 729-739.

Herrero, J.L., Roberts, M.J., Delicato, L.S., Gieselmann, M.A., Dayan, P., and Thiele, A. (2008). Acetylcholine contributes through muscarinic receptors to attentional modulation in V1. Nature *454*, 1110-1114.

Hershey, T., Black, K.J., Carl, J.L., and Perlmutter, J.S. (2000). Dopa-induced blood flow responses in nonhuman primates. Exp Neurol *166*, 342-349.

Hershey, T., Black, K.J., Hartlein, J., Braver, T.S., Barch, D.M., Carl, J.L., and Perlmutter, J.S. (2004). Dopaminergic modulation of response inhibition: an fMRI study. Brain Res Cogn Brain Res *20*, 438-448.

Hertz, L., Peng, L., and Dienel, G.A. (2007). Energy metabolism in astrocytes: high rate of oxidative metabolism and spatiotemporal dependence on glycolysis/glycogenolysis. J Cereb Blood Flow Metab *27*, 219-249.

Hillman, E.M. (2014). Coupling mechanism and significance of the BOLD signal: a status report. Annu Rev Neurosci *37*, 161-181.

Hirsch, J.A., Wang, X., Sommer, F.T., and Martinez, L.M. (2015). How inhibitory circuits in the thalamus serve vision. Annu Rev Neurosci *38*, 309-329.

Holroyd, S., and Wooten, G.F. (2006). Preliminary FMRI evidence of visual system dysfunction in Parkinson's disease patients with visual hallucinations. J Neuropsychiatry Clin Neurosci *18*, 402-404.

Honey, G., and Bullmore, E. (2004). Human pharmacological MRI. Trends in pharmacological sciences *25*, 366-374.

Horton, J.C. (1984). Cytochrome-Oxidase Patches - a New Cytoarchitectonic Feature of Monkey Visual-Cortex. Philos T Roy Soc B *304*, 199-253.

Hubel, D.H., and Wiesel, T.N. (1962). Receptive fields, binocular interaction and functional architecture in the cat's visual cortex. The Journal of physiology *160*, 106-154.

Humphrey, A.L., and Norton, T.T. (1980). Topographic organization of the orientation column system in the striate cortex of the tree shrew (Tupaia glis). I. Microelectrode recording. The Journal of comparative neurology *192*, 531-547.

Hurley, B.F., Hagberg, J.M., Allen, W.K., Seals, D.R., Young, J.C., Cuddihee, R.W., and Holloszy, J.O. (1984). Effect of training on blood lactate levels during submaximal exercise. J Appl Physiol *56*, 1260-1264.

Iadecola, C. (2004). Neurovascular regulation in the normal brain and in Alzheimer's disease. Nat Rev Neurosci *5*, 347-360.

Iadecola, C., and Nedergaard, M. (2007). Glial regulation of the cerebral microvasculature. Nat Neurosci *10*, 1369-1376.

Itoh, Y., Esaki, T., Shimoji, K., Cook, M., Law, M.J., Kaufman, E., and Sokoloff, L. (2003). Dichloroacetate effects on glucose and lactate oxidation by neurons and astroglia in vitro and on glucose utilization by brain in vivo. PNAS *100*, 4879-4884.

Ivanisevic, J., Epstein, A.A., Kurczy, M.E., Benton, P.H., Uritboonthai, W., Fox, H.S., Boska, M.D., Gendelman, H.E., and Siuzdak, G. (2014). Brain Region Mapping Using Global Metabolomics. Chem Biol *21*, 1575-1584.

Izpisua Belmonte, J.C., Callaway, E.M., Caddick, S.J., Churchland, P., Feng, G., Homanics, G.E., Lee, K.F., Leopold, D.A., Miller, C.T., Mitchell, J.F.*, et al.* (2015). Brains, genes, and primates. Neuron *86*, 617-631.

Jacob, S.N., Ott, T., and Nieder, A. (2013). Dopamine regulates two classes of primate prefrontal neurons that represent sensory signals. J Neurosci *33*, 13724-13734.

Jbabdi, S., Sotiropoulos, S.N., Haber, S.N., Van Essen, D.C., and Behrens, T.E. (2015). Measuring macroscopic brain connections in vivo. Nat Neurosci *18*, 1546-1555.

Jezzard, P., and Buxton, R.B. (2006). The clinical potential of functional magnetic resonance imaging. J Magn Reson Imaging *23*, 787-793.

Kaddurah-Daouk, R., and Krishnan, K.R. (2009). Metabolomics: a global biochemical approach to the study of central nervous system diseases. Neuropsychopharmacol *34*, 173-186.

Kadekaro, M., Crane, A.M., and Sokoloff, L. (1985). Differential-Effects of Electrical-Stimulation of Sciatic-Nerve on Metabolic-Activity in Spinal-Cord and Dorsal-Root Ganglion in the Rat. P Natl Acad Sci USA *82*, 6010-6013.

Kadekaro, M., Vance, W.H., Terrell, M.L., Gary, H., Eisenberg, H.M., and Sokoloff, L. (1987). Effects of Antidromic Stimulation of the Ventral Root on Glucose-Utilization in the Ventral Horn of the Spinal-Cord in the Rat. P Natl Acad Sci USA *84*, 5492-5495.

Kageyama, G.H., and Wong-Riley, M. (1986). Laminar and cellular localization of cytochrome oxidase in the cat striate cortex. The Journal of comparative neurology *245*, 137-159.

Kalisch, R., Salome, N., Platzer, S., Wigger, A., Czisch, M., Sommer, W., Singewald, N., Heilig, M., Berthele, A., Holsboer, F*., et al.* (2004). High trait anxiety and hyporeactivity to stress of the dorsomedial prefrontal cortex: a combined phMRI and Fos study in rats. Neuroimage *23*, 382-391.

Karlsgodt, K.H., Sun, D., and Cannon, T.D. (2010). Structural and Functional Brain Abnormalities in Schizophrenia. Curr Dir Psychol Sci *19*, 226-231.

Kasthuri, N., Hayworth, K.J., Berger, D.R., Schalek, R.L., Conchello, J.A., Knowles-Barley, S., Lee, D., Vazquez-Reina, A., Kaynig, V., Jones, T.R*., et al.* (2015). Saturated Reconstruction of a Volume of Neocortex. Cell *162*, 648-661.

Kayser, C., Petkov, C.I., and Logothetis, N.K. (2007). Tuning to sound frequency in auditory field Potentials. Journal of Neurophysiology *98*, 1806-1809.

Kida, I., Hyder, F., and Behar, K.L. (2001). Inhibition of voltage-dependent sodium channels suppresses the functional magnetic resonance imaging response to forepaw somatosensory activation in the rodent. J Cerebr Blood F Met *21*, 585-591.

Kida, I., Smith, A.J., Blumenfeld, H., Behar, K.L., and Hyder, F. (2006). Lamotrigine suppresses neurophysiological responses to somatosensory stimulation in the rodent. Neuroimage *29*, 216-224.

Kim, S.G. (1995). Quantification of relative cerebral blood flow change by flow-sensitive alternating inversion recovery (FAIR) technique: application to functional mapping. Magn Reson Med *34*, 293-301.

Kim, S.G., and Ogawa, S. (2012). Biophysical and physiological origins of blood oxygenation level-dependent fMRI signals. J Cereb Blood Flow Metab *32*, 1188-1206.

Knosche, T.R., and Tittgemeyer, M. (2011). The role of long-range connectivity for the characterization of the functional-anatomical organization of the cortex. Front Syst Neurosci *5*, 58.

Krimer, L.S., Muly, E.C., 3rd, Williams, G.V., and Goldman-Rakic, P.S. (1998). Dopaminergic regulation of cerebral cortical microcirculation. Nat Neurosci *1*, 286-289.

Ku, S.P., Tolias, A.S., Logothetis, N.K., and Goense, J. (2011). fMRI of the face-processing network in the ventral temporal lobe of awake and anesthetized macaques. Neuron *70*, 352-362.

Kujala, J., Jung, J., Bouvard, S., Lecaignard, F., Lothe, A., Bouet, R., Ciumas, C., Ryvlin, P., and Jerbi, K. (2015). Gamma oscillations in V1 are correlated with GABAA receptor density: A multi-modal MEG and Flumazenil-PET study. Sci Rep *5*, 16347.

Lee, J.H., Durand, R., Gradinaru, V., Zhang, F., Goshen, I., Kim, D.S., Fenno, L.E., Ramakrishnan, C., and Deisseroth, K. (2010). Global and local fMRI signals driven by neurons defined optogenetically by type and wiring. Nature *465*, 788-792.

Lee, W.H., Ngernsutivorakul, T., Mabrouk, O.S., Wong, J.M., Dugan, C.E., Pappas, S.S., Yoon, H.J., and Kennedy, R.T. (2016). Microfabrication and in Vivo Performance of a Microdialysis Probe with Embedded Membrane. Anal Chem *88*, 1230-1237.

Legatt, A.D., Arezzo, J., and Vaughan, H.G. (1980). Averaged Multiple Unit-Activity as an Estimate of Phasic Changes in Local Neuronal-Activity - Effects of Volume-Conducted Potentials. J Neurosci Meth *2*, 203-217.

Leithner, C., and Royl, G. (2014). The oxygen paradox of neurovascular coupling. J Cerebr Blood F Met *34*, 19-29.

Leonard, B.E., and Shallice, S.A. (1971). Some Neurochemical Effects of Amphetamine, Methylamphetamine and Para Bromomethyl Amphetamine in Rat. Br J Pharmacol *41*, 198-&.

Leontiev, O., and Buxton, R.B. (2007). Reproducibility of BOLD, perfusion, and CMRO2 measurements with calibrated-BOLD fMRI. Neuroimage *35*, 175-184.

Leontiev, O., Dubowitz, D.J., and Buxton, R.B. (2007). CBF/CMRO2 coupling measured with calibrated BOLD fMRI: sources of bias. Neuroimage *36*, 1110-1122.

Leopold, D.A. (2012). Primary visual cortex: awareness and blindsight. Annu Rev Neurosci *35*, 91-109.

Lewis, D.A., and Lund, J.S. (1990). Heterogeneity of chandelier neurons in monkey neocortex: corticotropin-releasing factor- and parvalbumin-immunoreactive populations. The Journal of comparative neurology *293*, 599-615.

Leybaert, L. (2005). Neurobarrier coupling in the brain: a partner of neurovascular and neurometabolic coupling? J Cerebr Blood F Met *25*, 2-16.

Li, B., and Freeman, R.D. (2015). Neurometabolic coupling between neural activity, glucose, and lactate in activated visual cortex. J Neurochem *135*, 742-754.

Li, J., von Pfostl, V., Zaldivar, D., Zhang, X., Logothetis, N., and Rauch, A. (2011). Measuring multiple neurochemicals and related metabolites in blood and brain of the rhesus monkey by using dual microdialysis sampling and capillary hydrophilic interaction chromatography-mass spectrometry. Anal Bioanal Chem.

Lidow, M.S., Goldman-Rakic, P.S., Gallager, D.W., and Rakic, P. (1991). Distribution of dopaminergic receptors in the primate cerebral cortex: quantitative autoradiographic analysis using [3H]raclopride, [3H]spiperone and [3H]SCH23390. Neuroscience *40*, 657-671.

Lidow, M.S., Goldman-Rakic, P.S., Rakic, P., and Gallager, D.W. (1990). Autoradiographic comparison of D1-specific binding of [3H]SCH39166 and [3H]SCH23390 in the primate cerebral cortex. Brain Res *537*, 349-354.

Linville, D.G., Williams, S., and Arneric, S.P. (1993). Basal forebrain control of cortical cerebral blood flow is independent of local cortical neurons. Brain Res *622*, 26-34.

Ljungberg, T., Apicella, P., and Schultz, W. (1992). Responses of monkey dopamine neurons during learning of behavioral reactions. J Neurophysiol *67*, 145-163.

Logothetis, N.K. (2008). What we can do and what we cannot do with fMRI. Nature *453*, 869-878.

Logothetis, N.K. (2010). Bold claims for optogenetics. Nature *468*, E3-E4.

Logothetis, N.K., Augath, M., Murayama, Y., Rauch, A., Sultan, F., Goense, J., Oeltermann, A., and Merkle, H. (2010). The effects of electrical microstimulation on cortical signal propagation. Nat Neurosci *13*, 1283-1291.

Logothetis, N.K., Eschenko, O., Murayama, Y., Augath, M., Steudel, T., Evrard, H.C., Besserve, M., and Oeltermann, A. (2012). Hippocampal-cortical interaction during periods of subcortical silence. Nature *491*, 547-553.

Logothetis, N.K., Kayser, C., and Oeltermann, A. (2007). In vivo measurement of cortical impedance spectrum in monkeys: implications for signal propagation. Neuron *55*, 809-823.

Logothetis, N.K., Pauls, J., Augath, M., Trinath, T., and Oeltermann, A. (2001). Neurophysiological investigation of the basis of the fMRI signal. Nature *412*, 150-157.

Logothetis, N.K., and Wandell, B.A. (2004). Interpreting the BOLD signal. Annu Rev Physiol *66*, 735-769.

Loubinoux, I., Pariente, J., Boulanouar, K., Carel, C., Manelfe, C., Rascol, O., Celsis, P., and Chollet, F. (2002). A single dose of the serotonin neurotransmission agonist paroxetine enhances motor output: double-blind, placebo-controlled, fMRI study in healthy subjects. Neuroimage *15*, 26-36.

Lundqvist, M., Rose, J., Herman, P., Brincat, S.L., Buschman, T.J., and Miller, E.K. (2016). Gamma and Beta Bursts Underlie Working Memory. Neuron *90*, 152-164.

Magistretti, P.J., and Allaman, I. (2015). A cellular perspective on brain energy metabolism and functional imaging. Neuron *86*, 883-901.

Magistretti, P.J., Morrison, J.H., Shoemaker, W.J., Sapin, V., and Bloom, F.E. (1981). Vasoactive intestinal polypeptide induces glycogenolysis in mouse cortical slices: a possible regulatory mechanism for the local control of energy metabolism. PNAS *78*, 6535-6539.

Magri, C., Mazzoni, A., Logothetis, N.K., and Panzeri, S. (2012a). Optimal band separation of extracellular field potentials. J Neurosci Methods *210*, 66-78.

Magri, C., Schridde, U., Murayama, Y., Panzeri, S., and Logothetis, N.K. (2012b). The amplitude and timing of the BOLD signal reflects the relationship between local field potential power at different frequencies. J Neurosci *32*, 1395-1407.

Maier, A., Aura, C.J., and Leopold, D.A. (2011). Infragranular sources of sustained local field potential responses in macaque primary visual cortex. J Neurosci *31*, 1971-1980.

Malyshev, A., Goz, R., LoTurco, J.J., and Volgushev, M. (2015). Advantages and Limitations of the Use of Optogenetic Approach in Studying Fast-Scale Spike Encoding. Plos One *10*.

Mandeville, J.B., Sander, C.Y., Jenkins, B.G., Hooker, J.M., Catana, C., Vanduffel, W., Alpert, N.M., Rosen, B.R., and Normandin, M.D. (2013). A receptor-based model for dopamine-induced fMRI signal. Neuroimage *75C*, 46-57.

Marder, E. (2012). Neuromodulation of neuronal circuits: back to the future. Neuron *76*, 1-11.

Marder, E., O'Leary, T., and Shruti, S. (2014). Neuromodulation of circuits with variable parameters: single neurons and small circuits reveal principles of state-dependent and robust neuromodulation. Annu Rev Neurosci *37*, 329-346.

Marder, E., and Thirumalai, V. (2002). Cellular, synaptic and network effects of neuromodulation. Neural Netw *15*, 479-493.

Marota, J.J., Mandeville, J.B., Weisskoff, R.M., Moskowitz, M.A., Rosen, B.R., and Kosofsky, B.E. (2000). Cocaine activation discriminates dopaminergic projections by temporal response: an fMRI study in Rat. Neuroimage *11*, 13-23.

Mathiisen, T.M., Lehre, K.P., Danbolt, N.C., and Ottersen, O.P. (2010). The perivascular astroglial sheath provides a complete covering of the brain microvessels: an electron microscopic 3D reconstruction. Glia *58*, 1094-1103.

Matthews, G.A., Nieh, E.H., Vander Weele, C.M., Halbert, S.A., Pradhan, R.V., Yosafat, A.S., Glober, G.F., Izadmehr, E.M., Thomas, R.E., Lacy, G.D.*, et al.* (2016). Dorsal Raphe Dopamine Neurons Represent the Experience of Social Isolation. Cell *164*, 617-631.

McKenna, M.C. (2007). The glutamate-glutamine cycle is not stoichiometric: Fates of glutamate in brain. Journal of Neuroscience Research *85*, 3347-3358.

Mesulam, M.M., Mufson, E.J., Levey, A.I., and Wainer, B.H. (1983). Cholinergic innervation of cortex by the basal forebrain: cytochemistry and cortical connections of the septal area, diagonal band nuclei, nucleus basalis (substantia innominata), and hypothalamus in the rhesus monkey. The Journal of comparative neurology *214*, 170-197.

Miledi, R. (1973). Transmitter Release Induced by Injection of Calcium-Ions into Nerve Terminals. Proc R Soc Ser B-Bio *183*, 421-425.

Miller, C.T., Freiwald, W.A., Leopold, D.A., Mitchell, J.F., Silva, A.C., and Wang, X. (2016). Marmosets: A Neuroscientific Model of Human Social Behavior. Neuron *90*, 219-233.

Minati, L., Aquino, D., Bruzzone, M.G., and Erbetta, A. (2010). Quantitation of normal metabolite concentrations in six brain regions by in-vivoH-MR spectroscopy. J Med Phys *35*, 154-163.

Mintun, M.A., Vlassenko, A.G., Rundle, M.M., and Raichle, M.E. (2004). Increased lactate/pyruvate ratio augments blood flow in physiologically activated human brain. PNAS *101*, 659-664.

Mitchell, J.F., and Leopold, D.A. (2015). The marmoset monkey as a model for visual neuroscience. Neurosci Res *93*, 20-46.

Mitterschiffthaler, M.T., Ettinger, U., Mehta, M.A., Mataix-Cols, D., and Williams, S.C. (2006). Applications of functional magnetic resonance imaging in psychiatry. J Magn Reson Imaging *23*, 851-861.

Mitzdorf, U. (1985). Current source-density method and application in cat cerebral cortex: investigation of evoked potentials and EEG phenomena. Physiol Rev *65*, 37-100.

Mitzdorf, U. (1987). Properties of the evoked potential generators: current source-density analysis of visually evoked potentials in the cat cortex. Int J Neurosci *33*, 33-59.

Nacher, V., Ledberg, A., Deco, G., and Romo, R. (2013). Coherent delta-band oscillations between cortical areas correlate with decision making. PNAS *110*, 15085-15090.

Nassi, J.J., and Callaway, E.M. (2009). Parallel processing strategies of the primate visual system. Nat Rev Neurosci *10*, 360-372.

Noudoost, B., and Moore, T. (2011). Control of visual cortical signals by prefrontal dopamine. Nature *474*, 372-375.

Nunez, P.L. (1981). Electric Fields of the Brain: The Neurophysics of EEG (Oxford, UK: Oxford University Press).

Oeltermann, A., Augath, M.A., and Logothetis, N.K. (2007). Simultaneous recording of neuronal signals and functional NMR imaging. Magn Reson Imaging *25*, 760-774.

Ogawa, S., Lee, T.M., Kay, A.R., and Tank, D.W. (1990). Brain Magnetic-Resonance-Imaging with Contrast Dependent on Blood Oxygenation. P Natl Acad Sci USA *87*, 9868-9872.

Ogawa, S., Tank, D.W., Menon, R., Ellermann, J.M., Kim, S.G., Merkle, H., and Ugurbil, K. (1992). Intrinsic signal changes accompanying sensory stimulation: functional brain mapping with magnetic resonance imaging. PNAS *89*, 5951-5955.

Ott, T., Jacob, S.N., and Nieder, A. (2014). Dopamine receptors differentially enhance rule coding in primate prefrontal cortex neurons. Neuron *84*, 1317-1328.

Oyono-Enguelle, S., Marbach, J., Heitz, A., Ott, C., Gartner, M., Pape, A., Vollmer, J.C., and Freund, H. (1990). Lactate removal ability and graded exercise in humans. J Appl Physiol *68*, 905-911.

Panzeri, S., Brunel, N., Logothetis, N.K., and Kayser, C. (2010). Sensory neural codes using multiplexed temporal scales. Trends Neurosci *33*, 111-120.

Papanikolaou, A., Keliris, G.A., Papageorgiou, T.D., Shao, Y., Krapp, E., Papageorgiou, E., Stingl, K., Bruckmann, A., Schiefer, U., Logothetis, N.K*., et al.* (2014). Population receptive field analysis of the primary visual cortex complements perimetry in patients with homonymous visual field defects. PNAS *111*, E1656-1665.

Parrot, S., Sauvinet, V., Xavier, J.M., Chavagnac, D., Mouly-Badina, L., Garcia-Larrea, L., Mertens, P., and Renaud, B. (2004). Capillary electrophoresis combined with microdialysis in the human spinal cord: A new tool for monitoring rapid peroperative changes in amino acid neurotransmitters within the dorsal horn. Electrophoresis *25*, 1511-1517.

Parys, B., Cote, A., Gallo, V., De Koninck, P., and Sik, A. (2010). Intercellular Calcium Signaling between Astrocytes and Oligodendrocytes Via Gap Junctions in Culture. Neuroscience *167*, 1032-1043.

Pellerin, L., and Magistretti, P.J. (2004). Neuroenergetics: calling upon astrocytes to satisfy hungry neurons. Neuroscientist *10*, 53-62.

Pessiglione, M., Seymour, B., Flandin, G., Dolan, R.J., and Frith, C.D. (2006). Dopamine-dependent prediction errors underpin reward-seeking behaviour in humans. Nature *442*, 1042-1045.

Petroff, O.A., Errante, L.D., Rothman, D.L., Kim, J.H., and Spencer, D.D. (2002). Glutamate-glutamine cycling in the epileptic human hippocampus. Epilepsia *43*, 703-710.

Pouwels, P.J.W., and Frahm, J. (1998). Regional metabolite concentrations in human brain as determined by quantitative localized proton MRS. Magnet Reson Med *39*, 53-60.

Puig, M.V., and Miller, E.K. (2012). The role of prefrontal dopamine D1 receptors in the neural mechanisms of associative learning. Neuron *74*, 874-886.

Quistorff, B., Secher, N.H., and Van Lieshout, J.J. (2008). Lactate fuels the human brain during exercise. Faseb J *22*, 3443-3449.

Rajalingham, R., Schmidt, K., and DiCarlo, J.J. (2015). Comparison of Object Recognition Behavior in Human and Monkey. J Neurosci *35*, 12127-12136.

Raman, L., Tkac, I., Ennis, K., Georgieff, M.K., Gruetter, R., and Rao, R. (2005). In vivo effect of chronic hypoxia on the neurochemical profile of the developing rat hippocampus. Brain Res Dev Brain Res *156*, 202-209.

Rao, V.R., and Finkbeiner, S. (2007). NMDA and AMPA receptors: old channels, new tricks. Trends Neurosci *30*, 284-291.

Rapoport, S.I. (1996). Modulation of blood-brain barrier permeability. J Drug Target *3*, 417-425.

Rashid, B., Arbabshirani, M.R., Damaraju, E., Miller, R., Pearlson, G., and Calhoun, V. (2015). Classification of Schizophrenia and Bipolar Patients Using Static and Dynamic Resting Fmri Connectivity. Schizophrenia Bull *41*, S237-S237.

Rauch, A., Rainer, G., Augath, M., Oeltermann, A., and Logothetis, N.K. (2008a). Pharmacological MRI combined with electrophysiology in non-human primates: effects of Lidocaine on primary visual cortex. Neuroimage *40*, 590-600.

Rauch, A., Rainer, G., and Logothetis, N.K. (2008b). The effect of a serotonin-induced dissociation between spiking and perisynaptic activity on BOLD functional MRI. PNAS *105*, 6759-6764.

Redish, A.D. (2004). Addiction as a computational process gone awry. Science *306*, 1944-1947.

Reese, T., Bjelke, B., Porszasz, R., Baumann, D., Bochelen, D., Sauter, A., and Rudin, M. (2000). Regional brain activation by bicuculline visualized by functional magnetic resonance imaging. Time-resolved assessment of bicuculline-induced changes in local cerebral blood volume using an intravascular contrast agent. NMR Biomed *13*, 43-49.

Richards, D.A., Tolias, C.M., Sgouros, S., and Bowery, N.G. (2003). Extracellular glutamine to glutamate ratio may predict outcome in the injured brain: a clinical microdialysis study in children. Pharmacol Res *48*, 101-109.

Roelfsema, P.R., and Treue, S. (2014). Basic neuroscience research with nonhuman primates: a small but indispensable component of biomedical research. Neuron *82*, 1200-1204.

Rogers, G.L. (2003). Functional magnetic resonance imaging (fMRI) and effects of L-dopa on visual function in normal and amblyopic subjects. Trans Am Ophthalmol Soc *101*, 401-415.

Romo, R., and Salinas, E. (2003). Flutter discrimination: neural codes, perception, memory and decision making. Nat Rev Neurosci *4*, 203-218.

Russ, B.E., and Leopold, D.A. (2015). Functional MRI mapping of dynamic visual features during natural viewing in the macaque. Neuroimage *109*, 84-94.

Samuelsson, C., Hillered, L., Zetterling, M., Enblad, P., Hesselager, G., Ryttlefors, M., Kumlien, E., Lewen, A., Marklund, N., Nilsson, P.*, et al.* (2007). Cerebral glutamine and glutamate levels in relation to compromised energy metabolism: a microdialysis study in subarachnoid hemorrhage patients. J Cereb Blood Flow Metab *27*, 1309-1317.

Schlichtherle-Cerny, H., Affolter, M., and Cerny, C. (2003). Hydrophilic interaction liquid chromatography coupled to electrospray mass spectrometry of small polar compounds in food analysis. Anal Chem *75*, 2349-2354.

Schultz, W. (2007). Multiple dopamine functions at different time courses. Annu Rev Neurosci *30*, 259-288.

Schwarz, A.J., Gozzi, A., Reese, T., and Bifone, A. (2007). In vivo mapping of functional connectivity in neurotransmitter systems using pharmacological MRI. Neuroimage *34*, 1627-1636.

Self, M.W., Kooijmans, R.N., Super, H., Lamme, V.A., and Roelfsema, P.R. (2012). Different glutamate receptors convey feedforward and recurrent processing in macaque V1. PNAS *109*, 11031-11036.

Self, M.W., Peters, J.C., Possel, J.K., Reithler, J., Goebel, R., Ris, P., Jeurissen, D., Reddy, L., Claus, S., Baayen, J.C.*, et al.* (2016). The Effects of Context and Attention on Spiking Activity in Human Early Visual Cortex. PLoS Biol *14*, e1002420.

Self, M.W., van Kerkoerle, T., Super, H., and Roelfsema, P.R. (2013). Distinct roles of the cortical layers of area V1 in figure-ground segregation. Curr Biol *23*, 2121-2129.

Sellers, K.K., Bennett, D.V., Hutt, A., and Frohlich, F. (2013). Anesthesia differentially modulates spontaneous network dynamics by cortical area and layer. J Neurophysiol *110*, 2739-2751.

Sellers, K.K., Bennett, D.V., Hutt, A., Williams, J.H., and Frohlich, F. (2015). Awake vs. anesthetized: layer-specific sensory processing in visual cortex and functional connectivity between cortical areas. J Neurophysiol *113*, 3798-3815.

Sengupta, B., Laughlin, S.B., and Niven, J.E. (2014). Consequences of converting graded to action potentials upon neural information coding and energy efficiency. PLoS Comput Biol *10*, e1003439.

Serences, J.T. (2008). Value-based modulations in human visual cortex. Neuron *60*, 1169-1181.

Servan-Schreiber, D., Printz, H., and Cohen, J.D. (1990). A network model of catecholamine effects: gain, signal-to-noise ratio, and behavior. Science *249*, 892-895.

Shackman, H.M., Shou, M., Cellar, N.A., Watson, C.J., and Kennedy, R.T. (2007). Microdialysis coupled on-line to capillary liquid chromatography with tandem mass spectrometry for monitoring acetylcholine in vivo. J Neurosci Methods *159*, 86-92.

Shen, J., Petersen, K.F., Behar, K.L., Brown, P., Nixon, T.W., Mason, G.F., Petroff, O.A.C., Shulman, G.I., Shulman, R.G., and Rothman, D.L. (1999). Determination of the rate of the glutamate glutamine cycle in the human brain by in vivo C-13 NMR. P Natl Acad Sci USA *96*, 8235-8240.

Shmuel, A., Augath, M., Oeltermann, A., and Logothetis, N.K. (2006). Negative functional MRI response correlates with decreases in neuronal activity in monkey visual area V1. Nat Neurosci *9*, 569-577.

Shuler, M.G., and Bear, M.F. (2006). Reward timing in the primary visual cortex. Science *311*, 1606-1609.

Sicard, K.M., and Duong, T.Q. (2005). Effects of hypoxia, hyperoxia, and hypercapnia on baseline and stimulus-evoked BOLD, CBF, and CMRO2 in spontaneously breathing animals. Neuroimage *25*, 850-858.

Siegelbaum, S.A., and Tsien, R.W. (1983). Modulation of Gated Ion Channels as a Mode of Transmitter Action. Trends Neurosci *6*, 307-313.

Simard, M., and Nedergaard, M. (2004). The neurobiology of glia in the context of water and ion homeostasis. Neuroscience *129*, 877-896.

Skelton, M.S., Kremer, D.E., Smith, E.W., and Gladden, L.B. (1998). Lactate influx into red blood cells from trained and untrained human subjects. Med Sci Sport Exer *30*, 536-542.

Slotnick, S.D., Thompson, W.L., and Kosslyn, S.M. (2005). Visual mental imagery induces retinotopically organized activation of early visual areas. Cerebral cortex *15*, 1570-1583.

Smith, E.W., Skelton, M.S., Kremer, D.E., Pascoe, D.D., and Gladden, L.B. (1997). Lactate distribution in the blood during progressive exercise. Med Sci Sports Exerc *29*, 654-660.

Sokoloff, L. (1977a). Relation between Physiological Function and Energy-Metabolism in Central Nervous-System. Journal of Neurochemistry *29*, 13-26.

Sokoloff, L. (1977b). Relation between physiological function and energy metabolism in the central nervous system. J Neurochem *29*, 13-26.

Sokoloff, L., Reivich, M., Kennedy, C., Des Rosiers, M.H., Patlak, C.S., Pettigrew, K.D., Sakurada, O., and Shinohara, M. (1977). The [14C]deoxyglucose method for the measurement of local cerebral glucose utilization: theory, procedure, and normal values in the conscious and anesthetized albino rat. J Neurochem *28*, 897-916.

Sperling, R., Greve, D., Dale, A., Killiany, R., Holmes, J., Rosas, H.D., Cocchiarella, A., Firth, P., Rosen, B., Lake, S.*, et al.* (2002). Functional MRI detection of pharmacologically induced memory impairment. PNAS *99*, 455-460.

Stanisor, L., van der Togt, C., Pennartz, C.M., and Roelfsema, P.R. (2013). A unified selection signal for attention and reward in primary visual cortex. PNAS *110*, 9136-9141.

Steriade, M. (1993). Cholinergic blockage of network- and intrinsically generated slow oscillations promotes waking and REM sleep activity patterns in thalamic and cortical neurons. Prog Brain Res *98*, 345-355.

Steriade, M. (2006). Grouping of brain rhythms in corticothalamic systems. Neuroscience *137*, 1087-1106.

Stobart, J.L., and Anderson, C.M. (2013). Multifunctional role of astrocytes as gatekeepers of neuronal energy supply. Front Cell Neurosci *7*.

Swadlow, H.A., and Gusev, A.G. (2001). The impact of 'bursting' thalamic impulses at a neocortical synapse. Nat Neurosci *4*, 402-408.

Takahata, T., Komatsu, Y., Watakabe, A., Hashikawa, T., Tochitani, S., and Yamamori, T. (2006). Activity-dependent expression of occ1 in excitatory neurons is a characteristic feature of the primate visual cortex. Cereb Cortex *16*, 929-940.

Takahata, T., Shukla, R., Yamamori, T., and Kaas, J.H. (2012). Differential Expression Patterns of Striate Cortex-Enriched Genes among Old World, New World, and Prosimian Primates. Cereb Cortex *22*, 2313-2321.

Timofeev, I., and Steriade, M. (1996). Low-frequency rhythms in the thalamus of intact-cortex and decorticated cats. J Neurophysiol *76*, 4152-4168.

Timofeev, I., and Steriade, M. (1998). Cellular mechanisms underlying intrathalamic augmenting responses of reticular and relay neurons. J Neurophysiol *79*, 2716-2729.

Tolias, A.S., Sultan, F., Augath, M., Oeltermann, A., Tehovnik, E.J., Schiller, P.H., and Logothetis, N.K. (2005). Mapping cortical activity elicited with electrical microstimulation using FMRI in the macaque. Neuron *48*, 901-911.

Uutela, P., Reinila, R., Piepponen, P., Ketola, R.A., and Kostiainen, R. (2005). Analysis of acetylcholine and choline in microdialysis samples by liquid chromatography/tandem mass spectrometry. Rapid Commun Mass Spectrom *19*, 2950-2956.

van Hall, G., Stromstad, M., Rasmussen, P., Jans, O., Zaar, M., Gam, C., Quistorff, B., Secher, N.H., and Nielsen, H.B. (2009). Blood lactate is an important energy source for the human brain. J Cerebr Blood F Met *29*, 1121-1129.

van Kerkoerle, T., Self, M.W., Dagnino, B., Gariel-Mathis, M.A., Poort, J., van der Togt, C., and Roelfsema, P.R. (2014). Alpha and gamma oscillations characterize feedback and feedforward processing in monkey visual cortex. PNAS *111*, 14332-14341.

Viswanathan, A., and Freeman, R.D. (2007). Neurometabolic coupling in cerebral cortex reflects synaptic more than spiking activity. Nat Neurosci *10*, 1308-1312.

von Pfostl, V., Li, J., Zaldivar, D., Goense, J., Zhang, X., Serr, N., Logothetis, N.K., and Rauch, A. (2012). Effects of lactate on the early visual cortex of non-human primates, investigated by pharmaco-MRI and neurochemical analysis. Neuroimage *61*, 98-105.

Voytko, M.L., and Tinkler, G.P. (2004). Cognitive function and its neural mechanisms in nonhuman primate models of aging, Alzheimer disease, and menopause. Front Biosci *9*, 1899-1914.

Wanger, T., Takagaki, K., Lippert, M.T., Goldschmidt, J., and Ohl, F.W. (2013). Wave propagation of cortical population activity under urethane anesthesia is state dependent. BMC Neurosci *14*, 78.

Watanabe, M., Cheng, K., Murayama, Y., Ueno, K., Asamizuya, T., Tanaka, K., and Logothetis, N. (2011). Attention but not awareness modulates the BOLD signal in the human V1 during binocular suppression. Science *334*, 829-831.

Weber, B., Keller, A.L., Reichold, J., and Logothetis, N.K. (2008). The microvascular system of the striate and extrastriate visual cortex of the macaque. Cerebral cortex *18*, 2318-2330.

Whittingstall, K., and Logothetis, N.K. (2009). Frequency-band coupling in surface EEG reflects spiking activity in monkey visual cortex. Neuron *64*, 281-289.

Winterer, G., and Weinberger, D.R. (2004). Genes, dopamine and cortical signal-to-noise ratio in schizophrenia. Trends Neurosci *27*, 683-690.

Wishart, D.S. (2016). Emerging applications of metabolomics in drug discovery and precision medicine. Nat Rev Drug Discov.

Xing, D., Yeh, C.I., Burns, S., and Shapley, R.M. (2012). Laminar analysis of visually evoked activity in the primary visual cortex. PNAS *109*, 13871-13876.

Yamada, M., Lamping, K.G., Duttaroy, A., Zhang, W., Cui, Y., Bymaster, F.P., McKinzie, D.L., Felder, C.C., Deng, C.X., Faraci, F.M.*, et al.* (2001). Cholinergic dilation of cerebral blood vessels is abolished in M(5) muscarinic acetylcholine receptor knockout mice. PNAS *98*, 14096-14101.

Yao, T., Yano, T., Nanjyo, Y., and Nishino, H. (2003). Simultaneous determination of glucose and L-lactate in rat brain by an electrochemical in vivo flow-injection system with an on-line microdialysis sampling. Anal Sci *19*, 61-65.

Yu, A.J., and Dayan, P. (2005). Uncertainty, neuromodulation, and attention. Neuron *46*, 681-692.

Zaldivar, D., Rauch, A., Whittingstall, K., Logothetis, N.K., and Goense, J. (2014). Dopamine-induced dissociation of BOLD and neural activity in macaque visual cortex. Curr Biol *24*, 2805-2811.

Zhang, X., Rauch, A., Lee, H., Xiao, H., Rainer, G., and Logothetis, N.K. (2007). Capillary hydrophilic interaction chromatography/mass spectrometry for simultaneous determination of multiple neurotransmitters in primate cerebral cortex. Rapid Commun Mass Spectrom *21*, 3621-3628.

Zhang, X., Rauch, A., Xiao, H., Rainer, G., and Logothetis, N.K. (2008). Mass spectrometry-based neurochemical analysis: perspectives for primate research. Expert Rev Proteomics *5*, 641-652.

Zheng, D., LaMantia, A.S., and Purves, D. (1991). Specialized vascularization of the primate visual cortex. J Neurosci *11*, 2622-2629.

Zlotnik, A., Ohayon, S., Gruenbaum, B.F., Gruenbaum, S.E., Mohar, B., Boyko, M., Klin, Y., Sheiner, E., Shaked, G., Shapira, Y.*, et al.* (2011). Determination of factors affecting glutamate concentrations in the whole blood of healthy human volunteers. J Neurosurg Anesthesiol *23*, 45-49.

Zonta, M., Angulo, M.C., Gobbo, S., Rosengarten, B., Hossmann, K.A., Pozzan, T., and Carmignoto, G. (2003). Neuron-to-astrocyte signaling is central to the dynamic control of brain microcirculation. Nat Neurosci *6*, 43-50.

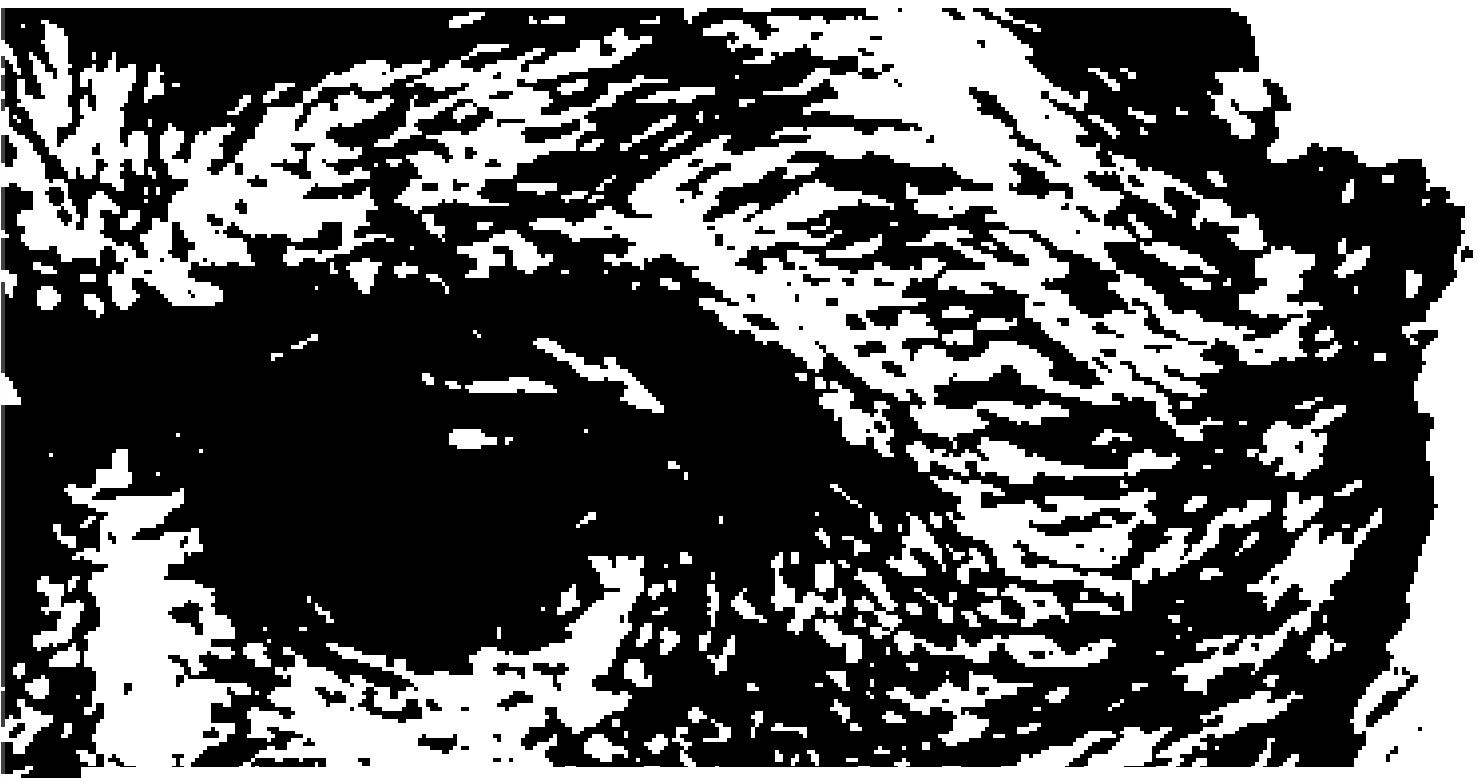

Contributions to papers and manuscripts

PRESENTATION OF OWN CONTRIBUTIONS TO PAPERS AND MANUSCRIPTS

(Darstellung des Eigenanteils bei Gemeinschaftsarbeiten nach §9 para. 2)

Manuscript Nr. 1:

Li J*, von Pfoestl V*, **Zaldívar D**, Zhang X, Logothetis NK & Rauch A (2012). Measuring multiple neurochemicals and related metabolites in blood and brain of the rhesus monkeys by using dual microdialysis sampling and capillary hydrophilic interaction chromatography-mass spectrometry. *Anal Bioanal Chem*.402: 2545-54.

**Equally contributed authors*

(i) J. Li, Zhang X. and A. Rauch designed the study under N. Logothetis' guidance and approval; *(ii)* Different anesthesia protocols were used for this study which were implemented and developed by V. von Pfoestl and D. Zaldivar; *(iii)* V. von Pfoestl and D. Zaldivar performed all the experiments and data collection; *(iv)* D. Zaldivar positioned the sampling probes for the blood and brain chemical sampling; *(iv)* D. Zaldivar and A. Rauch developed the software (MATLAB- and Phyton-based code) for the real-time data extraction and analysis from HPLC machine; *(v)* J. Li operated the LC-MS system and developed the HILIC protocol by her own with contributions from X. Zhang and A. Rauch; *(vi)* J. Li and X. Zhang analyzed the data. *(vii)* J. Li, V. von Pfoestl, D. Zaldivar and A. Rauch wrote the first draft of the manuscript; and *(viii)* J. Goense and N. Logothetis provided feedback on the evaluation of results and comments on the manuscript.

Manuscript Nr. 2:

Zaldívar D, Logothetis NK, Rauch A & Goense J (2016). Pharmaco-based fMRI and neurophysiology in non-human primates. In: *In vivo Neuropharmacology and Neurophysiology*, (Ed) Athineos Philippou. Neuromethods of Springer Science Series

(i) D. Zaldivar, and J. Goense designed the study under N. Logothetis' guidance and approval; *(ii)* The pressure-operated pumps were designed by A. Rauch; *(iii)* D. Zaldivar developed the MATLAB package that enabled the real-time control of the injection system; *(iii)* D. Zaldivar and J. Goense performed the experiments and data collection under N. Logothetis guidance and support; *(iv)* D. Zaldivar and A. Rauch developed the pharmacological probes; *(v)* Surgical interventions for the electrodes and probes insertion were conducted by D. Zaldivar; *(vi)* The pharmaco-MRI experiments were conducted by D. Zaldivar and J. Goense; *(vii)* J. Goense setup the fMRI scanning parameters; *(vii)* D. Zaldivar analyzed all the data with the guidance from J. Goense and N. Logothetis; *(viii)* D. Zaldivar, N. Logothetis and J. Goense wrote the manuscript.

Manuscript Nr. 3:

von Pfoestl V* , Li J*, **Zaldívar D**, Goense J, Zhang X, Logothetis NK & Rauch A (2012). Effects of lactate on early visual cortex of non-human primates investigated by pharmaco-MRI and neurochemical analysis. *Neuroimage* 61: 98–105.

**Equally contributed authors*

(i) V. von Pfoestl and D. Zaldivar designed the experiments with the guidance of A. Rauch and J. Goense;. *(ii)* J Goense, setup the fMRI scanning parameters; *(iii)* V. von Pfoestl and D. Zaldivar performed the fMRI experiments and collected the data; *(iv)* Simultaneous laminar neurophysiology and neurochemical sampling were standardized by D. Zaldivar; *(v)* J. Li performed the chemical sampling and analyzed the data in the HPLC-machine; *(vi)* V. von Pfoestl performed the fMRI data analysis with contributions from D. Zaldivar; *(vi)* V. von Pfoestl and D. Zaldivar analyzed the neurophysiology data; *(vii)* V. von Pfoestl, J. Li, D. Zaldivar and A. Rauch wrote the first draft of the manuscript; *(vii)* J. Goense, N.K. Logothetis provided valuable feedback on the evaluation of the results and comments to the manuscript.

Manuscript Nr. 4:

Zaldívar D, Rauch A, Whittingstall K, Logothetis NK & Goense J (2014). Dopamine-induced dissociation of BOLD and neural activity in macaque visual cortex. *Current Biology* 24: 2805–11.

(i) D. Zaldivar, A. Rauch and J. Goense designed the study with the guidance from N. Logothetis; *(ii)* Experiments were conducted by D. Zaldivar and J. Goense under the guidance and approval from N. Logothetis; *(iii)* D. Zaldivar and A. Rauch developed the pharmacological probes for the local and systemic injections; *(iv)* Surgical interventions were performed by D. Zaldivar which included the positioning of laminar electrodes and the pharmacological probes for both local and systemic pharmacological injections; *(vi)* The pharmaco-MRI, neurophysiology experiments and data collection were performed by D. Zaldivar and J. Goense; *(vii)* D. Zaldivar analyzed the neurophysiology data with the guidance from K. Whittingstall and N. Logothetis; *(viii)* the fMRI analysis (BOLD and CBF) was conducted by D. Zaldivar with the guidance from J. Goense; *(ix)* D. Zaldivar and J. Goense interpreted the data, and both wrote the first draft of the manuscript; *(x)* A. Rauch, K. Whittingstall and N. Logotheits provided valuable feedback on the first draft.

Manuscript Nr. 5:

Lowe S, **Zaldivar D,** Murayama Y, Logothetis NK & Panzeri S (*in preparation*). Laminar and frequency distribution of information in primary visual cortex of macaque.

(i) Lowe S, D. Zaldivar, Murayama Y, S. Panzeri and N. Logothetis designed the study; *(ii)* D. Zaldivar and Y. Murayama performed the experiments and collected the laminar-neurophysiology data; *(iii)* S. Lowe performed the data analysis with contributions from D. Zaldivar and Y. Murayama; *(iv)* S. Lowe , D. Zaldivar and S. Panzeri participated in the discussion and evaluation of the results; *(vi)* S. Lowe and S. Panzeri wrote the first draft of the manuscript; *(vii)* D. Zaldivar and N. Logothetis provided valuable feedback on the manuscript.

Manuscript Nr. 6:

Zaldivar D, Goense J, Lowe S, Logothetis NK & Panzeri S (*in preparation*). Dopamine elicits lamina and frequency specific increase of information in the macaque visual cortex.

(i) D. Zaldivar, S. Panzeri and N. Logothetis designed the study; *(ii)* D. Zaldivar and J. Goense performed the neurophysiology and pharmacology experiments, and collected the data; *(iii)* S. Lowe developed the CSD code; *(iv)* D. Zaldivar and S. Panzeri analyzed the data with contributions from N. Logothetis and J. Goense; *(v)* D. Zaldivar, J. Goense and S. Panzeri discussed and interpreted the data; *(vi)* D. Zaldivar and S. Panzeri wrote the first draft of the manuscript; *(vii)* all of the authors provided valuable feedback on the manuscript.

3. Manuscript Nr. 1

Measuring multiple neurochemicals and related metabolites in blood and brain of the rhesus monkeys by using dual microdialysis sampling and capillary hydrophilic interaction chromatography mass spectrometry

This chapter was published in 2012 in **Anal Bioanal Chem. 2012, 402(8):2545-54** by

Juan Li, Veronika von Pfoestl, Daniel Zaldivar, Jozien Goense, Xiaozhe Zhang, Nikos Logothetis & Alexander Rauch

doi: 10.1007/s00216-011-5427-z

3.1 INTRODUCTION

The physiological function of neurons and the correct information processing within the brain depend critically on neuroactive molecules and metabolites (NMs). These NMs consisting of neurotransmitters like glutamate or neuromodulators like acetylcholine can be detected by appropriate techniques in the extracellular fluid of the brain. The concentrations of these NMs are tightly controlled and stable within narrow boundaries. Many disorders of the central nervous system (CNS) such as Parkinson's disease (Calabresi et al., 2000), Alzheimer's disease (D'Aniello et al., 1998), and schizophrenia (Carlsson and Carlsson, 1990), are correlated with or even caused by changes in the concentrations of such substances. NMs can be sampled from the extracellular brain fluid (EBF) which allows us to investigate their dynamic reflecting changes in neuronal activity. The EBF forms a complex, dynamic environment embedding all neural elements and serves as medium for the cell-to-cell communication and metabolite transport. Many of these NMs also exist in the blood system, but their concentrations are commonly different from those in the brain because of the differential permeability of the blood brain barrier (BBB) and of differences in absorption mechanisms, synthesis, and metabolism. Simultaneous and quantitative monitoring of these NMs from the brain and the blood system will therefore allow us to assess their relation between the brain and the blood system.

In the present study, we focused on a selection of NMs functionally and metabolically related and developed a direct and sensitive analytical method to monitor acetylcholine, lactate, pyruvate, glutamine, and glutamate in parallel from the brain and the blood. All these five substances are derivates from glucose and the citrate cycles (Gibson et al., 1981; Hertz et al., 2007). Additionally, acetylcholine is able to modulate glutamatergic release and can interact with the brain energy metabolism (Andersson and Arner, 1995; Briand et al., 2007; Yang et al., 2009). To do so, we used microdialysis to collect samples from EBF and blood of anesthetized nonhuman- primates in parallel. This will allow us to investigate changes in their

relation caused by functional and metabolic challenges or by pathologies in the future. However, their chemical and physical properties are different which makes it difficult to separate and detect these NMs together. To the best of our knowledge, there is currently no report describing the simultaneous determination of all five aforementioned substances by a single analysis. Indeed, so far, most analytical methods developed were only focusing on the determination of one or two of such targeted substances. For example, electrochemical detection (ECD) is commonly used to monitor these compounds (Monge-Acuna and Fornaguera-Trias, 2009; Tsai et al., 1996; Yao et al., 2003), but an additional enzyme reactor is needed to generate electrochemically detectable hydrogen peroxide for acetylcholine detection(Huang et al., 1995), so it is difficult to monitor all these substances in a single analytical run using ECD as detector. Compared to the classical ECD, mass spectrometry (MS) is able to detect diverse NMs with high sensitivity and selectivity. Recent analytical advances have been made by using MS detection coupled with ion-pair reversed-phase liquid chromatography (RPLC) or ion exchange chromatography (IEC) as separation tools. For instance, acetylcholine has been analyzed by strong cation exchange (SCX)-MS (Shackman et al., 2007) or ion-pair RPLC-MS (Prokai et al., 2008; Zhu et al., 2000). Pyruvate was analyzed by weak anion exchange (WAX)-MS (van Dam et al., 2002), while lactate and pyruvate together were detected by RPLC-ESI/MS (electro spray ionization, ESI), but a time-consuming derivatization process with 3-nitrophenyl-hydrazine was needed (Uran et al., 2007). Glutamine and glutamate were determined by ion-pair RPLC-MS using an ion-pairing regent which might cause ESI suppression (Eckstein et al., 2008).

In contrast to ion-pair RPLC or IEC-based analytical approaches, hydrophilic interaction liquid chromatography (HILIC)–MS is an alternative technique that allows separating and determining multiple polar analytes irrespective of being a base or an organic acid (Alpert, 1990; Zhang et al., 2008). It already has proved its merits in determining peptides, proteins and small polar molecular compounds in complex matrices (Fu et al., 2008; Preinerstorfer et al., 2010; Schlichtherle-Cerny et al., 2003; Zhang et al., 2007). Recent reports demonstrated

that HILICMS is well suited to determine polar neurotransmitters in EBF offering high sensitivity combined with timesaving procedures for sample preparation (Uutela et al., 2005; Zhang et al., 2007).

In this study, we report the successful combination of capillary HILIC-ESI/MS with dual microdialysis sampling for simultaneous measurement of five NMs together in brain and blood dialysates of non-human primates. First, our approach allows us to compare the relation of these NMs to each other under different physiological and pathological states of the brain. Second, the simultaneous sampling from the brain and the blood can be used to extrapolate from blood measurements to brain concentrations of these NMs. Relation changes of these NMs detectable in the blood can serve as easy accessible biomarkers reflecting physiological or pathological states of the brain (Kaddurah-Daouk and Krishnan, 2009).

3.2 METHODS

3.2.1 Chemicals

HPLC-MS grade acetonitrile, formic acid, and ammonium formate were purchased from Sigma-Aldrich Munich, Germany). [3-^{13}C] lactate (as aqueous solution, 20% *w/w* in H_2O) (^{13}C-lactate), glutamine-L-2, 3, 3, 4, 4-d_5 (glutamine-d_5), and glutamic acid-L-2, 3, 3, 4, 4-d_5 (glutamate-d_5) were purchased from Cambridge Isotope Laboratories (Andover, USA). Acetylcholine-*N,N,N*-trimethyl-d_9 chloride (acetylcholine-d_9) was bought from Medical Isotopes, Inc (Pelham, USA). Acetylcholine chloride, sodium lactate (lactate), sodium pyruvate, glutamine, glutamate, [1-^{13}C] sodium pyruvate (^{13}C-pyruvate), and the chemicals for preparing frits were all obtained from Sigma-Aldrich. Pure water was produced by a TKA superpure water system (Niederelbert, Germany). Artificial cerebral spinal fluid (a-CSF) for standard solutions consisted of 148 mM NaCl, 3.00 mM KCl, 0.80 mM $MgCl_2$, and 1.40 mM $CaCl_2$, pH 7.3.

3.2.2 Fabrications of capillary columns

The preparation of capillary columns was adopted and modified from Zhang et al. (Zhang et al., 2007). To prevent the packing material from spilling out of the column a frit was formed at one end by in situ free radical polymerization modified from Viklund et al. (Viklund et al., 1997). Compared to the frit formed by sintered reaction, our frit can easily withstand long exposure to high pressure (>3,000 psi) and minimize extra-column band broadening. After the reaction, unreacted material and other soluble compounds were removed from the pores by washing with ethanol followed by purging with helium for 15 min. The column was packed with acetone slurry (1.5 mL) containing 50 mg of 5 µm polyhydroxyethyl aspartamide particles (PolyLC, USA) with the help of a helium pressure cell with a stirring bar to maintain particle suspension running under a pressure of 100 bars for 30 min. The packed column was cut to 15 cm for use.

3.2.3 Preparation of Calibration Standards and Internal Standards

To increase the reproducibility of the quantitative analysis of acetylcholine, lactate, pyruvate, glutamine, and glutamate, acetylcholine-d_9, ^{13}C-lactate, ^{13}C-pyruvate, glutamine-d_5, and glutamate-d_5 were used as their respective internal standards (IS). Stock solutions of the analytes were prepared in 30 % acetonitrile containing 0.1 % formic acid and stored at 5 °C in the refrigerator. To characterize the analytical performance of capillary HILIC-MS methods for the quantitative measurement of the analytes, the stock solution was serially diluted using a solution containing a-CSF/solution A (90 % acetonitrile, 0.1 % formic acid) (1:4, *v/v*). The calibration solutions of acetylcholine ranged from 0.5 to 250 nM and consisted of three levels (low, medium, and high) of quality control (QC) samples with 2.5, 25, and 125 nM. For lactate and pyruvate the calibration solutions ranged from 10 to 5000 µM, and QC samples were 50, 500, and 2500 µM. For glutamine the calibration solutions ranged from 0.5 to 250 µM, and QC samples were 2.5, 25, and 125 µM. For glutamate the calibration solutions ranged from 0.25 to 125 µM, and QC samples were 1.25, 12.5, and 62.5 µM. Two IS stock solutions were prepared in water containing 0.1 % formic acid: one (IS_1) is used for the calibration curve

preparation and the blood microdialysate samples analysis, which contains 500 nM acetylcholine-d_9, 10 mM ^{13}C-lactate, 10 mM ^{13}C-pyruvate, 500 µM glutamine-d_5, and 250 µM glutamate-d_5; the other one (IS_2) is used for the monkey brain microdialysate samples analysis containing 300 nM acetylcholine-d_9, 6 mM ^{13}C-lactate, 6 mM ^{13}C-pyruvate, 300 µM glutamine-d_5, and 150 µM glutamate-d_5. These internal standards were diluted 10 times (IS_1) and 6 times (IS_2) on the day of the assay using a-CSF/solution A (90 % acetonitrile, 0.1 % formic acid) (1:4, v/v). The calibration curve was constructed based on the response ratio of the peak area ($P_{analyte}$ / P_{IS}) versus the nominal standard concentrations by a least-squares regression using a weighting factor of 1/concentration^2.

3.2.4 Microdialysis Sampling

Two male rhesus monkeys (Macaca mulatta) were used with an age of 5 years weighing between 6 and 7 kg. The experimental procedures were approved by the local authorities (Regierungspraesidium) and are in agreement with guidelines of the European Community for the care of laboratory animals. During the experiment the monkeys were anesthetized with full monitoring of all vital parameters. Before the experiment the monkeys were sedated with ketamine (15 mg/kg). Anesthesia was induced with fentanyl (31 µg/kg), thiopental (5 mg/kg) and succinyl chloride (3 mg/kg). Afterwards the monkeys were intubated and ventilated with a Servo Ventilator 900C (Siemens, Germany). The maintenance of anesthesia was attained with remifentanyl (0.2-1 µg/kg/min) and mivacurium chloride (4-7 mg/kg/h). A crystalloid solution (Ionosteril, Fresenius Kabi, Germany) with 2.5 % glucose was infused at a rate of 10 ml/kg/h. During the experiment body temperature was kept between 38.5 and 39.5°C, SpO_2 above 95% and end tidal CO_2 at 35 mmHg.

The monkeys had a miniaturized PEEK chamber over primary visual cortex that gave access to the brain. The probe was inserted through a small incision in the dura. The probe for blood sampling was placed into a superficial leg vein trough a catheter.

For brain sampling microdialysis probes CMA 12 with 2 mm PAES membrane of 0.5 mm outer diameter (o.d.) and a 20 kDa cut-off (CMA Microdialysis AB, Sweden) were used. The probe was flushed with a-CSF solution at a flow rate of 2µL/min for 15 min, and then conditioned at a flow rate of 600 nL/min for 2 hrs before insertion into the cortex of the monkey. For the blood sampling a microdialysis catheter CMA 64, 20 mm PAES membrane, 0.6 mm o.d., 20 kDa cut-off (CMA Microdialysis AB, Sweden) was flushed with saline containing fragmin 25 IU/mL (Pfizer Pharma GmbH, Germany) at a flow rate of 2 µL/min for 2 hrs before insertion. The collections of microdialysis samples were started 2 hrs after the insertion of the probes for blood sampling as well as for brain sampling.

The dialysates were collected in parallel by two refrigerated fraction collectors CMA 740 (CMA Microdialysis AB, Sweden) at 6 °C for 1 hr. The samples were collected at an interval of 3 minutes for both brain and blood sampling. Before sampling the IS solution was added to the glass inserts used for sample collection and then put into the refrigerated fraction collectors. After the experiment the brain microdialysate samples were concentrated by a vacuum concentrator (Eppendorf, Germany) under room temperature for 5 min and reconstituted by solution B (60 % acetonitrile, 0.1 % formic acid) for further analysis. The blood microdialysate samples were directly diluted by solution C (80 % acetonitrile, 0.1 % formic acid) and then analyzed.

In vitro recovery of CMA 12 probes has been tested, and it was 50.2 % to 66.8% for all analytes with a reliable stability not exceeding 3.6 % standard errors. The measured *in vitro* recovery of CMA 64 probes for all analytes was 42.5 % to 49.3 % with good reliable stability not exceeding 4.3 % standard errors.

3.2.5 Capillary Liquid Chromatography and Mass Spectrometry

An Agilent capillary HPLC 1100 system coupled to a XCT plus ion trap mass spectrometer (Agilent, Waldbronn, Germany) was used for analysis. Mobile phase A was an aqueous solution containing 50 mM ammonium formate and 1.0 % formic acid (pH 2.87), and mobile

phase B was acetonitrile. The analysis was performed using a gradient profile: 0.0 to 10.0 min, 85 % B to 45 % B, then 45 % B was kept for 5 min. The column was reconditioned using an 85 % solution of B for 10 min before further injection. The flow rate was 3.5 µL/min, and a sample of 0.3 µL was injected in the column each time.

MS analysis was performed by switching between positive and negative ion mode. Tandem mass spectrometry (MS/MS) experiments were applied to isolate and fragment the precursor ions. Ion-trap tandem mass spectrometry (MS/MS) experiments were applied to isolate and fragment precursors ions. The mass spectrometer was operated in MRM mode (multiple-reaction-monitoring) for the quantitative analysis. Five scans were averaged for each spectrum with an scan range of *m/z* 50 – 2,000. MS scans were split into three segments considering the different MS behaviors of five compounds. In the first segment (0.0-3.5 min) acetylcholine and acetylcholine-d_9 were monitored under a positive mode with the capillary voltage of 3,5000 V, while lactate, ^{13}C-lactate, pyruvate and ^{13}C-pyruvate were monitored under a negative mode in the second segment (3.5-8.6 min) with the capillary voltage of 2,541 V, and glutamine, glutamin-d_5, glutamate and glutamate-d_5 were monitored under a positive mode in the third segment (8.6-15.0 min) with capillary voltage of 3,200 V. The MS parameters of five analytes and their corresponding internal standards are listed in Table 3.1. Lactate and pyruvate did not generate significant and stable product ions, so we could not use the product ions for lactate and pyruvate in MRM conditions. We used ion fragmentation amplitude of 0.5 V and ion fragmentation cut-off of 58 which reduced the background noise keeping the lactate and pyruvate unaffected. This procedure could compensate for the lack of specificity which is achieved by monitoring the transfer from the precursor ion to the product ion. The MS settings such as capillary exit, skimmer and lens voltages were optimized and tuned by the data acquisition software during infusion of a standard solution for each compound.

Table 3.1 MS parameters for five analytes and their internal standards

Compounds	MRM transition	Width	Frag. Cut-off (*m/z*)	Frag. Amplitude (V)	ICC smart target (*m/z*)	ICC accumulation time (ms)
Ach	146 → 87	1.0	62	1.38	200,000	200
Ach-d_9	155 → 87	1.0	62	1.38	200,000	200
Lac	89 → 89	1.0	58	0.50	200,000	100
^{13}C-Lac	90 → 90	1.0	58	0.50	200,000	100
Pyr	87 → 87	1.0	58	0.50	200,000	100
^{13}C-Pyr	88 → 88	1.0	58	0.50	200,000	100
Gln	147 → 130	1.0	69	1.20	50,000	200
Gln-d_5	152 → 135	1.0	69	1.20	50,000	200
Glu	148 → 130	1.0	60	0.98	50,000	200
Glu-d_5	153 → 135	1.0	60	0.98	50,000	200

3.3 RESULTS AND DISCUSSION

3.3.1 HILIC-MS Analytical Method Development

Highest intensities for all the analytes were achieved when both the positive and the negative ionization mode of the mass spectrometer were used in the ESI experiments. Previous studies showed that chemicals can have different ESI/MS responses because of their different physical and chemical properties (Cech and Enke, 2001). In our case, lactate and pyruvate, which are organic acids, had much higher intensities in negative ionization mode than in positive ionization mode. The other analytes, acetylcholine, glutamine and glutamate generated responses with high intensity only in positive ionization mode. For our experiments, we thus used positive ionization mode for detecting acetylcholine, glutamine, and glutamate, while negative ionization mode for lactate and pyruvate. In the analytical experiments, we selected HILIC as the method to separate the five polar analytes. Our initial tests showed that HILIC was able to separate them simultaneously (data not shown). The elution order was acetylcholine, lactate, pyruvate, glutamine, and glutamate. Because both positive and negative ionization mode were used for ESI/MS detection, the efficient separation of lactate and pyruvate from the other analytes has to be achieved to ensure that each analyte reliably matches the time window of the appointed ionization mode.

To achieve optimal separation and intensity of the five analytes on the HILIC-MS, we examined the influence of pH value, water content and buffer concentration of the mobile phase on the retention behavior and MS signal of each analyte. Figure 3.1a shows that the pH value had clearly stronger effects on lactate and glutamate compared to the other three analytes when we varied the pH of mobile phase A from 2.7–4.2 by adjusting formic acid proportions from 0.05–1.50%. In particular, the elution order of lactate and pyruvate reversed when pH value ranged from 3.9–2.7. This may be because lactate is ionized at higher pH values compared to its pKa of 3.85. Figure 3.1d indicates that the MS intensity of the five analytes was also affected by the pH value. Their intensities were on average higher at lower pH value; 1.0% formic acid (pH 2.9) was finally used for the following optimization warranting efficient separation combined with high intensity.

The water content had strong influence on the chromatographic behaviors and MS signal intensities of all five analytes. When the water content was decreased to 30% or lower, lactate and pyruvate could be very well separated from their neighboring peaks of acetylcholine and glutamine in the chromatogram (Figure 3.1b). Figure 3.1e illustrates that the reduced water content (from 60–30%) could enhance the MS intensity, which is the benefit of the increased electrospray ionization efficiency in a high organic phase. On the other hand, a MS signal decline was observed when the water content ranged from 30% to 20%. This might result from the low solubility of the polar compounds in the high organic phase mobile.

During the method development, we found that the salt content in the buffer solution had a great impact on the peak shapes and MS signal of the analytes (Figure 3.1f), but less effect on retention time (Figure 3.1c). Sharp peak shapes and high reproducible retention times were obtained for all analytes when the ammonium formate concentration was increased from 10–50 mM. Therefore, a higher concentration of buffer solution was used for the elution, although ion suppression could be observed at this level.

Taken together, the aqueous phase consisted of a buffer solution containing 50 mM ammonium formate and 1.0% formic acid using a gradient profile that started at 85% acetonitrile for separation of the targeted analytes. This optimized separation method ensured that each analyte was matching the appointed time window of the chosen ionization mode without any interferences. The typical HILIC-ESI/MS chromatograms containing the five NMs (acetylcholine, lactate, pyruvate, glutamine, and glutamate) are shown in Figure 3.2.

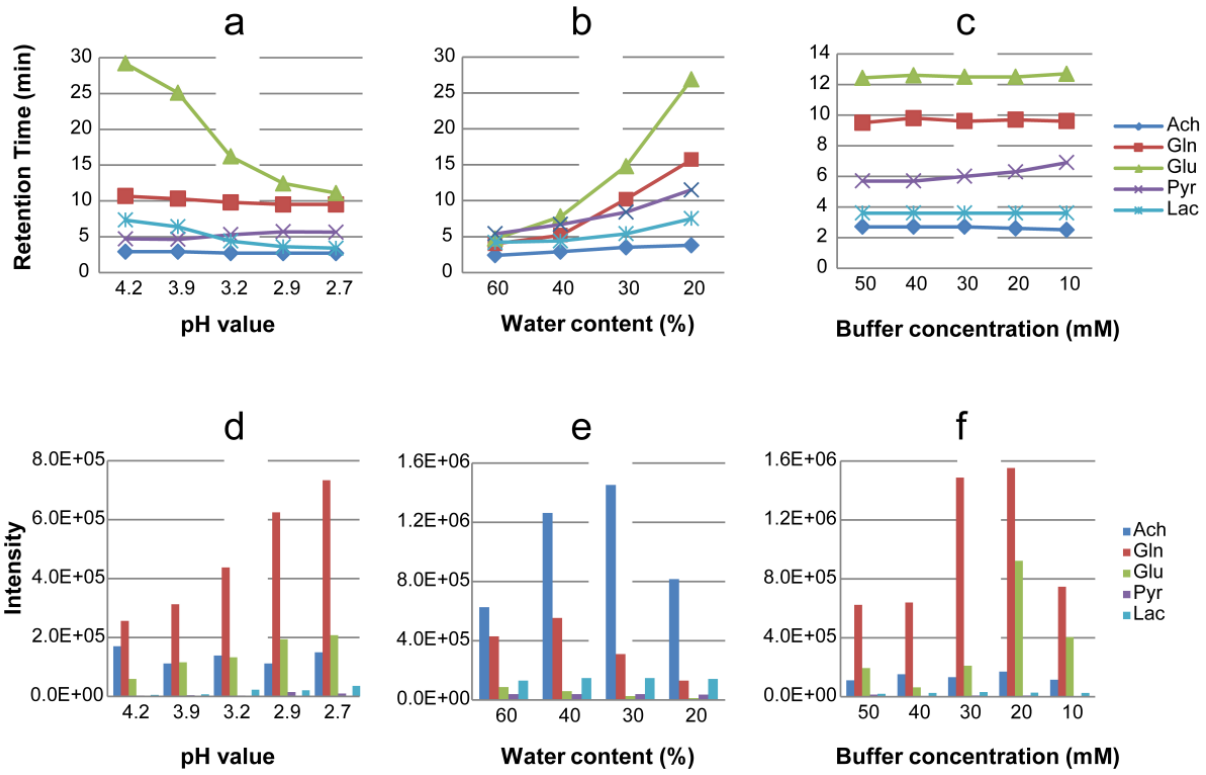

Figure 3.1 Influences of mobile phase on retention behavior and MS signal of the five analytes. a Effects of pH value on the retention time. b Effects of water content on the retention time. The aqueous phase containing 50 mM ammonium formate and 1.0% formic acid. C Effects of buffer concentration on the retention time. Mobile phase A containing 1.0% formic acid. d Effects of pH value on MS signal. E Effects of water content on MS signal. f Effects of buffer concentration on MS signal. An isocratic elution of mobile phase A: mobile phase B (15:75, v/v) was used to test the influence of pH value and buffer concentration. *Acetylcholine (Ach), Lactate (Lac), Pyruvate (Pyr), Glutamine (Gln), Glutamate (Glu).

3.3.2 Analytical performance of the capillary HILIC-ESMI/MS method

The capillary HILIC-ESI/MS method was validated for the quantitative measurements of acetylcholine, lactate, pyruvate, glutamine, and glutamate concentrations from in vivo

dialysates. We characterized a series of parameters like the limits of detection (LODs), limits of quantification (LOQs), linearity, selectivity, accuracy, precision and stability by analyzing different levels of standard mixtures of the target NMs while using optimized MRM transitions and positive/negative ionization modes. The validated results of the analytical performance are listed in Table 3.2. The LODs of lactate and pyruvate in negative mode were 3 and 2 μM, respectively, whereas the LODs of acetylcholine, glutamine, and glutamate in positive mode were 150 pM, 5 nM, and 50 nM, respectively. Although the LODs of lactate and pyruvate were much higher than those of the other three analytes (acetylcholine, glutamine, and glutamate) we still can measure them, because their basal concentrations in the brain as well in the blood are much higher than the other three. The matched MS/MS pattern between the endogenous NMs and their standards allowed confirming the high selectivity of the HILIC-MS method. Additionally, the retention time of the endogenous NMs always matched well with those of internal standards under different gradient elution conditions, which also proved the high selectivity of the method. The accuracy, precision and stability have been tested by replicate analysis (five determinations per concentration) of three different levels of QCs (see the section “Preparation of calibration standards and internal standards”). It is shown in Table 3.2 that the results of the accuracy, intra- and inter-day precisions were all in good agreement with the requirements of biological analysis (Shah et al., 1991). The stability test results indicated that the stock solution was stable for 1 month at −20 °C with the RSD< 12.5%, and the QCs were stable for about 2 weeks in the autosampler at 4 °C with the RSD<15.1%. Additionally, the freeze (−20 °C) and thaw stability has also been tested for these analytes. After two freeze-thaw cycles, the QCs were analyzed on the third cycle, and the results showed a good stability with the RSD<13.1%.

Table 3.2 Validation results of the HILIC-ESI/MS method for the analysis of the five neurochemical analytes

Compounds	LOD	LOQ	Linear range	r^2	Accuracy (%)	Precision [a]	
						Intra-day RSD %, n = 5	Inter-day RSD %, n = 3
ACh	150 pM	450 pM	0.5 - 250 nM	0.9989	82.6 - 109.0	11.6	12.8
Lac	3 µM	10 µM	10 - 5000 µM	0.9990	86.0 - 106.8	9.6	15.2
Pyr	2 µM	6 µM	10 - 5000 µM	0.9989	85.6 - 117.4	10.5	14.3
Gln	5 nM	15 nM	0.5 - 250 µM	0.9990	81.5 - 117.8	10.3	13.3
Glu	50 nM	150 nM	0.25 -125 µM	0.9988	86.0 - 106.9	14.6	15.0

[a] Intra-day and Inter-day precisions were analyzed by one-way ANOVA analysis.

In addition, we adopted the post-extraction spike method proposed by Matuszewski et al. (Matuszewski et al., 2003) to evaluate the matrix effect of the acquired in vivo samples in our study. To reliably determine the endogenous concentration of the five analytes we analyzed them according our developed method and then checked the same brain and blood samples by spiking with appropriate standard solutions. The spiked concentration of acetylcholine, lactate, pyruvate, glutamine, and glutamate was 8 nM, 150 µM, 10 µM, 40 µM, and 1 µM respectively for the brain samples, while 20 nM, 400 µM, 60 µM, 300 µM, and 30 µM for the blood samples. The total concentrations of the five analytes in the spiked samples and the endogenous concentrations in the nonspiked samples were then determined and used to calculate the recovery of each analyte. We used the following formula for calculating the recovery: (measured value−endogenous value)/ added value×100. The obtained recoveries for the five analytes fell in the range of 93–112%.

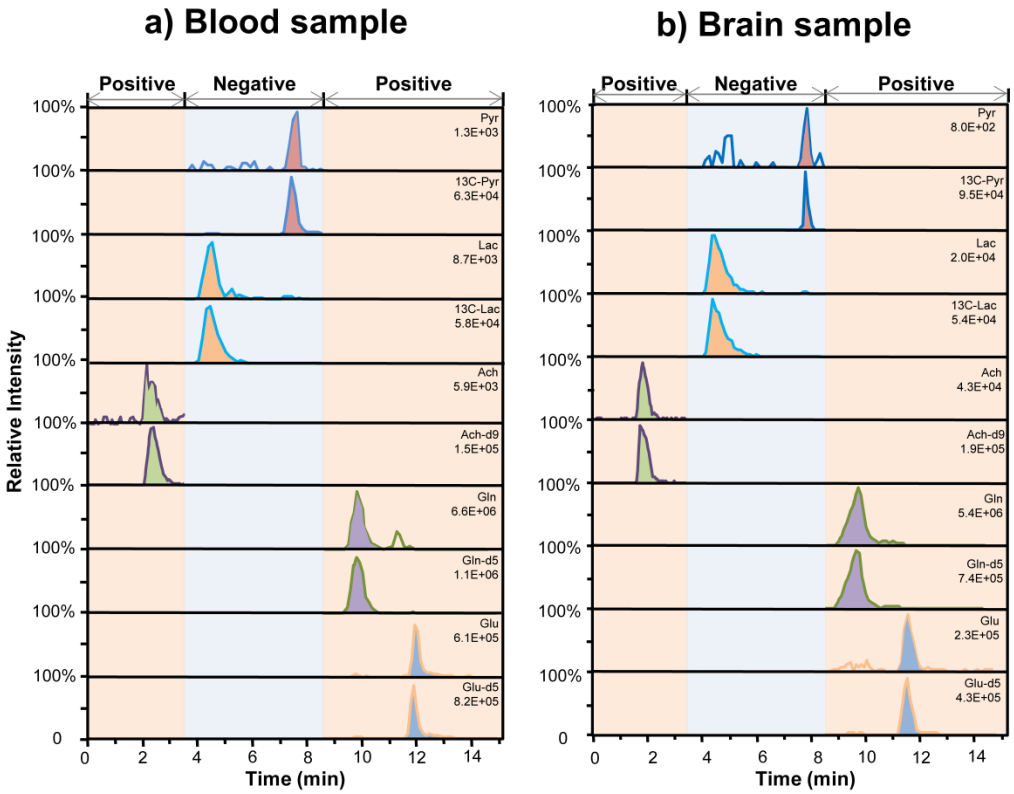

Figure 3.2 Representative HILIC-ESI/MS chromatograms of five NMs under the optimized conditions a blood sample b brain sample. Both positive and negative ion mode was adopted for the detection of five analytes during each run

3.3.3 Concentrations of acetylcholine, lactate, pyruvate, glutamine, and glutamate in the brain and blood microdialysates

We applied capillary HILIC-ESI/MS method together with simultaneous blood and brain microdialysis sampling to measure the concentrations of five NMs from two anesthetized male rhesus monkeys. The microdialysis probe in the brain was placed into the primary visual cortex (V1). The concentrations of acetylcholine, lactate, pyruvate, glutamine, and glutamate in dialysates from primary visual cortex and blood are shown in Table 3.3. The values we monitored were in good agreement with the Human Metabolome Database Version 2.5 (www.hmdb.ca), and the values reported in the literature (Bjerring et al., 2008; Boutelle et al., 1992; Cynober, 2002; Eckstein et al., 2008; Fujii et al., 1995; Hawkins, 2009; Kawashima et al., 1987; Mintun et al., 2004; Molina et al., 2005; Zhang et al., 2007).

Table 3.3 Concentrations of acetylcholine, lactate, pyruvate, glutamine and glutamate in the dialysates of brain and blood.

Compounds	Ach (nM)	Lac (μM)	Pyr (μM)	Gln (μM)	Glu (μM)
Brain	4.0 ± 1.4	220.4 ± 90.9	21.3 ± 8.3	50.4 ± 21.9	1.1 ± 0.2
Blood	10.3 ± 4.4	511.3 ± 78.7	91.5 ± 37.6	176.4 ± 45.3	26.7 ± 5.3

Anesthetized monkeys, resting status. Values are given as mean ± standard error of the mean (S.E.M.); n=4.

3.3.4 Comparison of lactate/pyruvate and glutamine/glutamate ratios in the brain and the blood

To further understand across the BBB, respectively, between the brain and the blood, we examined and compared the lactate/pyruvate and glutamine/glutamate ratios between the brain and blood dialysates. The results showed that the concentration ratio of lactate/pyruvate and glutamine/glutamate was significantly different between the brain and the blood. The values of lactate/pyruvate and glutamine/glutamate were calculated and are shown in Figure 3.3. The mean lactate/pyruvate ratio in the brain was 14.5, but only reached 9.0 in the blood system. The mean ratio of glutamine/glutamate in the brain was 53.4, significantly higher than the blood value of 7.9. One-way ANOVA analysis confirmed the statistical significance of these findings ($p<0.05$).

The lactate/pyruvate ratio in the human brain is currently considered a specific, sensitive marker that could potentially indicate whether glucose and oxygen supply meet the energy requirements of the brain tissue (Bellander et al., 2004). Such marker, that hint upon the adequacy of energy and metabolite supply are of great importance for the detection of onset of neurodegenerative diseases (Iadecola, 2004). In the human brain, a lactate/pyruvate ratio above 40 indicates an “energy crisis” (Samuelsson et al., 2007). Additionally it was shown that lactate can increase the cerebral blood flow which correlates with an increase of the lactate/pyruvate ratio in the plasma (Mintun et al., 2004). A decreased interstitial glutamine/glutamate ratio has been observed in acute and chronic brain damage such as traumatic brain injury (Richards et al., 2003), hypoxia (Raman et al., 2005), and epilepsy (Petroff et al., 2002). Although such findings are still preliminary for diagnosis, we consider the

simultaneous monitoring of blood and brain concentrations of important NMs a necessary step in this direction to get a clear understanding of their chemical relation across the BBB. On the basis of this data, extrapolations from the blood concentrations to brain concentrations of pathologically relevant NMs might be envisioned.

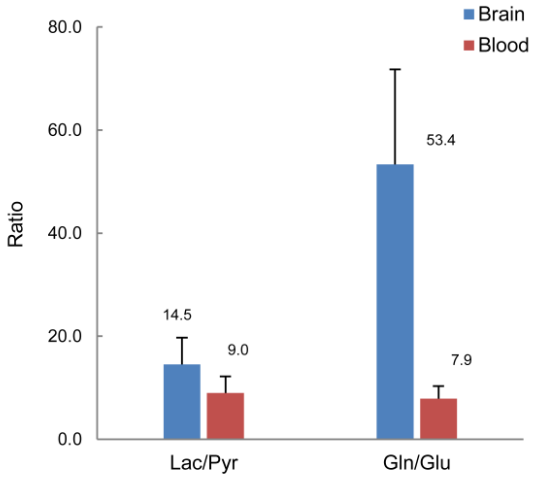

Figure 3.3 Comparison of lactate/pyruvate (Lac/Pyr) and glutamine/glutamate (Gln/Glu) in primary visual cortex and the blood system of rhesus monkey. Ratios of Lac/Pyr and Gln/Glu in monkey primary visual cortex were significantly higher than the blood system ($p<0.05$)

3.4 CONCLUSIONS

We developed a capillary HILIC-ESI/MS method for the simultaneous determination of multiple chemicals including acetylcholine, lactate, pyruvate, glutamine and glutamate from the brain (EBF) and blood system of anesthetized non-human primates. To achieve highest intensity of these NMs, positive and negative ionization modes were used for MS detection. The optimized chromatographic separation allowed us to switch between the two detection modes and to simultaneously measure these NMs in a single run. A simple and fast sample treatment was carried out after collection by microdialysis without any additional sample purification or derivatization. We have successfully demonstrated that our method can reliably quantify these NMs in dialysates collected from the blood and the primary visual cortex of non-human primates. Additionally we found that the concentration ratio of lactate/pyruvate and glutamine/glutamate was significantly different between the brain and the blood, reflecting the active transports and different metabolic processes between the blood and the nervous system respectively across the BBB. Quantified coupling parameters between the blood and the nervous system of NMs are of outmost importance due to their possible use in the

diagnosis of pathological processes in the brain. To further investigate the correlation of these NMs between the brain and the blood systems, we will use the developed analytical method to test the dynamic change of these NMs across the BBB by pharmacologically simulating dysfunctional states of the brain.

4. Manuscript Nr. 2

Pharmaco-based fMRI and neurophysiology in non-human primates

This chapter was published in 2016 in the book *In vivo Neuropharmacology and Neurophysiology*, (Ed) Athineos Philippou. Neuromethods of Springer Science Series by Daniel Zaldivar, Nikos Logothetis, Alexander Rauch & Jozien Goense.

doi: 10.1007/978-1-4939-6490-1_3

4.2 INTRODUCTION

One of the primary goals of systems neuroscience is to understand the neural mechanisms that underlie behavior. Although a great deal has been learned from characterizing the responses of single neurons involved in sensory-, motor- as well as cognitive functions and dysfunctions (Dayan, 2012; Yuste, 2015), little is known about collective properties of contiguous or distributed neural networks underlying such behavior (Boynton, 2011a; Logothetis, 2008; Yuste, 2015). Functional magnetic resonance imaging (fMRI) is an example par excellence of a method allowing non-invasive investigation of groups of neurons and networks involved in behavior and sensory processing, which cannot be identified by studying one neuron at a time (Boynton, 2011a; Logothetis, 2008; Logothetis et al., 2001). Furthermore, the response properties of neurons can be tuned and configured in different ways by different neuromodulators, such as dopamine, serotonin etc., and fMRI combined with electrophysiology and pharmacology may provide insights into the neural networks and how their dynamics are altered by neuromodulation (Logothetis, 2008).

The most commonly used fMRI technique measures the blood-oxygenation-level-dependent (BOLD) signal, which relies on changes in deoxyhemoglobin [dHb], which acts as an endogenous paramagnetic contrast agent (Ogawa et al., 1992). Following increases in neural activity due to a stimulus or performing a task, local cerebral blood flow (CBF) increases to meet the increased metabolic demand. This results in an increase in oxygen supply to the active tissue that is larger than the oxygen consumed, and hence there is a relative increase in the oxyhemoglobin concentration [Hb], and a decrease in the dHb content in the local capillaries, venules and draining veins, leading to an increase in image intensity. BOLD responses are therefore an indirect measure of neural activity, and changes in the CBF, cerebral blood volume (CBV) and the cerebral metabolic rate of oxygen ($CMRO_2$) all affect the BOLD response (Goense and Logothetis, 2008; Logothetis, 2008; Logothetis et al., 2001). Yet, despite progress in our understanding of the neural events underlying fMRI signals (Logothetis et al., 2001; Magri et al., 2012b), it is still not clear how faithfully the BOLD signal

reflects the patterns of neural activity underlying these changes in brain oxygenation. Especially unclear is how to differentiate between function-specific processing and neuromodulation, between bottom-up and top-down signals, or between excitation and inhibition (Shmuel et al., 2006). A clear answer to these questions will not only increase our knowledge of these various neural processes, but is also likely to help us to better understand the results obtained with fMRI.

Many of the questions above are being addressed using new technologies combining invasive measurements with fMRI. For instance, optogenetics combined with fMRI can be used to investigate genetically specified networks in the living brain (Lee et al., 2010). Yet, the combination cannot be readily used for the brain of primates given their diversity of neuron types (Logothetis, 2010), the lack of genetic tools for cell-type specific targeting of proteins in the primate brain (Izpisua Belmonte et al., 2015) and the invasiveness of local injection of viral vectors combined with laser stimulation. The combination of pharmacology and fMRI (phMRI) is a multimodal methodology that has already provided important evidence pertaining the neural events underlying the hemodynamic changes seen with fMRI and optical imaging (Gozzi et al., 2008; Gsell et al., 2006; Hamel et al., 2015; Hillman, 2014; Rauch et al., 2008a; Rauch et al., 2008c; Zaldivar et al., 2014). The importance of these techniques lies in their non-invasiveness, allowing us to test the same hypotheses in humans and in monkeys (Honey and Bullmore, 2004). However, it is worth noting that many pharmacological agents do not only affect neuronal activity, but also affect the blood flow directly, thereby complicating the interpretation of the signal. Hence, the combination of phMRI with concomitant electrophysiology offers the possibility to better test the relationships between neural and fMRI signals under the influence of different neuromodulators.

Neuromodulation affects how neural circuits process information during different cognitive states (Dayan, 2012; Marder et al., 2014). This is in contrast to classical neurotransmission, in which a presynaptic neuron directly and immediately influences its postsynaptic target(s). Neuromodulators and neurotransmitters have different temporal scales and dynamics, which

can be explained by differences in the structure and function of their receptors (Clapham, 1994; Dayan, 2012; Marder et al., 2014). For instance, responses elicited by neurotransmitters are fast because their receptors are linked to ion-channels that open and close when the neurotransmitter binds to the receptor. On the other hand, the effects elicited by neuromodulators tend be of slow onset and long duration since their receptors are coupled via second-messenger pathways, which do not directly open ion-channels but modulate their opening and closing time, as well as their affinity to specific ions (Clapham, 1994). Both neuromodulation and neurotransmission alter the regional metabolic demands, whether they modulate global activity of microcircuits or differentially affect a small subset of neurons. It follows that sheer observations of hemodynamic responses, however quantitatively such observations are made, may fail to discriminate between activations reflecting information processing and those associated to the different cognitive modalities. In this chapter we aim to provide an overview of fMRI, pharmaco-based fMRI (phMRI) and electrophysiology as tools to study the effects of neuromodulation on the BOLD and neurophysiological responses. We propose that such mixed invasive and non-invasive methods may provide greatly useful information related to the interpretation of neural and hemodynamic signals. It goes without saying that the latter can substantially improve the application of fMRI in translations research.

4.2.1 Mechanisms of BOLD responses

To better understand the relationship between any cognitive activity, such as perception, learning, memory, decision making or motor action, and the BOLD signal in any brain structure of interest, it is important to differentiate between neural activity related to information processing and that due to cognitive state, typically reflecting the interaction of various neuromodulatory systems (Logothetis, 2008). One way to achieve this is by combining intracortical neurophysiology with fMRI in monkeys or other animals, either simultaneously or consecutively (Goense and Logothetis, 2008; Logothetis et al., 2010; Logothetis et al., 2001; Zaldivar et al., 2014).

A large amount of our knowledge about neural and brain function is based on extracellular recording methods in anesthetized or alert animals (Belitski et al., 2008; Einevoll et al., 2013). The signal measured with extracellular electrodes captures the mean extracellular field potential signals (mEFP), representing the weighted sum of all sinks and sources including single unit action potentials, depending on the impedance of the electrode. Three different signals are usually extracted from the mEFP: single-unit activity (SUA) representing the action potentials of well-isolated neurons near the electrode tip (within 50 μm); multiple unit activity (MUA) reflecting the spiking activity of small neuronal populations occurring in a sphere of 100–300 μm around the electrode tip; and local field potentials (LFP), which represent mostly slow events reflecting cooperative activity in neural populations within 0.5–3 mm of the electrode tip (Mitzdorf, 1985, 1987). MUA and LFP encompass a range of frequencies (Belitski et al., 2008; Whittingstall and Logothetis, 2009). The frequency range of 900–3000 Hz is used in most recordings to obtain MUA. The modulations of the LFP are traditionally decomposed and interpreted in the frequency bands used in the electroencephalography (EEG) literature (Coenen, 1995; Nunez, 1981): delta (0 – 4 Hz), theta (4 – 8 Hz), alpha (8 – 12 Hz), beta (12 – 24 Hz), low-gamma (50 – 80 Hz) and high-gamma (90 – 150 Hz). This classification is based on the association of these band-limited power (BLP) signals with distinct behavioral states or sensory inputs. An alternative approach to define functionally meaningful frequency-bands is to quantify co-variations in amplitude across different bands (Belitski et al., 2008). This approach aims to detect if amplitude variations in one band are independent of amplitude variations in another, and if they are, then these two bands probably capture different neural contributions to the LFP (Belitski et al., 2008; Magri et al., 2012a).

Simultaneous measurements of intracortical neural activity and fMRI in behaving and anesthetized non-human primates have characterized the relationship between the LFP and BOLD, as well as between MUA and BOLD responses (Goense and Logothetis, 2008; Magri et al., 2012b; Rauch et al., 2008c; Zaldivar et al., 2014). These studies showed that correlation coefficients are higher between LFP and BOLD than between MUA and BOLD signals

(Goense and Logothetis, 2008; Logothetis et al., 2001; Magri et al., 2012b), implying that the overall synaptic activity or the input of an area is a stronger generator of BOLD signal than its output. Furthermore, these findings also demonstrated that BOLD signals and LFP are preferentially correlated at specific frequency bands of the LFP (Goense and Logothetis, 2008; Magri et al., 2012b). This is not surprising giving that different LFP bands correlate with distinct behavioral states and reflect to a large extent the activity of different neural processing pathways (Belitski et al., 2008).

In agreement with the aforementioned observations, studies using 2-deoxyglucose (2-DG) autoradiography have shown that local glucose utilization is directly associated with synaptic activity (Sokoloff, 1977; Sokoloff et al., 1977). For instance, the greatest 2-DG uptake was found to occur in the neuropil, i.e. in areas rich in synapses, dendrites, and axons, rather than in cell bodies. Furthermore, studies using electrical microstimulation have shown that during orthodromic and antidromic stimulation (the former activating pre- and postsynaptic terminals and the later activating postsynaptic terminals only) increases in glucose utilization only occurred at presynaptic terminals (Kadekaro et al., 1985; Kadekaro et al., 1987). Similarly, the highest density of cytochrome oxidase (enzyme of the respiratory chain) is found in somatodendritic regions adjacent to axons (Di Rocco et al., 1989; Kageyama and Wong-Riley, 1986).

Functional-MRI reflects best the regional modulation and/or processing of the input signals, which correlate largely with changes in the LFPs; in other words, it mostly mirrors regional perisynaptic activity (Goense and Logothetis, 2008; Logothetis et al., 2001; Oeltermann et al., 2007). The latter comprises the sum of excitatory and inhibitory postsynaptic potentials, as well as a number of integrative processes, including somatic and dendritic spikes with their ensuing afterpotentials, and voltage-dependent membrane oscillations. However, the coupling between neural activity and the BOLD signal usually changes under different cognitive conditions (Arsenault et al., 2013; Boynton, 2011b) and in some cases the BOLD responses

may not faithfully reflect changes in the expected (assumed) information processing (Boynton, 2011b; Zaldivar et al., 2014).

4.2.2 Pharmacological Magnetic Resonance Imaging (phMRI)

Pharmacology has been used to investigate how neurotransmitter- and neuromodulatory systems influence neural activity, providing the means to study the neurochemical basis of brain modulation. For instance, glutamate is an excitatory neurotransmitter that acts on postsynaptic neurons via AMPA (α-amino-3-hydroxy-5-methyl-4-isoxazolepropionic acid) and NMDA (N-methyl-D-aspartate) receptors (Hirsch et al., 2015; Rao and Finkbeiner, 2007; Siegelbaum and Tsien, 1983). Moreover, local excitation induced by sensory stimulation or by a cognitive task is strongly affected by recurrent inhibition mediated by GABAergic interneurons (Douglas and Martin, 2004; Kujala et al., 2015). Together, glutamate and GABA are the most abundant neurotransmitters in the brain and are responsible for a major part of neurotransmission, which in turn is accompanies by changes in the regional CBF (Goense and Logothetis, 2008; Logothetis, 2008; Logothetis et al., 2010).

The overall regulation of cortical dynamics and neural excitability is modulated by a number of other neurochemicals (neuromodulators) including dopamine (DA), acetylcholine (ACh), norepinephrine (NE), serotonin (5-HT), and various peptides (Dayan, 2012; Rauch et al., 2008c; Zaldivar et al., 2014), that alter the input-output properties of neural circuits as well as optimize their energy expenditure (Attwell and Laughlin, 2001; Marder et al., 2014; Sengupta et al., 2014). The aforementioned neuromodulatory systems, also known as “diffuse ascending systems” originate in various nuclei located in the brainstem and basal forebrain, and project diffusely to very large portions of cortical and subcortical regions (Dayan, 2012; Hasselmo, 1995). Examples include the dopaminergic (DAergic) ascending system innervating cortex from the ventral tegmental area (VTA), the cholinergic system from the nucleus basalis of Meynert, the serotonergic system from the middle and the raphe regions of the pons and upper brainstem, and the noradrenergic system originating in the locus coeruleus (Dayan, 2012).

Despite their seemingly ubiquitous projections, neuromodulatory systems have strikingly specific activity-modulations through multiple neurochemicals and layer-specific projection profiles. It follows that each system likely modulates different aspects of neural activity and behavior (Dayan, 2012). Hence, it is expected that different neuromodulators exert different effects on the hemodynamic signals, because they have different projection patterns and receptor types (Rauch et al., 2008c; Zaldivar et al., 2014). These receptors are located in all neuronal compartments, influencing every aspect of neural computation and metabolism (Dayan, 2012; Sengupta et al., 2014) and their effects highly depend on their location, density and distribution. Thus, the effects of neuromodulators cannot be simply viewed as increases or decreases in neural excitability, but rather, having divergent actions on multiple ion conductances, and consequently on the metabolism of a neural network (Attwell and Laughlin, 2001; Dayan, 2012; Sengupta et al., 2014).

Understanding how neuromodulators affect the BOLD response is evidently essential for an effective interpretation of fMRI-data, not only in task-related fMRI but may also aid diagnostic use of fMRI, since many psychiatric disorders are associated with alterations in neuromodulatory systems (Dayan, 2012; Mitterschiffthaler et al., 2006). Thus, the combination of fMRI and pharmacology can help understand neuromodulatory mechanisms, and combined with electrophysiology is a powerful means to test the coupling between fMRI signals, neural signals, and the different neuromodulators (Rauch et al., 2008c; Zaldivar et al., 2014).

Pharmacological fMRI (phMRI) was initially used to map spatiotemporal patterns of brain activity elicited by acute pharmacological challenges (Honey and Bullmore, 2004; Schwarz et al., 2007). For example, studies in humans using scopolamine (a selective acetylcholine-muscarinic receptor antagonist) to pharmacologically induce memory impairment, showed substantially reduced activation in the hippocampus, fusiform gyrus and prefrontal cortex (Honey and Bullmore, 2004; Sperling et al., 2002). Other studies found that cortical activation increased while subcortical activation decreased with the use of serotoninergic agonists (Loubinoux et al., 2002).

It is worth noting that the effects of drugs on neural responses, vascular reactivity and neurovascular coupling are complex, and judicious interpretation of data is often hampered by the indirect nature of the fMRI signals (Dayan, 2012; Noudoost and Moore, 2011; Zaldivar et al., 2014). Hence, studies that cross-validate BOLD measures of drug action with behavior, electrophysiological measures and/or with other neuroimaging techniques, are invaluable in resolving these important issues. For instance, the use of a GABA-antagonist induced a sustained increase in brain activation, likely due to reduced inhibition, whereas GABA-releasing agents correlated with decreased hemodynamic responses (Chen et al., 2005; Kalisch et al., 2004; Reese et al., 2000). Moreover, reduced tissue perfusion was accompanied by an increased tissue oxygen tension, demonstrating an overall reduction of oxidative metabolism due to GABAergic neurotransmission (Chen et al., 2005).

Similarly, studies have shown that when presynaptic glutamate release is blocked (Kida et al., 2001; Kida et al., 2006) or when selective antagonists either for AMPA- or NMDA- receptors are used (Rao and Finkbeiner, 2007), BOLD and CBF responses are reduced. Furthermore, Gsell, et al. (Gsell et al., 2006) showed a differential contribution of the two major ionotropic glutamate receptors to the hemodynamic response. The reductions in BOLD and CBF were dose-dependent and stronger when using AMPA-receptor antagonists than when blocking NMDA-receptors (Gsell et al., 2006). This difference may reflect the different roles of the receptors. For instance, blockade of AMPA-receptors disturbs the thalamocortical input (feedforward), decreasing all neural responses and consequently the blood flow (Logothetis, 2008; Rao and Finkbeiner, 2007). NMDA-receptor antagonists reduce the postsynaptic currents (feedback) without affecting the feedforward responses (Gsell et al., 2006; Rao and Finkbeiner, 2007). Another possible reason may be that NMDA-receptors exert an indirect vasomotor role via the release of nitric oxide (Faraci and Breese, 1993). Overall, different studies have shown that the effects mediated by GABAergic and glutamatergic neurotransmission (Chen et al., 2005; Gozzi et al., 2008; Gozzi et al., 2005; Zonta et al., 2003) are reflected in the fMRI signals.

Yet, despite the tight correlation between neural activity and the hemodynamic response, it is difficult to make inferences about particular brain functions by only using phMRI. For instance, Rauch et al. (Rauch et al., 2008c) showed how complex the relationship between neural activity and the hemodynamic response can be under the influence of neuromodulation. Using a selective serotonin (5HT1A-receptor) agonist in V1, which causes persistent hyperpolarization of pyramidal neurons, they found that despite the decreased spiking activity, both the local processing reflected in the LFP and the BOLD responses were unaffected. Thus, the output of a neural network poses relative little metabolic demands compared with the overall presynaptic and postsynaptic processing of the incoming afferent activity (Logothetis, 2008; Rauch et al., 2008c).

Hence, combining fMRI, neurophysiology and pharmacology may help us to disentangle the relationships between the hemodynamic signal and the neural activity. Although in some cases the interpretation of the signals is straightforward (Rauch et al., 2008a), in other cases the effects of neuromodulators will strongly depend on receptor type, location and density, as well as on the particular functions they modulate (Dayan, 2012; Rauch et al., 2008c; Zaldivar et al., 2014).

4.3 Materials

4.3.1 The animal model – non-human primates

Non-human primates (NHPs) are a common animal model for research in vision and higher cognitive functions (Rajalingham et al., 2015), owing to their evolutionary proximity to humans, which is reflected in the similarity of its cerebral anatomy and its perceptual and behavioral specializations (Buckner and Krienen, 2013). The neocortex forms 70-80% of the NHP and human brain respectively, while in rodents it is only 28% of their brains (Buckner and Krienen, 2013; Mantini et al., 2013). In addition, compared to other mammal species, the primary visual cortex (V1) of the NHPs has a high density and diversity of neural-cell types (Carlo and Stevens, 2013; Collins et al., 2010). It is therefore not surprising that findings from NHP research have triggered and guided fMRI experiments in humans, and have greatly helped

with interpretation of neuroimaging findings in the latter species (Goense and Logothetis, 2008; Logothetis, 2008; Zaldivar et al., 2014). Combining imaging with electrophysiological recordings and pharmacology in NHPs allow us to directly compare fMRI signals and neural activity associated with neuromodulatory pathways (von Pfostl et al., 2012; Zaldivar et al., 2014), and thereby better interpret human results as well. We acquired neurophysiology and fMRI responses from anesthetized NHPs (weight 6-11 kg) while the animals were viewing visual stimuli. We focused on V1, given that the activity of the neurons in V1 is strongly but selectively influenced by the stimuli (Callaway, 1998; Douglas and Martin, 2004).

The experimental procedures were carried out using 6 - 10 years old healthy rhesus monkeys (Macaca mulatta; four females and two males) weighing 5 – 12 kg. Animals are socially housed in an enriched environment, under daily veterinary care. Weight, food and water intake are monitored on a daily basis in full compliance with the guidelines of the European Community (EUVD 86/609/EEC).

4.3.2 Pressure-operated pumps for local and systemic pharmacology

Aside from carefully controlling the chemical properties and pH of the pharmacological solutions that are injected systemically or intracortically, it is important to precisely control the injected volume and flow of the solutions, because high volume and flow rates for intracortical injections can disturb the neural microenvironment and change the neural activity independent of the pharmacological challenge. Similarly, high systemic injection rates or volumes can alter the hemodynamic responses measured with fMRI due to blood volume changes, which may also affect the blood-pressure. Hence, we custom built pressure-operated pumps to precisely control the pharmacological injections (Figure 4.1A) The pumps consisted of two independent single-stage pressure regulators (one for local pharmacology and one for local and systemic applications depending on the experimental needs), each connected to a digital closed-loop electropneumatic controller (ER5000 with 267 ml capacity; TESCOM, Emerson Electric Co., Germany). Each controller houses two pulse-width-modulated solenoid valves (Nickel-plated brass, TESCOM, Emerson Electric Co., Germany) which are connected to a PID-based

microprocessor (16-bit microprocessor with ceramic sensors) and to a computer running custom-written MATLAB software to visualize and control the pressure and the resulting volume and flow-rates.

The aforementioned valves measure the pressure at two different points (Figure 4.1A, upper right corner); one of the valves measures the desired-pressure in the inlet (pressure set in the computer, setpoint) and the second detects the actual pressure in the line (outlet-line, feedback point). The signals emitted by the valves are compared every 25 ms and based on the pressure difference between the setpoint and the feedback-point, the electropneumatic controller opens or closes either of the valves to compensate for the pressure difference (Figure 4.1A, right corner). If the pressure-difference is greater than zero, the controller opens the inlet valve (Figure 4.1A, red arrows), if less than zero the exhaust valve is opened (Figure 4.1A, black arrows). Both valves remain closed if the pressure needs no adjustment. The gas at the desired pressure is distributed to the syringe pump (systemic pharmacology) or to the pressure-cells (intracortical pharmacology) through the outlet-line (Figure 4.1A, blue arrows).

The pressure-cells were custom-built and made of brass (80 mm diameter and 100 mm height), and housed four small compartments (15 mm inner-diameter and 35 mm height each) adequate for 2 ml bottles (12 mm outer-diameter and 32 mm height, Agilent Technologies, Santa Clara, CA, USA). This configuration allowed for independent lines to switch between different solutions during an experiment. Prior to the experiments, the bottles containing the solutions were positioned in the small compartments (Figure 4.1A)**.** The fused-silica infusion lines (50 µm inner diameter) were inserted in the bottles and the other end of the tubing was connected to the injector. As pressure is applied in the pressure-cells, it induces a positive displacement of the solution through the lines.

The syringe pump consisted of a self-contained double-acting cylinder made of aluminum (bore size 8 mm and 190 mm height). The double-acting cylinders have two gas-ports: one on the top and one on the bottom, and allow the cylinder-rod to move in or out depending on the

gas entry point (Figure 4.1A). Systemic injection using this device was achieved using the gas-port located at top of the cylinder, which drives the cylinder-rod inside the cylinder-bore which consequently pushes the syringe plunger. The infusion lines consisted of fused-silica tubing that was connected to the syringe and to the injector. All the injection lines (for systemic and local pharmacology) were monitored by liquid flow sensors (Sensorion SLx-Series, Switzerland) controlling the exact applied volume and flow. These sensors have an integrated CMOS-microchip, which is connected to the same computer used for controlling the electropneumatic controller. This allowed us to set the pressure to a certain value while simultaneously measuring the resulting flow-rate and volume of the applied substances.

All chemicals were purchased from Sigma Aldrich (Schnelldorf, Germany). Drugs and solutions were freshly prepared prior to the experiments. Drugs for systemic injection were diluted in a phosphate-buffered-saline (PBS) solution and for intracortical injection in artificial-cerebro-spinal-fluid (ACSF). The PBS solution contained NaCl 137 mM, KCl 2.7 mM, Na_2HPO_4 8.1 mM, KH_2PO_4 1.76 mM, and the pH was adjusted to 7.35 using NaOH. The ACSF contained 148.19 mM NaCl, 3.0 mM KCl, 1.40 mM $CaCl_2$, 0.80 mM $MgCl_2$, 0.80 mM Na_2HPO_4 and 0.20 mM NaH_2PO_4. As in the PBS solution, the pH was adjusted to 7.35 using NaOH. Control experiments were performed using the unmodified- PBS and ACSF solution at similar volumes and flow rates as used for drug injections.

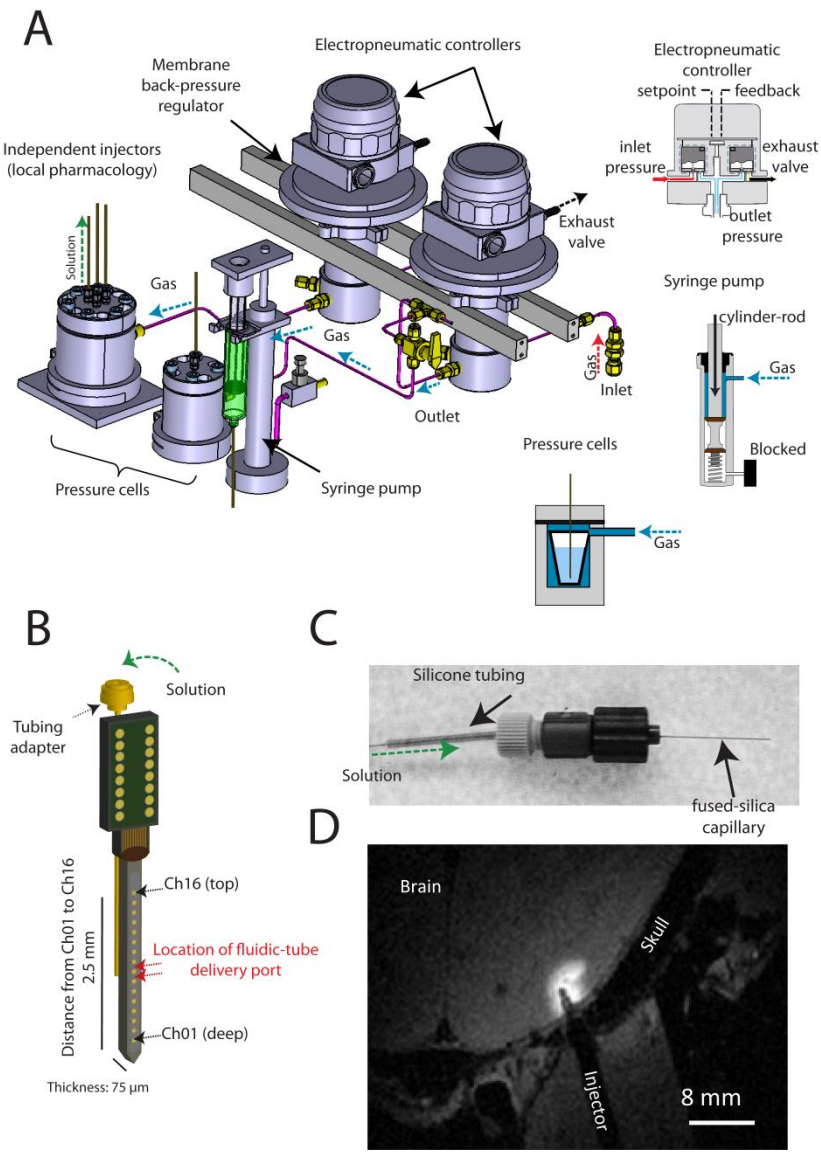

Figure 4.1 Injection setup used for combined fMRI and (intracortical and systemic) pharmacology.

(**a**) The pressure operated-pump consisted of electropneumatic-controllers that housed two solenoid valves connected to a computer running custom-written MATLAB software. Each of these valves had a sensor that measured the pressure in the inlet-line (pressure coming from the external gas-supply) and the pressure in the outlet-line (pressure going to the syringe pump and to the pressure-cells). The sensors detect differences in pressure between the inlet and the outlet lines; if differences are detected in either of the lines, it will automatically open one of the valves for compensation. This system provided us with an accurate pressure that was tightly controlled by a computer with negligible delays (25 ms time to reach the desired pressure). The resulting flow-rate and volume of the solution being injected were monitored using Sensirion liquid flow sensors (Sensirion, Switzerland) located at the side of the pump. Pressure-cells contained small compartments adequate for 2 ml bottles containing solutions. Once a bottle was placed inside the pressure-cell, it was tightly closed to prevent leakage. As pressure was applied in the pressure cell, it causes displacement of the solution through the lines. The infusion lines for the systemic and local pharmacology consisted of fused-silica tubing connecting the syringe and the pressure-cells to the injectors. (**b**) Neuronexus multicontact laminar electrodes were used to record neuronal activity across the cortex. The electrodes (50 µm thick) had 16 contact-points spaced 150 µm apart, with a recording area of 176 μm^2. These electrodes had a fused-silica injector attached for intracortical pharmacological injection. (**c**) The custom-built injectors for systemic pharmacological injection consisted of a fused-silica fluidic tube with an outer diameter of 100 µm and were attached to the infusion line prior to the experiments. (**d**) Intracortical injection of manganese (Mn^{2+}) at high pressure and volume in monkey V1 using a custom-built pharmacological-probe; see Rauch et al. (Rauch et al., 2008c) for details. This was used to evaluate the performance of the pump and to estimate the extent of diffusion using this approach.

4.3.3 Electrodes and Injectors

To reduce neural tissue damage due to the electrodes we used micro-electro-mechanical systems (MEMS), fabricated using silicon (NeuroNexus Technologies, Ann Arbor, USA). We used a multisite probe that had 16 contacts on a single shank of ~3 mm length and 50 µm thick. The contacts were arranged in a row and spaced 150 µm apart, with a recording area of 176 μm^2 (Figure 4.1B). The probes for combined pharmacology had a fused-silica fluidic tube mounted with an outer diameter of 75 µm, which combined with the neurophysiology probe resulted in a 125 µm thick probe. The fluidic tube was mounted on the back of the microelectrode array, and the delivery port was located at the level of the central electrodes (Figure 4.1B) and positioned in the middle of the cortex. The fluidic tube was connected to the pressure-operated pump using a HPLC pump-tubing adapter (Figure 4.1B). The injectors for systemic injections were custom-designed and were made of fused-silica capillary tubing (outer diameter 150 µm and inner diameter 100 µm) which was connected to the infusion line (Figure 4.1C).

We evaluated the performance of the pressure-operated pumps by intracortical injection of manganese (Mn^{2+}) in monkey V1 (Figure 4.1D). This allowed us to visualize the location of the signal enhancement and estimate the Mn^{2+}-diffusion. We applied a low concentration of 0.05 mM at a high flow-rate of 1.4 µl/min during 5 min, with an end volume of 7 µl, and observed that Mn^{2+} was dispersed within a radius of 2 mm.

4.3.4 MRI setup and monkey chair

fMRI experiments were conducted using two custom-built vertical primate scanners. See (Goense et al., 2010; Logothetis et al., 1999b; Pfeuffer et al., 2004) for a detailed description. Briefly: 1) a 4.7T scanner (BioSpec 47/40v, Bruker BioSpin GmbH, Ettlingen, Germany) with a 40 cm bore and equipped with a 48 mT/m (224 µs rise time) actively shielded gradient coil (Bruker, BGA26) of 26 cm inner diameter. 2.) a 7T scanner (BioSpec 70/60V, Bruker BioSpin GmbH, Ettlingen, Germany) with a 60 cm diameter bore, and a 75 mT/m actively shielded

gradient with 500 mT/m/ms slew rate (Bruker, BGA38S2). The MR systems were controlled by Bruker BioSpec consoles running ParaVision 5.1 under the Linux operating system.

Custom-built chairs were used to position the monkey in the magnet (Figure 4.2A) (Logothetis et al., 1999b; Pfeuffer et al., 2004). The chairs consisted of two parts made of NMR compatible materials. The lower part of the chair (Figure 4.2A, red arrow) was made of aluminum, which contained all the infusion lines (including the lines for systemic and local pharmacological injections), the tubing for the anesthesia machine, preamplifiers for electrophysiological recording and the lines to keep eyes hydrated (Figure 4.2A). The upper part of the chair (Figure 4.2A, green arrow) consisted of a semi-cylinder made of fiberglass impregnated with epoxy (GFK, epoxy-glass resin: Hippe, Hildesheim Germany). The monkeys sit on a platform made of plastic (Delrin Polyoxymethylene); the height of this platform is adjusted according to the length of the monkey's body. This cylinder had two openings that enable access to the seat for monitoring the monkey's position, both of which are closed using covers of the same material as the chair, and were easily and firmly closed using nylon screws. The infusion lines, the tubing for the anesthesia machine and the cables for the coils run along the inner surface of the chair.

4.4 Methods

4.4.1 Animal preparation, anesthesia and sensory stimulation

Detailed description can also be found in (Logothetis et al., 1999b; Zaldivar et al., 2014). Before each experiment the monkeys were given an intramuscular (IM) injection of glycopyrrolate (0.01 $mg \cdot kg^{-1}$) to reduce salivary, tracheobronchial and pharyngeal secretions, and prevent obstructive asphyxia. Subsequently, monkeys were sedated with an IM injection of ketamine (15 $mg \cdot kg^{-1}$). An intravenous (IV) cannula wais placed in the saphenous or posterior tibial vein to allow administration of fluids, medication and anesthetics. Subsequently, fentanyl (3 $mg \cdot kg^{-1}$), thiopental (5 $mg \cdot kg^{-1}$) and succinylcholine chloride (3 $mg \cdot kg^{-1}$) were injected via IV. Immediately after the application of these drugs, animals were intubated with an endotracheal tubus (Rusch, Teleflex, USA) and ventilated using a Servo

Ventilator 900C (Siemens, Germany) maintaining an end-tidal CO_2 of 33–35 mm Hg and oxygen saturation above 95%. General anesthesia was maintained with remifentanil (0.4 – 1 $\mu g \cdot kg^{-1}min^{-1}$) and mivacurium chloride (2 – 6 $mg \cdot kg^{-1}h^{-1}$) to ensure complete paralysis of the eye muscles. The combination of these drugs has been extensively used for combined fMRI and electrophysiology experiments, and neurovascular and neurophysiological responses in V1 of monkeys remain largely unaffected (Logothetis et al., 2010). A study combining experiments in anesthetized (using the same anesthesia protocol described above) and awake monkeys, reported few differences between the face-processing network in awake and anesthetized monkeys (Ku et al., 2011). Nonetheless, it is important to note that given the nature of the general anesthesia, one needs to be sure about possible interactions with the different neuromodulatory centers. By knowing the pharmacodynamics of the tested drugs, one can predict whether possible interactions might happen that affect the absorption, distribution, metabolism or elimination of the drugs or anesthetics. A critical point to know is whether an interaction between drugs is expected when two or more drugs produce similar effects by different mechanisms.

Given that changes in body temperature, pH, blood pressure and oxygenation can affect the fMRI signals, the physiological state of the animal was continuously monitored; the normal physiological values during the general anesthesia are shown in Table 4.1. We tightly maintained the body temperature between 38.5–39.5°C, and applied lactate Ringer's (Jonosteril, Fresenius Kabi, Germany) with 2.5% glucose at a rate of 10 $ml \cdot kg^{-1}h^{-1}$ to maintain an adequate acid-base balance, intravascular volume, and blood pressure; hydroxyethyl starch (Volulyte, Fresenius Kabi, Germany) was administered as needed. Prior to emergence of anesthesia, remifentanil and mivacurium were stopped. Emergence from anesthesia was typically without complication and lasted on average between 30 – 40 min after mivacurium was stopped. When spontaneous respiration was assured and an appropriate muscular tone was assessed, the trachea was extubated. Subsequently, the monkeys were placed inside an acrylic custom-built box to monitor their behavior after extubation. Once the monkeys were

freely moving with a full control of their body posture, they were taken to their cage. After each experiment, the monkeys were given a resting period of at least 15 days.

We applied 1-2 drops of 1% ophthalmic solution of anticholinergic cyclopentolate hydrochloride in each eye to achieve cycloplegia and myadriasis. The eyes of the monkeys were kept open with custom-made irrigating lid speculae to prevent drying of the eyes. The speculae irrigated the eyes at the medial and lateral canthus, with a saline infusion rate of 0.07 $ml \cdot min^{-1}$. Refractive errors were measured and hard contact lenses (Wöhlk-Contact-Linsen, Schönkirchen, Germany) were placed on the monkey's eyes. Lenses with the appropriate dioptic power were used to bring the animal's eyes to focus on the plane where stimuli were presented.

Table 4.1 Physiological parameters during the general anesthesia maintenance

Physiological Parameter	Units	Average Value
Heart rate	beats/min	128 ± 18
Systolic blood pressure	mm Hg	100 ± 12
Diastolic blood pressure	mm Hg	48 ± 15
Respiration rate	1/min	27 ± 6
Tidal volume	ml	98 ± 42
Oxygen saturation	%	97 ± 2
End-tidal CO_2	mm Hg	33 ± 2
Temperature	˚C	38.7 ± 0.8

Mean physiological parameters under general anesthesia during fMRI and neurophysiology experiments. Animal age and weight were comparable across all experiments (5 females and 2 males; 8-12 years, weight 6-12 kg). The parameters in the table were averaged across all experimental sessions (N = 40).

The visual stimuli were delivered using a PC equipped with two VX113 graphics systems. All image generation was in 24-bit true color, using hardware double buffering to provide smooth animation. The stimulation software was written in C and utilized Microsoft's OpenGL 1.1. The 640 x 480 VGA output was converted (Professional Graphic/TV Converter) to a video signal (NSTC) for driving the video interface using a fiber-optic system (Avotec, Silent Vision,

Florida). The field of view of the system was 30 horizontal x 23 vertical degrees of visual angle. The system's effective resolution, determined by the fiber-optic projection system, was 800 horizontal x 225 vertical pixels (Logothetis et al., 2001).

Binocular presentation of stimuli was done using a custom-built projector and SVGA fiber optic system. The periscopes for stimulus display (Figure 4.2A) were independently positioned using a modified fundus camera (Zeiss RC250, (Logothetis et al., 2001)) that permitted simultaneous observation of the fundus and a 30° horizontal x vertical calibration frame. This process ensured the alignment of the stimulus with the fovea.

The visual stimulation paradigm consisted of blocks of rotating black and white polar checkerboards of 10x10° in size lasting 48 s (ON, Figure 4.2B) alternated with an isoluminant gray blank period of equal length (OFF, Figure 4.2B). The stimulus timing was controlled by an industrial computer (Advantech 510, Germering, Germany), running a real-time OS (QNX, Ottawa, Canada). The direction of the rotation was reversed every 8 s to minimize adaptation. This block was repeated 29 times yielding a total of 46 min for each phMRI experiment. Usually three phMRI experiments were acquired per day: two consisted a pharmacological injection (either local or systemic) with a drug of interest and the other of a PBS-injection that was used as a control (see Methods).

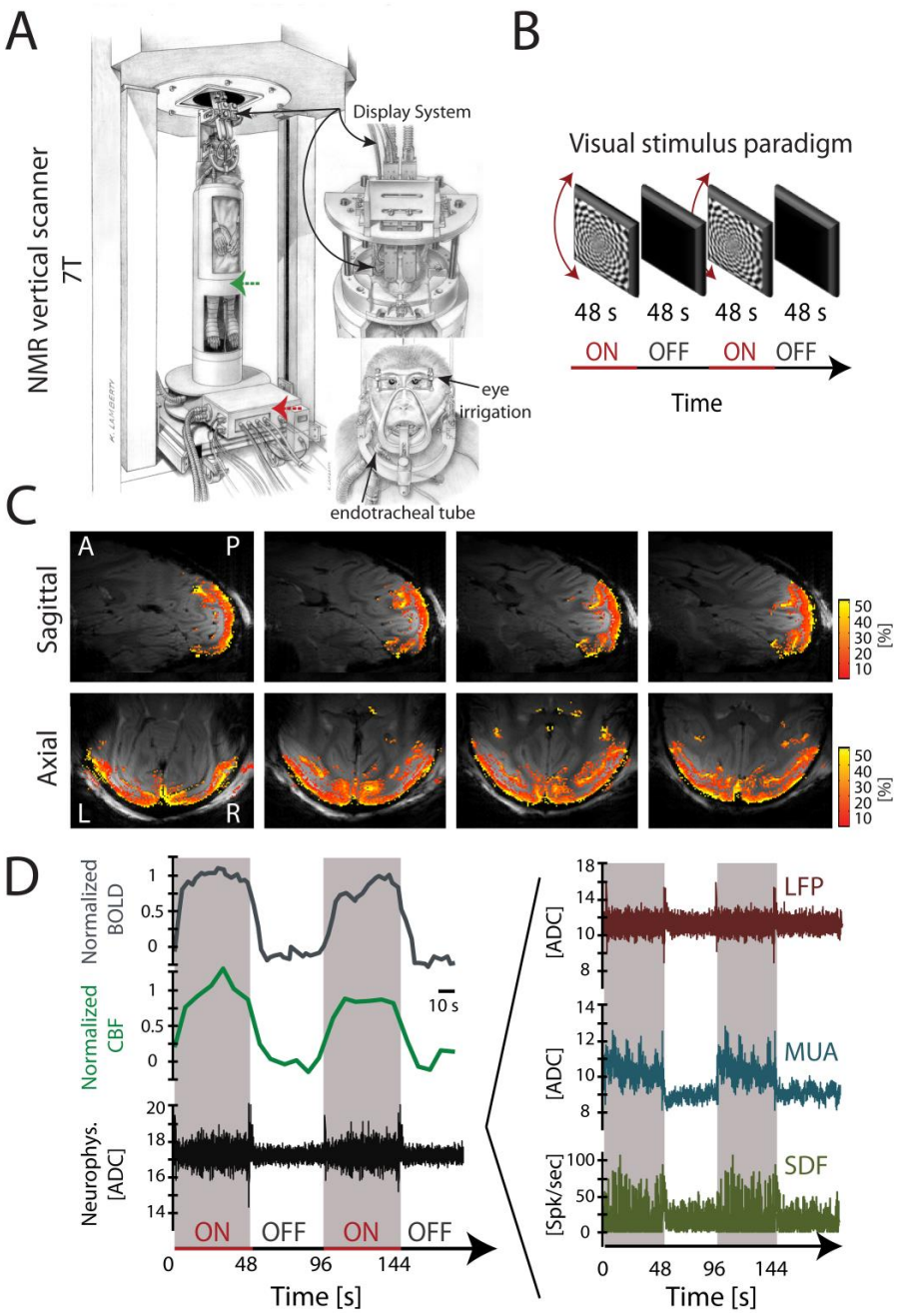

Figure 4.2 fMRI and neurophysiological responses to sensory stimulation.

(**a**) The 7T vertical primate scanner. The monkey chair consisted of two parts: the lower part (red arrow) consisted of an aluminum case that housed the tubing for the anesthesia machine and the infusion lines. The upper part of the chair is composed of a semi-cylinder made of fiberglass, which contained the seat for the monkeys. To position the monkey chair in the magnet, a vertical transport system based on spindle drives and magnetically screened motors was used; see Pfeuffer et al. (Pfeuffer et al., 2004) for details. (**b**) The stimulation paradigm consisted of blocks of a rotating polar black-and-white checkerboard followed by a blank period of equal duration. (**c**) Functional activation maps, acquired at 7T, showing voxels with significant responses to the visual stimulus; axial and sagittal slides were acquired using an 8-shot GE-EPI (FOV: 64x48 mm^2; TE/TR: 20/750 ms; flip-angle 40˚). (**d**) Representative time courses of BOLD, CBF and neural responses to visual stimulation (left panel) showing reliable visually induced modulation (acquired independently). The right panel shows the different neuronal events obtained by decomposing the raw neurophysiology signals into LFP (band-passed 0–150 Hz), MUA (band-passed 900–3000 Hz) and the spike density function (SDF, action potentials convolved with a Gaussian of fixed kernel).

4.4.2 Functional MRI in monkeys

Monkeys were positioned in the magnet in a custom-made chair (Figure 4.2A). For the BOLD experiments we used a custom-built quadrature volume coil that allows imaging of deep brain structures while maintaining a high signal-to-noise ratio in the visual cortex. We used a single-shot gradient-echo EPI with a FOV of 72x72 mm^2 and matrix size of 96x96. 11 slices were acquired with a thickness of 2 mm, TE/TR 20/3000 ms and flip angle of 90˚. Each experimental session consisted of 928 volumes. Shimming was done with FASTMAP over a volume of 12x12x12 mm^3. For functional CBF measurements, we used a Helmholtz volume coil to transmit in combination with a custom-built, 4-channel phased array (Goense et al., 2010). Perfusion imaging was performed using flow-sensitive alternating inversion recovery [FAIR; (Kim, 1995)]. At 7T we used an inversion time of 1400 ms, slab thickness 6 mm, FOV 5.5x2.4 mm^2, TE/TR 9.5/4500 ms and receiver BW 150 kHz. Experiments at 4.7T were performed using an inversion time 1400 ms, slab 6 mm, FOV 6x3.2 mm^2, TE/TR 9.1/4500 ms and BW 125 kHz (Goense et al., 2012).

We defined a region of interest (ROI) consisting of early visual cortex (V1-V2). A 12-min localizer scan was used to define the ROI that was subsequently used for the injection scan. We used a boxcar convolved with a haemodynamic response function (gamma variate function) as regressor to calculate the correlation coefficient. Voxels showing robust visually induced modulation ($p < 0.02$) were included for further analysis, and were then monitored during the 46-min injection scan.

Figure 4.2C shows typical functional activation maps in V1 and V2 with an in-plane resolution of 0.75 x 0.75 mm^2 and 2 mm slice thickness. The activated voxels are color-coded according to their percentage changes. The average time courses for the BOLD and the CBF responses are shown in Figure 4.2D (gray and green respectively), showing increases in response during stimulus presentations. To quantify changes in the visually induced modulation, we subtracted the ON-periods from the OFF periods, and then divided the result by the OFF-period. In addition, baseline changes were computed by taking the image intensity in the periods without

visual stimulation (OFF-periods). For both baseline and modulation we computed the percentage change relative to the before condition.

4.4.3 Neurophysiological Measurements in monkeys

Due to the complexity and experimental difficulties (multiple probes, fragile laminar probes, multichannel interference compensation at 7T), electrophysiological recordings were done in separate experiments, using the same methods for injection as described in the previous section. The electrophysiology preparation was done by making a small skull trepanation (~3 mm diameter) using an electrical drill with diamond tip (Storz, Switzerland). Subsequently, the meninges were carefully dissected under a microscope (Zeiss Opmi, MDU/S5, Germany) without damaging the cortical surface. The laminar probes were inserted using manual micromanipulators (Narashige Group, Japan) under visual and auditory guidance. The exact location of the electrode contacts was verified post-hoc based on the spontaneous spiking activity, coherence maps and current-source-density analysis (CSD, data not shown). We then positioned a flattened Ag wire under the skin that served as reference electrode (Murayama et al., 2010). Finally, in order to guarantee a good electrical connection between the animal and the ground contact, we filled the recording area with a mixture of 0.6% agar in NaCl 0.9% at pH 7.4. Note that we did not consider layer-specific changes here, and averaged the PSD over all contacts.

Signals were acquired using a multichannel Alpha-Omega amplifier system (Alpha-Omega Engineering, Nazareth, Israel), running their acquisition software. The signals were amplified and filtered into a band of 1 Hz – 8 kHz and digitized at 20.833 kHz with 16-bit resolution (National Instruments, Austin, TX), ensuring sufficient resolution for both LFPs and spikes. The time-course of the averaged raw electrophysiology data is shown in Figure 4.2D. Note that similar to the BOLD and CBF responses, the electrophysiological recording shows reliable visually evoked responses. We extracted the LFPs and MUA by band-pass filtering the signals using custom-written MATLAB routines. The broadband LFPs were obtained by band-pass filtering the neural responses between 1 and 150 Hz (Figure 4.2D, right panel). To filter, the

neural signals were digitized, and their sampling rate reduced by a factor 3 from 20.835 kHz to 6945 Hz. Subsequently, the signal was band-pass filtered and downsampled in two steps: 1) first to a sampling rate of 1.5 kHz using a fourth order Butterworth filter (500 Hz cutoff edge); and 2) to 500 Hz using a Kaiser window between 1 and 150 Hz, with a transition band (1 Hz) and stopband attenuation of 60 dB (Magri et al., 2012a; Magri et al., 2012b). This two-step procedure was computationally more efficient than a single filtering operation to the final sampling rate. The sharp second filter was used to avoid aliasing, without requiring a higher sampling rate attributable to a broad filter transition band, which would increase the computational cost of all subsequent operations. Forward and backward filtering was used to eliminate phase shifts introduced by the filters.

To extract MUA, the 6945 Hz signal was high-pass filtered at 100 Hz using a Butterworth fourth-order filter, and then band-pass filtered in the rage of 350 – 3000 Hz using a Kaiser window filter with a transition band of 50 Hz, stopband attenuation of 60 dB, and passband ripple of 0.01 dB. The absolute value of the signal was taken, and decimated by a factor of 8 to reduce computation time. Finally, it was low-pass filtered at 250 Hz and resampled at 500 Hz to match the sampling rate of the LFP. The MUA obtained in this way represents a weighted average of the extracellular spikes of neurons within a sphere of approximately 140 – 300 µm around the tip of the electrode, which helps to detect overlapping spikes produced by the synchronous firing of many cells (Einevoll et al., 2013; Einevoll et al., 2007). To extract single spikes, the 6945 Hz signal was filtered in a range of 900 – 3500 Hz. The threshold for spike detection was set at 3.5 SDs. The results of these procedures are shown in Figure 4.2D (right panel).

The MUA and spikes are primarily attributed to spiking activity of large pyramidal neurons, and thus they are considered measures of cortical output (Belitski et al., 2008; Rauch et al., 2008c). LFPs have been suggested to reflect the input and intracortical processing in a cortical area (Belitski et al., 2008; Rauch et al., 2008c; Whittingstall and Logothetis, 2009; Zaldivar et al., 2014) and they are traditionally decomposed and interpreted in the frequency domain (Belitski

et al., 2008; Whittingstall and Logothetis, 2009). Figure 4.3C, shows five band-limited power (BLP) LFP signals extracted from the recordings in V1. However, the definition of the frequency bands is often inconsistent and based on observations associated to distinct sensory inputs or behavioral states (Michels et al., 2010). For instance, quantifying amplitude co-variations across bands has been extensively used to define functionally meaningful LFP bands (Belitski et al., 2008; Magri et al., 2012a; Magri et al., 2012b). That is, if amplitude variation in one band is independent of amplitude variation in another, then the two bands presumably capture different neural contributions to the LFP. Two types of correlations are used to distinguish the boundaries between statistically independent frequency regions in the LFP and can be used to separate functionally distinct contributors to the LFP (Belitski et al., 2008; Einevoll et al., 2013; Magri et al., 2012a). Signal correlations reflect the similarity of different frequency bands in their tuning to external conditions (Figure 4.3B, top panel). Noise correlations reflect the trial-by-trial co-variations between different frequency bands after discounting for their similarities in tuning to external conditions (Figure 4.3B, bottom panel).

The combination of signal and noise correlations, allows us to determine LFP frequencies that share common neural properties (Einevoll et al., 2013). For example, the LFP-frequencies <50 Hz do not share any substantial signal or noise correlations with the higher LFP-frequencies (Figure 4.3B) suggesting they are driven by different neural processes. Indeed, combining this approach with information theoretical tools has helped determine which frequency bands carry information about the sensory stimulus (Belitski et al., 2008; Magri et al., 2012a; Magri et al., 2012b). Low frequencies <20 Hz and frequencies of 40 – 150 Hz (gamma range) were shown to be the most informative about naturalistic visual stimuli and both have high signal correlations (Figure 4.3B). In contrast, intermediate LFP frequency bands (18 – 38 Hz) carry little information about the stimulus and have low signal but high noise correlation (Figure 4.3B). Together with the fact that these frequency ranges do not increase in power during stimulation (Figure 4.3A), this suggests that they might be influenced by a common input, such

as diffuse neuromodulatory input (Belitski et al., 2008; Magri et al., 2012b). Further experimental work is needed to confirm this.

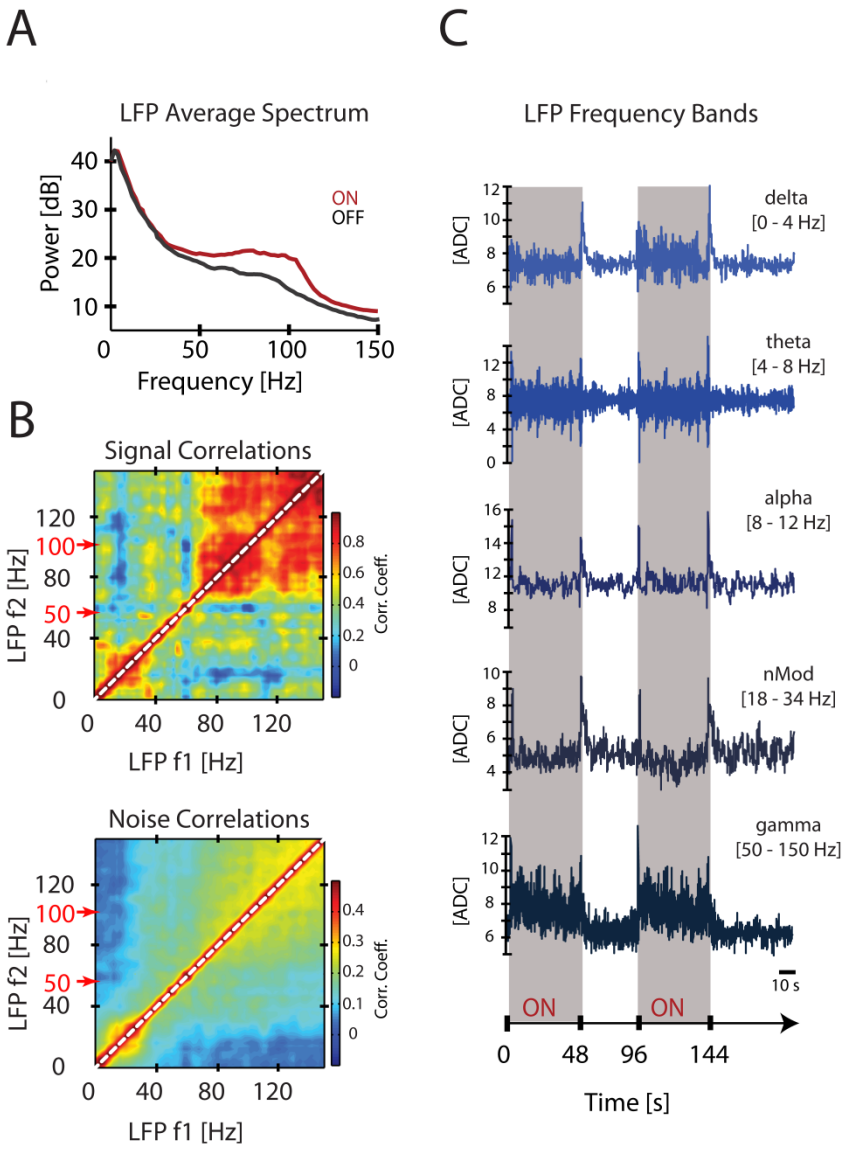

Figure 4.3 Separation of functionally distinct LFP frequency bands.

(a) Power spectrum of the LFPs during presentation of the checkerboard stimulus. The red line shows the trial-averaged LFP power spectrum during the ON-period. The black line shows the averaged LFP power spectrum during the OFF-period. LFP power was highest at low frequencies (≤8 Hz) and decreased at higher frequencies, with a second peak at 50 - 150 Hz. (b) Correlations between pairs of different LFP frequencies during visual stimulation (ON period). The signal correlation was calculated between the trial-averaged power at two different frequencies (f_1 and f_2) during visual stimulation (upper panel). Positive values indicate that the two frequencies have similar stimulus preferences, whereas a zero or negative value indicates that the two frequencies prefer un- or anti-correlated stimuli respectively. The noise correlation (i.e. trial-by-trail fluctuations around the mean) of the LFP power after discounting for their similarities in tuning, for each pair of frequencies (f_1 and f_2) during the presentation of visual stimulus. Positive values indicate that the mean fluctuations in the power of a frequency alters the fluctuations in other frequency. (c) Time courses of the different LFP frequency bands recorded in V1 in response to the visual stimulus.

4.4.4 Observations, Findings and Perspectives

To illustrate how the aforementioned methodology is used to assess the effects of neuromodulation on neurovascular coupling, we describe the effect of systemic and intracortical dopamine injection on the hemodynamic and neural responses (Zaldivar et al., 2014). DAergic neuromodulation is involved in many cognitive processes, including reward and addiction, learning and working memory (Dayan, 2012), motivation, attention and decision making (de Lafuente and Romo, 2011a), and it has also been shown to play a role in visual processing (Noudoost and Moore, 2011; Zaldivar et al., 2014). We mimicked DAergic neuromodulation by systemically applying L-DOPA and Carbidopa (LDC). The combination of these two agents is used for the treatment of Parkinson's disease, in which DA levels are depleted (Kwak et al., 2012). L-DOPA is used because it is the metabolic precursor of DA, which is metabolized to DA as soon as it crosses the blood-brain-barrier (BBB). Once in the brain it activates the DA-receptors (DARs). The role of Carbidopa is to enable the BBB-crossing of L-DOPA by inhibiting the breakdown of L-DOPA to DA in the periphery. This is important given that the activation of DARs in the periphery causes hypotension, which can alter brain perfusion and affect the interpretation of fMRI results (Black et al., 2003).

The experimental paradigm for the systemic DA injections is shown in Figure 4.4A. During and after the pharmacological manipulation with the LDC complex, the modulation in response to the visual stimulus decreased for the BOLD-responses while it increased for the CBF-responses (Figure 4.4B-C). Given that the combination of the two fMRI-based methods allows us to make predictions about the cerebral metabolic rate of oxygen consumption ($CMRO_2$), this dissociation of BOLD- and CBF responses is likely the consequence of increased energy metabolism induced by dopamine (Zaldivar et al., 2014). However, increases in BOLD signal are typically interpreted as increases in neural activity or increased processing, while decreases in BOLD signal are interpreted as decreases in neural activity. The combination of BOLD- and CBF-based fMRI already indicates that the effects of dopamine on neurovascular coupling are governed by multiple factors. To evaluate the effects of LDC on the neural activity

we computed the absolute power spectral density (PSD) in a one-second window for two bands: LFP-gamma and MUA (Figure 4.4C-E). These two bands are most informative about the visual stimulus (Goense and Logothetis, 2008; Logothetis et al., 2001). We calculated changes in the visually induced modulation (Figure 4.4D) and in the SNR (Figure 4.4E). Calculation of the SNR allowed us to assess whether DA influences the fidelity of the V1 responses (Sengupta et al., 2014) and was calculated by taking the power of the visually evoked responses (signal) and dividing it by the power during the OFF-periods (noise). Our results revealed that during and after the injection period the gamma and MUA amplitude of the visually-induced modulation increased, as did the SNR (Figure 4.4D-E).

Together these results show a clear method-dependent dissociation between the BOLD response and the neural activity induced by the systemic injection of DA. These findings highlight the different aspects of the hemodynamic response that are measured by the different CBF- and BOLD-based fMRI methods, and combining them can allow us to evaluate the effects of oxygen consumption and metabolism (Zaldivar et al., 2014). This can potentially be exploited to better understand fMRI signals or to disentangle the different neural events associated with different behavioral conditions.

Given the relative lack of DA receptors in V1, this raises the question whether DA influences visual processing in V1 directly or via a more remote influence. In patients with amblyopia, for instance, L-DOPA improves visual acuity while studies in rats and cats show that DA exerts an inhibitory influence on visually evoked responses in V1 (Gottberg et al., 1988; Reader, 1978). Thus, we locally applied DA in V1 at different concentrations and measured whether these manipulations exerted effects on gamma (Figure 4.5A, left panel) or MUA responses (Figure 4.5A, right panel), similar to those observed with systemic injections. Interestingly, our results revealed that visually induced modulations and SNR in the gamma and MUA frequency bands were unaffected by local DA application, independent of the concentration. This finding is in good agreement with the low density and sparse distribution of DARs in V1 (Lidow et al., 1991) and suggests that long-range interactions from higher-order regions, for instance frontal

regions (Noudoost and Moore, 2011) mediate the changes in neural activity shown in Figure 4.4.

To confirm that the methodology for delivering pharmacological agents in the cortex is adequate and that our protocol for local pharmacological application leads to measurable changes in neural activity, we applied GABA in V1 at different concentrations. Application of GABA decreased the power in both gamma and MUA bands (Figure 4.5B). These effects were concentration-dependent and in good agreement with previous studies (Kujala et al., 2015), indicating that the pressure operated system optimally delivers drugs at the desired concentration.

The multimodal methodology described here allows us to better understand the effects of neuromodulation on fMRI signals and neural metabolism. This was illustrated by showing the effect of systemic and intracortical application of dopamine on the neural and fMRI signals in macaque V1. Our findings suggest that under neuromodulation BOLD responses alone may not always faithfully reflect changes in neural activity (Zaldivar et al., 2014), and combining BOLD measurements with other methods such as electrophysiology, CBF and/or CBV can potentially help disentangle local sensory processing from neuromodulation.

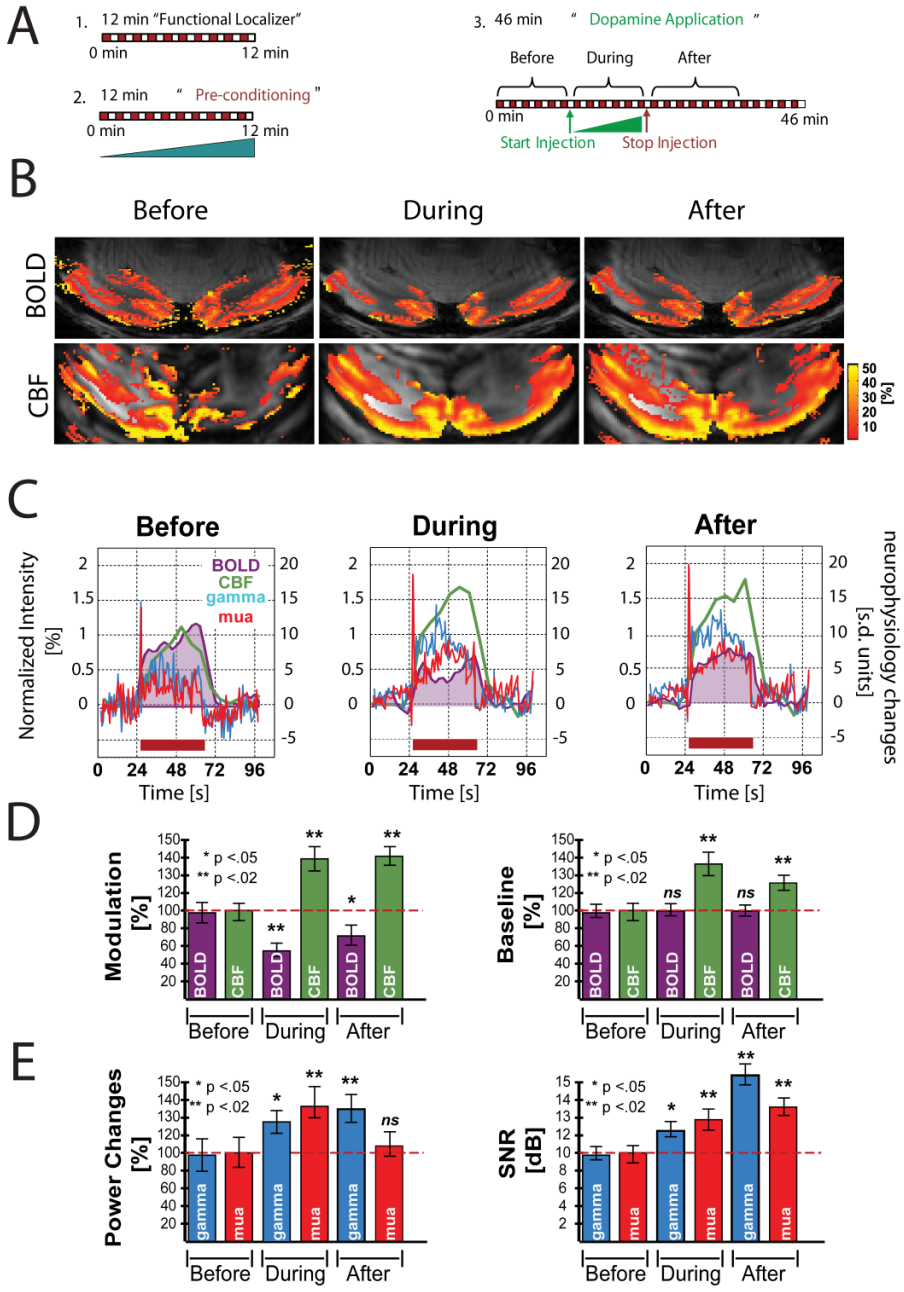

Figure 4.4 Effect of systemic Dopamine injection on neurovascular coupling.

(a) Experimental design and stimulus paradigm: 1) a functional localizer scan (12.8 min) was used to define voxels that respond to the visual stimulus; 2) Pre-conditioning (12.8 min) consisting of Carbidopa injection to prevent the breakdown of L-DOPA in the periphery; 3) a 46-min session during which L-DOPA+Carbidopa was injected. (b) fMRI activation maps for BOLD (acquired at 7T: eight-shot GE-EPI; FOV: 72x72 mm^2; resolution of 0.75x0.75 mm^2, 2 mm slice thickness; TE/TR 20/3000 ms; flip angle 90°) and CBF (acquired at 7T: FOV: 5.5x2.4 mm^2; 1x1 mm^2, 3 mm slice thickness ; TE/TR 9.5/4500 ms; TI 1400 ms; slab 6 mm). (c) Mean BOLD response (purple), CBF response (green), gamma LFP (blue) and MUA (red) responses during the different experimental periods. To asses statistical significance we computed the changes relative to the "Before" condition. Decreases in BOLD were observed during and after systemic LDC whereas CBF and neurophysiology (MUA and gamma) increased. (d) Mean percentage changes in visually induced modulation (left panel) and mean percentage baseline changes (right panel) of the BOLD (purple bars) and CBF (green bars) responses during each session. (e) Mean percentage changes in visually induced modulation (left panel) and SNR (right panel) for the gamma LFP band (blue bars) and the MUA (red bars). See Zaldivar et al. (Zaldivar et al., 2014) for details.

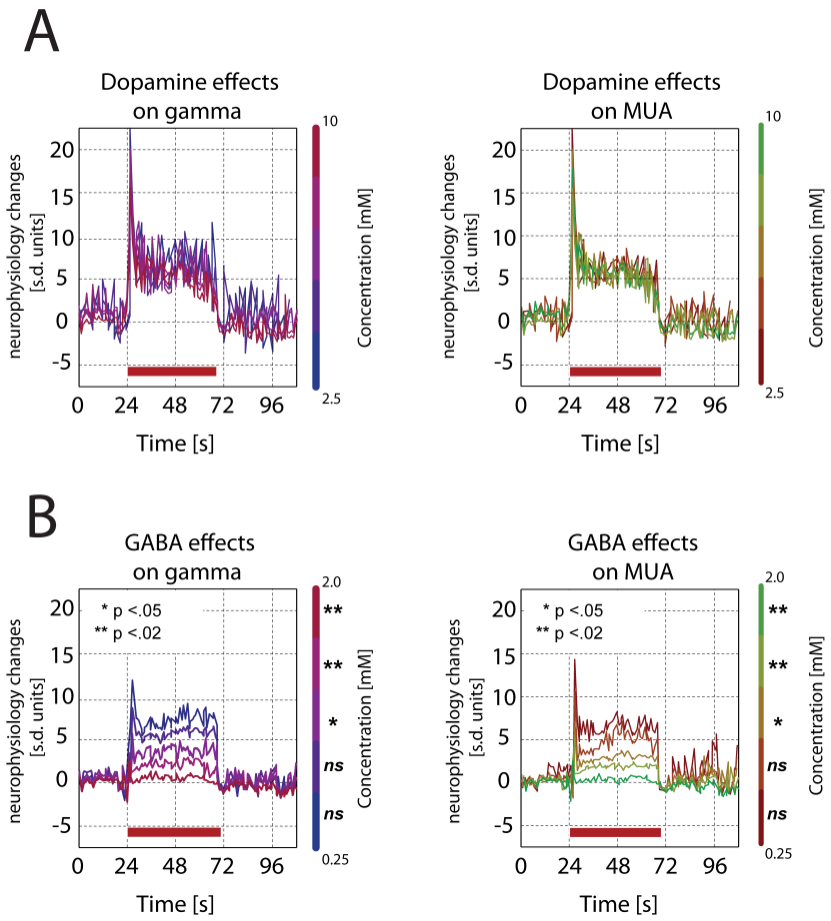

Figure 4.5 V1 neural responses following intracortical application of dopamine and GABA.

(a) Mean changes induced in gamma LFP (left panel) and MUA (right panel) after intracortical application of DA at different concentrations (2.5, 5, 7, 8 and 10 mM) are color-coded. No changes were observed at any concentration. (b) Mean changes induced in gamma LFP and MUA (left and right panel respectively) after intracortical application of GABA at different concentrations (0.25, 0.5, 1, 1.5 and 2 mM). Concentration-dependent effects were observed under influence of GABA. The effects of GABA at 0.25 and 0.5 mM did not significantly differ from the control condition. However, significant power changes were observed from concentrations of 1 to 2 mM.

4.5 Hints, tips and caveats

1) Monkeys should be fasted 8 hrs before any experimental procedure under anesthesia.
2) In some cases, to fully achieve sedation additional ketamine may be required. Under such circumstance, we recommended to inject an additional 10% of the initial dose.
3) Prior to the experiment, all infusion lines need to be flashed with saline. Similarly, all lines should be grounded by inserting Ag-wires in the lines.
4) Before endotracheal intubation, the tubus should be sprayed with lidocaine (1 or 2% solution). This suppresses airway-circulatory reflexes, which could lead to adverse

effects including hypertension, tachyarrhythmias, and increased intracranial pressure caused by endotracheal-tube induced coughing.

5) An important step for fMRI is accurate positioning of the monkey. The head should be supported by a skull fixation device. For this, we used earplugs made of acrylic that were inserted in ear canals.
6) The physiological state of the monkey should be continuously monitored and be kept stable within tight limits throughout animal preparation and experiment. Out-of-range values during preparation leads to a suboptimal physiological state and can potentially lower or abolish the BOLD signal for hours. Table 4.1 shows the normal physiological values from the macaques under anesthesia.
7) NMR coils should be tightly fixed throughout the experiment.
8) The image SNR (signal/SD of the noise in a single volume) in the region of interest should be higher than 50 but preferably >100. The noise level is best calculated by acquiring a volume with the transmitter turned off. Alternatively, an ROI outside the brain and free of artifacts can be used.
9) Before any incision, fur should be washed with detergent solution and alcohol to facilitate the shaving that should be performed up to 2 cm from the region of the surgical incision. This allows better fixating of the surgical field and reduces the risk of infection. Afterwards, antisepsis should be carried out with povidone and benzoin.
10) We performed craniotomies between 2 and 4 mm diameter, which provides sufficient space for the incision and dissection of the meninges. At the same time, the small craniotomy has neurosurgical advantages, which include improved postoperative recovery, decreased cerebral edema, and decreased risk of hemorrhage and infection. The meninges were dissected under the microscope. First, a linear incision of less than 1 mm was made parallel to the direction of the dura fibers, which facilitates CSF drainage and reduces the risk of meningeal infection. Both the arachnoid and pia mater can carefully be dissected layer-wise using dura dissectors. This minimally invasive procedure has been shown to be effective in achieving closure of the dura mater

avoiding the use of suturing techniques or any other product that could damage the brain surface.

11) A flattened Ag-wire was positioned under the skin and close to the entry point of the electrodes in the cortex. For laminar neurophysiology we recommend NeuroNexus probes because their long shank and thinness reduces neural tissue damage. The probes are reusable when properly cleaned and stored. Before the experiments electrode contacts were refreshed by discharging 100 µF capacitor through a 1 kOhm resistor in a normal saline bath. The capacitor was initially charged to +9 V, with a plus contact referring to the electrode and the minus contact to a platinum wire located in the saline bath (Murayama et al., 2010). After each experiment, the probes were cleaned by flashing them with H_2O_2, propranolol and distilled water, and were gently dried using a cotton tissue.
12) The final position of the laminar probes was based on three important points: a) the granular layer in sensory cortices (layer 4) usually has the highest spiking rate during spontaneous activity and this can be used for auditory guidance; b) the electrode contacts should all share the same ocular dominance and receptive field, otherwise electrode penetration is at an angle, in this case reposition the electrode; c) after detecting the receptive field present a brief block of the visual stimulus (2 s ON and 2 s OFF repeated 8 times) to perform CSD analysis on the LFP time series. We advise the reader to use the inverse CSD (iCSD) method given that it allows defining the geometrical distribution of the CSD sources. Unlike traditional CSD, the iCSD method can include any assumption or a priori knowledge about the neural sources, such as the lateral size of columnar activity and discontinuities or direction dependence of the extracellular conductivity; it can be applied to any geometrical arrangement of electrode contacts; and it can estimate the CSD at the positions of the electrode contacts at the boundary of the electrodes. For more detailed information about this method we reference the reader to (Einevoll et al., 2007). Furthermore, laminar LFP coherence can also be performed to determine the boundaries between infragranular

and granular layers. For more detailed information about this method we reference the reader to (Maier et al., 2010).

4.6 Conclusions

The findings from the aforementioned methodological approach support the notion that neuromodulators determine how neural circuits process information during a variety of cognitive states. It shows that neuromodulators can have strong effects on BOLD and CBF responses, and that combining fMRI with pharmacology and electrophysiology can aid understanding the effects of neuromodulation on neural circuits and neurovascular coupling. Ultimately, these combined approaches will contribute to the understanding of the BOLD response at a deeper level and more biological meaningful way. Through the use of these multimodal techniques, one can identify individual signatures of the different neuromodulators and help to differentiate their contributions from the cognitive and/or sensory evoked responses. The experiments shown here, where we describe how the DAergic neuromodulation affects the fMRI signals and neural activity, illustrate the usefulness of multimodal approaches. Furthermore, we found that systemically applied DA increased the neural and the CBF responses, while decreasing the BOLD response. Although we would expect similar effects in awake animals, it might be challenging to isolate pure dopamine effects from the multitude of cofounding behavioral effects (and associated neuromodulator concentration changes) inherent to the awake animal. Hence, using anesthetized NHPs offers the advantage of being able to focus on a single aspect of the neuromodulatory mechanism, and allowing assessment of the neurovascular coupling features that are affected under DA. Furthermore, the methodology and the findings presented here have important implications for diagnostic use of fMRI, since many psychiatric disorders are associated with alterations to neurmodulatory systems. Thus, if we are able to identify signatures of individual neuromodulators we may also be able to detect chemical imbalances associated with brain diseases.

5. Manuscript Nr. 3

Effects of lactate on early visual cortex of non-human primates investigated by pharmaco-MRI and neurochemical analysis

This chapter was published in 2012 in **Neuroimage 2012, 14;61(1): 98-105** by

Veronika von Pfoestl, Juan Li, Daniel Zaldivar, Jozien Goense, Xiaozhe Zhang, Nikos Logothetis, Alexander Rauch

doi: 10.1016/j.neuroimage.2012.02.082

5.1 INTRODUCTION

Functional magnetic resonance imaging (fMRI) is one of the most frequently used neuroimaging techniques for basic and clinical brain research in humans, and is used surprisingly less often for clinical diagnostics (Jezzard and Buxton, 2006). The systematic implementation of fMRI in diagnostics would evidently require extensive preliminary investigations of the degree to which fMRI may be sensitive to changes in the concentrations of various metabolites or neurotransmitters that are often induced by neurodegenerative disorders. For example, lactate exhibits a prominent role in brain metabolism (Fox and Raichle, 1986; Pellerin and Magistretti, 2004). Transient neuronal activation can apparently trigger glycolysis, resulting in elevated lactate levels (Hu and Wilson, 1997; Prichard et al., 1991). Lactate and pyruvate can then be funneled into the tricarboxylic acid cycle to provide neurons with energy (Pellerin and Magistretti, 2004). The apparent use of the glycolytic pathway was demonstrated by an increase in cerebral blood flow (CBF), and the metabolic rate of glucose which was accompanied by only a slight increase in the metabolic rate of oxygen (Fox and Raichle, 1986; Fox et al., 1988). The coupling of the CBF response to the NADH/NAD+ ratio which is in near equilibrium with the lactate/pyruvate ratio was then shown by (Mintun et al., 2004; Vlassenko et al., 2006). Given the importance of lactate in the context of physiological brain metabolism, changes in lactate levels are to be expected under pathological circumstances. For example, elevated lactate levels in the cerebrospinal fluid of patients suffering from Alzheimer disease (AD) have already been observed (Redjems-Bennani et al., 1998). Such changes reflect abnormalities in the regulation of cerebral metabolism and potentially neurovascular coupling, which in turn could have diverse effects on the fMRI signal (Iadecola, 2004; Reiman et al., 2001; Reiman et al., 2004, 2005). However, before one can investigate how these abnormalities affect the blood oxygen level-dependent (BOLD) signal, we should focus on the question of how the physiological formation of lactate contributes to the BOLD signal.

We set out to study fMRI responses in the monkey brain after moderate increases of systemic lactate concentration. To do so, we used direct systemic application to mimic the physiological formation of lactate and measured BOLD contrast in the early visual cortex of anesthetized macaques, while using microdialysis (venous catheter) to monitor blood lactate concentration. To best simulate the physiological formation of lactate in the brain, we increased plasma lactate levels moderately and continuously over the course of minutes, with overall increments in blood lactate concentration corresponding to light physical exercise (Freund et al., 1990). We present evidence that such moderate changes in blood lactate concentration are indeed detectable using BOLD fMRI, and are accompanied by moderate increases in neuronal activity. This finding suggests that, at least in principle, changes in lactate levels due to physiological, age-related, or pathological metabolic adaptations, such as those reported in neurodegenerative disorders, can be assessed using noninvasive BOLD fMRI methodology.

5.2 METHODS

For this study, we used ten anesthetized rhesus monkeys (Macaca mulatta, 7 male and 3 female, age range 4 to 11 years, weighing 4.6 to 12.5 kg). The experimental procedures were approved by the local authorities (Regierungspraesidium) and are in agreement with guidelines of the European Community for the care of laboratory animals. Procedures have previously been described in detail (Logothetis et al., 1999a). All vital parameters were monitored during anesthesia. After sedation of the animals using ketamine (15mg/kg), anesthesia was initiated with fentanyl (31 µg/kg), thiopental (5mg/kg), and succinylcholine chloride (3 mg/kg), and then the animals were intubated and ventilated. A Servo Ventilator 900C (Siemens, Germany) was used for ventilation, with respiration parameters adjusted to each animal's age and weight. Anesthesia was maintained using remifentanil (0.2–1 µg/kg/min) and mivacurium chloride (4–7 mg/kg/h). An isosmotic solution (Jonosteril, Fresenius Kabi, Germany) was infused at a rate of 10 ml/kg/h. During the entire experiment, each animal's body temperature was maintained between 38.5 °C and 39.5 °C, and SpO_2 was maintained above 95 %.

Every test subject received the same amount of lactate per minute adjusted to its individual body weight (0.04 mmol/kg/min) to ensure the comparability of any lactate-induced effects. The individual dose was adjusted by adapting lactate concentration and the infusion flow rate to each individual test subject. The lactate concentrations used ranged from 0.15 M to 0.6 M (pH, 7.2 – 7.35) and the flow rates ranged from 0.8 ml/min to 2.5 ml/min, resulting in an infusion time of 12 min to 20 min. Lactate solution was applied to the continuous infusion of Jonosteril electrolyte solution (10 ml/kg/h) to dilute lactate to the above-mentioned concentrations. This application protocol also ensured that any pH changes stayed within a small range. We explicitly did not use a bolus injection because we wanted to mimic a physiological lactate increase comparable to lactate increases during moderate physical exercise (Freund et al., 1990). We applied the same volume of phosphate-buffered-saline in five experimental sessions for control experiments (131.5 mM sodium chloride, 10 mM disodium hydrogen phosphate, 2.5 mM monosodium phosphate; pH = 7.2). Furthermore, we applied 0.04 mmol/kg/min of pyruvate in eight experimental sessions. Lactate was applied using a custom-made, pressure-operated pump that used high-precision flow meters to control flow and volume (Sensirion, Switzerland), in combination with Matlab functions to provide an online readout (The MathWorks, Natick, MA, USA). All chemicals were purchased from Sigma-Aldrich (Schnelldorf, Germany). MR images were acquired using a vertical 4.7 T Bruker BioSpec scanner with an inner bore diameter of 40 cm and a 7T Bruker BioSpec scanner with an inner bore diameter of 60 cm (Bruker BioSpin, Ettlingen, Germany). We performed three experiments at 4.7T (lactate), 40 experiments at 7T (27 lactate, five saline, eight pyruvate) and five cerebral blood flow (CBF) experiments at 7T (lactate). At 4.7T, we used a custom-built phased array (Goense et al., 2010) in combination with a linear transmit-coil and eight-shot gradient echo planar imaging (EPI) with a field of view (FOV)=64×48 mm, matrix=128×96, 7 slices (slice thickness=1 mm), echo time/repetition time (TE/TR)=20/500 ms, and flip angle (FA)=40°. At 7T, we used a custom-made quadrature volume coil (Augath et al., in preparation) and an eight-shot gradient echo EPI, FOV= 96×96 mm, matrix= 128 × 128, 13 slices (slice thickness=2 mm), TE/TR=20/750, and FA= 47.6°. To further improve efficiency at

7T, we also used a single-shot gradient EPI, with FOV= 72 × 72 mm, matrix= 96 × 96, 11 slices (slice thickness= 2 mm), TE/TR= 20/3000, and FA= 90°. For the six functional CBF measurements at 7T, we used a volume coil to transmit in combination with a custom-built, 4-channel phased array (Goense et al., 2010). Perfusion imaging was performed using flow-sensitive alternating inversion recovery (FAIR; (Kim, 1995)) for arterial spin labeling, with alternating slab-selective and nonselective inversion pulses (13–15 ms hyperbolic secant pulse). Inversion time was 1300 ms, slab 6 mm, FOV= 64 × 48 mm, resolution= 1 × 1 mm, slice thickness= 3 mm, receiver BW= 150 kHz, a shortest possible TE= 6 to 7 ms, TR= 3000 ms, and FA= 90°.

Visual stimuli were presented using a fiber optic system (Avotec, Silent Vision, USA). To adjust the plane of focus, contact lenses (hard PMMA lenses, Wöhlk, Kiel, Germany) were inserted to the monkey's eyes. The stimulus was presented in a block design that showed a full field rotating polar checkerboard for 48 s (ON period), followed by an isoluminant blank screen for the same duration (OFF period). The direction of rotation was reversed every 8 s to avoid adaptation.

We used low-flow microdialysis for systemic lactate sampling in 8 experiments. Lactate concentrations were analyzed using hydrophilic liquid interaction chromatography coupled to electro-spray ionization mass spectrometry (Li et al., 2011). We sampled from a superficial large leg vein using a microdialysis catheter CMA 64, 20-mm PAES membrane, 0.6 mm o.d., 20 kDa cut-off (CMA Microdialysis AB, Sweden). We allowed the semi-permeable membrane to stabilize for 1 h, then sampling was initiated with a flow rate of 2 µl/min. We used a refrigerated fraction collector CMA 740 (CMA Microdialysis AB, Sweden) in which the samples were stored at 6 °C. The temporal resolution of the sampling process was 3 min. After the experiment, the samples were diluted with a solution of 80% acetonitrile containing 0.1% formic acid, and then centrifuged for 3 min (4000 rpm at 4 °C). 3-^{13}C-Lactate (^{13}C-Lac) was used as internal standard for lactate. The mass spectrometer was operated in multiple-reaction monitoring (MRM) mode for quantitative analysis. Lactate and ^{13}C-Lac were

monitored based on transfers of *m/z* 89→89, and *m/z* 90→90, respectively. The detection limit of lactate was 0.9 pmol (for a 6-µl in vivo sample).

We applied lactate and pyruvate to two monkeys in nine electrophysiology experiments. These two monkeys had miniaturized chambers implanted over V1 and were used for invasive recordings. We used NeuroNexus probes (NeuroNexus Technologies, Ann Arbor, USA) of 150 µm thickness and 3 mm long shank with 16 electrode sites with 50 µm site spacing and 413 µm2 electrode sites. The impedance of the electrodes was in the range of 700 kΩ. The preamplifiers for the electrophysiological recordings were custom-made. The signals were amplified and filtered into a band of 1–8 kHz (Alpha-Omega Engineering, Nazareth, Israel) and then digitized at 20.833 kHz with 16-bit resolution (National Instruments, Austin, TX), ensuring enough resolution for both local field and spiking activities. The analog-to-digital converter was linked directly to a PC running a real-time QNX operating system, where the signal was stored.

5.2.1 Data Analysis

Our region of interest (ROI) consisted of the early visual cortex (V1 and V2). A short scan (12 min) preceding the injection scan was used to identify voxels within the ROI that showed reliable visually-induced modulation. We used a boxcar convolved with a hemodynamic response function (gamma variate function) as a regressor to detect visually-induced modulation. The correlation coefficient of every voxel with this regressor was calculated. Voxels demonstrating robust visually-induced modulation ($P < 0.02$) were considered for further analysis. The voxels identified by the short preceding scan were then monitored during the long (40 min) injection scan and studied for lactate-induced effects. This approach allowed us to investigate lactate-induced effects without making any *a priori* assumptions regarding the potentially induced BOLD response. The same approach was used for the CBF measurements, for which voxels were selected according their visually-induced modulation during the short scan preceding the injection scan. The time course of CBF changes was obtained with linear surround subtraction (Wong et al., 1997). We acquired BOLD fMRI data

in 35 sessions during lactate injections. Five of these scans were discarded: two because of a defect in the infusion pump, two because of artifacts caused by a shift in the monkey's position, and one because of a lack of visually-induced modulation. Additionally, one of the six functional CBF measurements was discarded because of a positioning artifact. The remaining 30 BOLD fMRI and five CBF voxel time courses were linearly detrended and then normalized. The single traces were normalized so that the mean amplitude of the stimulus-induced modulation before lactate injection corresponded to one. Every trace was tested for lactate-induced changes in the visually-induced modulation and the baseline. Visually-induced modulation was calculated by subtracting the OFF periods from the ON periods in the averaged voxel time course of our ROI. The baseline shifts in the BOLD signal were analyzed by calculating the mean values of the ON and OFF periods. The threshold for changes in modulation and baseline was set at $P > 0.05$. This threshold had to be crossed for at least 6.4 min (the duration of the pre-injection period). We determined four variables that defined the effect: the maximal percentage change, the start of the change (when modulation or baseline crossed the threshold), the time of the maximal effect, and the end of the effect (the last point above the threshold). For statistical analysis, a time window of 6.4 min around the maximum change was selected (range, 19.2 – 25.6 min) and the modulation and respective baseline during this window was compared with the pre-injection period (range, 0 – 6.4 min) with a two-tailed *t*-test (alpha = 0.05). Additionally, two other time windows before (range, 6.5 – 12.8 min) and after (range, 28.9 – 35.3 min) the maximum change were defined for further comparison. The plasma lactate levels were also compared using two-tailed *t*-tests (alpha = 0.05) during these different time windows. The time windows were adapted to match even numbers of scanned volumes, which explains the odd time stamps of the selected windows. Analysis was performed using custom written code based on Matlab.

To analyze the electrophysiological data, we used a one-second window to calculate the power spectral density of two bands: 24–90 Hz LfpH (high local field potential) and 800–3000 Hz MUA (multiunit activity, (Rauch et al., 2008c)). We did not consider layer-specific effects,

and averaged the obtained PSD trace over all 16 channels. Next, we calculated changes in modulation and baseline. Visually-induced modulation was calculated by subtracting the OFF periods from the ON periods in the averaged PSD trace. The baseline shifts were analyzed by calculating the mean values of the ON and OFF periods. From these traces, we extracted the maximal percentage change, the start of the change (when modulation or baseline crossed the threshold), the time of the maximal effect, and the end of the effect (the final point above the threshold). In addition, we performed two-tailed t-tests using the same time windows as were used for the BOLD analysis in the single experiments (averaged over 16 channels), as well as in the average of the six experiments.

5.3 RESULTS

We applied lactate systemically in eight monkeys, with a total of 30 fMRI scans. We used systemic lactate concentrations comparable to those produced by moderate physical exercise (Freund et al., 1990). The concentrations were adapted such that all monkeys received an identical amount of lactate per minute according to individual body weight (see Methods).

Figure 5.1 depicts the effects on the BOLD signal after a lactate infusion, and the corresponding plasma lactate concentrations for a single experiment (J08, an 8-year-old, 10.5-kg, male monkey). Figure 5.1A–C show the distribution of the visually-activated voxels in the early visual cortex (V1 and V2), while Figure 5.1D shows the averaged BOLD time course across the depicted voxels (gray) and the time course of the plasma lactate levels (green). We depict the distribution of the selected voxels for the three central slices in V1 and V2 with an in-plane resolution of 0.75 × 0.75 mm and 2-mm inter-slice distance; the depicted voxels are color-coded according to their correlation with the visual stimulation paradigm. Lactate application started after the fourth ON – OFF period (6.4 min) and lasted 14 min (gray shading). First, a reliable, visually-induced modulation was observed throughout the entire experimental period, and was not significantly affected by lactate. Second, we induced a positive baseline shift in the BOLD response after the systemic application of lactate. The positive shift in the BOLD response was tightly correlated with the monitored increase of

plasma lactate, which reached its peak at 24 min of total scan time. Plasma lactate levels reached 3.4 mM (which is comparable to serum lactate levels observed during moderate physical exercise; (Freund et al., 1990), starting from levels slightly above 2 mM before infusion.

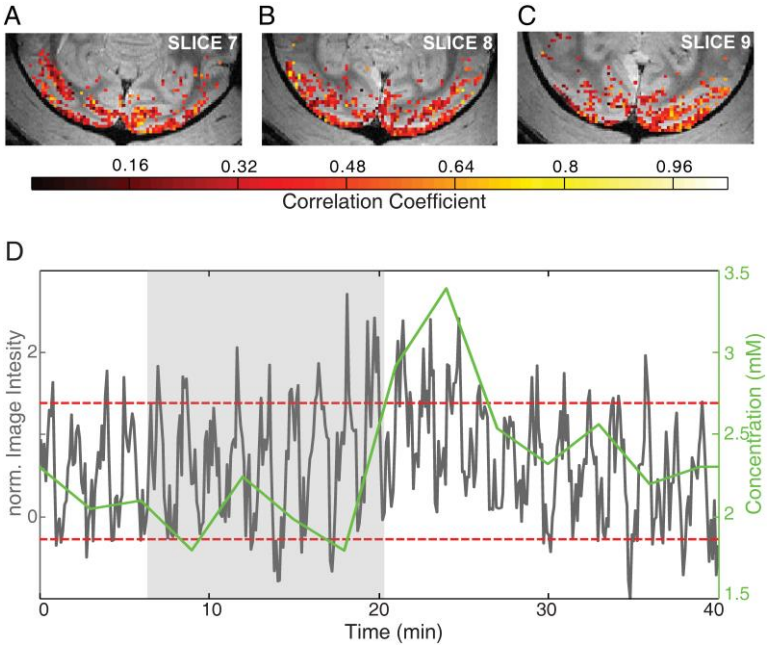

Figure 5.1 Example experiment functional magnetic resonance imaging (fMRI) and systemic lactate application: Panels A–C depict the distribution of voxels that are significantly correlated with the stimulus (eight-shot GE-EPI overlaid on an anatomical scan (FLASH), acquired at 7 T, slices 7 through 9, 0.75×0.75 mm resolution, and 2-mm inter-slice distance). The correlation coefficient with the regressor is color-coded. The gray trace in panel D depicts the mean time course of the above voxels during the scan with lactate infusion. The infusion began after the fourth stimulus repetition and lasted for 14 min (gray shading). The red dashed lines delineate the amplitude of stimulus-induced modulation during the pre-injection period. Image intensity has been normalized so that the modulation of the pre-injection period corresponds to one. The green trace shows the plasma lactate levels of the same monkey in a separate experiment using the same infusion protocol as was used for the fMRI experiment.

To test for the consistency of the observed effects on BOLD response and plasma lactate levels, we performed a group analysis of all 30 experiments. Our population of test animals consisted of 1 female and 7 male monkeys (J08, E04, I02, I08, A09, C06, K07, J07) with an age range from 4 to 11 years, weighing between 4.6 and 12.5 kg, provided with identical housing and comparable food supply. In Figure 5.2, the averaged time courses of the BOLD response across all 30 experiments are depicted with the onset of systemic lactate application after the fourth ON – OFF period. The time windows were selected to match even numbers of

acquired volumes and are of identical size. During the pre-infusion period (blue) we observed a reliable, visually-induced modulation of 2.8 ± 1.1%. As in the single experiment depicted in Figure 5.1, we observed a positive baseline shift in BOLD signal that peaked within a time window of 19.2 to 25.6 min (red). The positive baseline shift resulted in an increase of 0.6 ± 0.2% of the mean BOLD signal compared with pre-infusion (blue), which corresponds to 22.1 ± 7.4% of the visually-induced modulation (2.8 ± 1.1% of the signal). This baseline shift was significant in 26 of the 30 experiments ($P < 0.05$); no reliable effect was observed in the remaining four experiments. The lactate-induced BOLD response lasted up to 27.8 min of the total scan time, and then recovered so that no changes were detectable in the time window from 28.9 to 35.3 min (gray). In the time window just after the start of lactate application (from 6.5 to 12.8 min of total scan time; green), no apparent changes in BOLD response were observed, and plasma lactate remained at pre-infusion levels. This finding is most likely due to our slow infusion protocol and the capacity of erythrocytes to buffer lactate to a certain degree, mitigating sudden increases (Smith et al., 1997).

In Figure 5.2B, we compared the mean plasma lactate levels across eight experiments (blue trace) with the mean baseline shift over all 30 experiments (red trace). Four male monkeys (J08, C06, K07, J07; age range 6 to 9 years; weight range 5 to 11.5 kg) were used to monitor plasma lactate levels. The induced effects were compared for the identical time window as is depicted in Figure 5.2A. We observed significant plasma lactate increases in all eight experiments ($P < 0.05$). In the red time window (19.2 to 25.6 min), plasma lactate levels reached a mean maximum of 2.5 ± 0.9 mM, starting from a mean baseline concentration of 1.1 ± 0.5 mM (blue time window, 6.5 to 12.8 min). Maximum plasma lactate was reached at 22.9 ± 4.8 min of total scan time. Compared with lactate levels, BOLD response reached its maximum after 23.4 ± 8 min of total scan time, which we consider a very reliable match considering the different temporal resolutions of the fMRI and the sampling method. Reliability is also indicated by the high correlation between the plasma lactate time course and the BOLD

response at an individual level (coefficients of correlation: 0.60 for J08, 0.52 for C06, 0.69 for K07, and 0.85 for J07).

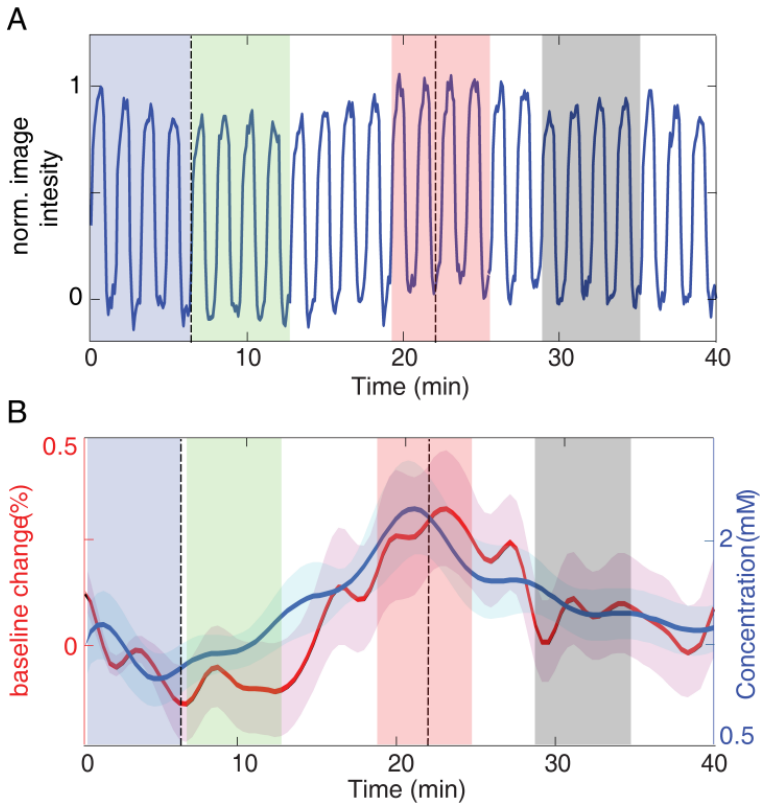

Figure 5.2. A) Mean time course over 30 functional magnetic resonance imaging (fMRI) sessions; the lactate infusion started after the fourth stimulus repetition (6.4 min) and lasted for a mean duration of 18 min (black dashed lines). Shading indicates the time windows used for statistical analysis: blue, before injection (0–6.4 min); green, during injection (6.5–12.8 min); red, shortly after injection (19.2–25.6 min); and gray, recovery phase (27.2–33.6 min). (B) The mean plasma lactate concentration over 8 experiments (blue) and the mean baseline change over 30 fMRI experiments (blood oxygen level-dependent signal, red); lactate injection started after 6.4 min and lasted for a mean duration of 18 min.

To estimate the distribution of the observed effects on BOLD response within the studied population, we extracted the timing and the peak of the lactate-induced baseline shift, and compared them to each other in a scatter plot (Figure 5.3A). The amplitude of the BOLD response was extracted as a percentage of the overall visually-induced modulation (see above). In every test subject, lactate induced a positive baseline shift in the BOLD signal, although the amplitude varied from 16 % in the weakest responder to 39 % in the strongest responder. The onset of the BOLD baseline increases began between 7.6 min (onset effect, early responder) and 19.8 min (onset effect, late responder), with a mean onset of 16.9 ± 7.5 min. The actual BOLD response lasted for a period of 5.6 to 27.6 min (short versus long pharmacokinetics), with a mean duration of 11.0 ± 8.5 min. Differences in the lactate-induced BOLD response are also reflected in the actual plasma lactate levels (Figure 5.3B). We extracted the individual lactate levels before and after infusion and the timing of the peak

concentration. The lactate levels ranged from 0.3 to 2.1 mM before infusion and reached maximum levels between 2.0 and 4.0 mM. The onset of plasma lactate increases began between 10.1 (early responder) and 20.6 min (late responder), with a mean onset of 14.1 ± 4.5 min. Lactate remained elevated for a duration of 12 to 21min (short versus long pharmacokinetics), with a mean duration of 18.4 ± 7.4 min. Lactate infusion is indicated by gray shading, and onset timings are provided in relation to total scan time (Figure 5.3A, B). Taken together, and also taking into account the variability within the studied population and irrespective of differences in temporal resolution between the methods used, the BOLD response and the actual plasma lactate levels correlated to a high degree. The variability observed in the timing and amplitude of the lactate-induced effects reflects known differences in lactate turnover that depend on the training level and metabolic state of the test subject (Oyono-Enguelle et al., 1990).

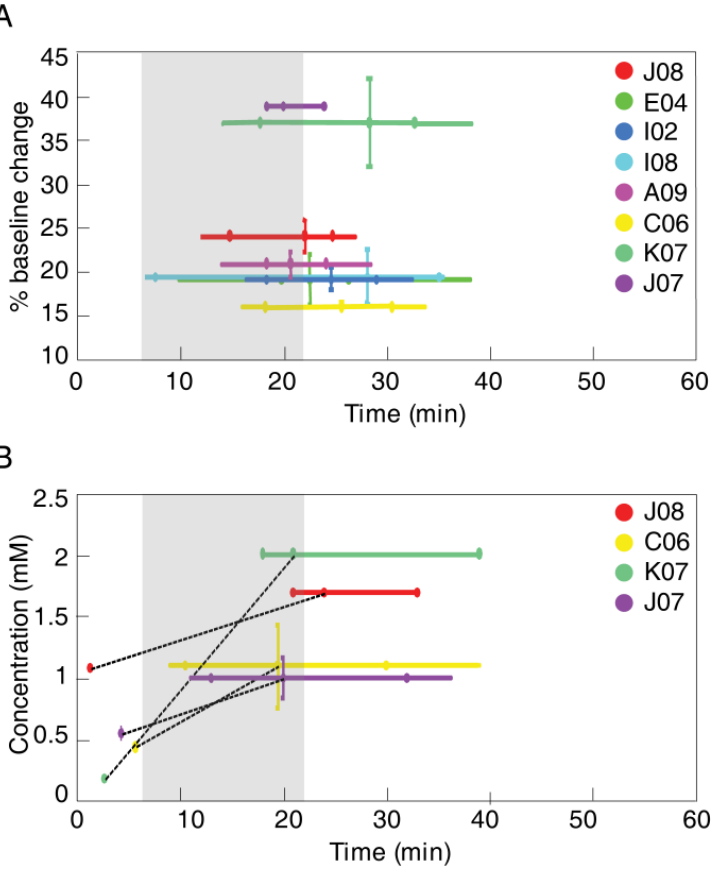

Figure 5.3 Inter-individual differences in blood oxygen level-dependent functional magnetic resonance imaging (BOLD-fMRI) (A) and plasma lactate concentration (B). For both datasets, we determined four variables that defined the effect: the maximal change, the start of the change (when baseline or concentration crossed the threshold of P=0.05), the time of the maximal effect, and the end of the effect (the final point above the threshold). These variables were averaged for each subject and plotted here. Panel A depicts the percentage BOLD baseline change and respective standard deviation for each subject; the percentage value is referenced to the stimulus-induced modulation before the injection (100%). Panel B depicts plasma lactate concentration before injection, and maximal concentration reached after lactate injection. For both panels, timing and standard deviation of the effect are plotted on the X-axis.

We were also interested in whether we could observe reliable vascular effects induced by lactate application, because it has already been shown that lactate has distinct vasodilatory effects (Reiman et al., 1989). However, these vascular effects were triggered by relatively high doses of lactate. Therefore, we only expected subtle changes in CBF using our infusion protocol, which is comparable to a protocol used by Ido et al. that produced CBF changes only in the range of 4 % (Ido et al., 2004). Figure 5.4 depicts the mean of five CBF measurements after lactate infusion. We observed reliable visually-induced modulation in the CBF recordings in the range of 19 ± 7 % (Zappe et al., 2008a), but did not detect any significant baseline shifts comparable to the changes in the BOLD recordings.

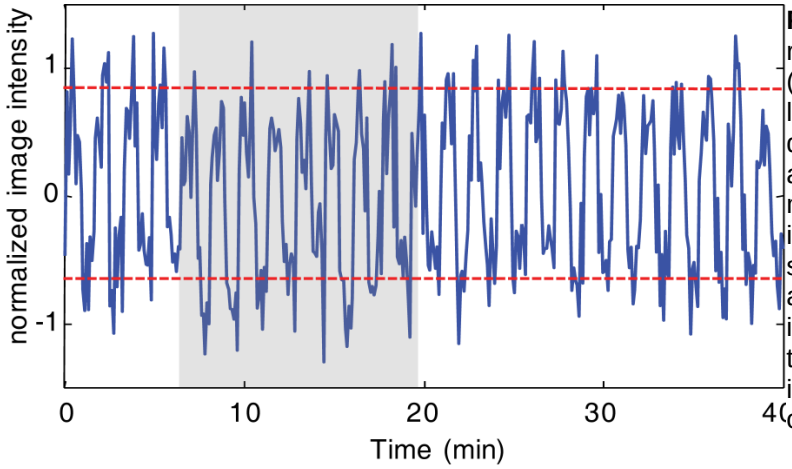

Figure 5.4 Mean time course of regional cerebral blood flow (CBF) measurements during lactate infusion (N=5). The red dashed lines delineate the amplitude of stimulus induced modulation during the pre-injection period. Gray shading symbolizes the time of lactate application (13.5 min). Image intensity has been normalized so that the modulation of the pre-injection period corresponds to one.

To investigate the neuronal activity underlying the BOLD effect, we performed six electrophysiological recordings in two monkeys. During the lactate infusion, we observed an effect in the LfpH band (24 – 90 Hz, Figure 5.5). Both baseline and stimulus-induced modulation increased significantly in five of six experiments. Lactate infusion induced a mean baseline increase of 23.0 ± 1.2% and a mean modulation increase of 76.0 ± 20%; this effect lasted from 12.5 ± 1.5 min to 32.0 ± 4.3 min. No significant effect was observed in the MUA (400–3000 Hz). We also tested the effect of pyruvate on the BOLD signal and electrophysiology, because of the dependence of lactate and pyruvate mediated by lactate dehydrogenase (Williamson et al., 1967). Here we report the electrophysiology results, the

BOLD effect is described later. The three pyruvate injections exhibited a comparable effect in the LfpH band (Figure 5.6) with a mean baseline increase of 31.0 ± 7.3%. This effect lasted from 8.5 ± 2.1 min to the end of the recording. In two cases, we also observed a significant increase in modulation. Also the pyruvate injections did not show a significant effect in the MUA.

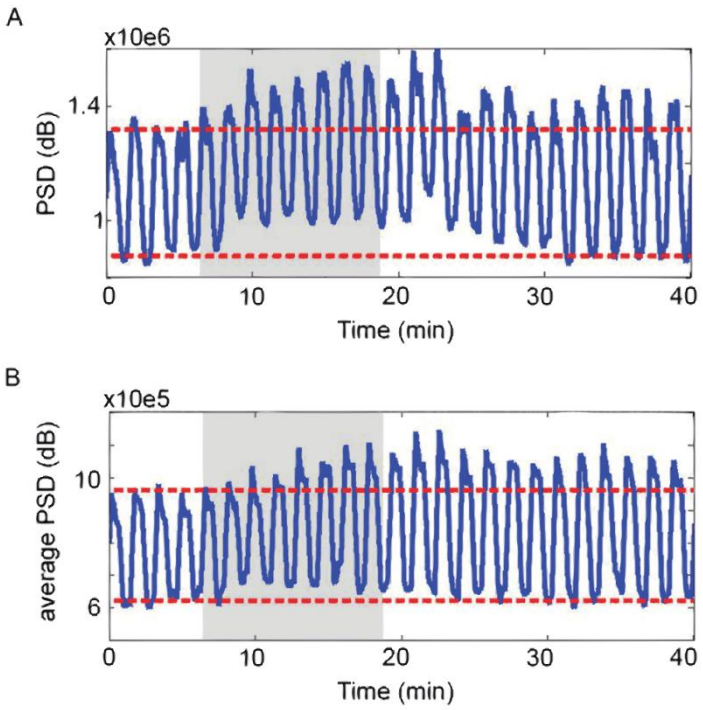

Figure 5.5 The power spectrum density of the LfpH band (24–90 Hz). Lactate injection started at 6.4 min and lasted for 12min (gray shading). The average over the 16 channels in one representative experiment (A), and the average over all six experiments (B) are shown. The red dashed lines depict the amplitude of stimulus induced modulation during the pre-injection period.

As control experiments, we infused buffered saline solution to ensure that lactate-induced BOLD responses were primarily caused by lactate itself. We also wanted to test whether the applied volumes (although relatively small) triggered any cardiovascular responses that interfered with the BOLD signal. We used buffered saline (pH= 7.2) for five applications in three monkeys (Figure 5.8). No significant changes were observed in the BOLD signal after saline infusion using the same protocol as was used for lactate infusion ($P > 0.05$). During pyruvate injection (Figure 5.7), we observed a mean baseline increase of 0.9 ± 0.5%, which corresponds to 98.9 ± 63.3 % of the stimulus-induced modulation. This effect exhibited earlier onset than the lactate effect, lasting from 9.2 ± 2.3 min to 27.5 ± 5.9 min, with the maximal effect at 17.1 ± 3.1 min.

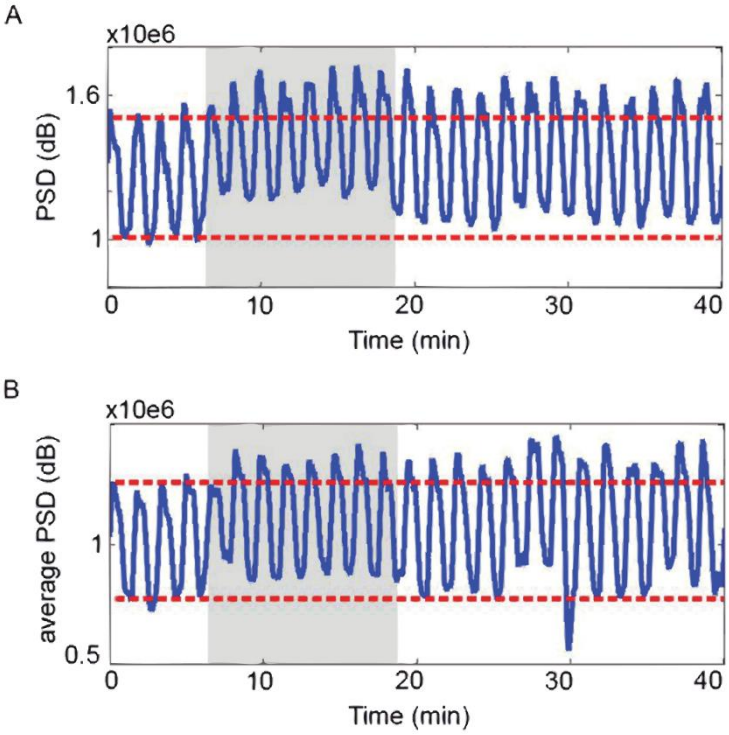

Figure 5.6 The power spectrum density of the LfpH band (24–90 Hz). Pyruvate injection started at 6.4 min and lasted for 12min (gray shading). The average over the 16 channels in one representative experiment (A), and the average over all six experiments (B) are shown. The red dashed lines depict the amplitude of stimulus-induced modulation during the pre-injection period.

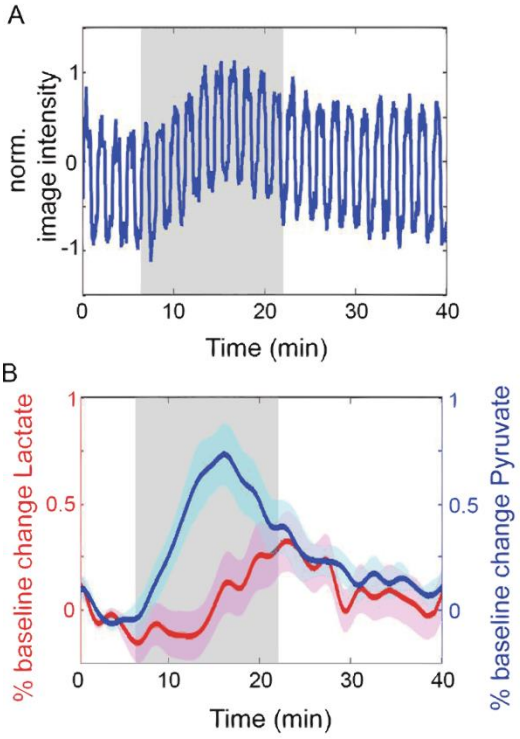

Figure 5.7 Mean time course over eight functional magnetic resonance imaging (fMRI) sessions. The pyruvate infusion started after the fourth stimulus repetition (6.4 min) and lasted for a mean duration of 18 min (gray shading). (B) The mean baseline change over 30 fMRI experiments with lactate injection (red), and the mean baseline change over eight fMRI experiments with pyruvate injection (blue).

5.4 DISCUSSION

Our study results demonstrate that lactate induces a reliably detectable BOLD response, with even low lactate doses producing plasma concentrations comparable to those brought about by moderate muscular exercise (Freund et al., 1990). We measured the BOLD response after a pharmacological challenge by lactate, which we induced by systemic application in eight anesthetized monkeys. We primarily observed an increase in the BOLD baseline in visually stimulated early visual cortex, with little effect on the visually-induced modulation. The BOLD baseline change correlated directly with the increase in systemic lactate levels. Moreover, even in this rather heterogeneous group of test subjects, we could reliably detect lactate-induced changes in the BOLD signal (this is an important finding because the differences in physiological respectively metabolic conditions did not interfere with our measurements). Especially if clinical applications are envisioned in the future, substantial jitter in the BOLD response must be anticipated precisely because of the above-mentioned physiological differences between individuals. Above all, lactate metabolism depends critically on the training condition and general physiology of human subjects (Oyono-Enguelle et al., 1990), and this should also hold true for non-human primates that show an overlap with human physiology to a very high degree (Voytko and Tinkler, 2004). Indeed, such metabolic differences are reflected in the different onsets and dynamics observed after lactate application. However, they were not substantial enough to jeopardize our use of subtle lactate concentrations, and at an individual level we have shown a high degree of consistency between BOLD response and plasma lactate levels.

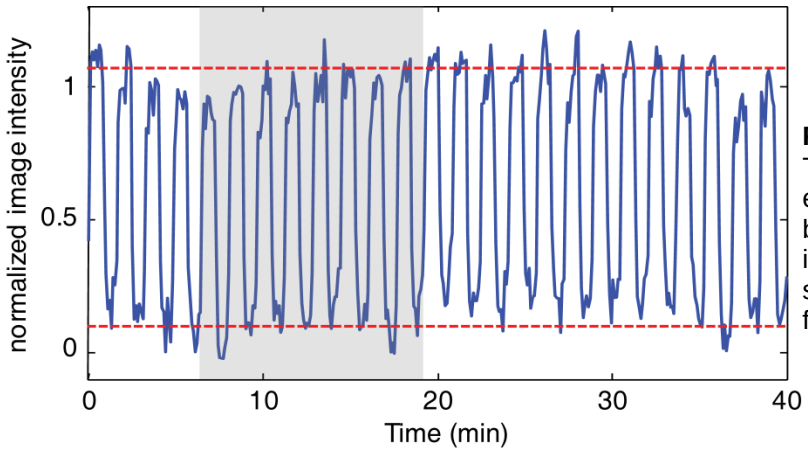

Figure 5.8 Control experiment: The mean time course of five experiments with phosphate buffered saline injection. Saline infusion began after the fourth stimulus repetition and lasted for 12 min (gray shading).

The observed increase in the BOLD response after lactate application most likely originates from a combination of neuronal and vascular effects. Therefore, we also performed electrophysiological recordings in two monkeys after lactate application, and observed an increase of neuronal activity in the LfpH band. From previous studies conducted in our lab, we had already shown that LfpH neuronal activity is a reliable driver of the BOLD signal (Logothetis et al., 2001; Rauch et al., 2008c). Although lactate-induced increases in neuronal activity have been described in rat hippocampus, the reason for these increases is yet not fully understood (Bergold et al., 2009). Furthermore, lactate is known to increase CBF by inducing the production of nitric oxide and other vasodilatory molecules (Gordon et al., 2008; Ido et al., 2004). However these CBF changes apparently depend to a certain degree on lactate dose and application modality (bolus vs. slow infusion). For example, a bolus injection that increases systemic lactate to 9.8 ± 2.4 mM has induced a change in CBF in the range of 38 – 53 % in human visual cortex (Mintun et al., 2004). This finding contrasts with the results of a subtle and continuous application of lactate (2 mmol/kg) in rats (reaching plasma concentrations of 3.5 ± 0.4 mM), which did not yield CBF changes greater than 4 % (Ido et al., 2004). We verified the CBF changes induced by lactate application (low-dose and continuous infusion) using FAIR recordings, which did not demonstrate reliable CBF changes. We must consider two possible reasons for the lack of CBF changes. The first reason is most likely the very low changes in CBF induced by our lactate application protocol, which would agree with the findings in rats described by (Ido et al., 2004). The second reason is related to the detection

threshold of the FAIR recordings, which is just within the range of the expected CBF changes (namely, approximately 5 %). Consequently, the detection threshold was better for the BOLD response (namely, 0.5 %) than for the FAIR recordings. Therefore the lactate challenge described herein (flow 0.04 mmol/kg/min) most likely does not trigger changes in CBF appreciably greater than 5 %. It follows that although we are reliably able to observe lactate-induced BOLD responses, a CBF increase in the range of 5 % cannot be excluded, but is not detectable to a statistically significant extent in the same animals. It has been hypothesized that the increase of CBF observed in the work of (Mintun et al., 2004) depends on NADH/NAD+ ratio which is in near equilibrium with the lactate/pyruvate ratio. Elevated NADH and lactate levels partially trigger the CBF increase, which in turn can be counterbalanced by increasing the levels of pyruvate and NAD+, respectively (Vlassenko et al., 2006). However, our systemic application of pyruvate (using a dosage identical to the dosage of lactate) did exhibit effects in BOLD and neuronal responses comparable to lactate. Apparently, in this low physiological range, lactate and pyruvate may serve as equivalent substrates to induce the BOLD and neuronal effects that we have observed. The faster BOLD response to pyruvate might be explained by pyruvate's direct access to the tricarboxylic acid cycle, while lactate must still be transformed into pyruvate.

The main focus of this study was to test the lower detection boundaries of lactate-induced BOLD responses to investigate the impact of the physiological formation of lactate on the BOLD signal. If the physiological formation of lactate has an impact on the BOLD signal (which we mimic using our slow infusion protocol), then a potential diagnostic application could be developed. For example, the changes in lactate metabolism in neurodegenerative disorders like AD are gradual and develop over a long period of time. Therefore, the lack of BOLD responsiveness to a lactate challenge within the physiological range of lactate formation might be a potential hallmark of AD. The reduced responsiveness of CBF to sensory stimulation has already been described in AD patients; this reduced CBF responsiveness also correlated with the severity of AD progression (Mentis et al., 1998). In agreement with these findings, Kalman

et al. did not observe a single-photon emission computed tomography response after a lactate challenge (2.5 mmol/kg) in AD patients induced plasma lactate levels of 5.5 ± 1.226 mM (Kalman et al., 2005). Reduced responsiveness to physiological lactate formation in AD is in agreement with a recent review highlighting the close resemblance of AD to a vascular disorder in which delayed and weakened responses to increased metabolic demand might be a preclinical feature (Iadecola, 2004).

Taken together, we demonstrate that physiological lactate formation can contribute to the BOLD signal, and therefore can be reliably traced by fMRI. This finding might be exploited for neurodegenerative disorders like AD in which lactate metabolism is disturbed (Redjems-Bennani et al., 1998). Patients at risk of (Richard and Amouyel, 2001) or in the early stages of AD might potentially exhibit a change of the BOLD signal in response to physiological lactate formation. Future clinical studies are needed to demonstrate whether our approach can deliver such diagnostics.

6. Manuscript Nr. 4

Dopamine-induced dissociation of BOLD and neural activity in macaque visual cortex

This chapter was published in 2014 in **Cur Bio. 2014, 1;24(23): 2805-11** by

Daniel Zaldivar, Alexander Rauch, Kevin Whittingstall,
Nikos Logothetis & Jozien Goense.

doi: 10.1016/j.cub.2014.10.006

6.1 INTRODUCTION

Neuromodulators determine how neural circuits process information during cognitive states such as wakefulness, attention, learning and memory (Dayan, 2012). fMRI can provide insight into their function and dynamics, but their exact effect on BOLD-responses remains unclear (Logothetis, 2008; Rauch et al., 2008c; Sirotin and Das, 2009), limiting our ability to interpret the effects of changes in behavioral state using fMRI. Here, we investigated the effects of dopamine (DA) injections on neural- and haemodynamic signals in macaque V1 using fMRI (7T) and intracortical electrophysiology. Aside from dopamine's involvement in diseases such as Parkinson's and schizophrenia, it also plays a role in visual perception (Arsenault et al., 2013; Noudoost and Moore, 2011; Rogers, 2003; Shuler and Bear, 2006). We mimicked DAergic neuromodulation by systemic injection of L-DOPA+Carbidopa (LDC) or by local application of DA in V1 and found that systemic application of LDC increased the signal-to-noise ratio (SNR) and amplitude of the visually evoked neural responses in V1. However, visually induced BOLD-responses decreased, while cerebral blood flow (CBF)-responses increased. This dissociation of BOLD and CBF suggests that dopamine increases energy metabolism by a disproportionate amount relative to the CBF-response, causing the reduced BOLD-response. Local application of DA in V1 had no effect on neural activity, suggesting the dopaminergic effects are mediated by long-range interactions. The combination of BOLD- and CBF-based fMRI can provide a signature of dopaminergic neuromodulation, indicating the application of multimodal methods can improve our ability to distinguish sensory processing from neuromodulatory effects.

6.2 METHODS

fMRI and electrophysiology data were collected from six (four females) healthy rhesus monkeys *(Macaca mulatta;* 5–11 kg, 6-12 years). All experimental procedures were carried out under approval of the local authorities (Regierungspräsidium, Baden-Württemberg, Tübingen, Germany, Project K4/09) and were in full compliance with the guidelines of the European Community (EUVD 86/609/EEC).

6.2.1 Anesthesia and visual stimulation for neurophysiology and fMRI experiments

The anesthesia protocol has been described previously (Logothetis et al., 1999a; Logothetis et al., 2001). Briefly, glycopyrrolate (0.01 mg·kg-1) and ketamine (15 mg·kg-1) were used for preanesthesia. After induction with fentanyl (3 mg·kg-1), thiopental (5 mg.kg-1) and succinylcholine chloride (3 mg.kg-1), animals were intubated and ventilated using a Servo Ventilator 900C (Siemens, Germany) maintaining an end-tidal CO2 of 33–35 mm Hg and oxygen saturation above 95%. The anesthesia was maintained with remifentanil (0.4 – 1 µg.kg-1min) and mivacurium chloride (2 – 6 mg.kg-1h) to ensure complete paralysis of the eye muscles. In our previous work on neurovascular coupling in V1 we showed that neural responses and neurovascular coupling under this anesthesia regimen are very similar to those in the awake state (Goense and Logothetis, 2008; Logothetis et al., 2001). In a comparison of (face-selective) visual responses between awake and anesthetized monkeys (Ku et al., 2011) few differences in the activated areas were seen throughout the brain. Furthermore, µ-opioid receptors are located at high densities in basal ganglia and thalamus, especially in regions associated to motor commands, but regions associated with cognition, ventral tegmental area, substantia nigra and frontal regions, have low densities of µ-opioid receptors. Therefore, we expect that the anesthesia used, does not cause major interference with DAergic effects on neural responses and neurovascular coupling.

fMRI signals are very sensitive to changes in body temperature, pH, blood pressure and oxygenation, the physiological state of the monkey was monitored continuously and kept within normal limits. Body temperature was tightly maintained at 38.5–39.5°C. Throughout the experiment lactate Ringer's (Jonosteril, Fresenius Kabi, Germany) with 2.5% glucose was continuously infused at a rate of 10 ml.kg-1.hr-1 to maintain an adequate acid-base balance and intravascular volume and blood pressure; hydroxyethyl starch (Volulyte, Fresenius Kabi, Germany) was administered as needed.

Two drops of 1% cyclopentolate hydrochloride were used in each eye to achieve mydriasis. The visual stimuli were presented binocularly using a custom-made MR-compatible display system with a resolution of 800 x 600 pixels and a frame rate of 60 Hz. Animals were wearing hard contact lenses (Wöhlk-Contact-Linsen, Schönkirchen, Germany) to focus the eyes on the stimulus plane. The eyepieces of the stimulus presentation system were positioned using a modified fundus camera (Zeiss RC250; see (Logothetis et al., 2001)). The visual stimulation protocol consisted of blocks of rotating black and white polar checkerboards of 10x10° in size lasting 48 seconds alternated with an isoluminant gray blank period of equal length. The stimulus timing was controlled by a computer running a real-time OS (QNX, Ottawa, Canada). The direction of the rotation was reversed every 8 s to minimize adaptation. This block was repeated 29 times yielding in total 46 minutes for each experiment.

6.2.2 Systemic and Local Injections

Systemic applications of L-DOPA and Carbidopa and saline were performed with a custom-made pressure-operated pump (von Pfostl et al., 2012). The actual flow and volume were continuously monitored by high precision flow-meters (Sensirion, Switzerland). The preconditioning with Carbidopa consisted of 1.5 mg/kg diluted in 50 ml and injected at 1.1 ml/min over a period of 12 minutes. The combined L-DOPA and Carbidopa applications consisted of a total amount of 2.1 mg/kg + 0.5 mg/kg, diluted in 50 ml injected at 1.1 ml/min over 12 min. All the drugs that were systemically applied were diluted in a phosphate-buffered-saline (PBS) solution and the pH was adjusted with NaOH to 7.35. The PBS solution was composed of NaCl 137 mM, KCl 2.7 mM, Na2HPO4 8.1 mM, KH2PO4 1.76 mM. The control experiments were performed with the PBS solution where we applied the same volume at similar flow rate (5 experimental sessions). Because of the sensitivity of the BOLD and CBF measurements, injections were done over a period of 12 min to avoid changes in blood volume or volume-related changes in other physiological parameters, and no adjustments to the anesthesia were made during the 46-min scan.

Local applications of DA in V1 were performed using three independent injection lines driven by three separate HPLC pumps (M5, VICI, USA; (Rauch et al., 2008c)). The three independent lines allowed us to switch between different solutions in successive trials within one experiment. All lines were monitored by high-precision flow meters (Sensirion, Switzerland) controlling the exact applied volume and flow. The DA-containing solution was freshly prepared using DA-hydrochloride diluted in artificial cerebrospinal fluid (ACSF) at final concentrations of 2.5-10 mM. The pH was adjusted to 7.35 with NaOH. The ASCF consisted of NaCl 148.19 mM, KCl 3.0 mM, CaCl2 1.40 mM, MgCl2 0.80 mM, Na2HPO4 0.20 mM. The control solution was the unmodified ACSF solution. All chemicals for local and systemic application were purchased from Sigma Aldrich (Schnelldorf, Germany). ACSF and DA injections were delivered at 0.6 µl/min for a duration of 12 min.

Data analysis procedures were implemented using custom-written routines in MatLab (Mathworks, Natick, MA). No smoothing was applied in any of the data sets. The electrophysiology and fMRI (BOLD and CBF) scans were divided in three epochs: the 'pre-drug', 'drug' and 'post-drug' periods. The 'pre-drug' period consisted of 8 blocks of visual stimulation (12.8 min) while the 'drug' condition consisted of systemic (L-DOPA and Carbidopa or PBS) or local (DA or ACSF) infusion starting immediately after 8 blocks of visual stimulation. We used the 'pre-drug' period as a reference to compute changes during the 'drug' and 'post-drug' periods, from the visual induced modulation, baseline and the SNR of the electrophysiology signals. Statistical significance in all the data was accessed by using a paired t-test comparing the 'pre-drug' period with the 'drug' and 'post-drug' period. This procedure was performed for the statistical significance in changes of the visual-induced modulation, baseline changes and SNR.

6.2.3 Neurophysiology data collection and analysis

For electrophysiological recordings first a small skull trepanation (~3 mm diameter) was made. Subsequently, the meninges were visualized with a microscope (Zeiss Opmi MDU/S5, Germany) and carefully dissected. Electrodes were NeuroNexus laminar probes (NeuroNexus

Technologies, Ann Arbor, USA) for all recordings. We used a 16-contact probe on a single shank of 3 mm length and 50 µm thickness. The electrode sites were spaced 150 µm apart, with a recording area of 413 µm2. The impedance of the contact points ranged from 500 to 700 kΩ. The electrodes were slowly advanced into the visual area under visual and auditory guidance using a manual micromanipulator (Narashige Group, Japan). The depth was determined based on the spontaneous spiking activity of each of the cortical layers (Self et al., 2013). The signals were amplified and filtered into a band of 1 Hz – 8 kHz (Alpha-Omega Engineering, Nazareth, Israel) and digitized at 20.833 kHz with 16-bit resolution (National Instruments, Austin, TX), ensuring sufficient resolution for both local field potentials and spiking activity. The recording area was filled with a mixture of 0.6% agar dissolved in NaCl 0.9%, pH 7.4 which guaranteed a good electrical connection between the ground contact and the animal (Oeltermann et al., 2007).

To analyze electrophysiology data, we used a one-second window to calculate the power spectral density in three frequency bands: low LFP (θ: 4-8 Hz), high LFP (γ: 40-150 Hz) and MUA (900-3000 Hz; (Belitski et al., 2008)). The θ-band was used to indicate whether LDC affects the broadband LFP power and to assess whether DA-injection induces changes in the level of anesthesia (Kortelainen et al., 2011). The signal-to-noise ratio (SNR) of the electrophysiological signals was calculated by dividing the power of the visually evoked responses (meaningful information) by the power of the responses during the off-period.

6.2.4 MRI data collection and analysis

The fMRI experiments were conducted in a vertical 7T scanner with a 60 cm diameter bore (Bruker BioSpin GmbH, Ettlingen, Germany) and in a vertical 4.7T with a 40 cm diameter bore. We performed fifteen BOLD experiments and five CBF experiments at 7T, and one CBF experiment at 4.7T. We used a custom-made chair to position the monkey into the magnet. For BOLD experiments, we used a custom-built quadrature volume coil that allows

imaging of deep brain structures while still maintaining a high signal-to-noise ratio in the visual cortex. We used a single-shot gradient-echo EPI with a FOV of 72x72 mm2 and matrix size of 96x96. 11 slices were acquired with a thickness of 2 mm, TE/TR 20/3000 ms and flip angle of 90˚. Each experimental session consisted of 928 volumes. Shimming was done with FASTMAP over a volume of 12 mm3. Six functional CBF measurements were acquired at 7T and one at 4.7T. For the CBF experiments we used a volume coil to transmit in combination with a custom-built, 4-channel phased array (Goense et al., 2010). Perfusion imaging was performed using flow-sensitive alternating inversion recovery (FAIR; (Kim, 1995), with alternating slab-selective and nonselective inversion pulses. At 7T we used inversion time 1400 ms, slab 6 mm, FOV 5.5x2.4 mm2, TE/TR 9.5/4500 ms and receiver BW 150 kHz. The experiments at 4.7T were performed using an inversion time 1400 ms, slab 6 mm, FOV 6x3.2 mm2, TE/TR 9.1/4500 ms and BW 125 kHz.

We included 15 of 18 data sessions during L-DOPA injections in the data analysis; the rest were devoted to the development of the injection technique. We defined a region of interest (ROI) consisting of early visual cortex (V1-V2). A short scan (12 min) preceding the injection scan was used to define the ROI that was subsequently used for the injection scan. We used a boxcar convolved with a haemodynamic response function (gamma variant function) as regressor to calculate the correlation coefficient. Voxels showing robust visually induced modulation ($p < 0.02$) were included for further analysis, and were then monitored during the long (46.4 min) injection scan to study L-DOPA induced effects. This approach allowed us to investigate L-DOPA induced effects without making a priori assumptions.

BOLD and CBF time courses were linearly detrended and normalized. Every trace was tested for L-DOPA induced changes in the visually induced modulation. For the calculation of the modulation we subtracted the ON periods from the OFF periods, the result was then divided by the OFF period and multiplied by 100. Baseline changes were computed by taking the image intensity in the periods without visual stimulation (OFF periods). To determine how LDC affected evoked BOLD- and CBF-responses, we analyzed the modulation in response to

visual stimulation normalized to the pre-drug condition. The BOLD-modulation in the pre-drug period was 2.5±1.1%, which is typical for anesthetized monkeys at 7T (Goense et al., 2010; von Pfostl et al., 2012; Zappe et al., 2008a). Similarly, baseline changes induced by LDC were calculated by computing OFF periods normalized to the pre-drug condition (von Pfostl et al., 2012).

6.3 RESULTS

We combined fMRI with neurophysiology and pharmacology in five anesthetized non-human primates (*Macaca mulatta*), where we acquired BOLD, functional CBF (fCBF) and electrophysiology data while the animals viewed a rotating checkerboard stimulus. Figure 1A shows the experimental paradigm. We pharmacologically mimicked DAergic neurotransmission by systemic application of L-DOPA and Carbidopa. Carbidopa inhibits the breakdown of L-DOPA in the periphery, thereby preventing systemic changes in cerebral blood volume (CBV) that may affect the fMRI results (Figure 6.5). The lack of systemic effects of the LDC injection is evidenced by the highly stable physiological parameters during and after injection (Table 6. 1).

6.3.1 Evoked BOLD and neural responses under systemic LDC

Figure 6.1B shows representative fMRI responses in V1 to visual stimulation. Figure 6.1C shows the changes in the BOLD-response over the course of the LDC injection. BOLD-modulation in the pre-drug period was 2.5±1.1%, which is typical for anesthetized monkeys at 7T (Goense et al., 2010; von Pfostl et al., 2012; Zappe et al., 2008a). During the drug infusion we observed a significant reduction in the visually induced modulation (Figure 6.1C,D; MOD_{drug}=50±5.3%; p=0.034), which was sustained after the infusion was stopped (MOD_{post}=60±4.2%; p=0.05). No significant changes in the baseline were found (Figure 6.1D).

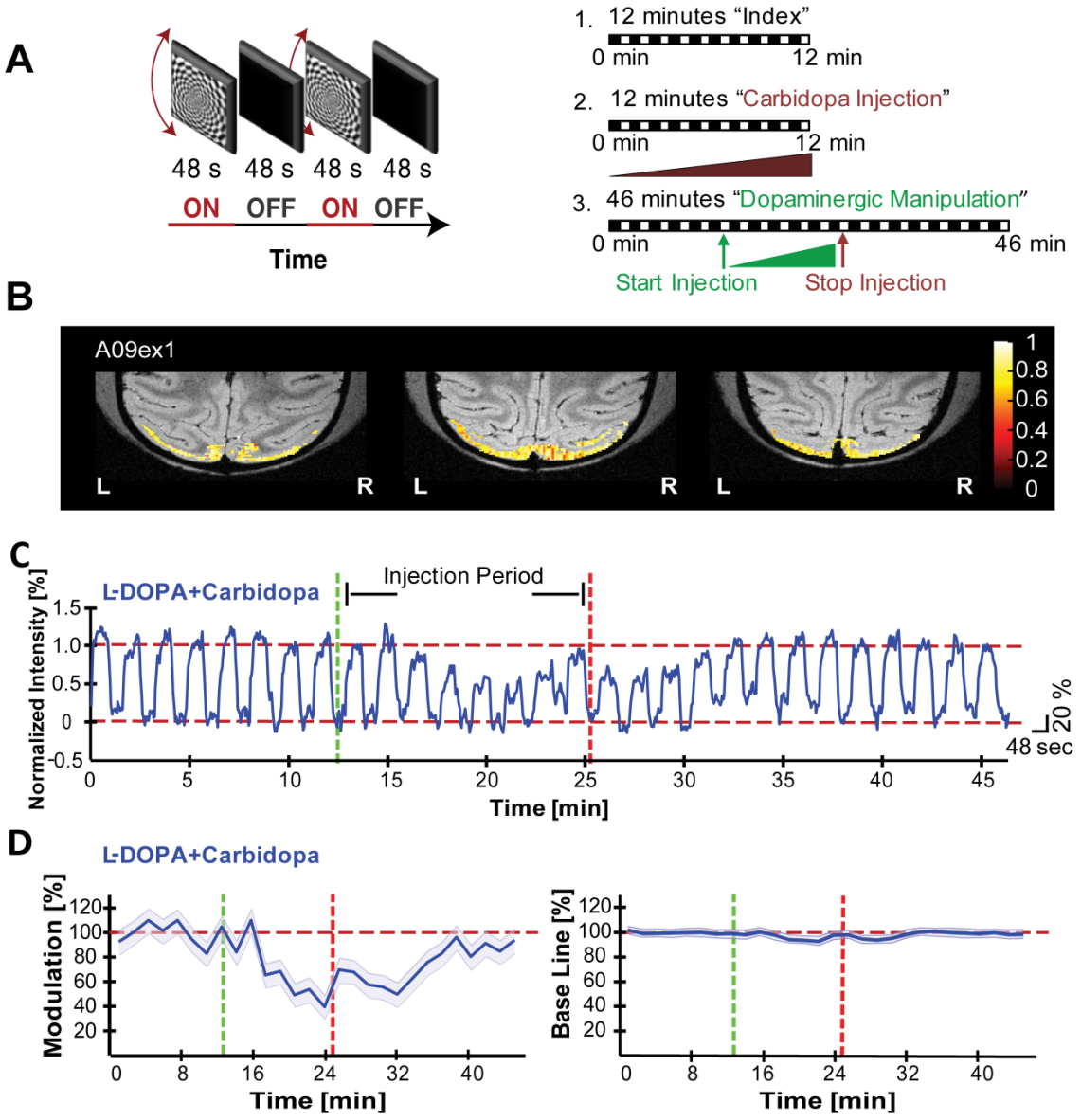

Figure 6.1 BOLD Responses under L-DOPA and Carbidopa Influence in Visual Cortex

(A) Experimental paradigm and design. The stimulus was a rotating checkerboard of 48 s followed by an isoluminant blank screen of 48 s (right). Every experiment was divided into three conditions: (1) a 12.8 min experiment without pharmacological manipulation, (2) a 12.8 min session with Carbidopa preconditioning (1.5 mg/kg diluted in 50 ml of PBS and injected at 1.1 ml/min), and (3) a 46 min session consisting of LDC manipulation (2.1 mg/kg + 0.5 mg/kg diluted in 50 ml of PBS and injected at 1.1 ml/min over a period of 12 min). (B) Activation maps showing voxels with a significant response to the visual stimulus (eight-shot GE-EPI; FOV: 72 3 72 mm2; TE/TR: 20/3,000 ms; flip angle 90°; matrix: 96 3 96), overlaid on an anatomical scan (FLASH), acquired at 7T with an in-plane resolution of 0.75 3 0.75 mm2 and 2 mm slice thickness. (C) The average BOLD time course (928 volumes) over 18 fMRI experimental sessions (five animals) shows a decrease in visually induced modulation by L-DOPA and Carbidopa; the green and the red lines show the start and stop of the L-DOPA-Carbidopa infusion. (D) The average BOLD response to the visual stimulus (left), decreased by 50% compared to the predrug period, whereas the baseline did not change under L-DOPA and Carbidopa (right). The shaded areas represent the SE.

We recorded local field potentials (LFP) and multiunit spiking activity (MUA) to evaluate the effects of LDC application on neural activity. The power in three different frequency ranges was calculated: γ (40-150 Hz) and MUA (900-3000 Hz), which are most strongly correlated with the BOLD signal (Goense and Logothetis, 2008; Logothetis, 2008; Rauch et al., 2008c), while θ (4-8 Hz) was used to indicate whether LDC affects the broadband-LFP power and to assess whether DA-injection induces changes in the level of anesthesia. Figure 6.2A-C shows the average time course across experiments for the θ-, γ- and MUA-bands respectively. LDC application resulted in an 18% increase in visual modulation in the γ-band (Figure 2D; $MOD_{\gamma,drug}$=118±4.2%; p=0.024) and a 19% increase in the MUA-band ($MOD_{MUA,drug}$=119±5%; p=0.031). The effect of LDC on the MUA-amplitude reached baseline values ~4.5 min after the infusion was stopped. In contrast, for the γ-band the increase in visually induced modulation was long-lasting and started to reduce ~12 min after the infusion was stopped. Additionally, we observed an increase in the SNR of the γ- and MUA-bands starting shortly after LDC injection (Figure 6.2E); the response to the stimulus increased while the variability decreased (Figure 6.2B,C). The SNR in the γ-band ($SNR_{\gamma,drug}$=13.7±2.0 dB; p=0.011) kept increasing after the infusion was stopped ($SNR_{\gamma,post}$=14.7±2.0 dB; p=0.012). The MUA-band also showed an SNR-increase after the start of the injection ($SNR_{MUA,drug}$=12.2±2.2 dB; p=0.012) which continued until the end of the trial ($SNR_{MUA,post}$=11.0±2.0 dB; p=0.026). In the θ-band (Figure 6.2A) neither visually induced modulation nor SNR changed upon LDC infusion.

6.3.2 Dopamine effects are not locally induced in V1

We next investigated whether the increases in neural activity are locally induced in V1 or are due to a remote influence from other regions by injecting DA intracortically in V1 to determine whether this induces similar effects as systemic dopamine. Figure 6.3A-C shows the averaged traces of the θ-, γ- and MUA-bands during intracortical application of DA (5 mM) and shows no discernible changes. Visually induced modulation in the γ- and MUA-bands (Figure 6.3D) was unchanged (p=0.23). The SNR of the γ- and MUA-bands also remained unchanged

during the experimental session (Figure 6.3E, $SNR_{\gamma,drug}$=9.0±1.5 dB; p=0.31; $SNR_{\gamma,post}$=8.8±2.0 dB; p=0.13; $SNR_{MUA,drug}$=10.1±0.5 dB; p=0.18; $SNR_{MUA,post}$=10.8±2.0 dB; p=0.18). Since different concentrations of DA can exert multiple modes of action (Seamans and Yang, 2004), we tested whether different concentrations of intracortical DA affected the responses in V1. However, no concentration dependent effects were observed (Figure 6.6).

6.3.3 The effects of LDC on CBF suggest an increase in energy expenditure

Stimulus-induced increases in γ-power and in MUA occurred simultaneously with a decrease in BOLD-modulation. To resolve this potential discrepancy we measured fCBF using arterial-spin-labeling (ASL). Figure 6.4A shows fCBF in early visual cortex and Figure 6.4B the averaged time course of the CBF across experiments. There was a reliable visually induced, CBF-modulation of 19±7% during the pre-drug period, in agreement with earlier studies (Zappe et al., 2008a). During the 'drug' period we observed an increase in modulation by 34% (MOD_{drug}=134±10%; p=0.045). The maximum CBF-increase of 43% was observed ~12 min after the infusion started and lasted ~20 min (MOD_{post}=143±10%; p=0.034). We also observed significant increases in baseline CBF during and after the injection. An increase in the baseline was evident ~8 min after the start of the injection ($CBF_{baseline,drug}$=128±5.2%; p=0.022). The time course of the CBF-changes upon LDC injection were similar to the time courses of the changes in the neuronal responses, suggesting that increases in neural activity may cause the CBF-increases.

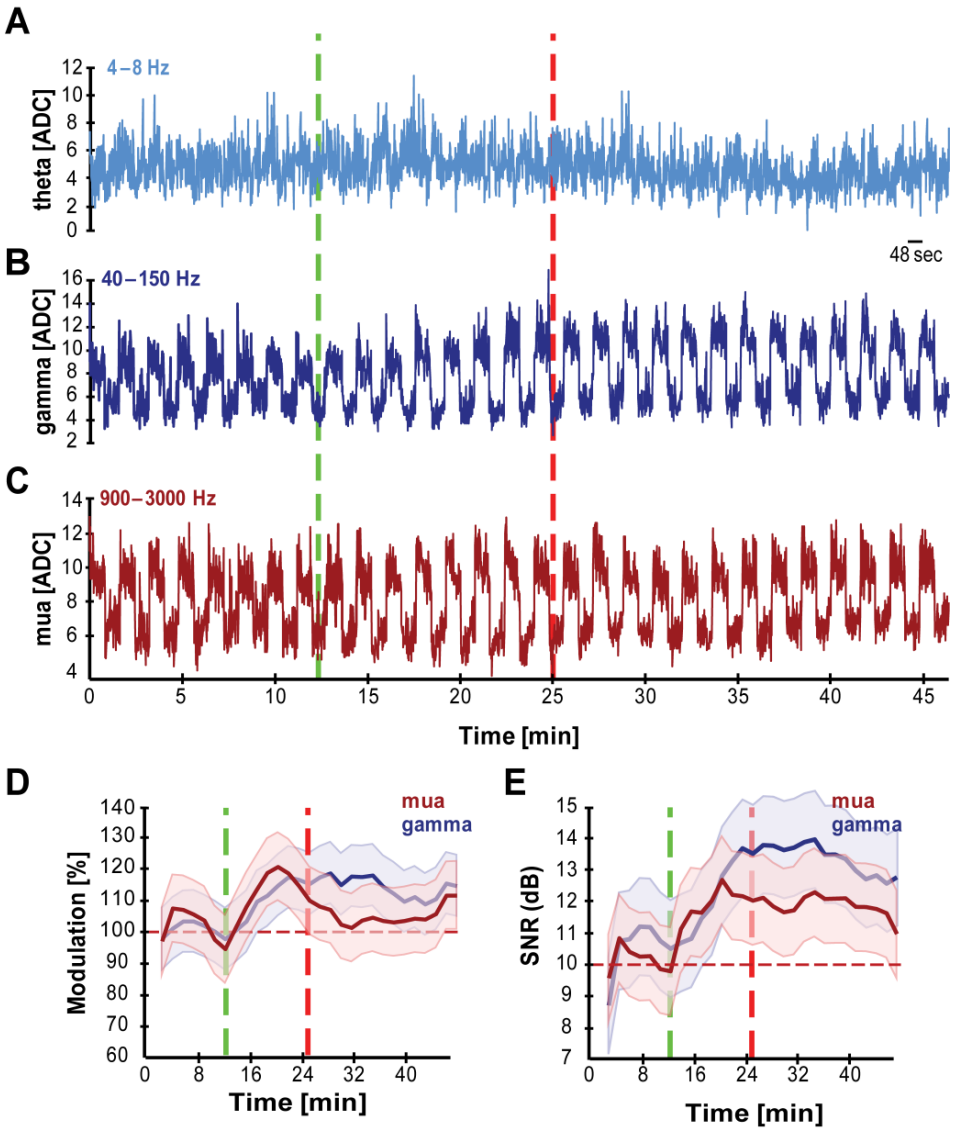

Figure 6.2 Systemic Application of L-DOPA and Carbidopa Increases Neural Responses in V1

Average time course of the neural activity (LFP and MUA bands) across experiments in response to LDOPA and Carbidopa injection (n = 16). (A) q LFP band (4–8 Hz). (B) g LFP band (40–150 Hz). (C) MUA band (900–3,000 Hz). The green and red lines denote the beginning and end of the systemic LDC infusion. In the MUA and g bands, the amplitude of the visual response increased after LDC, whereas the variability of the baseline decreased. (D) Percentage change in visual response of the g band (blue) and MUA (red). (E) The SNR of the g band (blue) and the MUA (red) increased upon DA infusion. No changes were observed in the q band. The shaded areas represent the SE.

6.4 DISCUSSION

Using BOLD- and CBF-based fMRI combined with intracortical electrophysiology, we found that DAergic neuromodulation increased neural- and CBF-responses to a visual stimulus,

while decreasing the BOLD-response. Neuromodulators can exert strong influences on neural responses and alter neurovascular coupling (Dayan, 2012; Logothetis, 2008); our results show that changes in the BOLD-fMRI signal alone cannot be used to make inferences about increases or decreases in the underlying neural activity.

6.4.1 Neurophysiological effects of dopamine injection

Neurophysiological recordings under systemic LDC injection showed an increase in the amplitude and SNR of visually evoked responses. DA has been shown to improve the SNR in PFC and in sensory areas, including V1 (de Lafuente and Romo, 2011a; Happel et al., 2014; Jacob et al., 2013; Shuler and Bear, 2006), thereby changing detection performance at the behavioural level (de Lafuente and Romo, 2011a; Servan-Schreiber et al., 1990; Shuler and Bear, 2006; Stanisor et al., 2013). Increased neuronal activity in V1 has been shown to predict the timing of reward delivery, even when the cells were not driven by a visual stimulus (Shuler and Bear, 2006; Stanisor et al., 2013), highlighting the importance of DA for extracting behaviourally relevant information (Serences, 2008; Servan-Schreiber et al., 1990).

However, local dopamine application did not change neural activity, in good agreement with the low density and sparse distribution of DARs in V1 (Lidow et al., 1991) and suggesting that DA does not exert its effects on V1 itself. The increase in neural activity upon systemic DA may be mediated by long-range interactions from higher-order regions, for instance frontal regions (Jacob et al., 2013; Noudoost and Moore, 2011). Large-scale interactions have been reported in other sensory modalities, including the visual-, somatosensory- and auditory systems, suggesting that DA prepares the higher-order area for the processing of incoming sensory signals, and promotes the readout of task-related information (de Lafuente and Romo, 2011a; Happel et al., 2014; Jacob et al., 2013). Manipulation of prefrontal D1-receptors increased the magnitude, reliability and selectivity of neuronal responses in V4 (Noudoost and Moore, 2011), and similar mechanisms may play a role in V1.

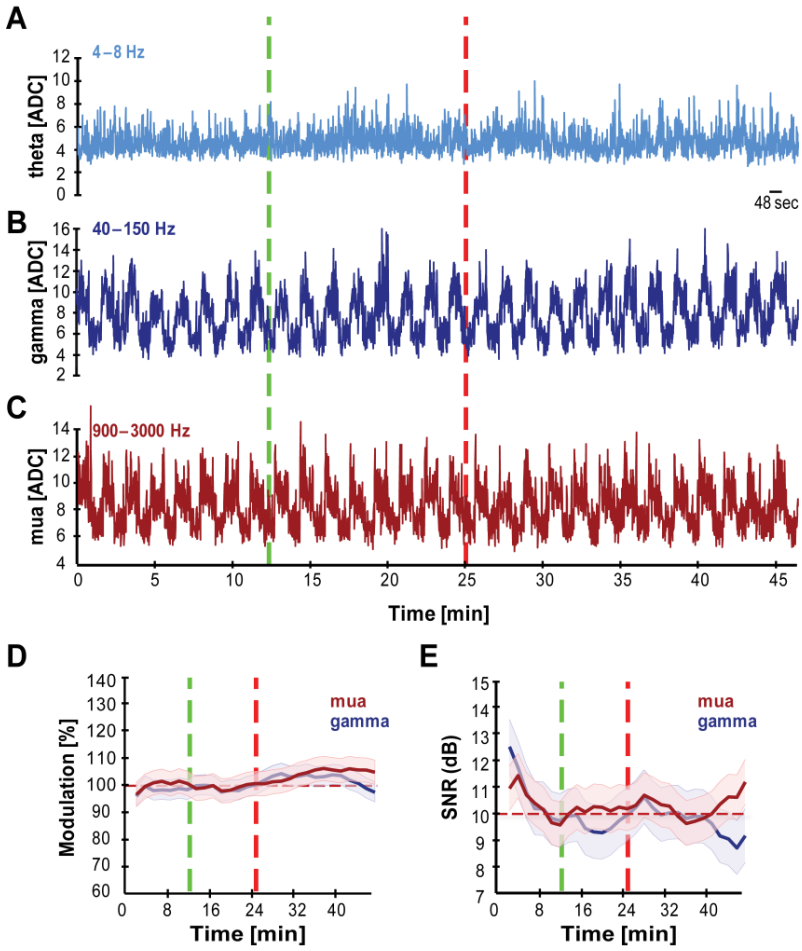

Figure 6.3 Local Application of DA Does Not Alter Neural Responses in V1

Average time course of the neural activity (LFP and MUA bands) across experiments, in response to local application of DA (n = 10; DA was diluted in artificial cerebrospinal fluid to a final concentration of 5 mM). (A) q LFP band (4–8 Hz). (B) g LFP band (40–150 Hz). (C) MUA band (900–3,000 Hz). The green and red lines denote the beginning and end of the DA infusion. In the MUA and g bands, the amplitude of the visual response was not affected by DA infusion. (D) Percentage change in visual response of the g (blue) band and MUA (red). (E) The SNR of the g band (blue) and the MUA (red) shows no changes upon DA. No changes were observed in the q band. The shaded areas represent the SE.

The lack of DAergic effects upon local application is contrary to the inhibitory responses observed earlier (Gottberg et al.; Reader, 1978). Although DA can exert different actions depending on concentration (Seamans and Yang, 2004), none of the DA concentrations used in this study changed the amplitude or SNR of the visually evoked responses. Aside from species differences (Lidow et al., 1991; Phillipson et al., 1987), another possibility that could explain the differences is that the earlier experiments were performed with solutions in which the pH was not tightly controlled, whereas acidic pH depresses neuronal excitability (Tombaugh and Somjen, 1996).

6.4.2 Functional imaging

Our finding of a decrease in the evoked BOLD-response and an increase in the CBF-response upon systemic LDC injection, extends previous observations in humans and macaques in

which fMRI responses in V1 decreased with cues that predict and anticipate reward (Arsenault et al., 2013; Serences, 2008). A decrease in BOLD-responses in V1 while behavioral performance improved after an acute dose of L-DOPA was seen in studies of amblyopia (Algaze et al., 2005; Rogers, 2003). However, BOLD-increases have also been observed in humans in primary auditory and somatosensory cortex after DA-agonist administration (Pleger et al., 2008; Weis et al., 2012). These differences in BOLD-responses upon DAergic neuromodulation can be partly explained by the difference in densities of DARs and DA-innervation between cortical regions. DARs and DA-innervations decrease along a rostro-caudal gradient having the highest density in PFC and the lowest (or almost nonexistent) in occipital cortex (Lidow et al., 1991). Thus, BOLD-responses to DAergic neuromodulation could differ in various sensory cortices, since local influences of DA on the vasculature may modulate the blood supply (Krimer et al., 1998a; Mandeville et al., 2001).

The effects of DA on the hemodynamic signals have been extensively addressed using different pharmacological agents in rats and monkeys (Delfino et al., 2007; Esaki et al., 2002; Jenkins et al., 2004; Mandeville et al., 2001; 2013). For instance, amphetamines decreased CBV-responses in occipital regions (Jenkins et al., 2004). However, amphetamines are known to increase DA-levels as well as alter the kinetics of other neurochemicals that affect the regional CBV (Leonard and Shallice, 1971), while CBV-responses may differ from BOLD-responses (Goense et al., 2012). Different DARs exert different effects on the hemodynamic signals (Mandeville et al., 2013); stimulation of D1-receptors (D1Rs) increases CBV and BOLD (Delfino et al., 2007; Mandeville et al., 2013) whereas blocking these receptors decreases it (Choi et al., 2010; Mandeville et al., 2013). The activation and deactivation of D2-receptors (D2Rs) produces opposite effects (Choi et al., 2006). The present study did not consider receptor specific-responses, but instead focused on understanding the balanced effects mediated by D1R and D2R interaction.

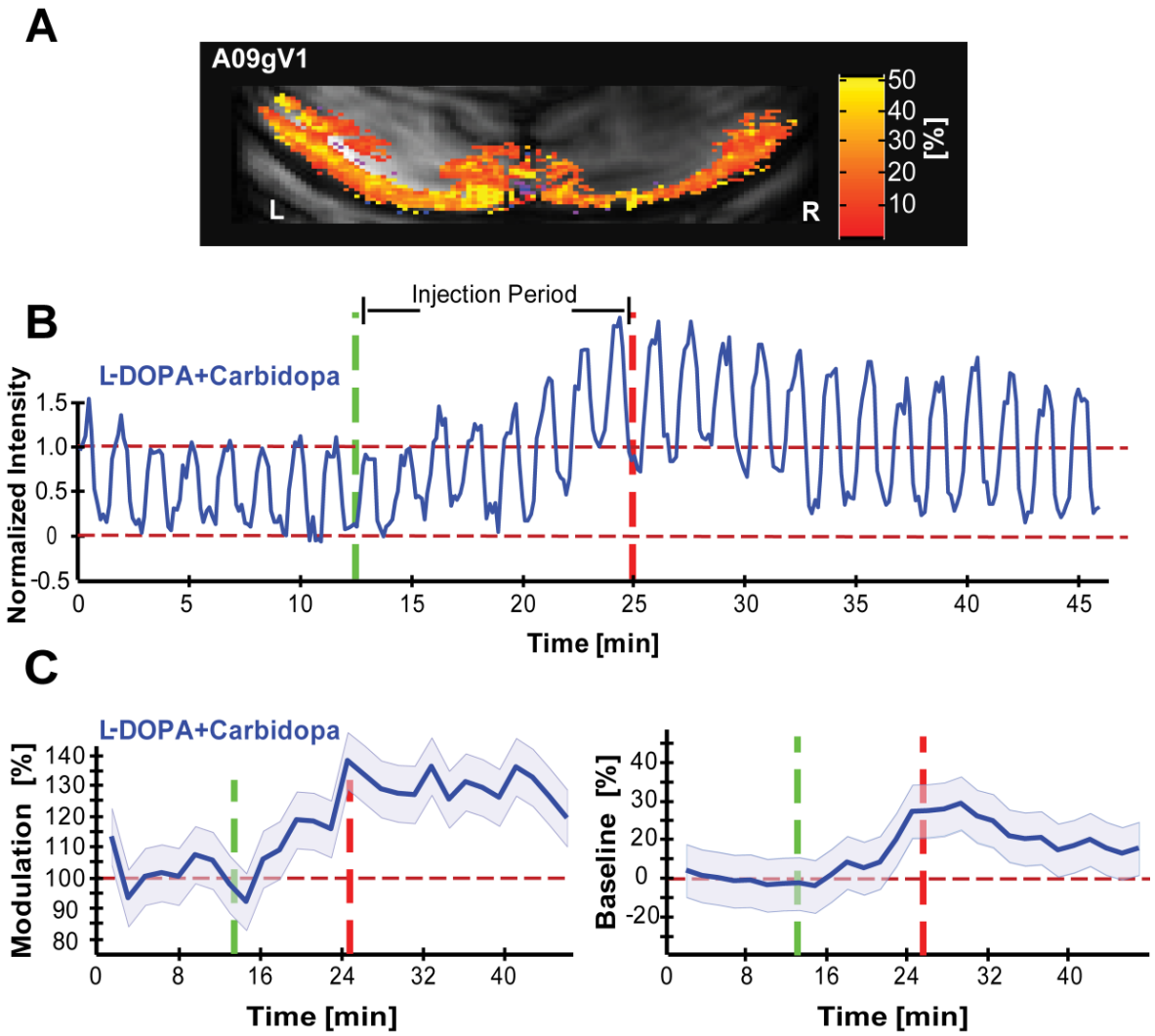

Figure 6.4 CBF Increases with L-DOPA and Carbidopa

(A) Activation patterns of functional CBF (using flow-sensitive alternating inversion recovery) in early visual cortex (monkey A09) in response to visual stimulation. (B) The average time course over six CBF experimental sessions shows an increase in baseline-induced as well as visually induced CBF (six sessions acquired at 7T: TI, 1,400 ms; slab 6 mm; FOV, 5.5 3 2.4 mm2; TE/TR, 9.5/ 4,500 ms; BW, 150 kHz, and one session acquired at 4.7T: TI, 1,400 ms; slab 6 mm; FOV, 633.2mm2 ; TE/TR, 9.1/4,500 ms; BW, 125 kHz). (C) The average visually induced modulation increased by 43% (left) and the baseline changed by 31% (right) upon L-DOPA and Carbidopa infusion. The shaded areas represent the SE.

6.4.3 Neurovascular coupling under dopamine

Changes in the LFP are usually mirrored by changes in spiking and in the haemodynamic responses (Goense and Logothetis, 2008). Our observation of a dissociation between the BOLD- and neurophysiological responses indicates that neurovascular coupling may differ

under states of neuromodulation. Our results suggest that the increase in neural activity and CBF and the decrease in BOLD are caused by a disproportionate increase in O_2-consumption due to DAergic neuromodulation. The BOLD-signal reflects the deoxyhemoglobin concentration [dHb], and is affected by CBF, CBV and the cerebral metabolic rate of oxygen consumption ($CMRO_2$). The stimulus-evoked BOLD-decrease could be due to a CBF-decrease or a [dHb] increase after dopamine application. Since CBF increased, dHb-production is most likely also increased, i.e. an increase in $CMRO_2$. An increase in CBF-modulation and a decrease in BOLD-response can occur when the O_2-consumption increases by a proportionally larger amount than the inflow of fresh blood, leading to a relative increase in [dHb] and a decrease in the BOLD-signal compared to the pre-injection response.

The increased neural activity also suggests a $CMRO_2$-increase, since it has been shown that improving neurons' sensitivity is energetically draining (Laughlin et al., 1998; Servan-Schreiber et al., 1990). Using autoradiography it has also been shown that the application of L-DOPA increases brain metabolism (Porrino et al., 1987a). These observations are not surprising given that energy usage is tightly coupled to neural performance (1998; Logothetis, 2008). The increase in CBF likely relates to neuronal activity because glucose metabolism, $CMRO_2$ and CBF are closely coupled (Kim and Ogawa, 2012; Logothetis, 2008). Increased neural activity in response to reward increases has been shown to increase the CBF (Obayashi et al., 2009).

The increased baseline CBF upon acute LDC injection commonly seen in humans and non-human primates (Hershey et al., 2000; Leenders et al., 1985; Montastruc et al., 1987) is usually attributed to vasodilation. However, the stimulus-induced CBF-increases cannot be attributed to vasodilation alone. Vasodilation increases the baseline CBF- and BOLD-signals, and reduces stimulus-evoked CBF- and BOLD-signals due to limited reserves, as seen in the case of hypercapnia (a potent vasodilator) (Sicard and Duong, 2005; Zappe et al., 2008b). The possibility that the BOLD-reduction is due to a ceiling effect, as seen in the case of

hypercapnia or in pathology, is therefore unlikely, since evoked CBF decreases in the case of vasodilation (e.g. in hypercapnia) or an inadequate CBF-response (Blicher et al., 2012).

PET-studies have shown little or no change in $CMRO_2$ upon L-DOPA administration (Leenders et al., 1985), the latter reflecting little or no change in baseline response, as was observed here. A lack of $CMRO_2$-increase however, would not be able to explain our stimulus-driven results: comparing again with hypercapnia where $CMRO_2$ and neural activity do not change considerably; this would lead to very different CBF- and BOLD-responses to the stimulus than observed here (Zappe et al., 2008b). Whether the increase in baseline CBF corresponds to an increase in metabolism cannot be deduced based on the current data. The baseline of the BOLD time-course did not change, with a minor tendency to go down. It is possible that the increase in CBF is balanced out by an increase in [dHb] in the baseline state, leading to little or no net baseline changes. Following the same reasoning as with the stimulus-induced responses, the small decrease in the baseline BOLD-trace may indicate a small increase in $CMRO_2$ in the baseline condition as well. However, further study is needed to verify this.

The effects observed here are unlikely to be due to DA-induced changes in the level of anaesthesia, since no differences were observed in the θ-band or the physiological parameters. The advantage of using anesthetized animals is that we could assess the effect of dopamine on neural and hemodynamic properties without needing to take behavioural parameters like attention, reward and anticipation into account. Anesthetized animals also allow us to discriminate small changes since it allows for longer averaging times. However, differences in regional CBF under DAergic influence have been observed between awake and anesthetized animals (Hershey et al., 2000), and differences may depend on the type anaesthesia. Since neuromodulatory properties strongly depend on the animal's behavioural state, including its level of alertness, this highlights the complexity of fMRI studies of neuromodulation, and ideal would be a comparison of dopaminergic effects in awake and anesthetized animals.

The findings presented here provide us with a better understanding of the influence of neuromodulation on fMRI-signals. The decrease of the BOLD-signal in the face of an increased energy use, implies that the BOLD-response may not always faithfully reflect the neural responses under neuromodulation, and imply caution is necessary in interpreting BOLD-signals under neuromodulation. Combining BOLD-measurements with CBF- and/or CBV-measurements can resolve these complexities and potentially provide a tool to discriminate sensory processing from neuromodulation. Such multidisciplinary approaches may improve the interpretation of fMRI-studies where neuromodulation plays a role, for example, studies of reward or attention, but also facilitate clinical applications of fMRI.

6.5 APPENDIX

6.5.1 L-DOPA without Carbidopa intervention and saline control

Systemic L-DOPA, without any Carbidopa was applied in three animals. Concentrations, flow and final volume were similar to those used in the L-DOPA and Carbidopa interventions. Figure 6.5A shows the averaged BOLD responses across all experimental sessions (n = 5, upper panel, blue). As in the L-DOPA and Carbidopa condition we divided each session in three conditions: 'pre-drug', 'drug' and 'post-drug' and calculated the changes in the visually induced modulation and in the baseline. There were no changes in the visually induced modulation during (MOD_{drug} = 99%; p = 0.09 paired t-test;) and after the injection (MOD_{post} = 104%; p = 0.09 paired t-test; $median_{post}$ = 101%). We observed a significant increase in the baseline BOLD signal during and after the injection period (Figure 6.5B). The increase was evident ~8 min after the start of the injection ($BOLD_{baseline,drug}$ = 112 ± 8%; p = 0.05 paired t-test; median $BOLD_{baseline,drug}$ = 108%). This increase lasted ~10 min after the injection was stopped ($BOLD_{post,drug}$ = 116 ± 6%; p = 0.05 paired-test; median $BOLD_{post,drug}$ = 112%). Systemic injection of saline showed that both the visually induced modulation and the baseline were unchanged during and after injection (Figure 6.5C and Figure 6.5D; MOD_{drug} = 102%; $median_{drug}$ = 107%; p = 0.08 paired t-test; MOD_{post} = 104%; $median_{post}$ = 102%; p = 0.23 paired t-test).

6.5.2 Effect of different concentrations of dopamine in V1

We locally applied dopamine at different concentrations in V1 (2.5 and 10 mM; Figure 6.6). Figure 6.6A and Figure 6.6B show the results for the 2.5 mM condition. Figure 6.6C,D show the 10 mM condition. Both pharmacological conditions were divided in pre-drug, drug and post-drug, for which we calculated the PSD for the θ (4 – 8 Hz), γ (40 – 150 Hz) and MUA- (900 – 3000 Hz) bands. No significant effects were observed in any of the computed frequency bands for both pharmacological manipulations.

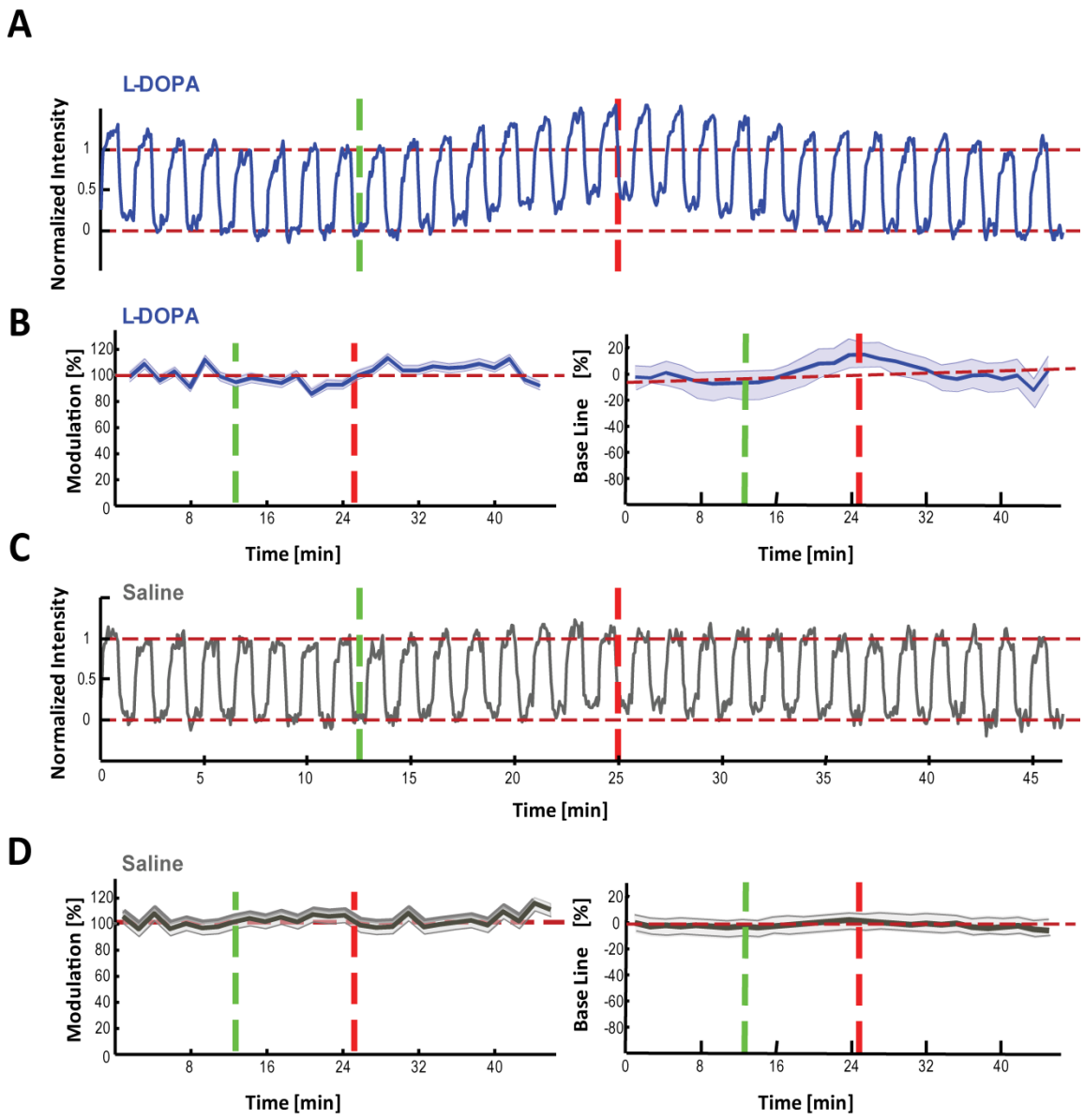

Figure 6.5 Effects of L-DOPA without Carbidopa and saline; Related to Figure 1.

A. Average BOLD time course over five fMRI experimental sessions of L-DOPA application without Carbidopa (shown in blue). The green and red lines show the start and stop of the L-DOPA infusion. B. The average visually induced modulation did not change (left) while the baseline showed a small increase (right). The systemic changes in the peripheral vascular system and the lack of effects on the visual modulation indicate the breakdown of L-DOPA in the periphery. C. Shows the average BOLD time course during saline infusion (shown in gray), similarly green and red lines denote the infusion period. D. Visually induced modulation (left) and baseline (right) did not change in response to saline infusion

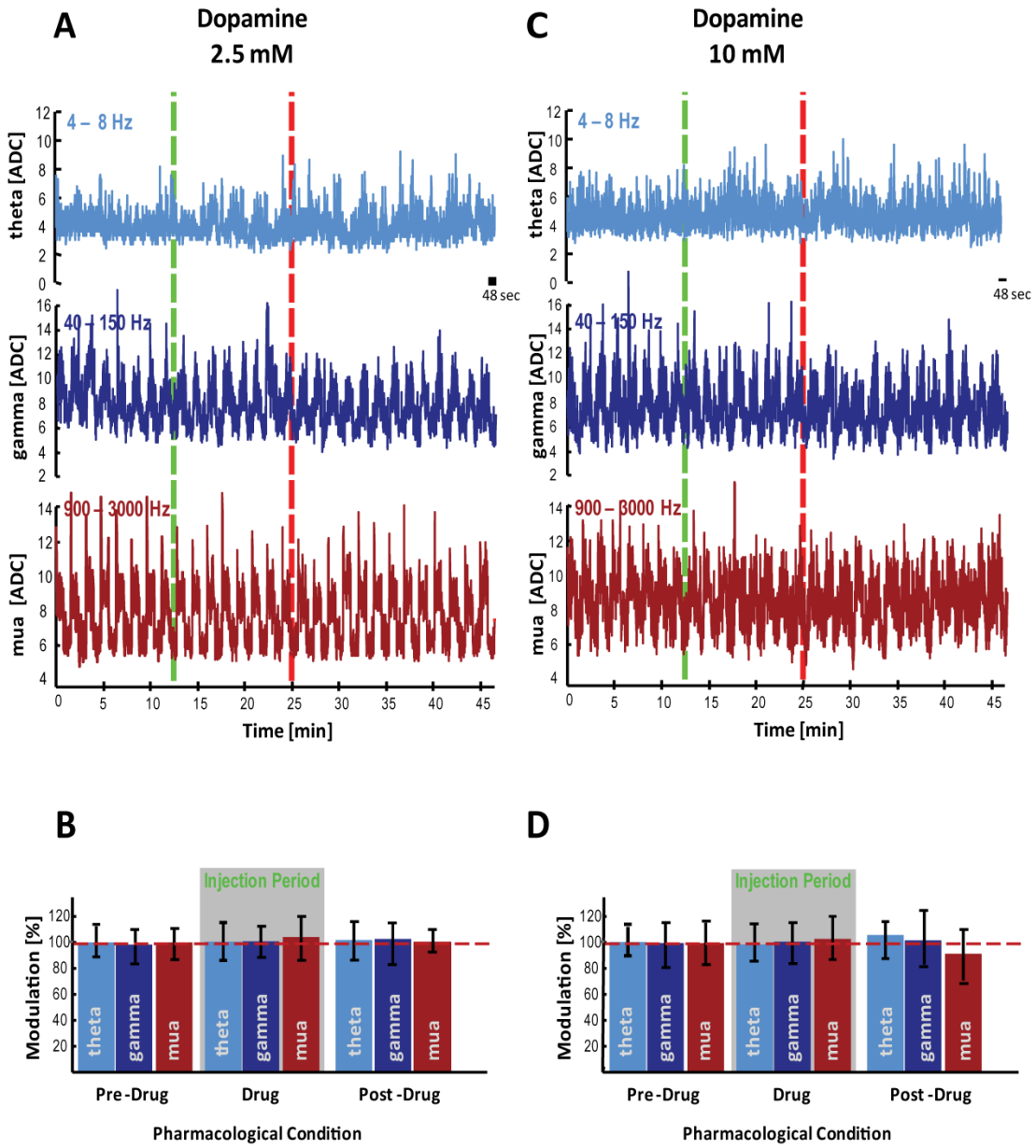

Figure 6.6 V1 responses to local DA application at different concentrations; Related to Figure 3.

Average time courses of the neural activity (LFP and MUA bands) across experiments, in response to local application of DA at different concentrations. A. DA at 2.5 mM: responses in θ-band (4 – 8 Hz), γ-band (40 – 150 Hz) and MUA (900 – 3000 Hz). The green and red lines denote the beginning and end of the DA infusion. B. Changes in visually induced modulation for each of the bands recorded during the pre-drug, drug, post-drug condition; no changes were observed at this concentration. C. DA at 10 mM: responses in θ–band, γ–band and MUA. D. No changes in visually induced modulation were observed upon dopamine application.

Table 6. 1 Mean physiological parameters under general anesthesia. Related to **Figure 6.1**and Figure 6.4

Animal	Heart Rate (pulse/min)			Blood Pressure (mm/Hg)			CO_2			SpO_2		
	Pre	Drug	Post	Pre	Drug	Post	Pre	Drug	Post	Pre	Drug	Post
A09	127.15	131.12	129.05	91/38	96/40	92/35	32.28	33.12	33.02	98	99	99
G09	123.02	112.28	112.30	109/53	111/47	112/47	33.12	33.15	33.12	100	99	990
H09	130.12	125.93	128.12	110/48	113/44	121/38	33.15	33.12	32.54	98	100	100
H11	110.82	114.15	120.2	152/56	152/54	149/51	33.19	32.21	33.23	99	99	98
K07	103.06	106.74	106.52	86/35	75/29	72/30	33.20	33.11	33.14	98	99	99
J08	98.43	99.66	98.34	78/43	74/39	85/29	32.12	33.05	33.09	98	100	99

Included in the table are the mean physiological parameters under general anesthesia during the pre-drug, drug and post-drug conditions (four females and two males). The parameters included in this table were computed across all experimental sessions.

7. Manuscript Nr. 5

Lamina and frequency specific distribution of information in primary visual cortex

This chapter will be submitted within the next month by

Scott C. Low, Daniel Zaldivar, Yusuke Murayama, Mark C. W. van Rossum,

Nikos Logothetis & Stefano Panzeri.

7.1 INTRODUCTION

The cortical column is widely regarded as the fundamental processing unit of the neocortex (Mountcastle, 1997). Under this hypothesis, there is a common microcircuit spanning the depth of the cortex which is repeated across the cortical plane. As the circuitry of the microcolumn is expected to have structural and functional similarities across the sensory modalities, therefore understanding this generic circuitry of the columnar computation will have far reaching impacts. However, despite some progress towards understanding knowing the different types of neurons in present in different layers (Briggs and Callaway, 2001, 2005; Callaway, 1998; Chatterjee and Callaway, 2003), and the distribution of their most prominent inter-connections (Hansen et al., 2012; Hansen and Dragoi, 2011), and a structural wiring diagram for the cortical microcircuit (Douglas and Martin, 2004), is still unknown. Furthermore, the functional structure and computation of the microcircuit, which is to say the purpose of the processing in each cortical layer, is also still unknown. In this paper, we aim to elucidate the functional structure of the cortical layers in primary visual cortex (V1) by examining the information contained in population activity at the various layers using local field potentials (LFPs).

LFPs are thought to reflect an integration of the membrane depolarization in the neurons surrounding the electrode location. The LFP captures changes within the dendritic trees of neighboring neurons as well as the soma. The low frequency LFP (< 20 Hz) captures slower changes in the population activity, and reflects more of the dendritic level of processing, integrated over a larger region than the high frequency LFP (Leski et al., 2013). We previously found that in the macaque V1 there are two LFP frequency bands, 1–8 Hz and 60–100 Hz, which encode independent information in the macaque V1 about natural stimuli (Belitski et al., 2008). In this study we expand the previous study by studying information as a function of cortical depth, and identify one aspect of natural scenes which is encoded differently by the two cortical frequency bands. We hypothesized the two bands of information are generated through different cortical processes and originate at different locations in the cortex. In this

study we expand the previous study by studying information as a function of cortical depth, and identify one aspect of natural scenes which is encoded differently by the two cortical frequency bands. Recent work has shown stimulation in V1 induces gamma activity in extrastriate visual cortex area V4 (V4) (feedforward), whilst stimulation in V4 induces alpha oscillations in V1 (feedback) (van Kerkoerle et al., 2014a).

7.2 METHODS

Data was collected from V1 in four healthy rhesus monkeys (Macaca mulatta; four males 8–11 kg; 10–12 years). All the experimental procedures were approved by the local authorities Regierungspräsidium, Baden-Württemberg, Tübingen, Germany; Project Number KY4/09) and were in full compliance with the guidelines of the European Community (EUVD 86/609/EEC) and were in concordance with the recommendation of the Weatherall report for the care and use of non-human primates (Weatherall, 2006). The animals were group-housed in an enriched environment, under daily veterinarian care. Weight, food and water intake were carefully monitored on a daily basis.

7.2.1 Anesthesia for Neurophysiology Experiments

The anesthesia protocol for all the experimental procedures have been described previously (Logothetis et al., 1999a; Logothetis et al., 2001). Briefly, glycopyrrolate (0:01 mg kg^{-1}) and ketamine (15 mg kg^{-1}), were used previous to general anesthesia. Induction with fentanyl (3 mg kg^{-1}), thiopental (5 mg kg^{-1}) and succinylcholine chloride (3 mg kg^{-1}), animals were intubated and ventilated using a Servo Ventilator 900C (Siemens, Germany) maintaining an end-tidal CO2 of 33–35mmHg and oxygen saturation above 95%. The anesthesia was maintained with remifentanil (0:5–2 μg kg^{-1}min) and mivacurium chloride (2–6 mg kg^{-1} h) which ensured no eye movement during electrophysiological recordings. The anesthetics dosage were established by measuring stress hormones and were selected to ensure unaffected physiological response at normal catecholamine concentrations (Logothetis et al., 1999a). In addition, it has been shown that using remifentanil has no significant effect on the neurovascular and neural activity of brain areas that do not belong to the pain matrix (Goense

and Logothetis, 2008). In particular, visual cortex does not bind remifentanil. We monitored the physiological state of the monkey continuously and kept within normal limits. Body temperature was tightly maintained at 38–39 °C. Throughout the experiment lactate Ringer's (Jonosteril, Fresenius Kabi, Germany) with 2:5% glucose was continuously infused at a rate of 10 ml $kg^{-1}1$ $h^{-1}1$ in order to maintain an maintained by the administration of hydroxyethyl starch as needed (Volulyte, Fresenius Kabi, Germany). We used anesthetized animals because the preparation allows longer data acquisition times and to associate particular neural events to specific stimulus features without the strong effects of animal cognitive state, including effects of attention and arousal that would introduce additional complication in the interpretation of signals.

7.2.2 Visual Stimulation

A few drops of 1% cyclopentolate hydrochloride were used in each eye to achieve mydriasis. Animals were wearing hard contact lenses (Wöhlk-Contact-Linsen, Schönkirchen, Germany) to focus the eyes on the stimulus plane. The visual stimulation in all experimental sessions was presented in the eye with stronger ocular preference of recording sites. The stimulus was presented using either an in-house custom-built projector (SVGA fibre-optic system with a resolution of 800 _ 600 pixels, a frame rate of 30 Hz), or a CRT monitor (Iiyama MA203DT Vision Master Pro 513, frame rate 118 Hz) placed at eye level, 50 cm in front of the eye. We found the same results with both display devices, except that monitor refresh with the 30 Hz stimulus induced cortical oscillations at 30 Hz. Since this is the result of using an artificial stimulus with a low refresh rate (a well-known issue at this stimulus frequency), we removed this from the data (see Artefact Removal) and pooled the results across all sessions. The visual stimulus consisted of high contrast (100%), gamma corrected, fast-moving, colourful movie clips (no soundtrack) from commercially available movies. Stimulus timings were controlled by a computer running a real-time OS (QNX, Ottawa, Canada). Stimulus-on periods of 120 s (5 sessions; 1 session: 40 s) were interleaved with stimulus-off periods (isoluminant grey screen) of 30 s.

7.2.3 Neurophysiology Data Collection and Analysis

The electrophysiological recordings were performed by doing a small skull trepanation, after which the dura was visualized with a microscope (Zeiss OpmiMDU/S5, Germany) and carefully dissected. The electrodes were slowly advanced into the visual areas under visual and auditory guidance using manual micromanipulator (Narashige Group, Japan). Electrodes consisted of laminar probes (NeuroNexus Technologies, Ann Arbor, USA). These electrodes contained 16 contacts on a single shank 3mm long and 150 µm thick. The electrode sites were spaced at 150 µm apart, with a recording area of 413 µm2 each. We used a flattened Ag wire, which was positioned under the skin, as reference electrode (Murayama et al., 2010). The recording access was filed with a mixture of 0:6% agar dissolved in NaCl 0:9%, pH 7.4 solution which guaranteed good electrical connection between the ground contact and the animal (Oeltermann et al., 2007). The impedance of the contact points was always measured during the experiments and ranged from 480–800 k. The signals were amplified and filtered into a broadband of 1–8000 Hz (Alpha-Omega Engineering, Nazareth, Israel) and then digitized at 20:833 kHz with 16 bit resolution (PCI-6052E; National Instruments, Austin, TX).

7.2.4 Luminosity Function

In order to best approximate the luminosity perceived by macaques, we relied on analogies with the human visual system. Research with humans suggest the luminosity function is linearly related to the long (L) and medium (M) cone activation, and independent of the short (S) cone activation (Stockman et al., 2008). Furthermore, the weighting of L and M activations towards perceived luminance is believed to be similar to the L:M ratio in the individual (Stockman et al., 2008). Old world monkeys such as macaques have an L:M ratio which is approximately 1:1 (Dobkins et al., 2000), so we assumed a luminosity function equally weighed between the L and M cone activations, $Y = L + M$. The 10° cone fundamentals of (Sharpe et al., 2005) were used since the cone fundamentals of old world monkeys are known to be very similar to humans (Dobkins et al., 2000). By taking the product of the emission spectra for pure red, green and blue with the luminosity function, integrating over wavelength

and normalizing, we obtained the following equations for relative luminance in terms of pixel intensity for the two devices used in the experiment.

$$Y_{\text{projector}} = 0.2171 \cdot R + 0.6531 \cdot G + 0.1298 \cdot B$$
$$Y_{\text{CRT}} = 0.1487 \cdot R + 0.6822 \cdot G + 0.1691 \cdot B$$

7.2.5 Artefact Removal

An artefact removal procedure was performed to reduce the effects of line noise (one session) and monitor refresh (the three sessions with 30 Hz stimulus). Artefact frequencies were identified by large, localized peaks in the power spectral density, which was computed with the periodogram method. In each case, the average artefact waveform was found and subtracted from the recorded signal. To correct for phase shifts of the artefact, the averaging and subsequent subtraction were performed in blocks of 50 artefact periods with a phase chosen to maximize the cross-covariance of the signal with the artefact waveform.

7.2.6 Current Source Density

The CSD was computed using the inverse CSD method (Pettersen et al., 2006). To compute this, we used a δ-source model of local field generation with a diameter of 500 μm, chosen to correspond to the effective size of columnar activity (Horton and Adams, 2005; Lund et al., 2003). Since this method requires an even spacing between voltage measurements, gaps caused by faulty recording contacts in the electrode were filled in with a local average (Wójcik and Leski, 2010). A homogeneous cortical conductivity of 0:4 Sm^{-1} was assumed (Logothetis et al., 2007). The agar solution placed on top of the recording access point had an NaCl concentration of 9 $mgmL^{-1}$, and the conductivity of this was estimated to be 2:2 Sm^{-1} (Kandadai et al., 2012). The CSD was spatially smoothed with a three-point Hamming filter (Einevoll et al., 2013).

7.2.7 Multiunit Activity

Figure 7.1 MUA was calculated by band-passing the voltage recording between 900 and 3000 Hz with a zero-phase sixth-order Butterworth filter, taking the absolute value, applying a 300 Hz low pass third-order Butterworth filter, and then down-sampling. This yields a smoothed spike rate, analogous to a population firing rate. Figure 7.3: MUA was calculated by down-sampling by a factor of 3, band-passing the voltage recording between 900–3000 Hz with a zero-phase sixth-order Butterworth filter, taking the absolute value, down-sampling by a further factor of 12.

7.2.8 Receptive Field Locations

The spatial RFs were found by reverse correlating the MUA and the pixel-by-pixel Z-scored frame-by-frame difference in luminance with a fixed lag of 66:7 ms. The rate of change in luminance was used because it is known to correlate well with thalamic drive. For each session, the RF center was located using the average of the reverse correlation across all cortical channels.

7.2.9 Identification of Cortical Laminae

Depth calibration of the electrode was performed by considering the spikes and CSD induced by both the onset of the movie and by 100 ms full-screen flashes (6 s flash interval). From the measured potentials, we determined the CSD and spike densities. Spikes were detected by high pass filtering the raw signal above 500 Hz with a zero-phase eighth-order Butterworth filter, and classifying any points more than 3.5 standard deviations above the mean signal during pre- and poststimulus periods as a spike, with a minimum inter-spike-interval of 1 ms. The majority of thalamic afferents in V1 stimulate L4 (indirectly: see Hansen et al., 2012), with the first cortical response manifesting at layer 4Cα (Callaway, 1998), resulting in an initial current sink and first burst of spiking activity located here. For each recording session, we found the contact exhibiting the first spiking and CSD response, the center of the most responsive region, and the center of the first CSD sink for both the movie onset and flash evoked activity. We took the average of these 8 locations and identified the closest electrode

contact as the location of layer 4C_. We estimated the laminar location of the rest of the recording depths by cross-referencing literature describing average thickness of cortical laminae in Macaca mulatta, area 17, (Lund, 1973). From this, the cortical depth was divided into 3 broad regions: supragranular (SG; layers 1– 3), granular (G; layer 4), and infragranular (IG; layers 5–6). High-resolution magnetic resonance imaging (MRI) scans of two of the animals were used to determine their cortical thickness at the recording location

To identify the depth of each contact, we measured the potential evoked in response to the onset of the movie clip, and in response to full-screen maximum luminance 100 ms flash stimuli with a 6 s interval. From the measured potentials we identified the boundary between the granular (G; layer 4) and infragranular (IG; layers 5–6) regions as the source/sink reversal in the evoked current source density (CSD; see Experimental Procedures and Supplementary Materials). We estimated the location of the boundary between the granular and supragranular (SG; layers 1–3) regions by cross-referencing literature describing average thickness of cortical laminae in Macaca mulatta, area 17 (Lund, 1973).

7.2.10 Power as a function of depth and frequency

To compute power and information as a function of temporal frequency, the cortical data (LFP and CSD) were filtered in a series of bands each with a fractional bandwidth of 50%, because cortical power falls off rapidly with frequency in a 1/f relationship. Each successive band begins and ends with frequencies 1.291 times higher than the last, so that each band has 0% overlap with bands further away than its immediate neighbors and a 44% and 56% overlap with its preceding and succeeding bands respectively. The data was filtered with a zero-phase sixth-order Butterworth filter, after which the instantaneous power was estimated by taking the squared absolute value of the Hilbert transform. The power in each band was integrated over a series of 50 ms windows, centered at the time of each frame change in the movie (once every 33 ms, leading to a 50% overlap of neighboring windows). The power in the 4–16 Hz and 60– 170 Hz bands was computed similarly. Figure 7.3A–B are plotted with power values averaged over all windows and trials, then expressed in decibels relative to the average power

1:5–248 Hz (estimated by summing the power in alternate bands). Throughout Figure 7.3A–B and Figure 7.10, data points are shown at the band centers.

7.2.11 Information as a function of depth and frequency

Power in each band was computed as above, then for each frequency band and depth we took a 10-bin histogram of the power across all the 50 ms windows for all repetitions. The bin edges were chosen such that 10% of the distribution fell into each bin, and the identity of which bin the window was allocated into was taken to be its "stimulus". We found the mutual information between the response and which frame was on screen at that time — the "stimulus" — by computing the Shannon information using the information breakdown toolbox (Magri et al., 2009b). Bias due to under-sampling was corrected for using the Panzeri-Treves method (PT) method (Treves and Panzeri, 1995). Each information calculation was also bootstrapped 20 times with a randomly shuffled mapping of stimulus to response (also bias-corrected). To ensure the amount of information was statistically significant, we checked each information estimate exceeded the bootstrap mean by more than 3 standard deviations of the bootstrap values. The bootstrap mean was then subtracted from the estimated information, to counter any residual bias.

7.2.12 Cortical Distribution of Power

For each session, the distribution of power across the cortical depth (Figure 7.2A–B right-hand insets) was determined by normalizing the power at each depth by the summed power across all cortical depths for that band. We then took an average across sessions, weighted by the number of cortical recording sites in each session to prevent faulty (omitted) electrode contact sites from distorting the result.

7.2.13 Information redundancy

Information redundancy was computed with the same stimuli windows as used in the information calculations. Let S denote the set of stimuli, and let X and Y each be the set of powers during each stimulus in one of the frequency bands at a particular depth. The

information in each $I(X;S)$ and $I(Y;S)$ was computed in the same manner as above. The information in the joint distribution $I(\{X,Y\};S)$ was computed by considering each combination of the binned X and Y as a different response, yielding a total of 100 different responses for $\{X,Y\}$.

The relative redundancy is then defined as

$$\text{Redundancy} = \frac{I(X;S) + I(Y;S) - I(\{X,Y\};S)}{I(\{X,Y\};S)}$$

and was computed using the information breakdown toolbox

7.2.14 Information about Spatial Components

The method to find the change in luminance in each spatial frequency band is illustrated in Figure 7.4. First, we took the 2D fast-Fourier transform of a 224 px square from the movie. A fourth-order Butterworth filter with a width of one octave was applied using a mask in the Fourier domain, and the result was projected back to the spatial domain. We then took the pixel-wise difference between each spatially filtered pair of consecutive frames. To provide a measure of the amount of change in luminance at this spatial resolution, we took the absolute amount of change in each pixel and summed this within a 2° diameter circular window centered at the receptive field location.

Applying this to the entire movie provided a temporal sequence of luminance changes in each spatial range. Similar to before, we took a 10-bin histogram and took the identity the bin in which each luminance change fell to be the “stimulus”. The mutual information between this stimulus and the neural response — the power within 4–16 Hz and 60–170 Hz frequency bands — was computed with a 67 ms lag between stimulus and response.

7.2.15 Information about Fine and Coarse Luminance Changes

Coarse and fine luminance changes in the stimulus were isolated in the same manner as the spatial components above, but using a low-pass (<0:3 cpd) and high-pass (>1 cpd) fourth-order Butterworth filter respectively. For both the 4–16 Hz and 6–170 Hz CSD powers, we computed the correlation and mutual information with the coarse and fine luminance changes, and averaged across sessions.

7.2.16 Information lag between granular and infragranular regions

The information about fine and coarse stimuli contained in 4–16 Hz and 60–170 Hz neural frequency bands was computed as a function of the lag between stimulus and response, in steps of 1:73 ms. For each cortical recording depth, we found response lag at which the information was at its maximum. For each session, the response peak-lag was averaged across the three electrode contacts in IG and also averaged across the three electrodes in G. A paired t-test was performed across all 6 sessions to test whether the G information peaked with a shorter lag than the IG information.

7.2.17 Cross-Frequency Phase-Amplitude Coupling

Strength of cross-frequency coupling was measured using the Modulation Index (Tort et al., 2010). CSD data was filtered for two bands, 4–16 Hz and 60–170 Hz, using a zero-phase sixth-order Butterworth filter, and the instantaneous phase of 4–16 Hz and envelope amplitude of 60–170 Hz were each estimated using a Hilbert transform. We took a histogram of the 4–16 Hz phase data points with 16 bins each of width π/8 radians, and took the average of the 60–170 Hz amplitudes simultaneous with the phase data points in each bin. This provides a distribution of amplitude at one depth as a function of phase at another. The Modulation Index is then the normalized Kullback-Leibler divergence of this distribution from a uniform distribution.

7.3 Results

To understand how oscillatory activity at different layers of primary visual cortex (V1) encodes naturalistic visual information, we recorded neural activity in cortical area V1 with a multi-contact laminar electrode array in four monkeys (Macaca mulatta), anaesthetized with opiates. The animals were presented with a clip from a Hollywood movie which lasted 30 s or 120 s and was repeated 40–150 times, depending on session (see Experimental Methods).

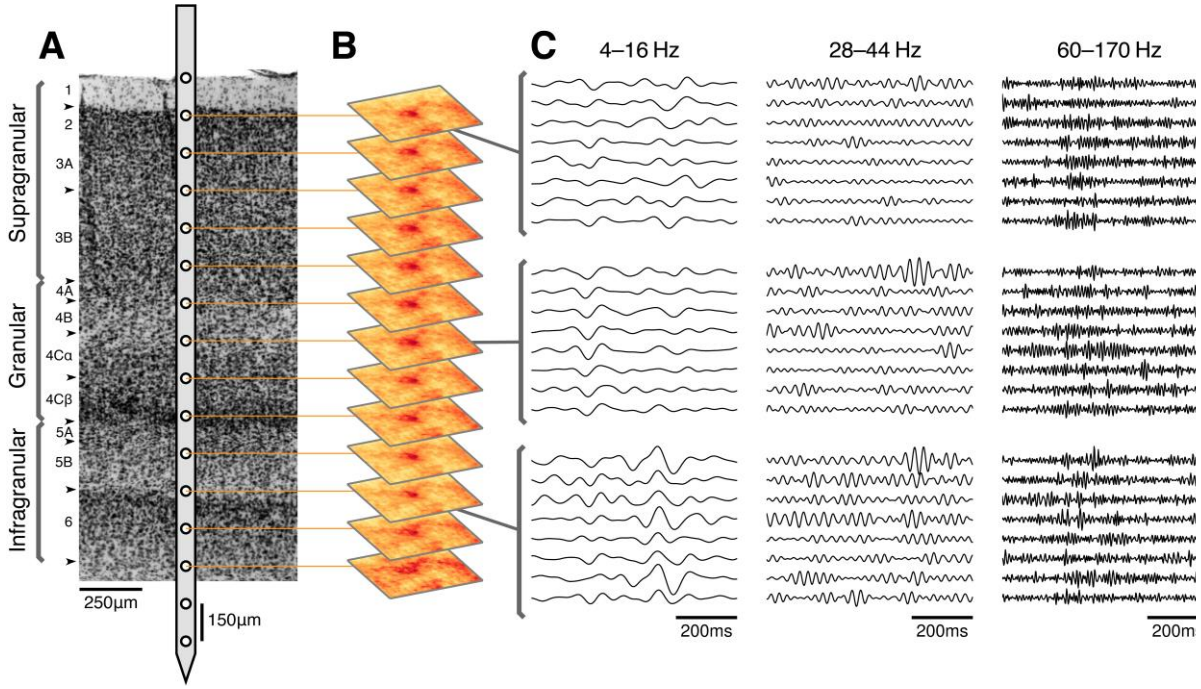

Figure 7.1 Overview of data collection and example data.
A: Illustration of experimental recording setup, showing approximate locations of electrode contacts in relation to a Nissl stained section of macaque V1 cortex. Boundaries between cortical laminae are indicated with arrowheads. (Stain reproduced from Tyler et al. (1998), with permission.) (Note: Electrode width is not to scale.) B: Receptive field locations were consistent across the cortical depth. Location of receptive field for each cortical recording site was identified by reverse correlating the MUA with the luminance changes of each pixel in the movie (session E07nm1). C: Example CSD traces from simultaneous recordings at three cortical depths for eight repetitions of a movie fragment (session H05nm7). The data are split into three temporal frequency bands (4–16 Hz, 28–44 Hz and 6–170 Hz, see Methods).

Each electrode housed 16 equally spaced (150 µm) contacts spanning a total depth of 2250 µm, and was inserted perpendicular to the cortical surface (Figure 7.1A). We recorded broadband LFPs from each electrode contact, and used the LFPs to compute at each electrode location the current source density (CSD), a measure of the local flow of charge at any given point (Einevoll et al., 2013). To align the depth of the electrodes across recording sessions, we identified the border between Layer 4 and 5 as the inversion of the CSD from sink to source in response to the onset of visual stimulation (Figure 7.8). We then divided the cortical depth into supragranular (G), supragranular (SG), and infragranular (IG) compartments (see Experimental Methods for details).

In order to identify the spatial regions of the movie stimulus that modulated the neural activity that we recorded, we estimated the spatial receptive field (RF) of the multi-unit activity (MUA)

recorded in each electrode contact site by reverse-correlating the rate of change of luminance of each pixel in the movie with the MUA. The spatial-RF locations that we identified (see Figure 7.1B for an example session) did not vary with depth, confirming the perpendicularity of the electrode penetration and that all electrode contacts were recording from the same cortical column.

7.3.1 Distribution of information across depth and frequency

We then considered how neural activity in different frequency bands was modulated by the movie. Figure 7.1C shows, at three cortical depths, CSD traces from eight example trials during a portion of the movie clip. We considered traces filtered within three frequency bands: 4–16 Hz, 28–44 Hz and 60–170 Hz. One can observe that the low-frequency activity repeats across trials for the G and IG depths. Activity in the 28–44 Hz range is inconsistent at all depths, and does not seem to be stimulus modulated. The envelope amplitude of the 60–170 Hz band is also consistent across trials, most clearly for the SG compartment.

We quantified these observations by computing the amount of information about the movie contained in the neural activity. We computed information about which frame is currently on screen in various frequency components of the LFP and CSD (see Experimental Methods). Excluding boundary effects at the top and bottom of the cortex where white matter contaminates estimates, power is fairly smooth across depth and decays as frequency increases (Figure 7.2A-B). However, the information contained in the power does not have such a smooth distribution and differs from this in both space and frequency domains. Instead, information is contained in specific frequencies at specific depths, in a similar manner for LFP and CSD (Figure 7.2C–D), with prominent maxima in the 4–16 Hz range at the top of the G region, and the 60–250 Hz range near the top of the SG region. Additionally, there are local maxima in IG for both the 4–16 Hz and 60 250Hz ranges. These results are consistent across sessions (Figure 7.9). As the information in the CSD has better spatial localization than the LFP (Einevoll et al., 2013; Kajikawa and Schroeder, 2011), for the remainder of the paper we

study only the CSD. These findings suggest that there are different information channels in a single cortical column.

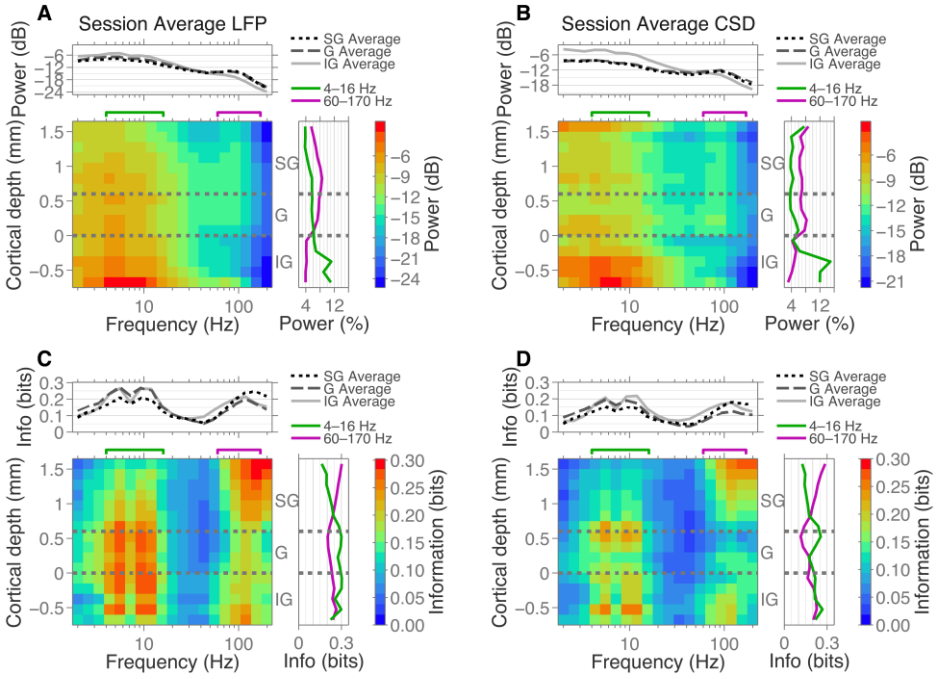

Figure 7.2 Distribution of visual stimulus information across both cortical depth and frequency.
A: Distribution of LFP power during stimulus presentation. Plot shows the geometric mean power over 6 sessions. Above, mean power within SG, G and IG regions. Right, laminar distribution of LFP power in 4–16 Hz and 6–170 Hz frequency bands. B: Same as A, but distribution of CSD power instead of LFP power. C: Distribution of information about the stimulus contained in LFP power. Plot shows the mean information over 6 sessions. Above, mean information within SG, G and IG regions. Right, cortical distribution of information in the power in 4–16 Hz and 6–170 Hz frequency bands. D: Same as C, but for information in CSD power instead of LFP power. Note that the information (C+D) is distributed very differently from the LFP and CSD power

7.3.2 Information redundancy between frequencies

Having identified the most informative regions in depth and frequency, there are two possibilities: either these regions contain the same information about the stimulus, through transcoding of one frequency range to another across the cortex, or the regions contain different information about the stimulus. We investigated how similar the information was by computing the redundancy of information contained in pairs of frequencies (see Experimental Methods). We found there are two frequency domains within which information is redundant: 4–40 Hz and >40 Hz (Figure 7.3A). Furthermore, the information contained in neural frequencies <40 Hz is different to the information contained in frequencies SI>40Hz, since

these measured to be independent (redundancy 0%). The same <40 Hz and >40 Hz division is observed for the signal correlation (Figure 7.10), and our results corroborate earlier findings (Belitski et al., 2008). Based on these and the above results, we extracted two bands (4–16 Hz and 60–170 Hz) that contain the most information and independently encode information about the stimulus.

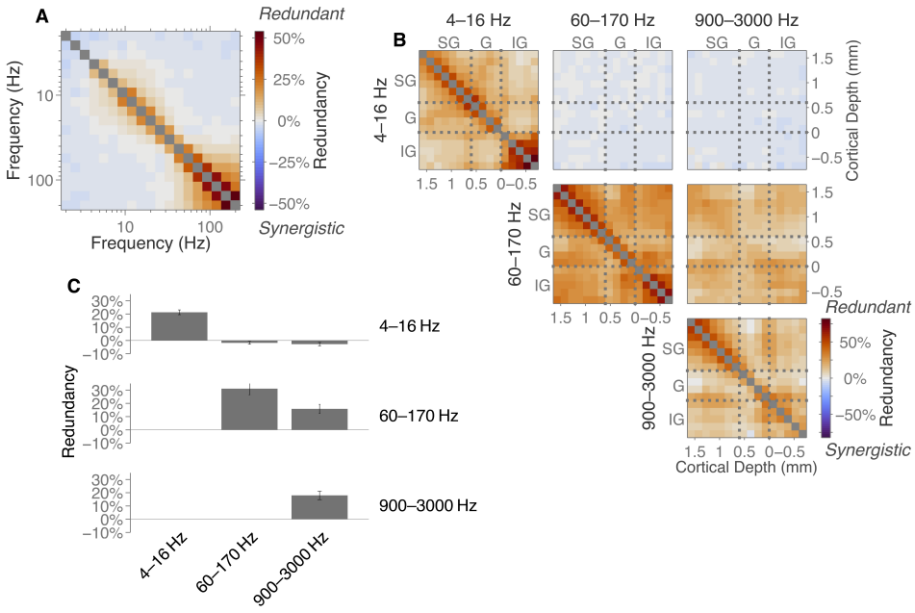

Figure 7.3 CSD information redundancy across frequency bands and laminae.
A: Median redundancy between pairs of frequencies over the 12 recording sites, averaged over 6 sessions. B: Redundancy between pairs of recording sites of the information in three frequency bands. Mean of 6 sessions. C: Average of cross-channel redundancy shown in B. Note, that while there is substantial redundancy within bands and between the 60–170 Hz and 900–3000 Hz bands, there is little redundancy between the 4–16 Hz and 6–170 Hz band, indicating independent coding.

7.3.3 Information redundancy across depth

Having established the independence of these bands, we investigated the redundancy between the power of oscillations at different cortical depths (Figure 7.3D). For the 4–16 Hz frequency range, we found there is some redundancy across the entire cortical depth, but there are two distinct cortical regions (above and below the CSD reversal, marked as 0mm depth) within which information is more redundant. These findings are in agreement with (Maier et al., 2010), who found a transition corresponding to the G/IG boundary which isolated two cortical regions with high coherence <100 Hz. Gamma oscillations (6–170 Hz) code, with substantial redundancy across the cortical depth, with some compartmentalization of SG and

IG activities. In addition we also included the MUA signal, which corresponds to the local population firing rate. There is less redundancy of information across cortical depths for MUA than for gamma; this observation is due to spiking activity being more localized than gamma oscillations. In agreement with previous findings (Belitski et al., 2008), we find that information contained in the gamma range and information in the MUA are redundant with each other. This is to be expected, since MUA is known to be correlated with the gamma cycle.(due to peaks/troughs in gamma relating to peaks/troughs in firing rate). Overall redundancy is summarized in Figure 7.3C, which shows the average across all cortical depths for each pair of frequency bands. Importantly, we find the information in the 4–16 Hz range is independent of the information contained in both gamma and MUA frequency ranges across all cortical depths. In particular, this means the two localized high information regions in depth-frequency space from Figure 7.2D contain independent information to one-another. Importantly, this mean this argues against a situation where SG contains the same information as G/IG activity transcoded from low-frequency to high-gamma oscillations; at least some of the information is unique to each.

7.3.4 Information about spatial frequency components of visual stimulus

In the above, we have seen there are two frequency bands in V1 which, across all the cortical depth, contain independent information to each other. Next we investigate what aspects of the visual scene these two independent components contain. Since neurons in the primary visual cortex are known to respond strongly to moving sinusoidal gratings with specific spatial frequencies, we considered how much information the frequency bands contained about changes in luminance as a function of spatial frequency. Hereto, we decomposed the series of frames in the movie into set of spatial frequency components by finding the rate of change of luminance within a given set of spatial frequency bands (see Figure 7.4; Experimental Methods), and then computed the amount of information about this series contained in the neural activity.

We found the low frequency CSD bands (<40 Hz) contained more information about low, coarse spatial frequencies (0:1–0:6 cpd), whereas the higher frequencies (>40 Hz) contained more information about high, fine spatial frequencies (0:6–5:0 cpd; Figure 7.5B). This was not a continuous transition; instead we observe an abrupt change at 40 Hz, with lower and higher neural oscillation frequencies tuned to stimulus features with different spatial frequencies. This was true across the entire cortical depth (Figure 7.5C–D), where the two frequency bands (4–16 Hz and 60–170 Hz) contained information about opposing spatial frequencies. The distribution of information across the cortical depth corresponds to that found in Figure 7.2D. These results are summarized in Figure 7.5A, which shows the average across the cortical depth. Information reaches its maxima around 0:2 cpd for the 4–16 Hz frequency range and 2:5 cpd for the 60–170 Hz frequency range.

In Figure 7.6, we summarise the previous results by extracting two spatial frequency bands: coarse (<0:3 cpd, low-pass spatial filter) and fine (>1 cpd, highpass spatial filter), example traces for which are shown above Figure 7.6A. These spatial components have low correlation between them (Figure 7.6B; r = 0:18). Example CSD traces are also shown for two electrode contacts over same time period (left side). Note that peaks and troughs in the coarse luminance signal are coincident with peaks and troughs with the alpha power, and similarly for the fine luminance and gamma power, indicating the positive relationship between stimulus and cortical response. This observation is quantified by the correlation and mutual information between these components (Figure 7.6A).

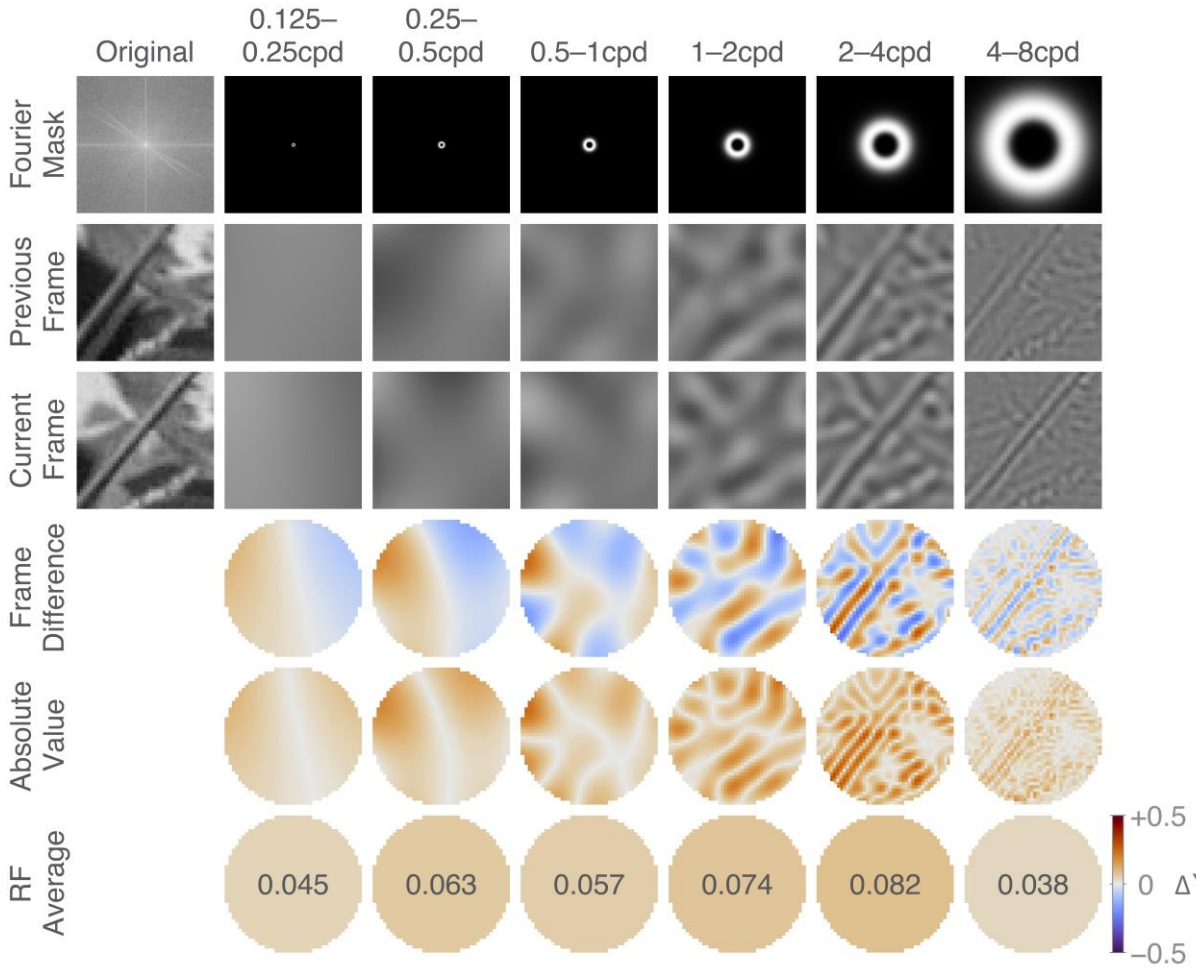

Figure 7.4 Extraction of spatially filtered luminance components.
The luminance of the original video (left) is fast-Fourier transformed in a 224 px χ 224 px square for each frame (top-left: FFT of "current frame"). The mask isolates bands of spatial frequencies that are one octave wide (Row 1), yielding the spatially filtered frames (Rows 2 and 3). The stimulus magnitude at each spatial frequency band was obtained by taking the luminance difference of successive frames (Row 4), taking its absolute value (Row 5), and averaging this within the receptive field (Row 6).

7.3.5 Layer 1 6–170 Hz amplitude is coupled to L5 4–16 Hz phase

In previous section "Information redundancy across depth", we showed that high and low LFP frequencies contain independent information to one-another. To further investigate the relationship between these two bands, we computed the cross-frequency coupling between the low frequency phase and high frequency oscillation amplitude. In agreement with previous work (Spaak et al., 2012), we found there is significant coupling between the 4–16 Hz phase in lower-G and mid-IG with the and amplitude of 6–170 Hz oscillations in upper SG (Figure

7.7). There is also localized coupling between the 4–16 Hz phase with 6–170 Hz amplitude in G and IG. These findings were all true of both the stimulus driven and spontaneous recordings.

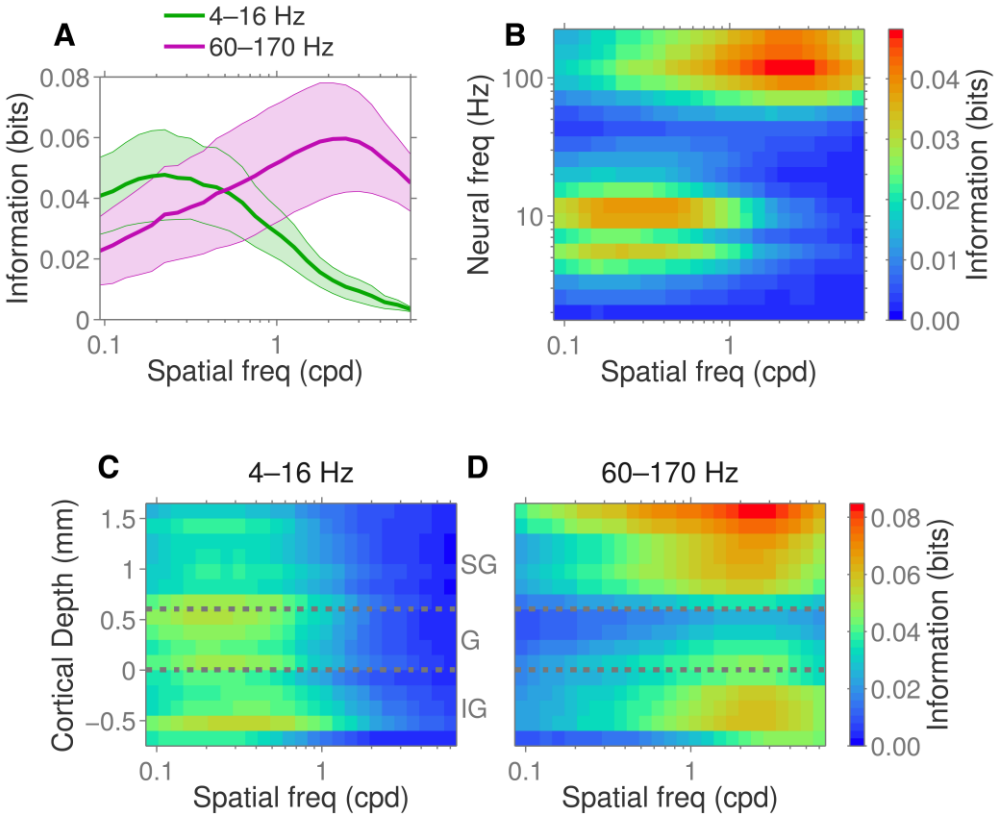

Figure 7.5 Information about different spatial components across laminae and frequency bands.
A: Information about spatial components of the stimulus contained in low frequency CSD power (4–16 Hz, average of information within G region; green) and high frequency CSD power (6–170 Hz, average of information within SG region; purple). Shaded region: standard error across 6 sessions. B: Information about visual spatial components contained in a range of CSD frequencies, median over 12 recording sites. C,D: Information in low (4–16 Hz) and high (6–170 Hz) CSD frequency bands across cortical laminae. Plots A-D are mean of 6 sessions.

7.4 DISCUSSION

In summary, we find while LFP power is smooth and its depth profile is close to flat (Figure 7.2) the information that the LFP encodes reveals much more structure. We found there are two cortical regions at which oscillations in these frequency ranges are much more informative. Namely 4–16 Hz at upper granular and mid-infragranular, and 6–170 Hz at upper supragranular and mid-infragranular regions.Previous work (Belitski et al., 2008) has shown that in the macaque primary visual cortex information is coded in two frequency bands (<40 Hz and >40 Hz) containing independent information about natural visual scenes. Our analysis

extended across the cortical depth, and we found there are two cortical regions at which oscillations in these frequency ranges are much more informative (4–16 Hz at upper-G and mid-IG; 6–170 Hz at upper-SG and mid-IG regions).

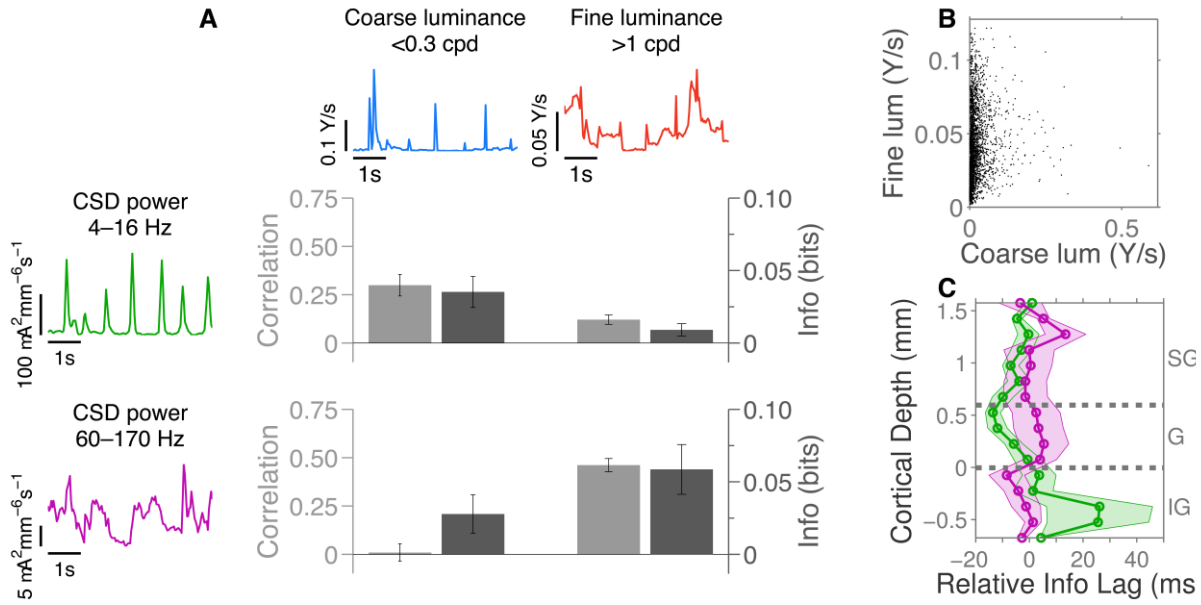

Figure 7.6 Overview of information components.
A: Relationship between Coarse/Fine changes in luminance and Low/High frequency neural activity. Left: Instantaneous power in 4–16 Hz band (averaged over trials and SG layers) and 6–170 Hz band (averaged over trials and G layers) for an example session (H05nm7). Above: Coarse (<0:3 cpd) and fine (>1 cpd) rate of change in luminance over the same time period. The barchart shows, for each pair of stimulus and response, Pearson's correlation coefficient (pale grey; left-hand axis) and mutual information (dark grey; right-hand axis). B: Fine versus coarse change in luminance for each frame change in the stimulus. C: Lag between stimulus and response yielding maximal information (green: 4–16 Hz and coarse luminance; purple: 6–170 Hz and fine luminance).

We also examined whether changes in luminance at different spatial frequencies induced differential changes in the cortex as a function of neural frequency and depth. Namely, high spatial frequencies are encoded in oscillations faster than 40 Hz and low spatial frequencies are encoded in oscillations slower than 40 Hz. We found that frequencies below and above 40 Hz contain information about different spatial frequencies.

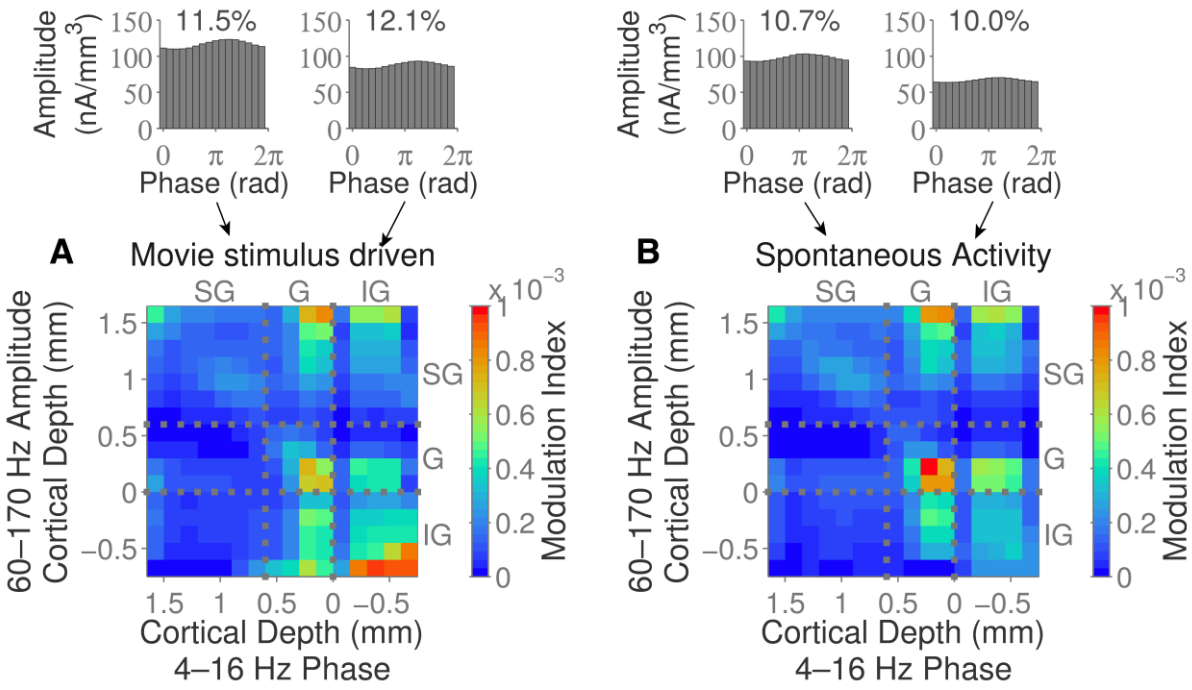

Figure 7.7 Cross-frequency phase-amplitude coupling
Phase-amplitude modulation index between low frequency (4–16 Hz) phase and high frequency (6–170 Hz) amplitude (A: movie driven activity; B: spontaneous activity). Mean of 5 sessions. Above, amplitude as a function of binned phase for an example session (H05391). Left inset: IG/IG coupling; Right inset: IG/SG coupling.

There are multiple possible interpretations of these findings, of which one, many, or even none may be correct. Firstly, it is conceivable that the coding of different aspects of the stimulus into different frequency bands is a computational strategy of the cortex. Our results suggest there is multiplexing in the cortex, with low frequency and high frequency oscillations of the same population activity simultaneously encoding low and high spatial frequency components of the stimulus respectively. The idea of different frequency bands conveying different spatial frequency components of the stimulus has been proposed before from the results of an EEG study (Smith et al., 2006).

One would expect that if certain oscillation frequencies in the visual cortex contain information about specific aspects of the stimulus, this is likely to be because the brain has encoded this information into oscillations in the activity of the local population. This would only make sense if the information is utilized by the brain in order to interpret its stimuli. Consequently, our results indicate there is multiplexing in the cortex, with low frequency and high frequency

oscillations of the same population activity simultaneously encoding low and high spatial frequency components of the stimulus respectively. Intuitively, information contained in the two frequency bands can be combined by downstream visual cortical regions to regain the original stimulus as necessary. The idea of different frequency bands conveying different spatial frequency components of the stimulus has been proposed before from the results of an EEG study (Smith et al., 2006).

Additionally, we can speculate about why separating the visual scene into low frequency (coarse) and high frequency (fine) components in V1 is useful. One possibility is that low frequency oscillations are output from V1 along the dorsal visual stream, whereas high frequency oscillations travel propagate through the ventral stream. Another possibility is that broad, coarse changes in the stimulus are useful for making rapid responses in the motor cortex to sudden changes, such as approaching threats.

Separation into low and high frequency domains with different properties seems to be a common property of the cortex. In motor cortex, activity at <13 Hz and >60 Hz relates to behavior but there is a separating band ≈30 Hz which does not (Rickert et al., 2005). In the hippocampus, there is a gating effect between 30 Hz and 40 Hz, with lower but not higher frequencies able to propagate to the cortex (Moreno et al., 2015). This suggests this encoding scheme is common across the cortex. Some studies have suggested that the coupling of oscillations between two cortical regions facilitates the transmission between them (Buffalo et al., 2011; Fries et al., 2001; Rossi et al., 2001).

A separation of visual stimuli into coarse and fine channels is known to occur before the stimuli arrive in the cortex. The outputs from different types of retinal ganglion cells (RGCs) travel to the cortex through different regions of a lateral geniculate nucleus (LGN). The M-pathway arises from RGCs with large, achromatic receptive fields, and projects mainly onto layer 4Cα in V1. The P-pathway originates with RGCs with smaller, chromatic RFs providing higher spatial resolution but lower temporal resolution; this pathway projects onto layer 4Cβ

(Callaway, 1998). It is possible that the two frequency channels in V1 relate to the two pathways providing its inputs.

Since layer 4 of V1 (L4) is generally regarded as the primary layer of V1 which receives afferent inputs from a LGN, some readers might wonder how information in the gamma band has “arisen” in SG layers without passing through G. However, our results do not necessitate this. Fine-resolution information about the visual stimulus can arrive from the LGN into L4 of V1, with the information encoded into which neurons the afferent connections target. This information is not detectable from the population level activity.

We observed that each frequency has a similar amount of power across the cortical depth, but oscillations at these frequency ranges contain much more information at particular cortical depths. This is curious as it indicates that, for any given frequency band, oscillations are present in all cortical depths, but most of the oscillations exhibited are not stimulus encoding.

We observed qualitatively that information-carrying events in L4 were large, temporary deflections with a long duration (low frequency), whereas L5/6 contained sustained oscillations (Figure 7.1 for examples). The deflections in L4 were usually coincident with scene cuts or rapid changes in the stimulus. This could be interpreted as an error signal, since sudden, large changes in the stimulus would result in any predictive model of the stimulus making large errors. However, a more simple interpretation is these deflections correspond to changes in the afferent input to V1 from LGN. In support of this, we note that the spatial scale of the information in the low frequency band (0:25 cpd) approximately corresponds to the size of receptive fields for regions of the V1 corresponding to the parafovea (2°).

The sustained oscillations in L5/6 also contain information about coarse changes in the stimuli. These cortical layers are known to have connections to the motor cortex, feedback to a LGN and receiving feedback from higher cortical regions.

Recent work has indicated that alpha and gamma bands are important for feedback and feedforward activity respectively (van Kerkoerle et al., 2014a). This study found that gamma

waves are initiated at L4 and propagate outwards to the top of SG and bottom of IG, with alpha waves propagating in the opposite direction. Our study finds the most information in gamma bands at the very top (and very bottom) of the cortex, and the most information in alpha bands at the top of L4 (and layer 6 of V1 (L6)). Reconciling these results together, we find that there is most information in the power of the alpha and gamma oscillations at the cortical depths where they terminate, and the least where they originate. This suggests that the oscillations are generated at one cortical depth without much stimulus dependency, but as the oscillations propagate up and down the cortex they are either amplified or suppressed in a stimulus dependent manner.

In agreement with previous work (Spaak et al., 2012), we found there was cross-frequency coupling between the stimulus-encoding power of gamma oscillations in layer 1 of V1 (L1) and the phase of alpha oscillations in lower L4. Anatomically, we believe this is related to the pyramidal cell bodies in layer 5A of V1 (L5A), which have apical dendritic tufts in L1 (Hill et al., 2013) (Zhu and Zhu, 2004). This cross-frequency coupling could be one mechanism through which the L1 gamma wave containing high levels of information about the stimulus is converted into an alpha oscillation for feedback into the hierarchically lower cortical region. Neurons in layer 5 of V1 (L5) are known to be related to long-range cortical output (Hill et al., 2013).

7.5 APPENDIX

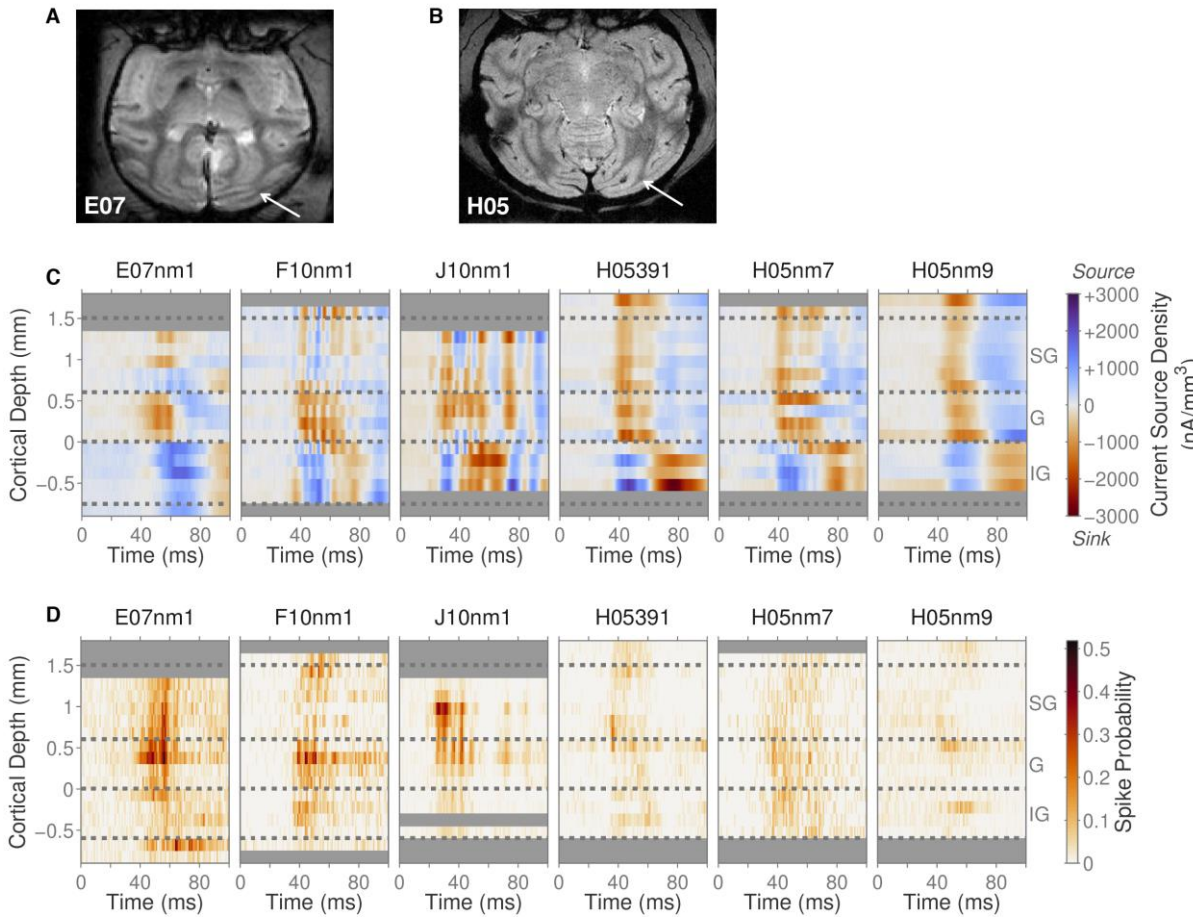

Figure 7.8 Electrode alignment.
A-B: High resolution MRI scans of two animals used to measure cortical thickness. C: Stimulus triggered average CSD responses. For sessions H05391, H05nm7, H05nm9 and E07nm1, the average response to onset of the movie stimulus is shown, whereas for sessions F10nm1 and J10nm1 the response to a full-field flash is shown. D: Corresponding spike densities for the responses in panel C (1ms window duration). [Accompanies Figure 7.1]

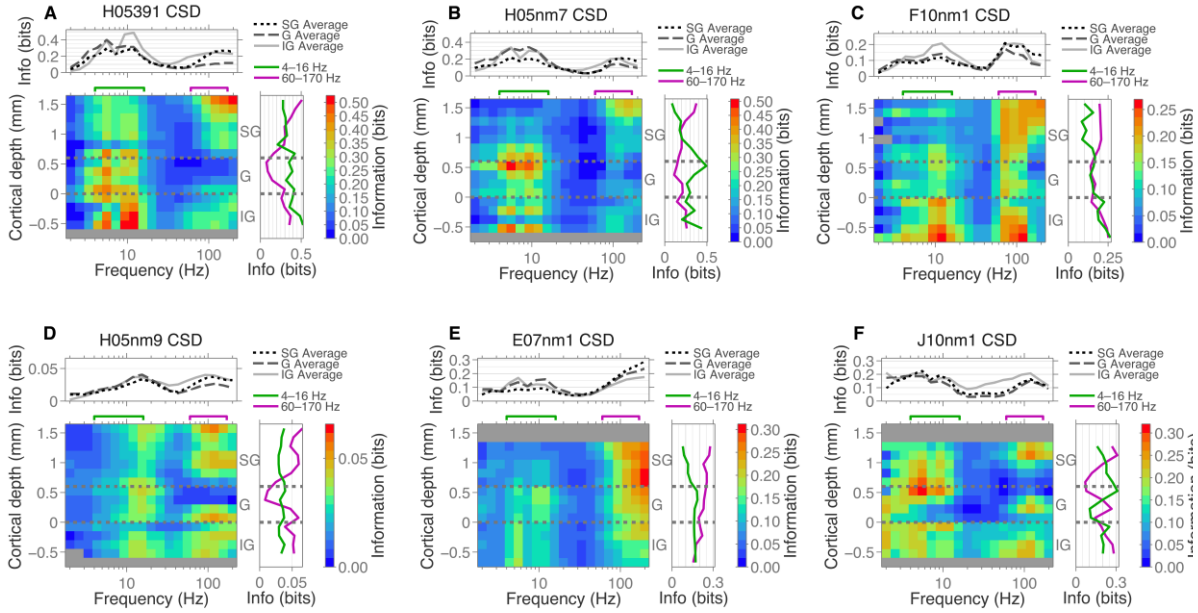

Figure 7.9 Distribution of information about the movie across both cortical depth and frequency for individual sessions

A-F: Same as Fig. 2D, but shown for each recording session individually. Distribution of information about movie stimulus contained in power. Plot shows the mean information over 6 sessions. Above, mean information within SG, G and IG regions. Right, cortical distribution of information in the power of two frequency bands; 4-16Hz and 60-170Hz. [Accompanies Figure 7.2]

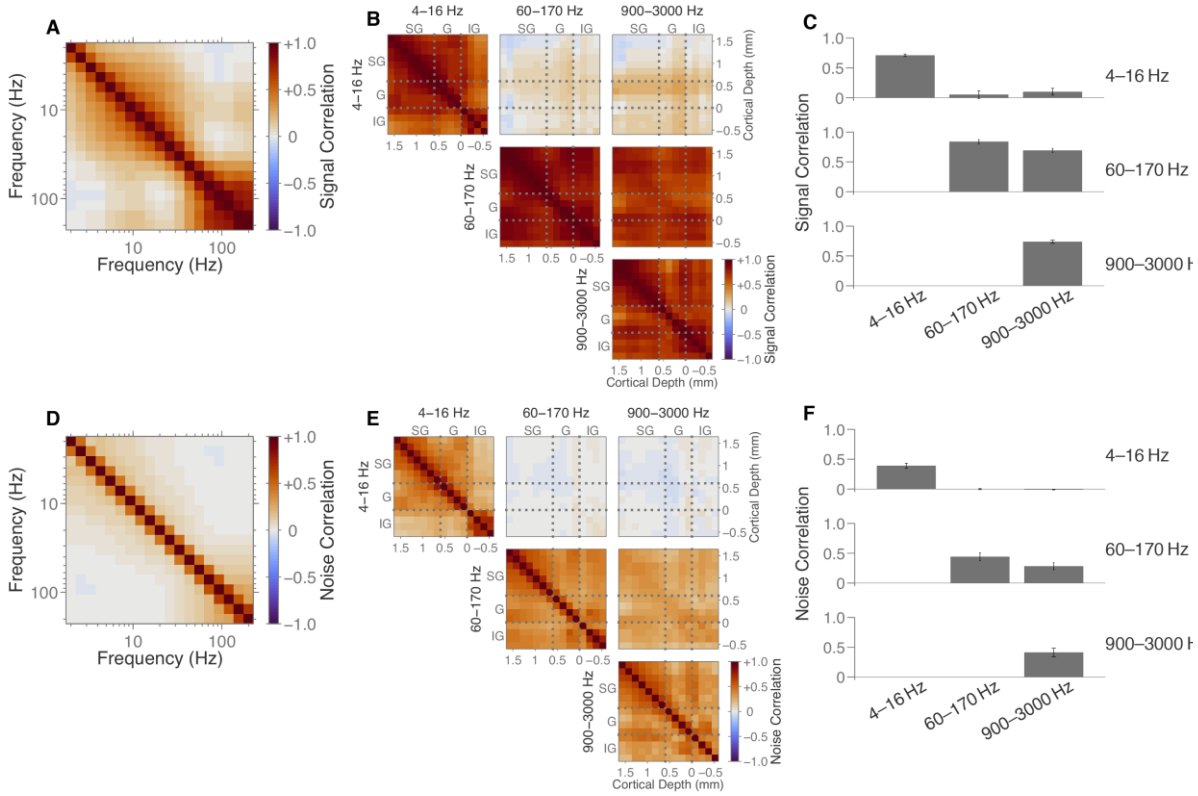

Figure 7.10 Signal and noise correlations.
A: Median signal correlation between pairs of frequencies of the 12 recording sites, mean across 6 sessions. B: Signal correlation between pairs of recording sites across the three frequency bands. Mean of 6 sessions. C: Average signal correlation shown in B. D-F: Same as in A-C, but for noise correlation instead of signal correlation. [Accompanies Figure 7.3].

8. Manuscript Nr. 6

Dopamine boosts mid-frequency oscillations and visual information in output layers of macaque visual cortex

This chapter has been submitted to **Curr. Biol.**

Daniel Zaldivar, Jozien Goense, Scott C. Lowe,

Nikos Logothetis & Stefano Panzeri.

8.1 INTRODUCTION

An animal's response to a sensory stimulus depends not only on the stimulus but also on the animal's cognitive state. These cognitive states are under the control of diverse neuromodulators that enable transitions across brain states. Neuromodulators have a wide range of effects on the highly nonlinear dynamics of membrane properties and synapses (Dayan, 2012; Grashow et al., 2009). This complexity of the effects of neuromodulation likely serves key computations, enabling neurons to be more flexible in their ability to encode and process differently information in different contexts (Dayan, 2012; Marder et al., 2014). For this reason, the effect of neuromodulation must adapt to the intrinsic dynamics of target neurons or circuits (Dayan, 2012) and it may be profoundly different, for example, between resting state and sensory- or task-related neural responses. Understanding the effects of neuromodulators on neural information processing is thus essential to understand the neural bases of adaptive computations. Furthermore, identifying signatures of neuromodulation-induced changes in neural activity is key to reveal the potential causes of cognitive deficits and establish potential links to the pathophysiology of brain disorders (Uhlhaas and Singer, 2015).

Here we investigate the effect of neuromodulation on mesoscopic cortical activity measured by the local field potential (LFP). LFPs capture synaptic activity and other integrative neural processes expressed by neural populations located a few hundred microns from the electrode tip (Belitski et al., 2008; Magri et al., 2012b; van Kerkoerle et al., 2014b; Whittingstall and Logothetis, 2009). Importantly, LFP recordings reveal oscillatory activity expressed by interacting networks of neurons over a wide range of frequencies (Einevoll et al., 2013; Logothetis, 2008), which are traditionally decomposed into bands which correlate with distinct behavioral states (Basar et al., 1980; Lindsley and Wicke, 1974; Steriade et al., 1991; Steriade and Hobson, 1976), and are thought to originate from distinct types of neural events triggered by different processing pathways. This network-level oscillatory activity is viewed as an

important “middle ground” linking single-neuron activity to behavior (Buzsaki and Draguhn, 2004), and has been implicated in several brain computations, including sensory coding (Belitski et al., 2008; Schroeder and Lakatos, 2009; van Kerkoerle et al., 2014b; van Kerkoerle et al., 2017) and dynamically modulating information transmission along feedforward, lateral and feedback pathways (Einevoll et al., 2013; Logothetis, 2008; van Kerkoerle et al., 2014b).

The mammalian sensory cortex has a clear six-layered organization (“laminar”) structure (Lund, 1988). Every layer is composed of excitatory and local inhibitory neurons that have distinct patterns of projections within and between layers, and to other cortical and sub-cortical areas (Callaway, 1998; Henry et al., 1979; Lund, 1973, 1988; Nassi and Callaway, 2009). For example, input layers project locally to superficial and deep layers; superficial layers project to higher-order visual areas and also locally to superficial and deep layers; deep layers project primarily to subcortical nuclei. Such laminar organization of projection suggest that sensory coding, and possibly its neuromodulation, must be layer-dependent.

To study how neuromodulation affects visually-evoked and intrinsic neural processes, it is therefore critical to investigate the laminar influence of neuromodulators in the cortical laminae. We used laminar probes to simultaneously record LFPs at different depths and investigated the effects of systemically injected dopamine (DA) in V1 of anesthetized monkeys. We focused on the effects of DA because it is known to improve visual sensory processing through long-range interactions (Moore and Zirnsak, 2017; Noudoost and Moore, 2011; Zaldivar et al., 2014) and because alterations in the dopaminergic (DAergic) system are associated with visual deficiencies in Parkinson’s disease patients. Presentation of naturalistic movies elicits a rich spectrum of LFP activity because it introduces sufficiently high variations in the experimental conditions that are more likely to engage distinct neural processes (Belitski et al., 2008; Belitski et al., 2010; Szymanski et al., 2011). We found a clear marker of the presence of DA in the power of mid-frequency [19-38 Hz] spontaneous (i.e., non-stimulus driven) LFP oscillations. We found that DA increased the stimulus information encoding over all frequencies, both more markedly in the gamma range and in the superficial and deep

layers, suggesting that DAergic neuromodulation may prepare the higher order area for the processing of incoming sensory signals and promote the readout of task-related information.

8.2 METHODS

8.2.1 Ethical Statement

Data were collected from the visual cortex of adult monkeys *(Macaca mulatta: three female, H09, G09, and G11; one male, K07;* 5–11 kg, 6-12 years). All the experimental procedures were approved by the local authorities (Regierungspräsidium, Baden-Württemberg, Tübingen, Germany, Projects Nr. KY 4-09 and KY 4-16) and were in full compliance with the guidelines of the European Community (EUVD 86/609/EEC) and following the recommendations of the Weatherall report for the care and use of non-human primates.

8.2.2 Pharmacological Injections

Each experiment (n = 15 in 4 animals) consisted of neural recording during which systemic applications of L-DOPA+Carbidopa were performed. We used a custom-built pressure operated pump to systemically inject dopamine (Zaldivar et al., 2017). The actual flow and volume were continuously monitored by high precision flowmeters (Sensirion, Switzerland). Preconditioning was done with 1.5 mg/kg Carbidopa diluted in 50 ml phosphate-buffered-saline (PBS) and injected at 1.1 ml/min over a period of 12 minutes. The combined L-DOPA+Carbidopa applications used 2.1 mg/kg + 0.5 mg/kg L-DOPA+Carbidopa, diluted in 50 ml PBS and injected at a rate of 1.1 ml/min over 12 min. The PBS solution consisted of NaCl 137 mM, KCl 2.7 mM, Na_2HPO_4 8.1 mM, KH_2PO_4 1.76 mM, and had a pH of 7.35. All chemicals were purchased from Sigma-Aldrich (Schnelldorf, Germany).

8.2.3 Neurophysiology Data Collection and Analysis

We performed a small skull trepanations (4-5 mm diameter) in primary visual cortex (V1) using the stereotaxic coordinates in each monkey. Subsequently, the meninges were carefully dissected layer-wise (~1mm dissection diameter) under the microscope (Zeiss Opmi MDU/S5, Germany). The laminar electrodes (NeuroNexus Technologies, Ann Arbor, USA) were slowly

advanced into the cortex under visual- and auditory guidance using a manual micromanipulator (Narashige Group, Japan). The final electrode position was determined based on CSD analysis (Pettersen et al., 2006) and coherence analysis (Maier et al., 2010). Coherence analysis measures the similarity in the temporal structure of two signals and quantifies the extent to which they are linearly correlated. This helped us to better estimate the boundaries between deep and middle layers (Maier et al., 2010). As a final confirmation, the location of layer 4 was confirmed by analysis of multi-unit-activity (MUA) that identified layers with shortest latency of spiking activity (not shown). Our laminar probes contained 16-contacts on a single shank of 3 mm length and 50 µm thicknesses. The contacts were spaced 150 µm apart, with a recording area of 176 μm^2 each. We used a flattened Ag wire positioned under the skin as reference (Zaldivar et al., 2017). The area around the electrode was filled with a mixture of 0.6% agar dissolved in NaCl 0.9%, pH 7.4 which guaranteed good electrical contact between the ground and the animal. The impedance of the electrodes sites was measured before and during the experiments and ranged from 500 to 800 kΩ.

The signals were amplified and filtered into a band of 1-8 kHz using a multi-channel-processor amplifier system (Alpha-Omega Engineering, Nazareth, Israel) and then digitized at 20.833 kHz with a 16-bit resolution ADC-converter (National Instruments, Austin, TX), ensuring sufficient resolution to capture both local field potentials and spiking activity. The LFPs were extracted from the raw recordings by bandpass filtering the signals between 1 and 150 Hz. The filtering procedure was as follows: First, the neural signals sampling rate was reduced from the original sampling rate by a factor of 3 (from 20,835 to 6945 Hz). It was then bandpassed filtered and down-sampled in two steps: first to a sampling rate of 1.5 kHz with a fourth order Butterworth filter (500 Hz cutoff), and then to a rate of 500 Hz using a Kaiser window between frequencies of 1 and 150 Hz, sharp transition bandwidth (1 Hz). The two-step procedure was computationally more efficient than a single filtering operation to the final sampling rate. The sharpness of the second filter was used to avoid aliasing, without requiring a higher sampling rate attributable to a broad filter transition band, which would increase the

computational cost of all subsequent operations. Forward and backward filtering was used to eliminate phase shifts introduced by the filters. The PSD were computed over 500ms non-overlapping windows using the multitaper method. The normalized PSDs were obtained by dividing the power at each frequency by the average power computed during the pre-injection movie presentations at that frequency.

8.2.4 Information Theoretic Analysis

To determine how well the power, r_f, (of either LFP or spikes) at a certain frequency, *f*, encodes the visual features in the movie, we computed the mutual information, $I(S;R_f)$ (Quian Quiroga and Panzeri, 2009; Shannon, 1948), between the stimulus window in the movie and the power at frequency f as

$$I(S;R_f) = \sum_s P(s) \sum_{r_f} P(r_f \mid s) \log_2 \frac{P(r_f \mid s)}{P(r_f)} , \qquad (1)$$

where $P(s)$ is the probability of presentation of the stimulus window *s* (here equal to the inverse of the total number of stimulus windows), $P(r_f \mid s)$ is the probability of observing a power r_f at frequency *f* in response to a single trial to stimulus *s*, and $P(r_f)$ is probability of observing power r_f across all trials in response to any stimulus. $I(S;R_f)$ quantifies the reduction of the uncertainty about the stimulus that can be gained from observing, in a single-trial, the power at frequency f. Since we use base-two logarithms, $I(S;R_f)$ is expressed in units of bits. One bit of information means that, on average, observation of the neuronal response in one trial reduces the observer's stimulus uncertainty by a factor of two.

To estimate numerically from the LFP power the values of information in Eq (1) in the real data, we used the information breakdown toolbox (Magri et al., 2009a) and proceeded as follows. First, the power values across trials at each frequency was discretized into 5 equally populated bins. The binned values were then used to estimate the stimulus – LFP power

probabilities in Eq 1. We used the Panzeri-Treves algorithm (Panzeri and Treves, 1996) for estimating and subtracting out the bias in information estimates due to limited sampling. We assessed the statistical significance of the information values against a null-hypothesis "bootstrap" distribution of values obtained by pairing at random movie scenes and power of neural responses in each trials, thus effectively removing any relationship between the power at a given frequency and the movie scene eliciting it (bootstrap test).

8.2.5 LFP- signal and noise correlations across different frequencies and layers

We determined which frequencies have related stimulus selectivity, and which have shared sources of stimulus-unrelated variability, by performing a linear analysis of correlation (signal and noise) across frequencies. The signal correlation coefficient was computed for each frequency pair ($f1$ and $f2$) and channel as the Pearson's correlation coefficient across stimuli of the trial averaged response (Belitski et al., 2008). Positive values resulting from this analysis are an indication that two frequencies have similarities in their stimulus preferences, whereas zero value indicates that the two frequencies have not relationship in their activity (Averbeck et al., 2006; Panzeri et al., 1999).

The noise correlations are defined as covariations in the trial-by-trial fluctuations around the mean response. (Averbeck et al., 2006; Einevoll et al., 2013). The noise correlation coefficient was computed for each frequency pair ($nf1$ and $nf2$) and channel as the Pearson's correlation coefficient across stimuli of the trial-averaged-subtracted power. This quantifies the correlations of the variations around the mean of each trial and stimulus window (Averbeck et al., 2006; Belitski et al., 2008). Positive values for the noise correlation indicate that when the power of one frequency raises above its mean, the power in the other frequency is also more likely to do so (Belitski et al., 2008).

The overall amount of correlation across all trials and stimulus windows between the responses at frequencies $f1$ and $f2$, is the result of both noise and signal correlations. The strength of correlations was quantified as the Pearson correlation coefficient (across all trials

and stimulus windows) of the powers $f1$ and $f2$. The overall correlation is typically higher than the noise correlation if both noise and signal are positively correlated, whereas it can be smaller than the noise correlation if the noise correlation is positive and the signal correlation is negative or null (Belitski et al., 2008).

8.2.6 Coefficient of Variations of Signal and Noise

The information analysis determines which frequencies allow better discrimination among stimuli on a single trial, but it does not tell if the increase in information increase at certain frequencies can be attributed to greater reliability across trials of the responses at these frequencies, or to a more marked stimulus modulation of neural activity. To separate out the contribution of stimulus modulation and of response variability, it is useful to characterize the response *rf* in each stimulus window as "signal plus noise" (Averbeck et al., 2006; Belitski et al., 2008; Belitski et al., 2010) as follows:

$$r_f = \overline{r_f} + n_f \qquad (2)$$

where the "signal" $\overline{r}_f$ is the trial-averaged power (the bar denotes the average across trials at fixed stimulus) and the "noise" the trial-by-trial fluctuations n_f of the response around their averaged across trials. We stress that such "noise" does not necessarily reflect only noise in the real sense, but reflects all types of variations at fixed stimulus, which may well include the effect of various types of potentially important neural contributions such as modulation from a common ascending pathway.

To quantify how well the stimuli are encoded, we computed the coefficient of variation (CV) for the signal and the noise of each channel and frequency. The $signalCV$, is defined as the coefficient of variation (CV) of the trial-averaged power across the stimulus windows in the movie, as follows:

$$signalCV = \frac{std_{stim}(\bar{r}_f)}{\langle \bar{r}_f \rangle_{stim}}, \quad (3)$$

where $\langle ... \rangle_{stim}$ and std_{stim} denotes the mean and the standard deviation (SD) over the stimulus windows respectively. Furthermore, we also quantified the unreliability of the power across trials by computing the CV of the power fluctuations across trials about its mean for each stimulus and frequency ($noiseCV$).

$$noiseCV = \left\langle \frac{std_{stim}(n_f)}{\bar{r}_f} \right\rangle_{stim}, \quad (4)$$

where std_{trl} denotes the SD across trials at fixed stimulus window.

8.3 RESULTS

We simultaneously recorded the LFP from the different laminae of area V1 of anaesthetized macaque monkeys using a laminar, vertically inserted, linear probe with 16 with 150 µm spacing (Figure 8.1A). We recorded a total of 15 experimental sessions obtained in 4 different animals.

To determine the cortical layer in which each electrode site was located, we used established methods based on the analysis of the current source density (CSD) extracted from the laminar LFP (Figure 8.1B and Figure S2A). The CSD estimates the net current density that, at each particular depth and time, enters or leaves the extracellular medium through cell membranes (Einevoll et al., 2013; Mitzdorf and Singer, 1979), and was used to assign electrode locations to either supragranular (SG), granular (G), or infragranular (IG) compartments. In brief (see Materials and Methods), we used the trial-averaged CSD (average over all sessions shown in Figure 8.1B, top), computed after the onset of the movie, to identify the border between G and IG (the bottom end of the early sink at 40-60 after movie onset). The G/IG border was confirmed as the point where a sudden drop is found in the LFP gamma-band coherence with

the electrodes placed above (Dougherty et al., 2017; Maier et al., 2010; Maier et al., 2011; Pettersen et al., 2006); see Figure 8.1B, bottom. The cortical boundaries and the location of the SG/G boundary were determined based on the average thickness of cortical laminar compartments in macaques (Lund, 1973; O'Kusky and Colonnier, 1982; Self et al., 2013).

To investigate both endogenous and stimulus-driven processes, we recorded neural activity in V1 both in absence of visual stimulation (isoluminant gray screen, which we termed "spontaneous activity") and during the presentation of Hollywood movie clips (Figure 8.1A). Such movies contain a wide range of naturalistic variations of visual features and thus elicit a rich spectrum of LFP activity likely capturing several distinct neural processes (Belitski et al., 2008; Belitski et al., 2010; Szymanski et al., 2011). Our stimulus protocol consisted of a block paradigm alternating Hollywood movie-clips (20 seconds) with two isoluminant gray screen periods (each lasting 20 seconds before and after each clip; Figure 8.1A, top panel). Using techniques developed in our previous work (Zaldivar et al., 2017; Zaldivar et al., 2014), we mimicked dopaminergic (DAergic) neuromodulation by systemic injections (injection period of 12 min, corresponding to 12 blocks of visual stimulation) of L-DOPA and Carbidopa (LDC; 2.1 mg/kg and 0.5 mg/kg respectively, (Black et al., 2003)). L-DOPA is the metabolic precursor of DA, which is metabolized to DA once it crosses the blood-brain barrier (BBB). Once in the brain it activation DA-receptors. The role of Carbidopa, on the other hand, is to prevent the breakdown of L-DOPA in the periphery, thereby optimizing the BBB's crossing of L-DOPA. We used systemic LDC injections rather than local application of DA in V1 because we previously found that only the former modulates neural activity in V1 (Zaldivar et al., 2014). This pharmacological approach is widely used for the treatment of Parkinson's disease patients and it has also been shown to be effective in treating amblyopia (Algaze et al., 2005).

8.3.1 Visually driven and spontaneous oscillatory activity in V1

First, in this section we considered the characteristics of oscillatory activity before the injection of LDC (Figure 8.1C-D).

To investigate how oscillation strength was modulated by the presentation of a visual stimulus, we quantified the strength of the oscillatory activity across different frequencies by computing the average LFP spectrum (see Materials and Methods) separately for spontaneous and movie-evoked activity. Figure 8.1D shows the spectrum averaged over all electrode sites in all sessions. We found, in both conditions, activity distributed with significant power ($p = 0.0012$; t test) over the entire frequency range (1 to 150 Hz) considered. The highest LFP power was at low frequencies (peak at 7 ± 2 Hz), and decreased steeply at increasing frequencies. By comparing the averaged LFP spectrum evoked during the movie with the LFP spectrum during spontaneous activity, we found an increase of power during movie stimulation over that of spontaneous activity throughout the entire spectrum (Figure 8.1D). Consistent with previous studies (Belitski et al., 2008; Frien et al., 2000; Henrie and Shapley, 2005), the larger movie-evoked power increase over spontaneous activity was, both in absolute and proportional terms, in the gamma (γ, 50-100 Hz) and high-γ bands (maximal peak during movie 24 ± 3 dB at 99 ± 3 Hz; maximal response during spontaneous activity 16 ± 3 dB at 90 ± 2 Hz; Figure 8.1D and S1A-B).

A large increase in neural oscillation power during visual stimulation does not necessarily imply that neural oscillations carry visual information. The amount of information carried by neural activity is determined by the combination of how large are the modulations of neural activity across different movies scenes and how small is the trial-to-trial variability of neural activity across multiple repetitions of the same scene. The combined effect of stimulus modulation and across-trial reliability is quantified by the mutual information that the LFP power at each frequency conveys about the section of the movie being presented. This measure, in units of bits, captures the information about all the possible visual attributes occurring in the movies and does not depend on assumptions about which features in the movie are encoded by the neural signals (Belitski et al., 2008; de Ruyter van Steveninck et al., 1997). Results averaged over all electrodes in all sessions are shown in Figure 8.1E. In agreement with a previous study in the same cortical area and under the same anesthesia

condition, but without laminar resolution (2008; Belitski et al., 2010), we found two informative bands in the LFP spectrum. The first informative LFP region was the low-LFP-frequency range (up to 15 Hz, covering the delta, δ; theta, θ; alpha, α, bands), with a peak information in this region reaching a value of 0.15 ± 0.02 bits (significantly non-zero; $p<0.05$; bootstrap test) at 7 Hz (Figure 8.1E). (Hereafter, unless otherwise stated results are reported as mean ± sem across all available channels in the dataset). The second LFP frequency range with highly informative (and thus reliably stimulus modulated, see Figure 8.1C) power was a broad region covering the γ and high-γ range of 50 – 150 Hz (Figure 8.1E). The peak information value in the high frequency region was 0.26 ± 0.02 bits (significantly positive; $p<0.05$; bootstrap test) at 60 Hz. Importantly, previous work (Belitski et al., 2008), as well as our further analyses (see later Sections) showed that low and high-frequency LFP bands carry independent information about the movie, and should thus be considered as different bands.

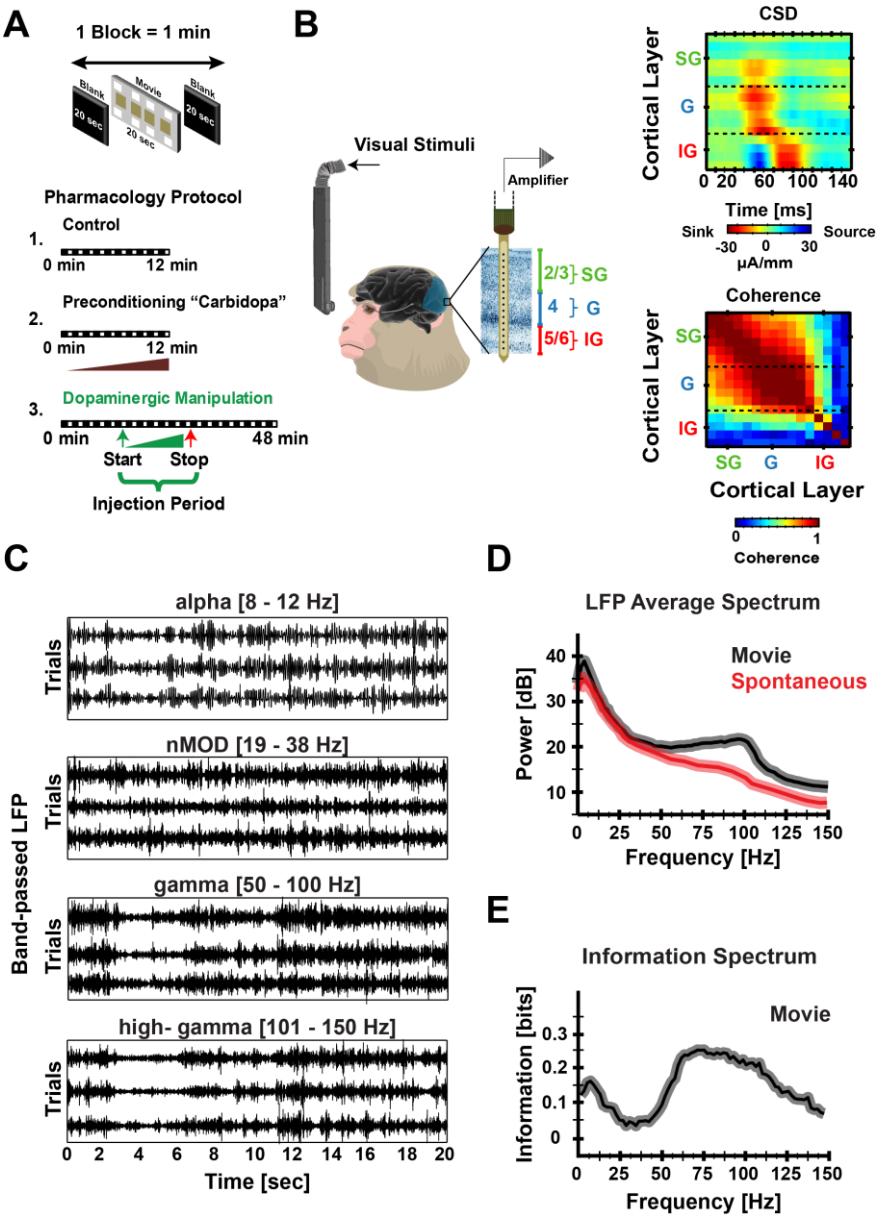

Figure 8.1 Experimental Design, Spontaneous Neural Activity and Response to Movie Clips
(A) Experimental paradigm and design. The stimulus consisted of movie clips of 20 sec followed by a 20 sec presentation of isoluminant blank screen. Each experiment consisted of three phases: (1) 12 min recording without pharmacological intervention; (2) 12 min recording with carbidopa preconditioning, which does not affect neural activity and prevents the peripheral conversion of L-DOPA to DA; (3) a 48 min long session in which L-DOPA and carbidopa were injected. **(B)** Left: Multicontact laminar electrodes were used to record neural activity across the cortical layers. Top right: Session averaged current-source density after the movie onset. The sink polarity inversion was used to identify the G/IG border. Bottom right: session average of the coherence between gamma-band LFPs across electrode pairs are used to confirm the location of the G/IG border. The borders of the IG compartment and corical thickness were determined from averaged anatomical data **(C)** Example LFP traces during presentation of a 20 s long movie. **(D)** Power spectrum of the spontaneous LFP (red) and the LFP during movie presentation (black). **(E)** Information about the movie in the total LFP power across all layers. Shaded areas show the SE.

Despite their relatively high power (on average 18 ± 3 dB), LFP frequencies in the middle frequency range (19–38 Hz) conveyed much less information about the movie (0.04 ± 0.01

bits; Figure 8.1E and S1C; significantly non-zero; $p<0.05$; bootstrap test) and was not reliably stimulus-modulated (see Figure 8.1C). This result was consistent with previous studies in monkeys (Belitski et al., 2008; Whittingstall and Logothetis, 2009) and humans (Donner et al., 2007). Given that the powers of pairs of frequencies within this high-power, low information mid-frequency region share strong noise correlations (see (Belitski et al., 2008) and later Sections) we previously suggested on statistical bases that this band may capture the fluctuations of one or few sources of stimulus-unrelated neuromodulation; we therefore have termed this band "neuromodulation band" (nMOD; see Belitski et al., 2008; Belitski et al., 2010). However, until now the hypothesis that this band reflects neuromodulation has not been causally tested.

Based on the above results, hereafter we singled out four frequency bands for further analyses. Three bands cover the stimulus-informative range: α [8 – 15 Hz], γ [50 – 100 Hz] and high-γ [101 – 150 Hz], with the high frequency range partitioned into two ranges that may have a different neural origin (Gieselmann and Thiele, 2008; Ray and Maunsell, 2011). One band covers the stimulus-unrelated middle-frequency range (nMOD [19-38 Hz]). To avoid biasing the results with the choice of specific band boundaries, we complemented the band analysis with an analysis of the power of individual Fourier coefficients, which is completely free from assumptions about band partitions.

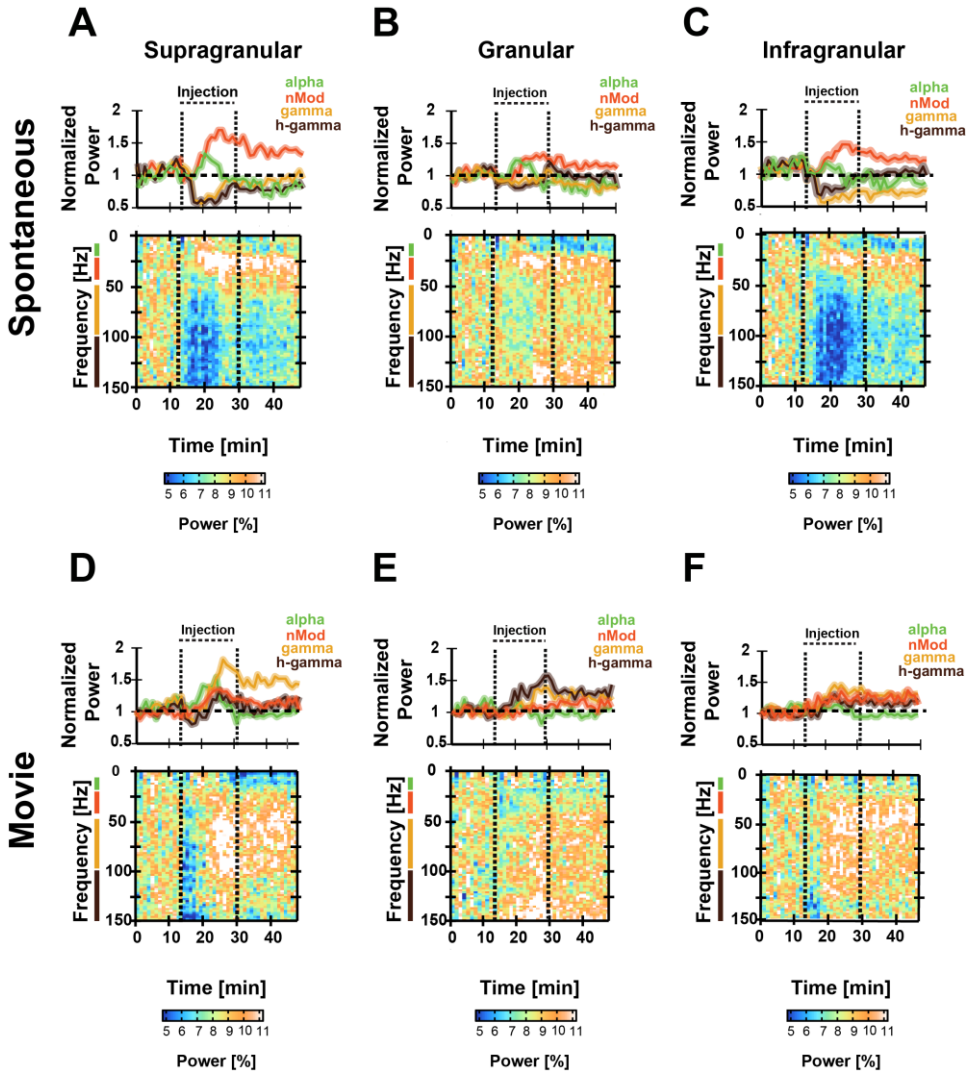

Figure 8.2 Dopamine Increases nMOD Oscillations and Induces Frequency and Stimulus Specific Power Changes in Other Bands
Average across trials and sessions of effects of L-DOPA on the LFP in supragranular **(A** and **D)**, granular **(B** and **E)** and infragranular **(C** and **F)** layers during spontaneous activity **(A-C)** and during the presentation of movie clips **(D-F)**. The plots above each spectrogram show the mean time course for the LFP bands: alpha (8 – 12 Hz, green), nMOD (19 – 38 Hz, red), gamma (50 – 100 Hz, yellow) and high-gamma (101 – 150 Hz, brown). Dashed lines denote the beginning and the end of the systemic L-DOPA infusion. In the nMOD band, the power during spontaneous activity increases as a result of DA injection, suggesting that the activity in this band is sensitive to neuromodulation. The power in the gamma and high-gamma bands decreases during the injection of dopamine for spontaneous activity but increases during the movie clips. LFP averaged over 15 neurophysiology sessions totaling 240 electrode sites. Shaded areas show the SEM across session.

8.3.2 Layer- and frequency-specific power changes induced by dopamine during visual stimulation and spontaneous activity.

We next explored how oscillations in different LFP bands are affected by DAergic neuromodulation. Given that the effect of neuromodulation on V1 likely depends on the current

operational mode of the network, we examined the LFP-spectrum under systemic injection of LDC, either during trials without stimulus presentation (Spontaneous; Figure 8.2A-C top panels) or while presenting movie clips (Movie; Figure 8.2A-C bottom panels). Since different cortical layers show distinct patterns of connectivity and physiology related to sensory processing (Callaway, 1998; Lund, 1973; Nassi and Callaway, 2009) we quantified the effect of DAergic neuromodulation separately on the LFP spectrum recorded in each of the three laminar compartments (SG, G and IG). Importantly was to stablished how DA links local and global cortical circuit systems by determining how cortical layer.

We observed profound changes in V1 LFP power during injection of LDC compared to before the injection (Figure 8.2). These effects are highly dependent on cortical depth and frequency, and were different for the movie-evoked and spontaneous activity.

We quantified the changes in power after DA injection by normalizing the power of each band so that its value, averaged across trials and time points in the 12 min preceding the injection, was set to 1. When considering spontaneous activity, we found that during the LDC injections the LFP-power increased in the middle-frequency nMOD band (19 – 38 Hz; Figure 8.2 A-C, top panel), while it decreased in the γ-band (50 - 150 Hz; Figure 8.2 A-C, top panel). These effects were larger in the SG (nMOD: averaged normalized power = 1.73 ± 0.12, p = 0.021, t-test; γ average normalized power = 0.53 ± 0.08, p = 0.038, t-test) and IG layers (nMOD: averaged normalized power = 1.45 ± 0.08, p = 0.035, t-test; γ: average normalized power = 0.53 ± 0.07, p = 0.026, t-test). Modulation of nMOD and γ during DA injection was much weaker in the G than in the IG or SG compartment (nMOD: average normalized power 1.22 ± 0.04, p= 0.041, paired t-test; γ: average normalized power = 0.085 ± 0.03, p = 0.048, paired t-test). The change of power after injection was significantly weaker (high significance in SG, p= 0.043, paired t-test) in the α band than in the other bands (Figure 8.2A-C).

These results, obtained after partitioning the LFPs into three separate bands, were confirmed by a further analysis that was free from assumptions about the boundaries of the frequency

bands (Figure 8.2 A-C, bottom panels). We computed the LFP power of each Fourier coefficient and we quantified its time course as percentage changes relative to the pre-injection period. The single Fourier coefficient analysis confirmed the results obtained using band-limited power, indicating in particular a strong increase in power in the 19-38 Hz range and a strong decrease in power in the 50-150 Hz range in the SG and IG compartments (Figure 8.2 A-C, bottom panels).

These results show that DA elicited highly frequency- and layer-specific changes in power of the spontaneous activity, instead of unspecific broadband LFP-power changes, suggesting effects of DA in different sets of networks.

Frequency-specific changes in power following LDC injection were also found during stimulation with natural movies (Figure 8.2 D-F). Interestingly, the DA-induced changes observed during movie were very different from those observed for spontaneous activity. We observed a significant increase in the nMOD-power in the SG ($p = 0.028$, paired t-test), and IG compartments ($p = 0.033$, paired t-test), but not in the G compartment ($p = 0.058$, paired t-test). However, the γ power in all cortical layers significantly increased during the injection (SG: $p = 0.024$; IG: $p = 0.031$; G: $p = 0.032$, all paired t-tests; Figure 8.2A-C, bottom panel).

In the post-injection recovery phase, we observed a tendency of all bands to return to baseline both during spontaneous and movie-evoked activity; however, the trend toward return to baseline appeared slower in the nMOD and the α band (Figure 8.2C, F), suggesting that systemic injection of DA has a particularly strong and prolonged effect on these bands. This can, in principle, be ascribed to the slow clearance of DA from the brain (Black et al., 2003).

In summary, these results suggest that DA elicits LFP power changes in V1 that were not only frequency- and layer-specific, but that were also profoundly different depending on whether or not the V1 network was processing a visual stimulus. This highlights the strong dependence of the effect of DA neuromodulation on the operational state of the network.

8.3.3 Layer- and Frequency-Specific Changes in Information Induced by Dopamine.

The above results indicate an increase in power during movie stimulation in several bands (Figure 8.2A-C), and suggest that DA may alter how oscillations encode visual information. However, an increase or a decrease in power with visual stimulation per se does not imply an increase or decrease of visual information, as power and information do not necessarily correlate (Belitski et al., 2010). To address directly the effect of DA on the information carried by different oscillation frequencies in different laminae, we computed the information carried by the power at each frequency about which movie scene was being presented (Eq. 1), both before, during and after DA injection (Figure 8.3).

When computing the power in the four predefined bands, we found that the γ and high-γ bands carried the most information about the movie, reaching the highest values of 0.24 ± 0.021 and 0.23 ± 0.015 bits in the SG layers, respectively (Figure 8.3B). γ and high-γ had lower values in the G layers (0.15 ± 0.012 and 0.12 ± 0.020 bits, respectively) and intermediate in the IG layers (0.17 ± 0.021 and 0.12 ± 0.015 bits, respectively). The α band carried less information than the γ, reaching values of 0.15 ± 0.013 bits in the G layer and showing overall a less pronounced layer dependence than γ and high-γ. The nMOD power carried little movie information, with a less pronounced layer dependence and was maximal (0.04 ± 0.011 bits) in the SG layers.

The results were confirmed when considering the individual Fourier coefficient analysis, which showed high information in the SG for the entire high frequency range (50 – 150 Hz, covering the γ and high-γ ranges, with a maximal information of 0.23 ± 0.02 bits; Figure 8.3A). Information in the (50 – 150 Hz) high frequency range was lower for the G (0.15 ± 0.04 bits) and IG (0.17 ± 0.02 bits). In addition, the information in frequencies below 50 Hz was lower and less layer dependent than the information in the frequencies above 50 Hz. Moreover, the information in the middle frequency range (19 – 38 Hz), corresponding to the nMOD band, was particularly low, thereby confirming the results of the analysis of discrete frequency bands.

We then tested the effect of DA injection on the frequency- and layer-specific distribution of information (Figure 8.3A-B). Interestingly, we found that following DA injection there was a tendency to an increase in information about the movie across a wide spectrum of frequencies and cortical depths. However, this increase on information was more pronounced when considering activity from SG layers. In particular, we observed an increase in the information content in the γ range in the SG layers (50 – 100 Hz) during injection (γ: 0.34 ± 0.02 bits, p = 0.031; high-γ: 0.32 ± 0.021 bits, p = 0.021; α: 0.22 ± 0.021 bits, p = 0.013; nMOD: 0.15 ± 0.02, and p = 0.039; all comparisons made with paired t-test, n = 60). In the G layer, the increase in information during DA injection was significant for the α band (0.21 ± 0.020 bits, p = 0.031). In the IG layers, the increase in movie information after DA injection was significant for nMOD (0.10 ± 0.03 bits, p = 0.043), γ and high-γ (0.30 ± 0.04 bits, p = 0.045; and 0.23 ± 0.02 bits, p = 0.037, respectively, see Figure 8.3). The pattern of these effects of DA injection on the selected frequency bands and cortical layers was also visible when considering individual Fourier coefficients and electrodes, as shown in Figure 8.3.

We also observed that the information about the movie remained high after the end of the injections (Figure 8.3B, 'after period' shown in red). In particular, we observed that the information in the SG in the γ and high-γ bands remained high compared to the pre-injection period (0.29 ± 0.03 bits, p = 0.030; 0.27 ± 0.03 bits, p = 0.033, see Figure 8.3A-B shown in red). We observed a similar pattern in the information in IG (0.17 ± 0.04 bits, p = 0.038 in the γ range and 0.18 ± 0.02 bits, p = 0.037 for the high-γ range). However, this profile of changes in information about the movie in the γ and high-γ was not observed in the G layer, where we saw that the information in this layer remained high for the α range after the injection period (0.23 ± 0.011 bits, p = 0.032).

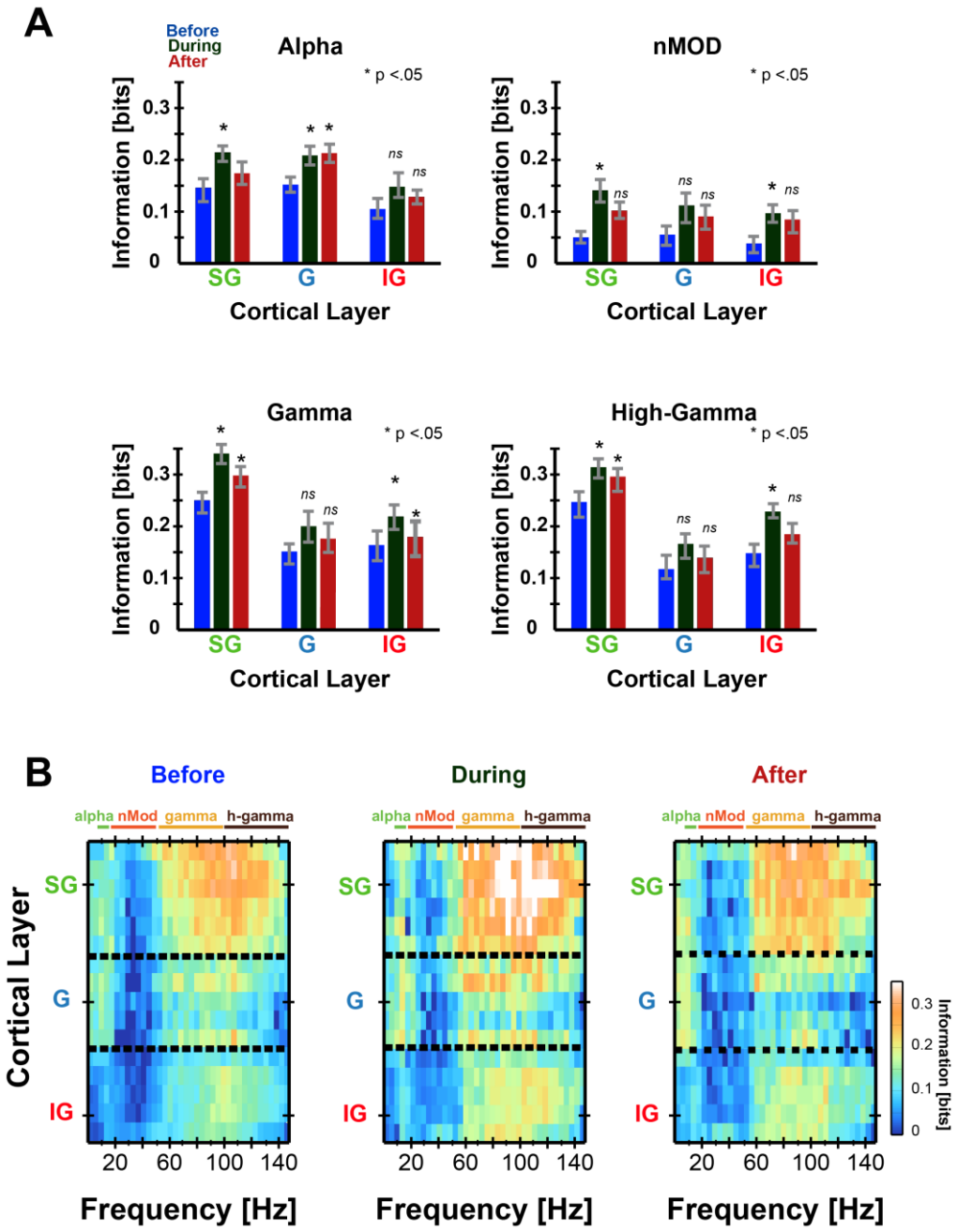

Figure 8.3 Dopamine Increases the Information Content in SG and IG layers
(A) Average over all sessions of changes in information content in individual frequency bands (alpha, nMOD, gamma and high-gamma) across cortical layers: supragranular (SG), granular (G) and infragranular (IG) layers before (blue), during (black) and after (red) DA injection. Error bars represent SE. **(B)** Average over all sessions of the information in the power of the LFP before, during and after injection of dopamine. Before the injection, the information about the visual stimulus was frequency- and layer-dependent in the majority of the bands. During and after injection of DA there was an overall increase in information, which did not affect the information distribution across layers.

8.3.4 Dopamine Induced LFP-Variability Changes

The amount of information about the movie carried by the LFP power depends on both the signal (how the LFP changes across different movie scenes) and the noise (variability of LFP power to repeated presentations of the same movie scene, Eq. 2). The changes of information caused by the injections of DA may thus be attributable to a higher signal or to lower noise, or both. We address this question by quantifying, independently for each frequency, changes in the signal and noise after DA injection. For this, we computed the changes in the signal, as the coefficient of variation (CV) of the trial-averaged evoked LFP-power responses across different scenes of the movie ("signalCV"; Eq. 3; solid lines in Figure 8.4). Furthermore, we quantified the changes in the noise as the CV from the trial-to-trial response variability unrelated to the stimulus ("noiseCV"; Eq. 4; dashed lines in Figure 8.4).

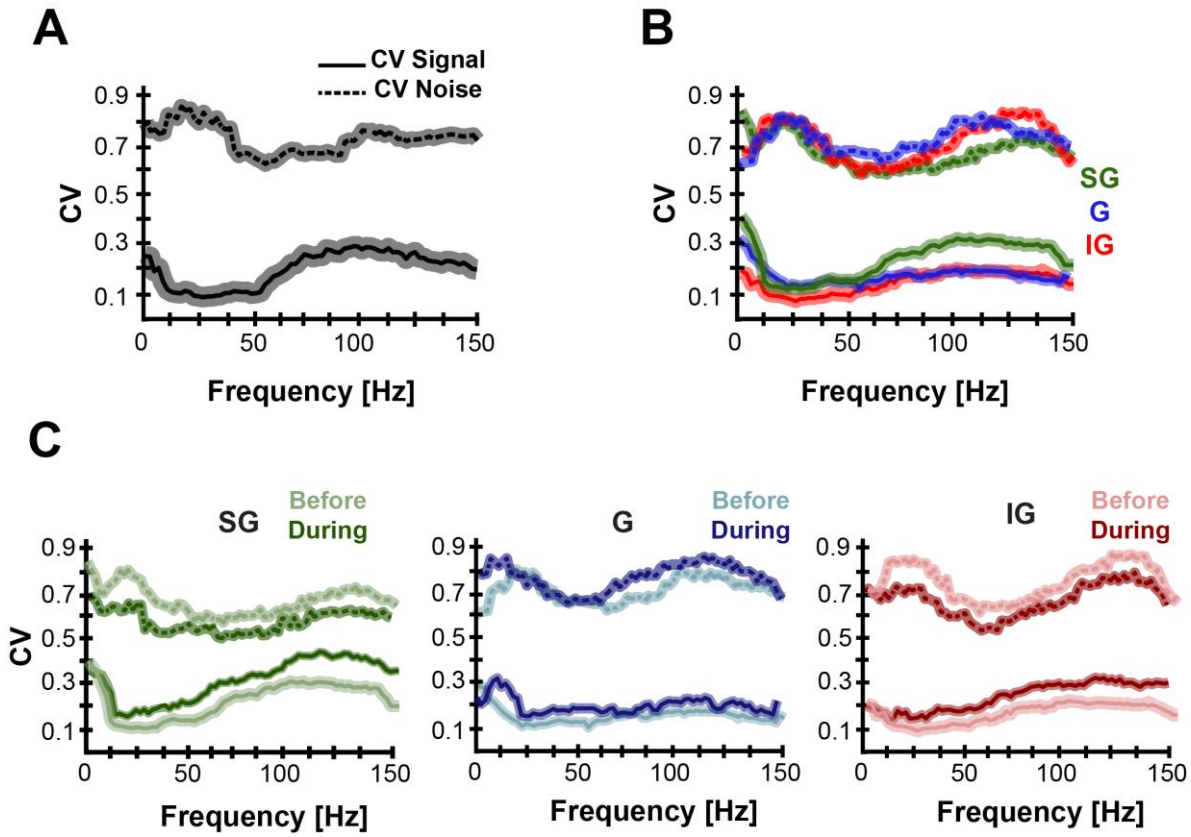

Figure 8.4 Layer Dependent Increase in Signal and Noise Variability Induced by Dopamine
(A) The session-averaged average signal-CV (solid line) and noise-CV (dashed line) across all experiments and electrodes, shows high CV values for frequencies <12 Hz and frequencies >50 Hz **(B)** Layer specific differences in the session-averaged signal-CV and noise-CV: supragranular (SG, green), granular (G, blue) and infragranular (IG, red) layers. **(C)** Effect of DA on the session-averaged signal-CV and noise-CV in different cortical layers. DA injection increased the signal-CV in SG and IG layers while the signal-CV in G layers was changed only at low frequencies. The noise-CV decreased for SG and IG mostly in frequencies <50 Hz. The shaded area indicates the SEM across sessions.

We first considered the distribution of signal and noise across layers before DA injection (Figure 8.4A). In agreement with previous studies, that did not record laminar specific changes (Belitski et al., 2008), we found that on average across layers, the γ and high-γ band contained more information because they had both a high signalCV and low noiseCV. More specifically, the γ band had the highest signal (peaking at 0.31 ± 0.04 at 99 ± 4 Hz) and the lowest noise (dipping at 0.64 ± 0.05 at ~55 Hz). Frequencies in the nMOD band had the lowest signal (0.09 ± 0.01) and a particularly high noise (0.88 ± 0.02), which explains the very little information seen in this band.

Since our results indicate that information is not uniformly distributed across layers (Figure 8.3A), we quantified whether such laminar information profiles can be ascribed to differences in the signal or noise from the different layers. For this, we computed the signal and noise variability from each cortical layer before DA injection (Figure 8.4B). We found that LFPs in SG layers tended to have more signal than G and IG layers across a wide frequency spectrum (covering the α-band; $p = 0.035$, but especially prominent in γ and high-γ bands; $p = 0.031$ and $p = 0.035$) and less noise specifically in the in γ and high-γ bands (Figure 8.4B, $p < 0.038$ and $p = 0.042$)).

We further quantified how the injection of DA affected the noise and signal across cortical layers and frequency bands (Figure 8.4C). Therefore, we computed the signal and noise across the recording depths and frequencies before and after DA injection. In general, injection of DA tended to both increase signal and decrease noise in a layer dependent fashion. In particular, we observed a more marked effect in SG and IG layers than in the G layer (Figure 8.4C). In the SG, the maximal increase of signal due to DA injection was 0.43 ± 0.03 at ~105 Hz, and maximal decrease of noise was 0.64 ± 0.02 at 75 Hz). More specifically, injection of DA increased the signal CV over a wide frequency range including nMOD, γ and high-γ bands in SG and IG layers (Figure 8.4C). Injection of DA also decreased the noise throughout the spectrum in the α, nMOD, γ and high-γ bands in SG layers, and decreased the noise in the nMOD, γ and high-γ bands in IG layers (Figure 8.4C).

In summary, DA increases the information in SG and IG due to the increased signal and decreased noise in these cortical layers. In contrast, the signal and noise in the G layers did not change much after the injections of DA, which supports the idea that information content in this layer is largely unaffected by DAergic neuromodulation.

8.3.5 Layer Dependent Changes in the LFP Correlated Variability

Another important question is whether DA changes not only the information content of individual frequency bands, but also the relationship between oscillations in different bands (Averbeck et al., 2006; Einevoll et al., 2013). Following previous studies (Averbeck et al., 2006; Belitski et al., 2008; Panzeri et al., 1999), we distinguish between two possible types of correlations between the power of different bands. The first is signal correlation, quantifying the similarity of stimulus preferences between the power of different frequencies, and defined as the Pearson correlation between the trial averaged-induced power to each movie scene. The second is noise correlation, quantifying the correlation in neural activity not due to stimulus covariation, and defined here as the Pearson correlation at fixed movie scene between the trial-to-trial fluctuations of the power of the two frequencies around their across-trial average (Averbeck et al., 2006; Belitski et al., 2008; Panzeri et al., 1999). Figure 8.5 reports the average signal correlation over the entire dataset for different oscillation frequencies and cortical depths, before and during DA injection, for individual frequencies (Figure 8.5A) and band-limited data (Figure 8.5B). Before the injection, signal correlation was highest in the γ and high-γ band, particularly in SG and IG layers. The mean signal correlation over all frequency pairs within the γ band was 0.60 ± 0.02 in SG; 0.38 ± 0.01in G; 0.59 ± 0.03 in IG layers. The mean signal correlation within the high-γ band was 0.44 ± 0.02 for SG, 0.36 ± 0.01 for G; and 0.38 ± 0.02 for IG, respectively. Signal correlation within the α band was relatively high, with a mean of 0.58 ± 0.03 in the SG layers, and was much smaller for the nMOD band, with a mean of 0.38 ± 0.03 in the SG layers. Signal correlations across bands were smaller than those within the same band (Figure 8.5).

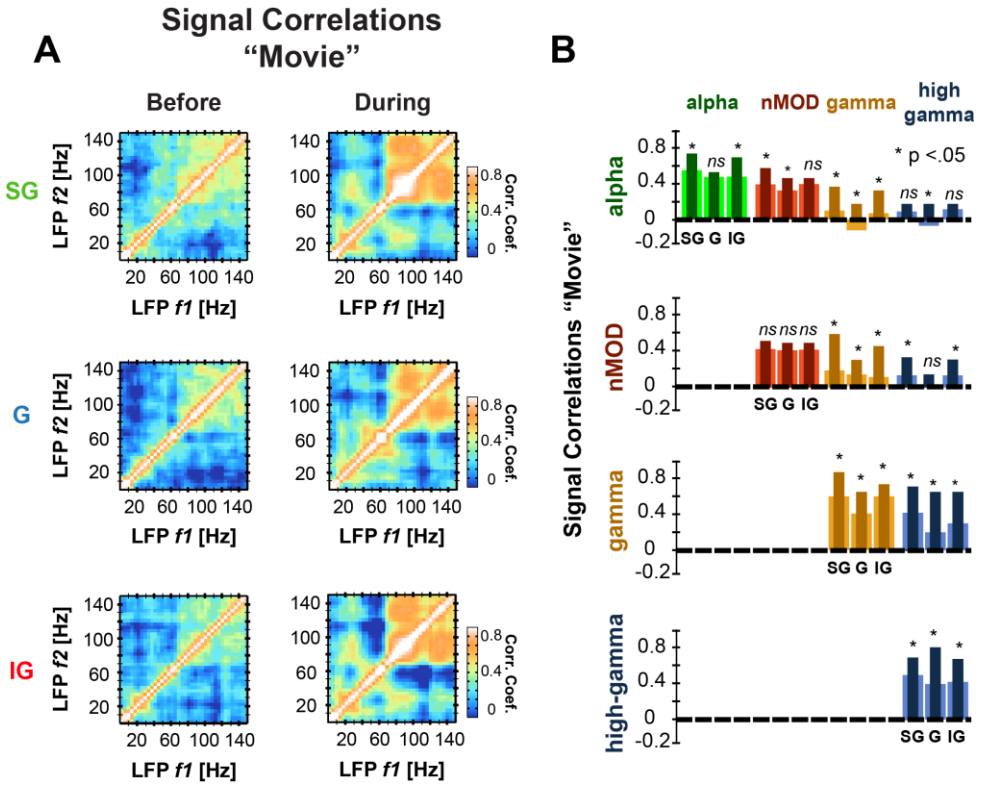

Figure 8.5 Dopamine Increases LFP Signal Correlations Across Frequencies and Layers
(A) Pearson signal correlations between pairs of LFP frequencies ($f1$ and $f2$) in supragranular (SG), granular (G) and infragranular (IG) layers before and during dopamine injection (12 sessions). Correlations within and between gamma and high-gamma frequencies increased during DA injection **(B)** Mean ± SEM over sessions of the correlations within and between LFP bands across different cortical layers before (light) and during (dark) pharmacological injection.

The most prominent effect of DA was to greatly increase the signal correlation (and thus the similarity of stimulus preferences of LFP power response across different movie scenes) in the γ and high-γ range. In the γ band, the effect was pronounced and significant ($p< 0.05$; paired t test) in each layer (Figure 8.5B), but most prominently in G and IG. The γ-band signal correlation before and during DA injection was 0.60 ± 0.02 vs 0.82 ± 0.03 ($p< 0.05$) in SG, 0.38 ± 0.03 vs 0.63 ± 0.05 ($p< 0.05$) in G; and 0.59 ± 0.03 vs 0.72 ± 0.03 ($p < 0.05$) in IG. The increase of within-band signal correlation was also found for the α band, particularly for the SG (0.73 ± 0.02) and IG (0.66 ± 0.02) layers, but not within the nMOD band. Notably, DA injection also increased across band signal correlations in all layers, but especially in the SG layer.

Interestingly, we also observed that DA increased the correlations between different bands. For instance, the pairwise correlations between frequencies in the α and nMOD bands increased in the SG layers (mean of all frequencies in α correlated with the mean of all frequencies in nMOD 0.58 ± 0.02) as well as in the G layer (correlations between α and nMOD 0.44 ± 0.03). In addition, the correlations between α and γ increased in all layers (SG: 0.38 ± 0.02; G: 0.12 ± 0.02; IG: 0.33 ± 0.04). Furthermore, the strength of the correlations between nMOD and γ were layer dependent (SG: 0.62 ± 0.02; G: 0.34 ± 0.03; IG: 0.45 ± 0.04) while the correlations between γ and high-γ increased in all layers with similar values (SG: 0.63 ± 0.02; G: 0.61 ± 0.03; IG: 0.60 ± 0.04).

In summary, as well as increasing the amount of information over a wide range of oscillations, a second effect of DA injection was to make different frequency ranges respond more similarly to different stimuli, as DA increased signal correlation across frequencies and particularly in the SG and IG layers.

One possibility is that the increased similarity of the stimulus tuning of different frequencies with DA injection is due to individual frequency bands becoming larger in width and thus overlapping more. If that were the main reason for a signal correlation increase, we would expect to also observe an increase in noise correlation across frequencies. However, we found that noise correlation did not change in any band at any depth during injection (Figure S4). Also, correlations among frequencies during spontaneous activity did not change during DA injection (Figure S5).

Interestingly, and consistent with a previous study (Belitski et al., 2008), noise correlations were much larger between α and nMOD frequencies than between γ and high-γ frequencies. This is the opposite of what we found for signal correlation. These results suggest that, while the γ band is primarily driven by the stimulus, the α band and particularly the nMOD band are primarily driven by, and covary with, internal rather than external factors.

8.4 DISCUSSION

Neuromodulation provides to anatomically defined circuits with the flexibility to adjust their activity and reconfigure networks into different functional neural circuits in order to meet cognitive demands. An important question regards the effects of neuromodulation in the power and information content of oscillatory activity, an aspect of neural activity thought to be central to cortical information processing. By recording neural activity in different cortical layers of V1 in anesthetized monkeys, and pharmacologically mimicking DAergic neuromodulation, we demonstrated that the power on middle-frequency endogenous oscillations correlates with the level of DA. Furthermore, we demonstrated that these changes in the levels of DA significantly enhances the sensory information throughout the cortex over a wide range of frequencies, but it especially increases the information in the γ range in the cortical output layers. We discuss our findings in greater detail and provide possible explanations that could account for our results.

8.4.1 Endogenous middle-frequency [19-38 Hz] oscillations as marker of neuromodulation

The effects of neuromodulation are not stationary but, rather, produce a dynamic regulation of neural circuits (Dayan, 2012; Grashow et al., 2009). Hence, being able to follow the elicited changes of neuromodulators over the course of time, and even at the level of individual trials, is important for many reasons. In principle, it is crucial to understand how neuromodulators affect neural oscillations and how to impute disorder-specific abnormalities of cortical oscillations to dysfunction of neuromodulatory systems. In addition, it is also important to stablish how neuromodulators dynamically regulate cortical computations in healthy brains, and shape cognitive functions such as learning and attention. Given that in many experiments only cortical recordings are available, and it is difficult to simultaneously record the activity from neuromodulatory nuclei, it is important to be able to find statistical markers of fluctuations of neuromodulation in cortical activity. We found that the power of the middle frequency [19-38 Hz] band was the most suitable statistical marker of the level of DA, because it increases

in power when DA was pharmacologically increased. The power in this band increases markedly during spontaneous activity and to a lesser extent during movie stimulation, when interventionally changing the level of DA modulation with systemic LDC injection. Statistical analysis of naturally varying activity confirmed previous results that this band is less modulated by external factors such as stimulus drive, and all frequencies in this range strongly covary together according to non-stimulus driven factors (Belitski et al., 2008; Belitski et al., 2010). The relatively weak dependence of this band on external sensory stimuli, as well as its weak correlation with the power of other stimulus-driven bands, allows to ascribe its changes to internal state variations driven by DAergic modulation. These findings suggest that this band can, at least in V1, be rightfully termed a neuromodulatory "nMOD" band, and that can be used to statistically infer changes of neural activity associated to the levels DA. Importantly, the LFP shares the same biophysical origin with surface EEG recordings and correlates well with EEG at the single trial level (Whittingstall and Logothetis, 2009). This suggests that pre-stimulus fluctuations in power in occipital EEG electrodes in the middle frequency band could be used to mark, to some extent, the level of fluctuations of DA and, perhaps, from other neuromodulators.

We also found that the γ and high-γ bands dramatically decreased their spontaneous power after injecting DA. However, given the stronger modulation of γ and high-γ power by exogenous factors such as sensory stimulation, found here and in other studies, (Belitski et al., 2008; Fries, 2009; Whittingstall and Logothetis, 2009) it is difficult to use the γ band as a direct marker of neuromodulation and DA. In this respect, the decrease of γ power with DA injection, that we found during spontaneous activity, may be more directly interpreted as an increase of a difference between baseline and visually-evoked activity. This in turn would underlie an increase of the signal-to-noise ratio of stimulus detection, and would thus still be interpreted as evidence that DA enhances γ-band visual processing.

Our findings fit well with earlier studies suggesting that middle-frequency power modulations reflect endogenous ongoing neural (Belitski et al., 2008; Buschman and Miller, 2007; Engel

and Fries, 2010; Haegens et al., 2011; Lundqvist et al., 2016; Whittingstall and Logothetis, 2009) and are not visually driven processes (Schmiedt et al., 2014; Wrobel, 2000). It also in accordance with studies linking oscillations in the mid-frequency range to the ongoing mechanisms that help the brain to maintain its current cognitive status (Engel and Fries, 2010; Haegens et al., 2011). For instance, increase in power in this range have been associated with maintenance of the current cognitive set, whereas decreases in power of this band have been associated with unexpected or novel events (Engel and Fries, 2010). It is thus natural to suggest that cortical nMOD power changes reflect changes in cortical operations, which can be instantiated by fluctuations in the concentration of neuromodulators (Dayan, 2012; Engel and Fries, 2010; Yu and Dayan, 2005).

8.4.2 Layer dependent increase of informations due to dopamine

Our study confirmed earlier results that the power in the γ-band and low frequencies (<20 Hz) are the ones conveying the most visual information (Belitski et al., 2008; Belitski et al., 2010; Magri et al., 2012b). However, our findings provide additional knowledge about the differences in the information distribution across layers from the different oscillatory bands. Studies considering the firing rates of individual neurons have revealed laminar profiles of information content that suggest that different cortical layers employ different coding strategies, probably reflecting their differences in anatomical projection patterns (Callaway, 1998; Hansen et al., 2012; Lund, 1973, 1988; Nassi and Callaway, 2009). Our results show that similar laminar diversity of coding applies also to the oscillatory activity expressed in each layer.

In particular, we found that across all bands the information was higher in the SG layers, and especially for the most informative band, the γ-band. Information in the γ-band was also lower in the G than in the IG layer. Gamma oscillations are thought to be generated by local interactions between inhibitory neurons, and between excitatory and inhibitory neurons (Buzsaki and Wang, 2012; Einevoll et al., 2013). The fact that the amount of information in the γ-band from the SG layer was higher, with respect to the information in the thalamic recipient G layers, may arise because of the larger number of recurrent connections between excitatory

and inhibitory neurons in the upper layers, which may facilitate the generation and dynamic variations of such γ oscillations.

Our examination of the effect of DA on information coding revealed a general increase of information across layers, but also shows layer and frequency dependence of the information gain induced by DA. The most notable effect was that DA pronouncedly increased the information of the γ band in the SG and IG layers. Gamma oscillations have been implicated in the dynamical transmission of information along feedforward pathways (Bosman et al., 2012; van Kerkoerle et al., 2014b), and SG neurons project in a feedforward manner to higher cortical areas (Rockland and Pandya, 1979). These facts suggest that the DA-mediated increase in γ SG information may reflect a DA-mediated higher efficiency in the propagation of sensory information to higher areas (Fries et al., 2008; Jacob et al., 2013; Self et al., 2013; van Kerkoerle et al., 2014b). This, in turn, may enhance the readout of task-related information, a role often imputed by models to dopamine (de Lafuente and Romo, 2011b; Happel et al., 2014; Jacob et al., 2013). For example, manipulation of prefrontal D1-receptors increase the magnitude, reliability and selectivity of neuronal responses in V4 (Noudoost and Moore, 2011), and similar mechanisms may play a role in V1.

The larger increase in visual information in IG and SG layers during DA injection, with respect to what observed in G layers, may at least in part be mediated by cross laminar feedback loops that dynamical regulate the stimulus-response gain and that are known to be enhanced by DA (Happel, 2015; Happel et al., 2014).

We also found that information in the α-band increases in the SG and G layers. Recent studies proposed that the α frequencies mediate top-down information flow (Dougherty et al., 2017; van Kerkoerle et al., 2014b). One possible interpretation of the information increase in the α range during DA injection may be that DA improves the cortico-cortical communication from higher areas to V1 (Noudoost and Moore, 2011; van Kerkoerle et al., 2014b; Zaldivar et al., 2014). However, it should be noted that the involvement of the top-down component of α

oscillations in our anaesthetized data is likely to be limited with respect to other experiments showing a prominent role of these oscillations in operations such as figure-ground segregation, attention and working memory (Ekstrom et al., 2008; Self et al., 2013; van Kerkoerle et al., 2017).

In sum, we suggest that the increase in information in the γ band promotes the readout of sensory information and improving behavioral performance (Happel et al., 2014; Shuler and Bear, 2006).

8.4.3 Shared sources of signals between nMOD and the other bands

The effect of DA was not only to increase the information across laminae and across the frequency spectrum. DA also increased the signal correlation, that is the similarity of tuning to different movie scenes, of different frequency bands. Given that we found that DA did not change the noise correlation, the effect of an increase of signal correlation is to increase the coherence, or redundancy, of the information carried by each band. One function of representing some visual features in a similar way across several frequency bands is that this enhanced redundancy across frequencies could facilitate the behavioral readout of such set of visual features, because information about them can be read out by more than one band. This finding fits with theories suggesting that the extraction and amplification of specific sensory features, whose high behavioral relevance to a particular situation has been established by reinforcement learning, is orchestrated in a layer-dependent way by dopamine (Happel et al., 2014).

These results may also provide insight into the possible mechanisms that might underlie DA-mediated neuromodulation. For instance, the fact that DA increases the signal correlations between nMOD and γ might be because the mechanisms involved in their generation are affected by DA in the same way (Lundqvist et al., 2016; Trevino et al., 2007). Both oscillations are thought to depend on the dynamics of the interaction between excitatory and inhibitory neurons, and among inhibitory neurons (Buzsaki and Wang, 2012; Kopell et al., 2000;

Logothetis, 2008; Siegel et al., 2012; Traub et al., 1999; Trevino et al., 2007). Gamma oscillations seem more closely related to the time constants of GABA and AMPA receptors (Buzsaki and Wang, 2012; Isaacson and Scanziani, 2011) whereas slower frequencies in the nMOD range appear to be mediated by the interaction between NMDA, GABA and metabotropic-glutamate receptors (mGlutR; Kopell et al., 2000; Traub et al., 1999). DA enhances both GABA- and NMDA-mediated synaptic inputs, resulting in sustained and elevated neural firing rates in a stimulus-specific manner (Seamans et al., 2001a; Seamans et al., 2001b). Such changes induced by DA have been extensively reported as mechanisms regulating goal-directed behaviors and working memory (Jacob et al., 2013; Noudoost and Moore, 2011; Ott et al., 2014), which also appear to enhance the modulation of the power in the nMOD frequency regime (Haegens et al., 2011). Thus, the fact that DA increases both information and power of the nMOD band might reflect DA increasing recurrence between sensory- and higher-order areas (Jacob et al., 2013).

8.4.4 Implications for neuroimaging

It is worth noting that the activity in different LFP-bands is correlated with distinct features of the blood-oxygen level dependent (BOLD) signal commonly measured in functional magnetic resonance imaging (fMRI) experiments. (Goense and Logothetis, 2008; Magri et al., 2012b; Zaldivar et al., 2014). In particular, the power in the γ band is mostly correlated to the BOLD amplitude (Magri et al., 2012b; Rauch et al., 2008b) while the nMOD band is closely linked to temporal shifts of the BOLD response peak (Magri et al., 2012b). If the power in nMOD is high, the BOLD response increases faster than when the power in nMOD is low (Magri et al., 2012b; Scheeringa et al., 2011). Our results, thus led us to suggests that temporal shifts in the BOLD signal may be related to variations in neuromodulation, likely due to the role of neuromodulators in promptly adjusting responses of cortical microcirculation to meet metabolic demands (Krimer et al., 1998b). This idea is supported by our earlier study, which showed that DA (using the same pharmacological approach as we did here) dissociated the BOLD-response signal from the activity in the γ band and cerebral blood flow (CBF, see

(Zaldivar et al., 2014)). We explained this dissociation as the result of increased energy use, given that the increase in CBF and neural activity and the decrease in BOLD indicate enhanced cerebral metabolic rate of oxygen ($CMRO_2$, (Zaldivar et al., 2014)), agreeing with autoradiography studies in monkeys showing increases brain metabolism due to LDC injection (Porrino et al., 1987b). We thus suggest that future studies combining BOLD with CBF or CBV can provide a better picture about the coupling between γ power, neuromodulation and variations in the metabolic demands (Goense et al., 2016; Zaldivar et al., 2014).

8.4.5 Considerations on the effects of other neuromodulators in oscillatory cortical processing

Effects of neuromodulators may differ from one structure to another, likely depending on receptor location, distribution and expression level (Dayan, 2012; Gu, 2002; Happel, 2015; Zaldivar et al., 2017). For example, neuromodulators can mediate local recurrent excitation (if receptors are expressed within one area), recruit of long-range corticocortical feedback (if receptors are expressed in a higher order area, which reciprocally connect with a region without receptor) or the combination of both (Dayan, 2012; Happel, 2015). Therefore, further experimental work is needed to understand how different neuromodulators, such as acetylcholine (ACh) or noradrenaline (NA), affect oscillatory cortical processing. In particular, whether the fluctuations of other neuromodulators affect the same [19-38 Hz] band that we showed here to reflect changes in DA, and whether other neuromodulators affect information processing in the same or different way. For example, changes in ACh have been reported to reduce excitatory recurrent interactions and increase inhibitory drive, resulting in enhanced signal-to-noise ratio of cortical responses (Minces et al., 2017). On the other hand, NA has been associated with modulation of the stimulus-response gain of cortical afferents (Safaai et al., 2015). Nonetheless, further studies are needed to determine the laminar and frequency-band specificity of such effects, and to find markers able to dissociate the effect of different neuromodulatory systems and their effect on cortical information processing.

8.5 APPENDIX

8.5.1 Animal Preparation and Anesthesia

The anesthesia protocol for all the experimental procedures has been described previously (Logothetis et al., 2012; Zaldivar et al., 2014). Briefly, before each experiment the monkeys were sedated with intramuscular (IM) injections of glycopyrrolate (0.01 $mg \cdot kg^{-1}$) and ketamine (15 $mg \cdot kg^{-1}$). An intravenous (IV) cannula was placed in the saphenous- or posterior tibial vein for administration of liquids, medication and anesthetics. After induction with fentanyl (3 $mg \cdot kg^{-1}$), thiopental (5 $mg \cdot kg^{-1}$) and succinylcholine chloride (3 $mg \cdot kg^{-1}$), animals were tracheally intubated (Rusch, Teleflex, USA) and ventilated using a Servo Ventilator 900C (Siemens, Germany) maintaining an end-tidal CO_2 of 33-35 mm Hg and O_2 saturation above 95%. Balanced anesthesia was maintained with remifentanil (0.5 – 2 $\mu g \cdot kg^{-1} min^{-1}$) and muscle relaxation was achieved with mivacurium chloride (2 – 6 $mg \cdot kg^{-1} h^{-1}$) to ensure complete paralysis of the eye muscles. The physiological state of the monkey was kept within normal limits throughout the experiment. Body temperature was maintained at 38-39°C. Lactate Ringer's (Jonosteril, Fresenius Kabi, Germany) with 2.5% glucose was continuously infused at a rate of 10 $ml \cdot kg^{-1} \cdot hr^{-1}$ in order to maintain an adequate acid-base balance and intravascular volume and blood pressure; hydroxyethyl starch (Volulyte, Fresenius Kabi, Germany) was administered as needed.

Two drops of 1% ophthalmic solution of anticholinergic cyclopentolate hydrochloride was applied into each eye to achieve cycloplegia and mydriasis. The eyes of the monkeys were kept open with custom-made irrigating-lid speculae to prevent drying of the tissue. The speculea irrigated the eyes with saline from the medial and lateral canthus at an infusion rate of 0.07 $ml \cdot min^{-1}$. Refractive errors were measured and hard contact lenses (Wöhlk-Contact-Linsen, Schönkirchen, Germany) were placed on the monkey's eye to focus on the plane on which stimuli are presented.

8.5.2 Visual Stimulation

The visual stimulus was presented using an in-house custom-built projector (SVGA fiber optic system with a resolution of 800x600 pixels). All image generation was done in 24-bit true color, using hardware double-buffering to provide smooth animation. The eyepieces of the stimulus presentation system were positioned and adjusted using a modified fundus camera (Zeiss RC250; see Logothetis et al., 1999a). The visual stimulus consisted of high contrast (100%) gamma corrected, fast-moving, colorful movie clips (no soundtrack) from commercially available movies. Stimulus timing was controlled by a Pentium computer (Advantec) running a real-time OS (QNX-Ottawa, Canada). We induced activity in V1 by using a block paradigm consisting isoluminant blank screen lasting 20 seconds, subsequently a 20 seconds movie segment (full field) was presented followed by a 20 seconds grey screen (spontaneous; Figure 1a). This block design was repeated 48 times yielding a 48-minutes experiment time (Figure 1a). A photodiode attached to the stimulus presentation monitor was used to ensure accurate control of the timing of stimulus presentation.

8.5.3 LFP average spectrum across monkeys

We computed the LFP-average spectrum from individual monkeys during the two stimuli conditions (spontaneous and movie clips) and found consistency in the LFP-average spectrum shape across all monkeys. Figure S1 depicts typical spectrograms from recordings in V1 from every monkey that participated in this study (Figure S1, monkeys are color coded; K07, n = 3; G11, n = 2; G09, n = 4; H09, n = 3). In good agreement with Figure 1c and with the study from Belitski, et al. (2008), we found significant power at frequencies between 0 – 150 Hz. In both stimuli condition the power steeply decreased at higher frequencies after a peak at the low frequencies (7 ± 2 Hz). This analysis also showed that power differences between spontaneous and sensory-evoked activity from each monkeys, was mostly located in the gamma range (50 – 150Hz; Figure S1a-b) as we reported in Figure 1c. We also computed the mutual information carried by the LFP power at each frequency from every monkey (Figure S1c). In consistency with Figure 1d we found two informative bands in the LFP spectrum from

all monkeys. These peaks corresponded to frequencies <20 Hz and to frequencies in the gamma range (>50 Hz; Figure S1c).

8.5.4 Correlations

We computed the noise correlation in oscillations at different cortical depths, both within the same band at each depth, and between different bands (Figure S4 a-b). We did not observe layer dependency in the correlation values between all frequencies. We first considered the correlations shared by two frequencies, ***f1*** and ***f2,*** in frequencies <40 Hz given that this was the region in which correlations were maximal before the injections. We found that the pairwise correlation between frequencies in the nMOD-range exhibited higher correlation values (mean pairwise correlations over all frequencies at 18 and 38 Hz and accords all layers: 0.38 ± 0.02) compared to the pairwise correlation between frequencies in the alpha-range (mean pairwise correlations over all frequencies at 8 and 12 Hz and accords all layers: 0.24 ± 0.03). Therefore, the results of high noise-correlations (Figure S4) and low signal-correlations (Figure 8.5) in the nMOD range are fully compatible with the observations from Belitski et al (2008), in which they suggested that the activity reflected in this frequency regime originates from a common source that is not sensitive to the sensory stimulation. In contrast, the pairwise correlation between frequencies in the alpha range exhibited high noise-correlation and signal correlations which suggested that the frequencies in this range share both sources of noise and of signal. In addition, the noise-correlation between two frequencies in the whole gamma range was similar in all layer (mean pairwise correlations in the gamma range: 0.13 ± 0.03, Figure S4). Non-changes in the noise correlations were observed due to the injections of DA (Figure S4b)

We also computed the correlations during spontaneous activity across all frequency pairs and layers (Figure S5). Note that for spontaneous activity and noise correlation are similar because there is no stimulus. We found that the correlations were also highest for the low frequencies (< 40 Hz). We found that the pairwise correlation in the nMOD range was high (mean pairwise correlations over all frequencies at 18 and 38 Hz and across all layers: 0.22 ± 0.02) as well as

the correlations between pairs of alpha range (mean pairwise correlations over all frequencies at 8 and 12 Hz and accords all layers: 0.23 ± 0.02). However, the correlations between pairs of frequencies in the gamma range were the lowest (mean pairwise correlations in the gamma range: 0.08 ± 0.03, Figure S5). We did not observe changes in the correlations during spontaneous activity due to the injections of DA.

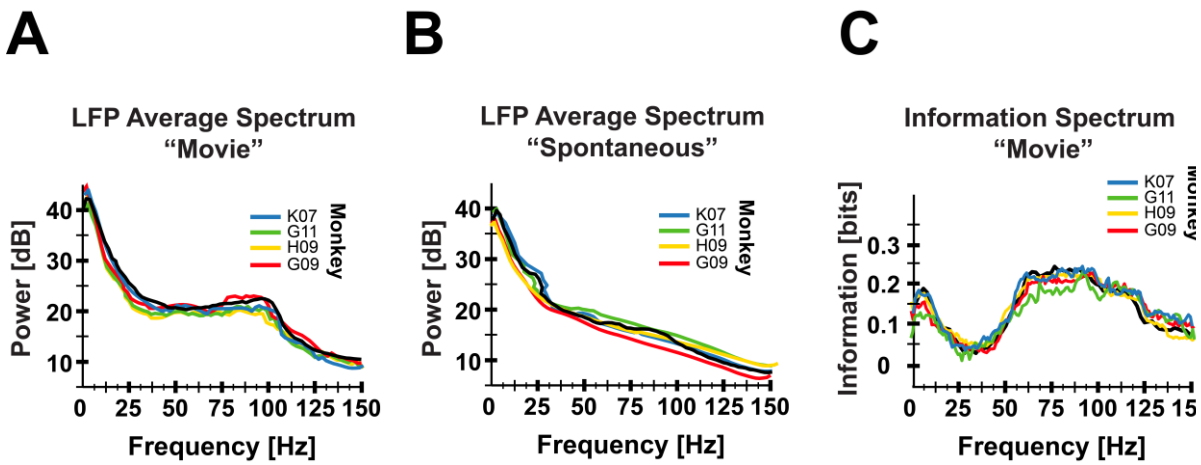

Figure S 1: Individual LFP-power Spectrum During Spontaneous and Movie Clips
(A) Average LFP power spectrum over the entire movie clips for different animals and without pharmacological injections (K07 shown in blue, n = 4; G11 shown in green, n = 3; G09 shown in red, n = 4; H09 shown in yellow, n = 4). **(B)** Average LFP power spectrum during spontaneous activity from different monkeys. **(C)** Information about the movie in the LFP power from different monkeys.

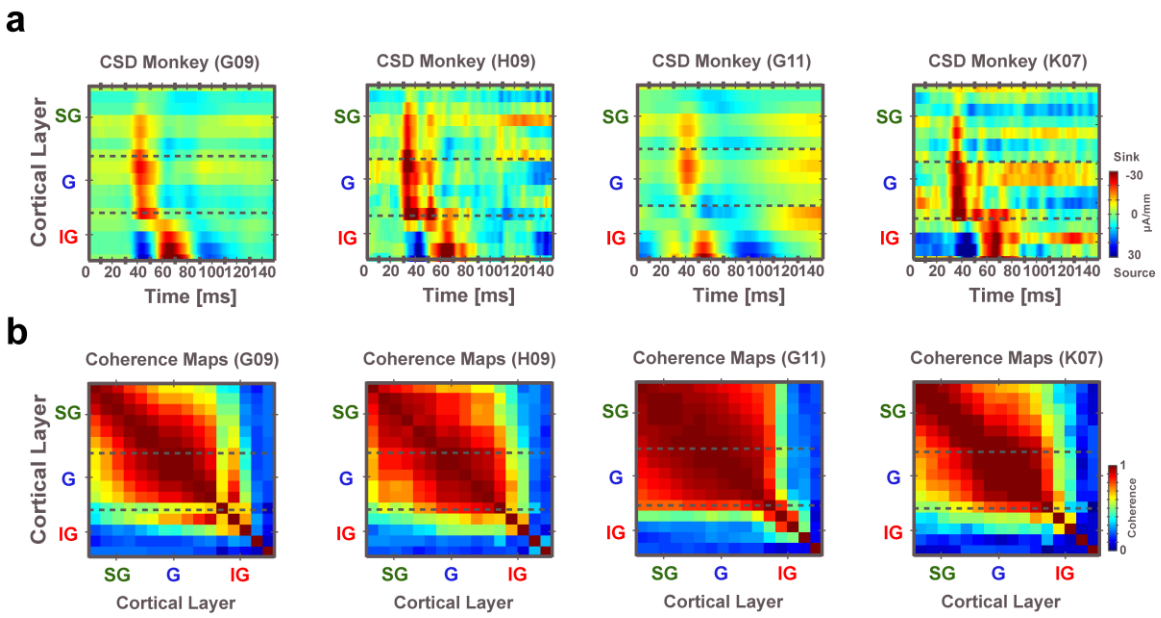

Figure S 2: CSD and coherence profiles from different monkeys used for the electrode alignment

(A) Stimulus triggered average CSD response from four monkeys. Averaged CSD profiles were computed before any pharmacological manipulation and for each monkey individually (n = 15 experiments). **(B)** Mean LFP coherence (30 – 100 Hz) computed between all pairs or laminar positions. This shows the inter-compartmental coherence over all session collected in all monkeys. Note that contact in the G and SG layers show string coherence with other G and most of the SG positions, but the coherence level fell abruptly in the IG. This coherence analysis helped us to determine the boundaries between IG and G.

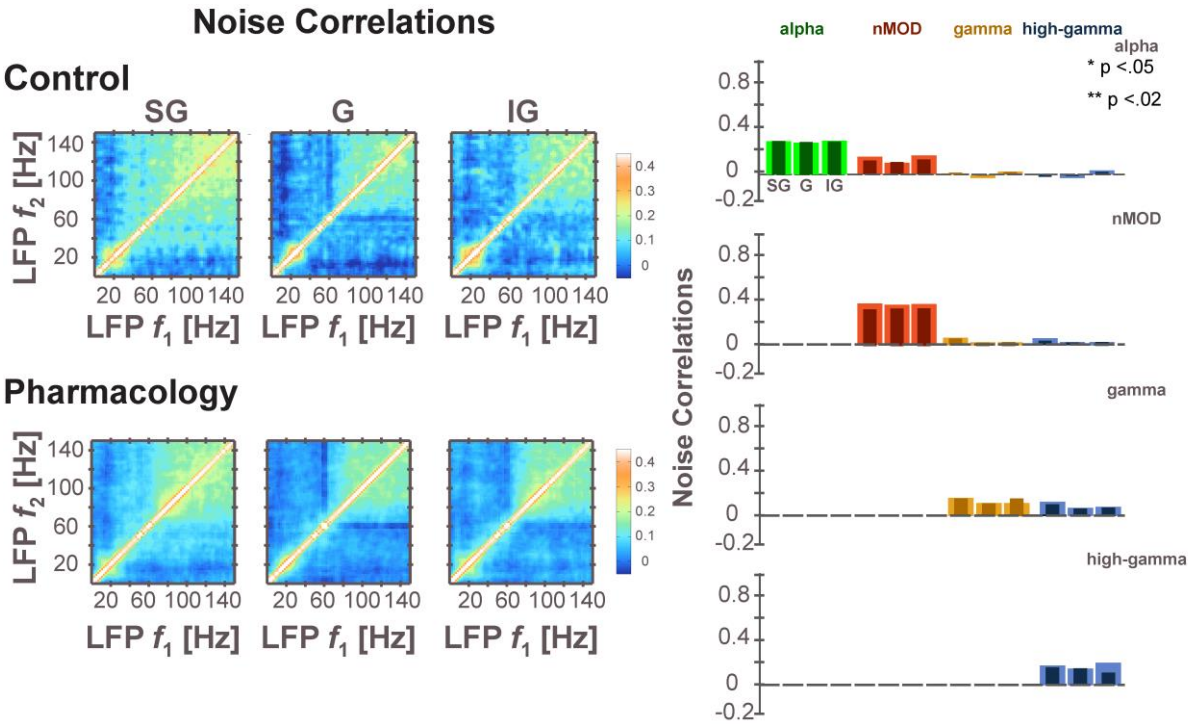

Figure S 3 (related to Figure 5)**. Noise Correlations among pairs of LFP frequencies.** **(A)** Noise correlations between pairs of LFP frequencies from different cortical depths; SG, G and IG layers (15 sessions in total). The figure shows the averaged Pearson noise correlation between the LFP power at frequencies $f1$ and $f2$ (15 neurophysiology sessions). **(B)** Average correlation within and between individual LFP bands before (light) and during pharmacological injection (dark).

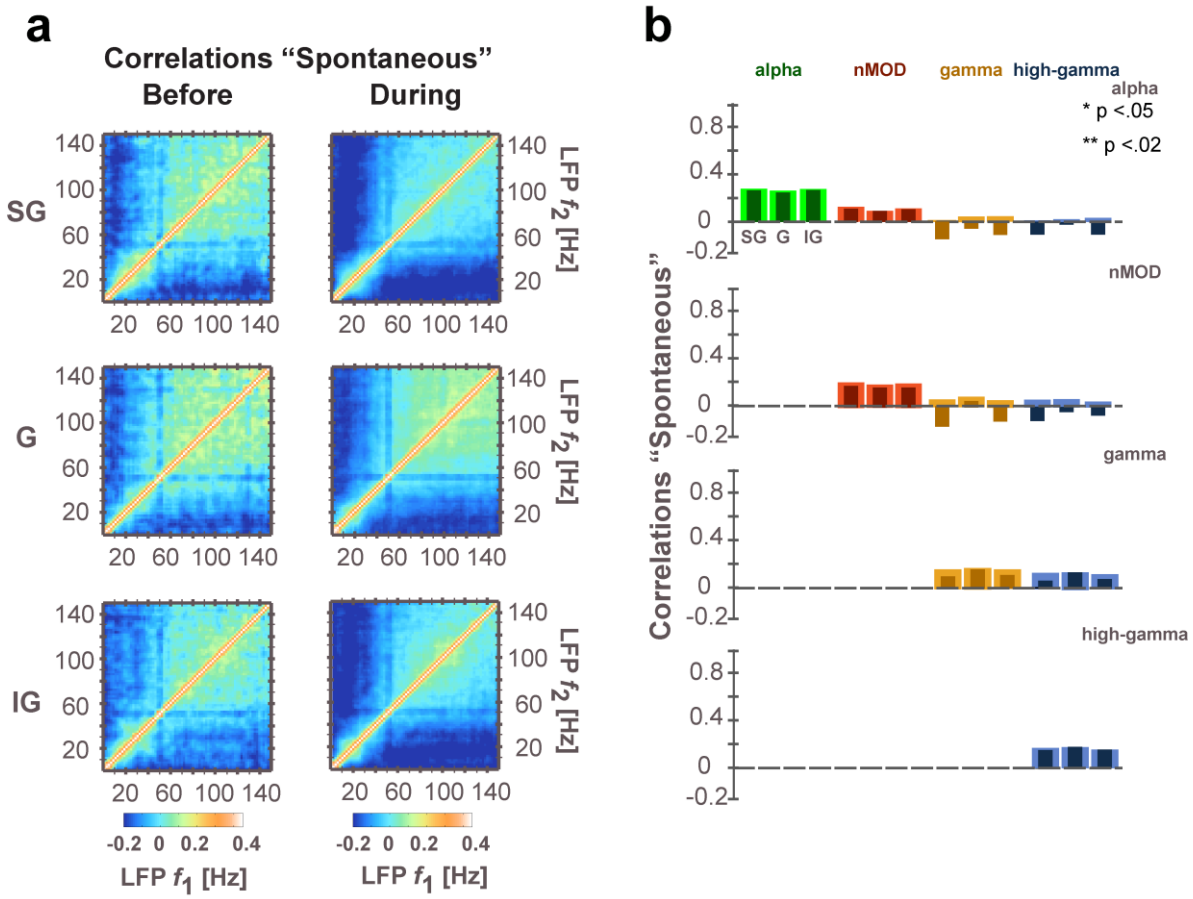

Figure S 4: Correlations during Spontaneous among pairs of LFP frequencies.
(A) Correlations during spontaneous activity between pairs of different LFP frequencies from different cortical depths; supragranular (SG), granular (G) and infragranular (IG) layers (15 sessions in total). It shows the averaged Pearson correlation between the powers observed at two different LFP frequencies $f1$ and $f2$ during spontaneous activity. **(B)** Average correlation within and between individual LFP bands before (light) and during pharmacological injection (dark).

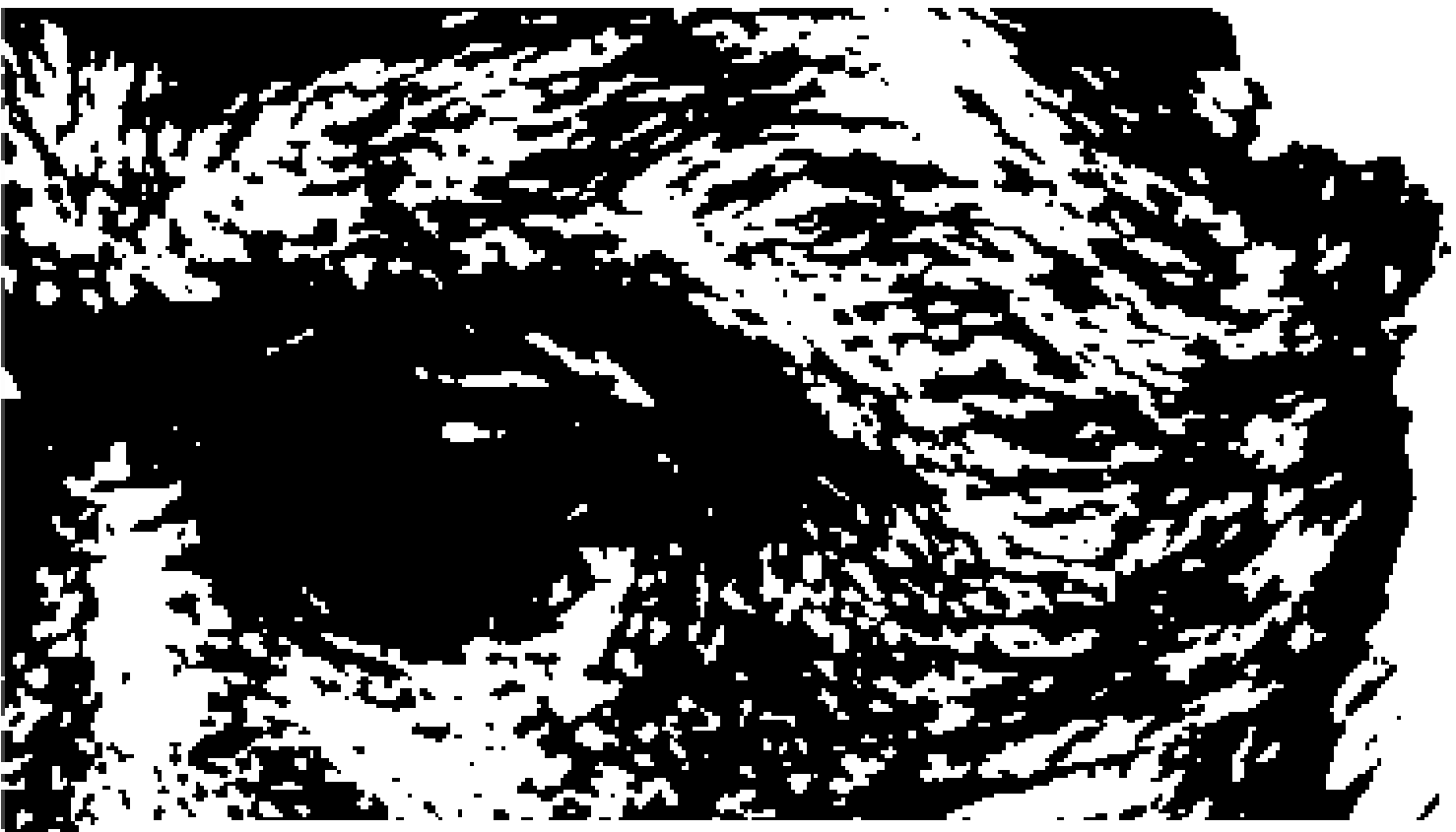

9. References

9. References

Algaze, A., Leguire, L.E., Roberts, C., Ibinson, J.W., Lewis, J.R., and Rogers, G. (2005). The effects of L-dopa on the functional magnetic resonance imaging response of patients with amblyopia: a pilot study. J AAPOS *9*, 216-223.

Alpert, A.J. (1990). Hydrophilic-interaction chromatography for the separation of peptides, nucleic acids and other polar compounds. J Chromatogr *499*, 177-196.

Andersson, K., and Arner, P. (1995). Cholinoceptor-mediated effects on glycerol output from human adipose tissue using in situ microdialysis. Br J Pharmacol *115*, 1155-1162.

Arsenault, J.T., Nelissen, K., Jarraya, B., and Vanduffel, W. (2013). Dopaminergic reward signals selectively decrease fMRI activity in primate visual cortex. Neuron *77*, 1174-1186.

Attwell, D., and Laughlin, S.B. (2001). An energy budget for signaling in the grey matter of the brain. J Cereb Blood Flow Metab *21*, 1133-1145.

Averbeck, B.B., Latham, P.E., and Pouget, A. (2006). Neural correlations, population coding and computation. Nature Reviews Neuroscience *7*, 358-366.

Basar, E., Gonder, A., and Ungan, P. (1980). Comparative frequency analysis of single EEG-evoked potential records. J Biomed Eng *2*, 9-14.

Belitski, A., Gretton, A., Magri, C., Murayama, Y., Montemurro, M.A., Logothetis, N.K., and Panzeri, S. (2008). Low-frequency local field potentials and spikes in primary visual cortex convey independent visual information. J Neurosci *28*, 5696-5709.

Belitski, A., Panzeri, S., Magri, C., Logothetis, N.K., and Kayser, C. (2010). Sensory information in local field potentials and spikes from visual and auditory cortices: time scales and frequency bands. J Comput Neurosci *29*, 533-545.

Bellander, B.M., Cantais, E., Enblad, P., Hutchinson, P., Nordstrom, C.H., Robertson, C., Sahuquillo, J., Smith, M., Stocchetti, N., Ungerstedt, U*., et al.* (2004). Consensus meeting on microdialysis in neurointensive care. Intensive Care Med *30*, 2166-2169.

Bergold, P.J., Pinkhasova, V., Syed, M., Kao, H.Y., Jozwicka, A., Zhao, N., Coplan, J.D., Dow-Edwards, D., and Fenton, A.A. (2009). Production of panic-like symptoms by lactate is associated with increased neural firing and oxidation of brain redox in the rat hippocampus. Neurosci Lett *453*, 219-224.

Bjerring, P.N., Hauerberg, J., Frederiksen, H.J., Jorgensen, L., Hansen, B.A., Tofteng, F., and Larsen, F.S. (2008). Cerebral glutamine concentration and lactate-pyruvate ratio in patients with acute liver failure. Neurocrit Care *9*, 3-7.

Black, K.J., Carl, J.L., Hartlein, J.M., Warren, S.L., Hershey, T., and Perlmutter, J.S. (2003). Rapid intravenous loading of levodopa for human research: clinical results. J Neurosci Methods *127*, 19-29.

Blicher, J.U., Stagg, C.J., O'Shea, J., Ostergaard, L., MacIntosh, B.J., Johansen-Berg, H., Jezzard, P., and Donahue, M.J. (2012). Visualization of altered neurovascular coupling in chronic stroke patients using multimodal functional MRI. J Cereb Blood Flow Metab *32*, 2044-2054.

Bosman, C.A., Schoffelen, J.M., Brunet, N., Oostenveld, R., Bastos, A.M., Womelsdorf, T., Rubehn, B., Stieglitz, T., De Weerd, P., and Fries, P. (2012). Attentional Stimulus Selection through Selective Synchronization between Monkey Visual Areas. Neuron *75*, 875-888.

Boutelle, M.G., Fellows, L.K., and Cook, C. (1992). Enzyme packed bed system for the on-line measurement of glucose, glutamate, and lactate in brain microdialysate. Anal Chem *64*, 1790-1794.

Boynton, G.M. (2011a). Spikes, BOLD, attention, and awareness: a comparison of electrophysiological and fMRI signals in V1. J Vis *11*, 12.

Boynton, G.M. (2011b). Spikes, BOLD, attention, and awareness: a comparison of electrophysiological and fMRI signals in V1. J Vis *11*, 1-16.

Briand, L.A., Gritton, H., Howe, W.M., Young, D.A., and Sarter, M. (2007). Modulators in concert for cognition: modulator interactions in the prefrontal cortex. Prog Neurobiol *83*, 69-91.

Briggs, F., and Callaway, E.M. (2001). Layer-specific input to distinct cell types in layer 6 of monkey primary visual cortex. Journal of Neuroscience *21*, 3600-3608.

Briggs, F., and Callaway, E.M. (2005). Laminar patterns of local excitatory input to layer 5 neurons in macaque primary visual cortex. Cereb Cortex *15*, 479-488.

Buckner, R.L., and Krienen, F.M. (2013). The evolution of distributed association networks in the human brain. Trends Cogn Sci *17*, 648-665.

Buffalo, E.A., Fries, P., Landman, R., Buschman, T.J., and Desimone, R. (2011). Laminar differences in gamma and alpha coherence in the ventral stream. PNAS *108*, 11262-11267.

Buschman, T.J., and Miller, E.K. (2007). Top-down versus bottom-up control of attention in the prefrontal and posterior parietal cortices. Science *315*, 1860-1862.

Buzsaki, G., and Draguhn, A. (2004). Neuronal oscillations in cortical networks. Science *304*, 1926-1929.

Buzsaki, G., and Wang, X.J. (2012). Mechanisms of gamma oscillations. Annu Rev Neurosci *35*, 203-225.

Calabresi, P., Centonze, D., Gubellini, P., Marfia, G.A., Pisani, A., Sancesario, G., and Bernardi, G. (2000). Synaptic transmission in the striatum: from plasticity to neurodegeneration. Prog Neurobiol *61*, 231-265.

Callaway, E.M. (1998). Local circuits in primary visual cortex of the macaque monkey. Annu Rev Neurosci *21*, 47-74.

Carlo, C.N., and Stevens, C.F. (2013). Structural uniformity of neocortex, revisited. PNAS *110*, 1488-1493.

Carlsson, M., and Carlsson, A. (1990). Interactions between glutamatergic and monoaminergic systems within the basal ganglia--implications for schizophrenia and Parkinson's disease. Trends Neurosci *13*, 272-276.

Cech, N.B., and Enke, C.G. (2001). Practical implications of some recent studies in electrospray ionization fundamentals. Mass Spectrom Rev *20*, 362-387.

Chatterjee, S., and Callaway, E.M. (2003). Parallel colour-opponent pathways to primary visual cortex. Nature *426*, 668-671.

Chen, Z., Silva, A.C., Yang, J., and Shen, J. (2005). Elevated endogenous GABA level correlates with decreased fMRI signals in the rat brain during acute inhibition of GABA transaminase. J Neurosci Res *79*, 383-391.

Choi, J.K., Chen, Y.I., Hamel, E., and Jenkins, B.G. (2006). Brain hemodynamic changes mediated by dopamine receptors: Role of the cerebral microvasculature in dopamine-mediated neurovascular coupling. Neuroimage *30*, 700-712.

Choi, J.K., Mandeville, J.B., Chen, Y.I., Grundt, P., Sarkar, S.K., Newman, A.H., and Jenkins, B.G. (2010). Imaging brain regional and cortical laminar effects of selective D3 agonists and antagonists. Psychopharmacology (Berl) *212*, 59-72.

Clapham, D.E. (1994). Direct G protein activation of ion channels? Annu Rev Neurosci *17*, 441-464.

Coenen, A.M. (1995). Neuronal activities underlying the electroencephalogram and evoked potentials of sleeping and waking: implications for information processing. Neurosci Biobehav Rev *19*, 447-463.

Collins, C.E., Airey, D.C., Young, N.A., Leitch, D.B., and Kaas, J.H. (2010). Neuron densities vary across and within cortical areas in primates. PNAS *107*, 15927-15932.

Cynober, L.A. (2002). Plasma amino acid levels with a note on membrane transport: characteristics, regulation, and metabolic significance. Nutrition *18*, 761-766.

D'Aniello, A., Lee, J.M., Petrucelli, L., and Di Fiore, M.M. (1998). Regional decreases of free D-aspartate levels in Alzheimer's disease. Neurosci Lett *250*, 131-134.

Dayan, P. (2012). Twenty-five lessons from computational neuromodulation. Neuron *76*, 240-256.

de Lafuente, V., and Romo, R. (2011a). Dopamine neurons code subjective sensory experience and uncertainty of perceptual decisions. PNAS *108*, 19767-19771.

de Lafuente, V., and Romo, R. (2011b). Dopamine neurons code subjective sensory experience and uncertainty of perceptual decisions. Proc Natl Acad Sci U S A *108*, 19767-19771.

de Ruyter van Steveninck, R.R., Lewen, G.D., Strong, S.P., Koberle, R., and Bialek, W. (1997). Reproducibility and variability in neural spike trains. Science *275*, 1805-1808.

Delfino, M., Kalisch, R., Czisch, M., Larramendy, C., Ricatti, J., Taravini, I.R., Trenkwalder, C., Murer, M.G., Auer, D.P., and Gershanik, O.S. (2007). Mapping the effects of three dopamine agonists with different dyskinetogenic potential and receptor selectivity using pharmacological functional magnetic resonance imaging. Neuropsychopharmacol *32*, 1911-1921.

Di Rocco, R.J., Kageyama, G.H., and Wong-Riley, M.T. (1989). The relationship between CNS metabolism and cytoarchitecture: a review of 14C-deoxyglucose studies with correlation to cytochrome oxidase histochemistry. Comput Med Imaging Graph *13*, 81-92.

Dobkins, K.R., Thiele, A., and Albright, T.D. (2000). Comparison of red-green equiluminance points in humans and macaques: evidence for different L:M cone ratios between species. Optical Society of America *17*, 545-556.

Donner, T.H., Siegel, M., Oostenveld, R., Fries, P., Bauer, M., and Engel, A.K. (2007). Population activity in the human dorsal pathway predicts the accuracy of visual motion detection. J Neurophysiol *98*, 345-359.

Dougherty, K., Cox, M.A., Ninomiya, T., Leopold, D.A., and Maier, A. (2017). Ongoing Alpha Activity in V1 Regulates Visually Driven Spiking Responses. Cereb Cortex *27*, 1113-1124.

Douglas, R.J., and Martin, K.A. (2004). Neuronal circuits of the neocortex. Annu Rev Neurosci *27*, 419-451.

Eckstein, J.A., Ammerman, G.M., Reveles, J.M., and Ackermann, B.L. (2008). Analysis of glutamine, glutamate, pyroglutamate, and GABA in cerebrospinal fluid using ion pairing HPLC with positive electrospray LC/MS/MS. J Neurosci Methods *171*, 190-196.

Einevoll, G.T., Kayser, C., Logothetis, N.K., and Panzeri, S. (2013). Modelling and analysis of local field potentials for studying the function of cortical circuits. Nat Rev Neurosci *14*, 770-785.

Einevoll, G.T., Pettersen, K.H., Devor, A., Ulbert, I., Halgren, E., and Dale, A.M. (2007). Laminar population analysis: Estimating firing rates and evoked synaptic activity from multielectrode recordings in rat barrel cortex. Journal of Neurophysiology *97*, 2174-2190.

Ekstrom, L.B., Roelfsema, P.R., Arsenault, J.T., Bonmassar, G., and Vanduffel, W. (2008). Bottom-up dependent gating of frontal signals in early visual cortex. Science *321*, 414-417.

Engel, A.K., and Fries, P. (2010). Beta-band oscillations--signalling the status quo? Curr Opin Neurobiol *20*, 156-165.

Esaki, T., Itoh, Y., Shimoji, K., Cook, M., Jehle, J., and Sokoloff, L. (2002). Effects of dopamine receptor blockade on cerebral blood flow response to somatosensory stimulation in the unanesthetized rat. J Pharmacol Exp Ther *303*, 497-502.

Faraci, F.M., and Breese, K.R. (1993). Nitric oxide mediates vasodilatation in response to activation of N-methyl-D-aspartate receptors in brain. Circ Res *72*, 476-480.

Fox, P.T., and Raichle, M.E. (1986). Focal physiological uncoupling of cerebral blood flow and oxidative metabolism during somatosensory stimulation in human subjects. PNAS *83*, 1140-1144.

Fox, P.T., Raichle, M.E., Mintun, M.A., and Dence, C. (1988). Nonoxidative glucose consumption during focal physiologic neural activity. Science *241*, 462-464.

Freund, H., Oyono-Enguelle, S., Heitz, A., Ott, C., Marbach, J., Gartner, M., and Pape, A. (1990). Comparative lactate kinetics after short and prolonged submaximal exercise. Int J Sports Med *11*, 284-288.

Frien, A., Eckhorn, R., Bauer, R., Woelbern, T., and Gabriel, A. (2000). Fast oscillations display sharper orientation tuning than slower components of the same recordings in striate cortex of the awake monkey. Eur J Neurosci *12*, 1453-1465.

Fries, P. (2009). Neuronal Gamma-Band Synchronization as a Fundamental Process in Cortical Computation. Annual Review of Neuroscience *32*, 209-224.

Fries, P., Reynolds, J.H., Rorie, A.E., and Desimone, R. (2001). Modulation of oscillatory neuronal synchronization by selective visual attention. Science *291*, 1560-1563.

Fries, P., Womelsdorf, T., Oostenveld, R., and Desimone, R. (2008). The effects of visual stimulation and selective visual attention on rhythmic neuronal synchronization in macaque area V4. J Neurosci *28*, 4823-4835.

Fu, B., Gao, X., Zhang, S.P., Cai, Z., and Shen, J. (2008). Quantification of acetylcholine in microdialysate of subcutaneous tissue by hydrophilic interaction chromatography/tandem mass spectrometry. Rapid Commun Mass Spectrom *22*, 1497-1502.

Fujii, T., Yamada, S., Yamaguchi, N., Fujimoto, K., Suzuki, T., and Kawashima, K. (1995). Species differences in the concentration of acetylcholine, a neurotransmitter, in whole blood and plasma. Neurosci Lett *201*, 207-210.

Gibson, G.E., Peterson, C., and Sansone, J. (1981). Neurotransmitter and carbohydrate metabolism during aging and mild hypoxia. Neurobiol Aging *2*, 165-172.

Gieselmann, M.A., and Thiele, A. (2008). Comparison of spatial integration and surround suppression characteristics in spiking activity and the local field potential in macaque V1. Eur J Neurosci *28*, 447-459.

Goense, J., Bohraus, Y., and Logothetis, N.K. (2016). fMRI at High Spatial Resolution: Implications for BOLD-Models. Front Comput Neurosci *10*, 66.

Goense, J., Logothetis, N.K., and Merkle, H. (2010). Flexible, phase-matched, linear receive arrays for high-field MRI in monkeys. Magn Reson Imaging *28*, 1183-1191.

Goense, J., Merkle, H., and Logothetis, N.K. (2012). High-resolution fMRI reveals laminar differences in neurovascular coupling between positive and negative BOLD responses. Neuron *76*, 629-639.

Goense, J.B., and Logothetis, N.K. (2008). Neurophysiology of the BOLD fMRI signal in awake monkeys. Curr Biol *18*, 631-640.

Gordon, G.R., Choi, H.B., Rungta, R.L., Ellis-Davies, G.C., and MacVicar, B.A. (2008). Brain metabolism dictates the polarity of astrocyte control over arterioles. Nature *456*, 745-749.

Gottberg, E., Montreuil, B., and Reader, T.A. (1988). Acute effects of lithium on dopaminergic responses: iontophoretic studies in the rat visual cortex. Synapse *2*, 442-449.

Gozzi, A., Large, C.H., Schwarz, A., Bertani, S., Crestan, V., and Bifone, A. (2008). Differential effects of antipsychotic and glutamatergic agents on the phMRI response to phencyclidine. Neuropsychopharmacol *33*, 1690-1703.

Gozzi, A., Schwarz, A.J., Reese, T., Crestan, V., Bertani, S., Turrini, G., Corsi, M., and Bifone, A. (2005). Functional magnetic resonance mapping of intracerebroventricular infusion of a neuroactive peptide in the anaesthetised rat. J Neurosci Meth *142*, 115-124.

Grashow, R., Brookings, T., and Marder, E. (2009). Reliable neuromodulation from circuits with variable underlying structure. Proc Natl Acad Sci U S A *106*, 11742-11746.

Gsell, W., Burke, M., Wiedermann, D., Bonvento, G., Silva, A.C., Dauphin, F., Buhrle, C., Hoehn, M., and Schwindt, W. (2006). Differential effects of NMDA and AMPA glutamate receptors on functional magnetic resonance imaging signals and evoked neuronal activity during forepaw stimulation of the rat. J Neurosci *26*, 8409-8416.

Gu, Q. (2002). Neuromodulatory transmitter systems in the cortex and their role in cortical plasticity. Neuroscience *111*, 815-835.

Haegens, S., Nacher, V., Hernandez, A., Luna, R., Jensen, O., and Romo, R. (2011). Beta oscillations in the monkey sensorimotor network reflect somatosensory decision making. Proc Natl Acad Sci U S A *108*, 10708-10713.

Hamel, E.J., Grewe, B.F., Parker, J.G., and Schnitzer, M.J. (2015). Cellular level brain imaging in behaving mammals: an engineering approach. Neuron *86*, 140-159.

Hansen, B.J., Chelaru, M.I., and Dragoi, V. (2012). Correlated variability in laminar cortical circuits. Neuron *76*, 590-602.

Hansen, B.J., and Dragoi, V. (2011). Adaptation-induced synchronization in laminar cortical circuits. PNAS *108*, 10720-10725.

Happel, M.F. (2015). Dopaminergic impact on local and global cortical circuit processing during learning. Behav Brain Res *299*, 32-41.

Happel, M.F., Deliano, M., Handschuh, J., and Ohl, F.W. (2014). Dopamine-modulated recurrent corticoefferent feedback in primary sensory cortex promotes detection of behaviorally relevant stimuli. J Neurosci *34*, 1234-1247.

Hasselmo, M.E. (1995). Neuromodulation and cortical function: modeling the physiological basis of behavior. Behav Brain Res *67*, 1-27.

Hawkins, R.A. (2009). The blood-brain barrier and glutamate. Am J Clin Nutr *90*, 867S-874S.

Henrie, J.A., and Shapley, R. (2005). LFP power spectra in V1 cortex: the graded effect of stimulus contrast. J Neurophysiol *94*, 479-490.

Henry, G.H., Harvey, A.R., and Lund, J.S. (1979). The afferent connections and laminar distribution of cells in the cat striate cortex. The Journal of comparative neurology *187*, 725-744.

Hershey, T., Black, K.J., Carl, J.L., and Perlmutter, J.S. (2000). Dopa-induced blood flow responses in nonhuman primates. Exp Neurol *166*, 342-349.

Hertz, L., Peng, L., and Dienel, G.A. (2007). Energy metabolism in astrocytes: high rate of oxidative metabolism and spatiotemporal dependence on glycolysis/glycogenolysis. J Cereb Blood Flow Metab *27*, 219-249.

Hill, D.N.V., Z., Jia, H., Sakmann, B., and Konnerth, A. (2013). Multibranch activity in basal and tuft dendrites during firing of layer 5 cortical neurons in vivo. PNAS *110*.

Hillman, E.M. (2014). Coupling mechanism and significance of the BOLD signal: a status report. Annu Rev Neurosci *37*, 161-181.

Hirsch, J.A., Wang, X., Sommer, F.T., and Martinez, L.M. (2015). How inhibitory circuits in the thalamus serve vision. Annu Rev Neurosci *38*, 309-329.

Honey, G., and Bullmore, E. (2004). Human pharmacological MRI. Trends in pharmacological sciences *25*, 366-374.

Horton, J.C., and Adams, D.L. (2005). The cortical column: a structure without a function. Philos Trans R Soc Lond B Biol Sci *360*, 837-862.

Hu, Y., and Wilson, G.S. (1997). A temporary local energy pool coupled to neuronal activity: fluctuations of extracellular lactate levels in rat brain monitored with rapid-response enzyme-based sensor. J Neurochem *69*, 1484-1490.

Huang, T., Yang, L., Gitzen, J., Kissinger, P.T., Vreeke, M., and Heller, A. (1995). Detection of basal acetylcholine in rat brain microdialysate. J Chromatogr B Biomed Appl *670*, 323-327.

Iadecola, C. (2004). Neurovascular regulation in the normal brain and in Alzheimer's disease. Nat Rev Neurosci *5*, 347-360.

Ido, Y., Chang, K., and Williamson, J.R. (2004). NADH augments blood flow in physiologically activated retina and visual cortex. PNAS *101*, 653-658.

Isaacson, J.S., and Scanziani, M. (2011). How inhibition shapes cortical activity. Neuron *72*, 231-243.

Izpisua Belmonte, J.C., Callaway, E.M., Caddick, S.J., Churchland, P., Feng, G., Homanics, G.E., Lee, K.F., Leopold, D.A., Miller, C.T., Mitchell, J.F*., et al.* (2015). Brains, genes, and primates. Neuron *86*, 617-631.

Jacob, S.N., Ott, T., and Nieder, A. (2013). Dopamine regulates two classes of primate prefrontal neurons that represent sensory signals. J Neurosci *33*, 13724-13734.

Jenkins, B.G., Sanchez-Pernaute, R., Brownell, A.L., Chen, Y.C., and Isacson, O. (2004). Mapping dopamine function in primates using pharmacologic magnetic resonance imaging. J Neurosci *24*, 9553-9560.

Jezzard, P., and Buxton, R.B. (2006). The clinical potential of functional magnetic resonance imaging. J Magn Reson Imaging *23*, 787-793.

Kaddurah-Daouk, R., and Krishnan, K.R. (2009). Metabolomics: a global biochemical approach to the study of central nervous system diseases. Neuropsychopharmacol *34*, 173-186.

Kadekaro, M., Crane, A.M., and Sokoloff, L. (1985). Differential-Effects of Electrical-Stimulation of Sciatic-Nerve on Metabolic-Activity in Spinal-Cord and Dorsal-Root Ganglion in the Rat. PNAS *82*, 6010-6013.

Kadekaro, M., Vance, W.H., Terrell, M.L., Gary, H., Eisenberg, H.M., and Sokoloff, L. (1987). Effects of Antidromic Stimulation of the Ventral Root on Glucose-Utilization in the Ventral Horn of the Spinal-Cord in the Rat. PNAS *84*, 5492-5495.

Kageyama, G.H., and Wong-Riley, M. (1986). Laminar and cellular localization of cytochrome oxidase in the cat striate cortex. The Journal of comparative neurology *245*, 137-159.

Kajikawa, Y., and Schroeder, C.E. (2011). How local is the local field potential? Neuron *72*, 847-858.

Kalisch, R., Salome, N., Platzer, S., Wigger, A., Czisch, M., Sommer, W., Singewald, N., Heilig, M., Berthele, A., Holsboer, F.*, et al.* (2004). High trait anxiety and hyporeactivity to stress of the dorsomedial prefrontal cortex: a combined phMRI and Fos study in rats. Neuroimage *23*, 382-391.

Kalman, J., Palotas, A., Kis, G., Boda, K., Turi, P., Bari, F., Domoki, F., Doda, I., Argyelan, M., Vincze, G.*, et al.* (2005). Regional cortical blood flow changes following sodium lactate infusion in Alzheimer's disease. Eur J Neurosci *21*, 1671-1678.

Kandadai, M.A., Raymond, J.L., and Shaw, G.J. (2012). Comparison of electrical conductivities of various brain phantom gels: Developing a 'Brain Gel Model'. Materials science & engineering C, Materials for biological applications *32*, 2664-2667.

Kawashima, K., Oohata, H., Fujimoto, K., and Suzuki, T. (1987). Plasma concentration of acetylcholine in young women. Neurosci Lett *80*, 339-342.

Kida, I., Hyder, F., and Behar, K.L. (2001). Inhibition of voltage-dependent sodium channels suppresses the functional magnetic resonance imaging response to forepaw somatosensory activation in the rodent. J Cerebr Blood F Met *21*, 585-591.

Kida, I., Smith, A.J., Blumenfeld, H., Behar, K.L., and Hyder, F. (2006). Lamotrigine suppresses neurophysiological responses to somatosensory stimulation in the rodent. Neuroimage *29*, 216-224.

Kim, S.G. (1995). Quantification of relative cerebral blood flow change by flow-sensitive alternating inversion recovery (FAIR) technique: application to functional mapping. Magn Reson Med *34*, 293-301.

Kim, S.G., and Ogawa, S. (2012). Biophysical and physiological origins of blood oxygenation level-dependent fMRI signals. J Cereb Blood Flow Metab *32*, 1188-1206.

Kopell, N., Ermentrout, G.B., Whittington, M.A., and Traub, R.D. (2000). Gamma rhythms and beta rhythms have different synchronization properties. Proc Natl Acad Sci U S A *97*, 1867-1872.

Kortelainen, J., Vayrynen, E., and Seppanen, T. (2011). Depth of Anesthesia During Multidrug Infusion: Separating the Effects of Propofol and Remifentanil Using the Spectral Features of EEG. Ieee T Bio-Med Eng *58*, 1216-1223.

Krimer, L.S., Muly, E.C., 3rd, Williams, G.V., and Goldman-Rakic, P.S. (1998a). Dopaminergic regulation of cerebral cortical microcirculation. Nat Neurosci *1*, 286-289.

Krimer, L.S., Muly, E.C., Williams, G.V., and Goldman-Rakic, P.S. (1998b). Dopaminergic regulation of cerebral cortical microcirculation. Nature Neuroscience *1*, 286-289.

Ku, S.P., Tolias, A.S., Logothetis, N.K., and Goense, J. (2011). fMRI of the face-processing network in the ventral temporal lobe of awake and anesthetized macaques. Neuron *70*, 352-362.

Kujala, J., Jung, J., Bouvard, S., Lecaignard, F., Lothe, A., Bouet, R., Ciumas, C., Ryvlin, P., and Jerbi, K. (2015). Gamma oscillations in V1 are correlated with GABAA receptor density: A multi-modal MEG and Flumazenil-PET study. Sci Rep *5*, 16347.

Kwak, Y., Peltier, S.J., Bohnen, N.I., Muller, M.L., Dayalu, P., and Seidler, R.D. (2012). L-DOPA changes spontaneous low-frequency BOLD signal oscillations in Parkinson's disease: a resting state fMRI study. Front Syst Neurosci *6*, 1-15.

Laughlin, S.B., de Ruyter van Steveninck, R.R., and Anderson, J.C. (1998). The metabolic cost of neural information. Nat Neurosci *1*, 36-41.

Lee, J.H., Durand, R., Gradinaru, V., Zhang, F., Goshen, I., Kim, D.S., Fenno, L.E., Ramakrishnan, C., and Deisseroth, K. (2010). Global and local fMRI signals driven by neurons defined optogenetically by type and wiring. Nature *465*, 788-792.

Leenders, K.L., Wolfson, L., Gibbs, J.M., Wise, R.J., Causon, R., Jones, T., and Legg, N.J. (1985). The effects of L-DOPA on regional cerebral blood flow and oxygen metabolism in patients with Parkinson's disease. Brain *108 (Pt 1)*, 171-191.

Leonard, B.E., and Shallice, S.A. (1971). Some Neurochemical Effects of Amphetamine, Methylamphetamine and Para Bromomethyl Amphetamine in Rat. Br J Pharmacol *41*, 198-&.

Leski, S., Linden, H., Tetzlaff, T., Pettersen, K.H., and Einevoll, G.T. (2013). Frequency dependence of signal power and spatial reach of the local field potential. PLoS Comput Biol *9*, e1003137.

Li, J., von Pfostl, V., Zaldivar, D., Zhang, X., Logothetis, N., and Rauch, A. (2011). Measuring multiple neurochemicals and related metabolites in blood and brain of the rhesus monkey by using dual microdialysis sampling and capillary hydrophilic interaction chromatography-mass spectrometry. Anal Bioanal Chem.

Lidow, M.S., Goldman-Rakic, P.S., Gallager, D.W., and Rakic, P. (1991). Distribution of dopaminergic receptors in the primate cerebral cortex: quantitative autoradiographic analysis using [3H]raclopride, [3H]spiperone and [3H]SCH23390. Neuroscience *40*, 657-671.

Lindsley, D.B., and Wicke, J.D. (1974). The Electroencephalogram: Autonomous Electrical Activity in Man and Animals. In Bioelectric Recording Techniques: Electroencephalography and Human Brain Potentials, R.F. Thompson, and M.M. Patterson, eds., pp. 3-83.

Logothetis, N.K. (2008). What we can do and what we cannot do with fMRI. Nature *453*, 869-878.

Logothetis, N.K. (2010). Bold claims for optogenetics. Nature *468*, E3-E4.

Logothetis, N.K., Augath, M., Murayama, Y., Rauch, A., Sultan, F., Goense, J., Oeltermann, A., and Merkle, H. (2010). The effects of electrical microstimulation on cortical signal propagation. Nat Neurosci *13*, 1283-1291.

Logothetis, N.K., Eschenko, O., Murayama, Y., Augath, M., Steudel, T., Evrard, H.C., Besserve, M., and Oeltermann, A. (2012). Hippocampal-cortical interaction during periods of subcortical silence. Nature *491*, 547-553.

Logothetis, N.K., Guggenberger, H., Peled, S., and Pauls, J. (1999a). Functional imaging of the monkey brain. Nat Neurosci *2*, 555-562.

Logothetis, N.K., Guggenberger, H., Peled, S., and Pauls, J. (1999b). Functional imaging of the monkey brain. Nat Neurosci *2*, 555-562.

Logothetis, N.K., Kayser, C., and Oeltermann, A. (2007). In vivo measurement of cortical impedance spectrum in monkeys: implications for signal propagation. Neuron *55*, 809-823.

Logothetis, N.K., Pauls, J., Augath, M., Trinath, T., and Oeltermann, A. (2001). Neurophysiological investigation of the basis of the fMRI signal. Nature *412*, 150-157.

Loubinoux, I., Pariente, J., Boulanouar, K., Carel, C., Manelfe, C., Rascol, O., Celsis, P., and Chollet, F. (2002). A single dose of the serotonin neurotransmission agonist paroxetine enhances motor output: double-blind, placebo-controlled, fMRI study in healthy subjects. Neuroimage *15*, 26-36.

Lund, J.S. (1973). Organization of neurons in the visual cortex, area 17, of the monkey (Macaca mulatta). The Journal of comparative neurology *147*, 455-496.

Lund, J.S. (1988). Anatomical organization of macaque monkey striate visual cortex. Annu Rev Neurosci *11*, 253-288.

Lund, J.S., Angelucci, A., and Bressloff, P.C. (2003). Anatomical Substrates for Functional Columns in Macaque Monkey Primary Visual Cortex. Cerebral cortex *12*, 15-24.

Lundqvist, M., Rose, J., Herman, P., Brincat, S.L., Buschman, T.J., and Miller, E.K. (2016). Gamma and Beta Bursts Underlie Working Memory. Neuron *90*, 152-164.

Magri, C., Mazzoni, A., Logothetis, N.K., and Panzeri, S. (2012a). Optimal band separation of extracellular field potentials. J Neurosci Methods *210*, 66-78.

Magri, C., Schridde, U., Murayama, Y., Panzeri, S., and Logothetis, N.K. (2012b). The amplitude and timing of the BOLD signal reflects the relationship between local field potential power at different frequencies. J Neurosci *32*, 1395-1407.

Magri, C., Whittingstall, K., Singh, V., Logothetis, N.K., and Panzeri, S. (2009a). A toolbox for the fast information analysis of multiple-site LFP, EEG and spike train recordings. BMC Neurosci *10*, 81.

Magri, C., Whittingstall, K., Singh, V., Logothetis, N.K., and Panzeri, S. (2009b). A toolbox for the fast information analysis of multiple-site LFP, EEG and spike train recordings. Bmc Neuroscience *10*.

Maier, A., Adams, G.K., Aura, C., and Leopold, D.A. (2010). Distinct superficial and deep laminar domains of activity in the visual cortex during rest and stimulation. Front Syst Neurosci *4*.

Maier, A., Aura, C.J., and Leopold, D.A. (2011). Infragranular sources of sustained local field potential responses in macaque primary visual cortex. J Neurosci *31*, 1971-1980.

Mandeville, J.B., Jenkins, B.G., Kosofsky, B.E., Moskowitz, M.A., Rosen, B.R., and Marota, J.J. (2001). Regional sensitivity and coupling of BOLD and CBV changes during stimulation of rat brain. Magn Reson Med *45*, 443-447.

Mandeville, J.B., Sander, C.Y., Jenkins, B.G., Hooker, J.M., Catana, C., Vanduffel, W., Alpert, N.M., Rosen, B.R., and Normandin, M.D. (2013). A receptor-based model for dopamine-induced fMRI signal. Neuroimage *75C*, 46-57.

Mantini, D., Corbetta, M., Romani, G.L., Orban, G.A., and Vanduffel, W. (2013). Evolutionarily novel functional networks in the human brain? J Neurosci *33*, 3259-3275.

Marder, E., O'Leary, T., and Shruti, S. (2014). Neuromodulation of circuits with variable parameters: single neurons and small circuits reveal principles of state-dependent and robust neuromodulation. Annu Rev Neurosci *37*, 329-346.

Matuszewski, B.K., Constanzer, M.L., and Chavez-Eng, C.M. (2003). Strategies for the assessment of matrix effect in quantitative bioanalytical methods based on HPLC-MS/MS. Analytical Chemistry *75*, 3019-3030.

Mentis, M.J., Alexander, G.E., Krasuski, J., Pietrini, P., Furey, M.L., Schapiro, M.B., and Rapoport, S.I. (1998). Increasing required neural response to expose abnormal brain function in mild versus moderate or severe Alzheimer's disease: PET study using parametric visual stimulation. Am J Psychiatry *155*, 785-794.

Michels, L., Bucher, K., Luchinger, R., Klaver, P., Martin, E., Jeanmonod, D., and Brandeis, D. (2010). Simultaneous EEG-fMRI during a working memory task: modulations in low and high frequency bands. PLoS One *5*, e10298.

Minces, V., Pinto, L., Dan, Y., and Chiba, A.A. (2017). Cholinergic shaping of neural correlations. Proc Natl Acad Sci U S A *114*, 5725-5730.

Mintun, M.A., Vlassenko, A.G., Rundle, M.M., and Raichle, M.E. (2004). Increased lactate/pyruvate ratio augments blood flow in physiologically activated human brain. PNAS *101*, 659-664.

Mitterschiffthaler, M.T., Ettinger, U., Mehta, M.A., Mataix-Cols, D., and Williams, S.C. (2006). Applications of functional magnetic resonance imaging in psychiatry. J Magn Reson Imaging *23*, 851-861.

Mitzdorf, U. (1985). Current source-density method and application in cat cerebral cortex: investigation of evoked potentials and EEG phenomena. Physiol Rev *65*, 37-100.

Mitzdorf, U. (1987). Properties of the evoked potential generators: current source-density analysis of visually evoked potentials in the cat cortex. Int J Neurosci *33*, 33-59.

Mitzdorf, U., and Singer, W. (1979). Excitatory synaptic ensemble properties in the visual cortex of the macaque monkey: a current source density analysis of electrically evoked potentials. The Journal of comparative neurology *187*, 71-83.

Molina, J.A., Gomez, P., Vargas, C., Ortiz, S., Perez-Rial, S., Uriguen, L., Oliva, J.M., Villanueva, C., and Manzanares, J. (2005). Neurotransmitter amino acid in cerebrospinal fluid of patients with dementia with Lewy bodies. Journal of Neural Transmission *112*, 557-563.

Monge-Acuna, A.A., and Fornaguera-Trias, J. (2009). A high performance liquid chromatography method with electrochemical detection of gamma-aminobutyric acid, glutamate and glutamine in rat brain homogenates. J Neurosci Methods *183*, 176-181.

Montastruc, J.L., Celsis, P., Agniel, A., Demonet, J.F., Doyon, B., Puel, M., Marc-Vergnes, J.P., and Rascol, A. (1987). Levodopa-induced regional cerebral blood flow changes in normal volunteers and patients with Parkinson's disease. Lack of correlation with clinical or neuropsychological improvements. Mov Disord *2*, 279-289.

Moore, T., and Zirnsak, M. (2017). Neural Mechanisms of Selective Visual Attention. Annu Rev Psychol *68*, 47-72.

Moreno, A., Morris, R.G., and Canals, S. (2015). Frequency-Dependent Gating of Hippocampal-Neocortical Interactions. Cerebral cortex.

Mountcastle, V.B. (1997). The columnar organization of the neocortex. Brain *120 (Pt 4)*, 701-722.

Murayama, Y., Biessmann, F., Meinecke, F.C., Muller, K.R., Augath, M., Oeltermann, A., and Logothetis, N.K. (2010). Relationship between neural and hemodynamic signals during spontaneous activity studied with temporal kernel CCA. Magn Reson Imaging *28*, 1095-1103.

Nassi, J.J., and Callaway, E.M. (2009). Parallel processing strategies of the primate visual system. Nat Rev Neurosci *10*, 360-372.

Noudoost, B., and Moore, T. (2011). Control of visual cortical signals by prefrontal dopamine. Nature *474*, 372-375.

Nunez, P.L. (1981). Electric Fields of the Brain: The Neurophysics of EEG (Oxford, UK: Oxford University Press).

O'Kusky, J., and Colonnier, M. (1982). A laminar analysis of the number of neurons, glia, and synapses in the adult cortex (area 17) of adult macaque monkeys. The Journal of comparative neurology *210*, 278-290.

Obayashi, S., Nagai, Y., Suhara, T., Okauchi, T., Inaji, M., Iriki, A., and Maeda, J. (2009). Monkey brain activity modulated by reward preferences: a positron emission tomography study. Neurosci Res *64*, 421-428.

Oeltermann, A., Augath, M.A., and Logothetis, N.K. (2007). Simultaneous recording of neuronal signals and functional NMR imaging. Magn Reson Imaging *25*, 760-774.

Ogawa, S., Tank, D.W., Menon, R., Ellermann, J.M., Kim, S.G., Merkle, H., and Ugurbil, K. (1992). Intrinsic signal changes accompanying sensory stimulation: functional brain mapping with magnetic resonance imaging. PNAS *89*, 5951-5955.

Ott, T., Jacob, S.N., and Nieder, A. (2014). Dopamine receptors differentially enhance rule coding in primate prefrontal cortex neurons. Neuron *84*, 1317-1328.

Oyono-Enguelle, S., Marbach, J., Heitz, A., Ott, C., Gartner, M., Pape, A., Vollmer, J.C., and Freund, H. (1990). Lactate removal ability and graded exercise in humans. J Appl Physiol *68*, 905-911.

Panzeri, S., Schultz, S.R., Treves, A., and Rolls, E.T. (1999). Correlations and the encoding of information in the nervous system. P Roy Soc B-Biol Sci *266*, 1001-1012.

Panzeri, S., and Treves, A. (1996). Analytical estimates of limited sampling biases in different information measures. Network-Comp Neural *7*, 87-107.

Pellerin, L., and Magistretti, P.J. (2004). Neuroenergetics: calling upon astrocytes to satisfy hungry neurons. Neuroscientist *10*, 53-62.

Petroff, O.A., Errante, L.D., Rothman, D.L., Kim, J.H., and Spencer, D.D. (2002). Glutamate-glutamine cycling in the epileptic human hippocampus. Epilepsia *43*, 703-710.

Pettersen, K.H., Devor, A., Ulbert, I., Dale, A.M., and Einevoll, G.T. (2006). Current-source density estimation based on inversion of electrostatic forward solution: effects of finite extent of neuronal activity and conductivity discontinuities. J Neurosci Methods *154*, 116-133.

Pfeuffer, J., Merkle, H., Beyerlein, M., Steudel, T., and Logothetis, N.K. (2004). Anatomical and functional MR imaging in the macaque monkey using a vertical large-bore 7 Tesla setup. Magn Reson Imaging *22*, 1343-1359.

Phillipson, O.T., Kilpatrick, I.C., and Jones, M.W. (1987). Dopaminergic Innervation of the Primary Visual-Cortex in the Rat, and Some Correlations with Human Cortex. Brain Res Bull *18*, 621-633.

Pleger, B., Blankenburg, F., Ruff, C.C., Driver, J., and Dolan, R.J. (2008). Reward facilitates tactile judgments and modulates hemodynamic responses in human primary somatosensory cortex. J Neurosci *28*, 8161-8168.

Porrino, L.J., Burns, R.S., Crane, A.M., Palombo, E., Kopin, I.J., and Sokoloff, L. (1987a). Local cerebral metabolic effects of L-dopa therapy in 1-methyl-4-phenyl-1,2,3,6-tetrahydropyridine-induced parkinsonism in monkeys. PNAS *84*, 5995-5999.

Porrino, L.J., Burns, R.S., Crane, A.M., Palombo, E., Kopin, I.J., and Sokoloff, L. (1987b). Local cerebral metabolic effects of L-dopa therapy in 1-methyl-4-phenyl-1,2,3,6-tetrahydropyridine-induced parkinsonism in monkeys. Proc Natl Acad Sci U S A *84*, 5995-5999.

Preinerstorfer, B., Schiesel, S., Lammerhofer, M., and Lindner, W. (2010). Metabolic profiling of intracellular metabolites in fermentation broths from beta-lactam antibiotics production by liquid chromatography-tandem mass spectrometry methods. J Chromatogr A *1217*, 312-328.

Prichard, J., Rothman, D., Novotny, E., Petroff, O., Kuwabara, T., Avison, M., Howseman, A., Hanstock, C., and Shulman, R. (1991). Lactate rise detected by 1H NMR in human visual cortex during physiologic stimulation. PNAS *88*, 5829-5831.

Prokai, L., Frycak, P., Stevens, S.M., Jr., and Nguyen, V. (2008). Measurement of Acetylcholine in Rat Brain Microdialysates by LC - Isotope Dilution Tandem MS. Chromatographia *68*, s101-s105.

Quian Quiroga, R., and Panzeri, S. (2009). Extracting information from neuronal populations: information theory and decoding approaches. Nat Rev Neurosci *10*, 173-185.

Rajalingham, R., Schmidt, K., and DiCarlo, J.J. (2015). Comparison of Object Recognition Behavior in Human and Monkey. J Neurosci *35*, 12127-12136.

Raman, L., Tkac, I., Ennis, K., Georgieff, M.K., Gruetter, R., and Rao, R. (2005). In vivo effect of chronic hypoxia on the neurochemical profile of the developing rat hippocampus. Brain Res Dev Brain Res *156*, 202-209.

Rao, V.R., and Finkbeiner, S. (2007). NMDA and AMPA receptors: old channels, new tricks. Trends Neurosci *30*, 284-291.

Rauch, A., Rainer, G., Augath, M., Oeltermann, A., and Logothetis, N.K. (2008a). Pharmacological MRI combined with electrophysiology in non-human primates: effects of Lidocaine on primary visual cortex. Neuroimage *40*, 590-600.

Rauch, A., Rainer, G., and Logothetis, N.K. (2008b). The effect of a serotonin-induced dissociation between spiking and perisynaptic activity on BOLD functional MRI. Proc Natl Acad Sci U S A *105*, 6759-6764.

Rauch, A., Rainer, G., and Logothetis, N.K. (2008c). The effect of a serotonin-induced dissociation between spiking and perisynaptic activity on BOLD functional MRI. PNAS *105*, 6759-6764.

Ray, S., and Maunsell, J.H. (2011). Different origins of gamma rhythm and high-gamma activity in macaque visual cortex. PLoS Biol *9*, e1000610.

Reader, T.A. (1978). The effects of dopamine, noradrenaline and serotonin in the visual cortex of the cat. Experientia *34*, 1586-1588.

Redjems-Bennani, N., Jeandel, C., Lefebvre, E., Blain, H., Vidailhet, M., and Gueant, J.L. (1998). Abnormal substrate levels that depend upon mitochondrial function in cerebrospinal fluid from Alzheimer patients. Gerontology *44*, 300-304.

Reese, T., Bjelke, B., Porszasz, R., Baumann, D., Bochelen, D., Sauter, A., and Rudin, M. (2000). Regional brain activation by bicuculline visualized by functional magnetic resonance imaging. Time-resolved assessment of bicuculline-induced changes in local cerebral blood volume using an intravascular contrast agent. NMR Biomed *13*, 43-49.

Reiman, E.M., Caselli, R.J., Chen, K., Alexander, G.E., Bandy, D., and Frost, J. (2001). Declining brain activity in cognitively normal apolipoprotein E epsilon 4 heterozygotes: A foundation for using positron emission tomography to efficiently test treatments to prevent Alzheimer's disease. PNAS *98*, 3334-3339.

Reiman, E.M., Chen, K., Alexander, G.E., Caselli, R.J., Bandy, D., Osborne, D., Saunders, A.M., and Hardy, J. (2004). Functional brain abnormalities in young adults at genetic risk for late-onset Alzheimer's dementia. PNAS *101*, 284-289.

Reiman, E.M., Chen, K., Alexander, G.E., Caselli, R.J., Bandy, D., Osborne, D., Saunders, A.M., and Hardy, J. (2005). Correlations between apolipoprotein E epsilon4 gene dose and brain-imaging measurements of regional hypometabolism. PNAS *102*, 8299-8302.

Reiman, E.M., Raichle, M.E., Robins, E., Mintun, M.A., Fusselman, M.J., Fox, P.T., Price, J.L., and Hackman, K.A. (1989). Neuroanatomical correlates of a lactate-induced anxiety attack. Arch Gen Psychiatry *46*, 493-500.

Richard, F., and Amouyel, P. (2001). Genetic susceptibility factors for Alzheimer's disease. Eur J Pharmacol *412*, 1-12.

Richards, D.A., Tolias, C.M., Sgouros, S., and Bowery, N.G. (2003). Extracellular glutamine to glutamate ratio may predict outcome in the injured brain: a clinical microdialysis study in children. Pharmacol Res *48*, 101-109.

Rickert, J., Oliveira, S.C., Vaadia, E., Aertsen, A., Rotter, S., and Mehring, C. (2005). Encoding of movement direction in different frequency ranges of motor cortical local field potentials. J Neurosci *25*, 8815-8824.

Rockland, K.S., and Pandya, D.N. (1979). Laminar origins and terminations of cortical connections of the occipital lobe in the rhesus monkey. Brain Res *179*, 3-20.

Rogers, G.L. (2003). Functional magnetic resonance imaging (fMRI) and effects of L-dopa on visual function in normal and amblyopic subjects. Trans Am Ophthalmol Soc *101*, 401-415.

Rossi, A.F., Desimone, R., and Ungerleider, L.G. (2001). Contextual modulation in primary visual cortex of macaques. J Neurosci *21*, 1698-1709.

Safaai, H., Neves, R., Eschenko, O., Logothetis, N.K., and Panzeri, S. (2015). Modeling the effect of locus coeruleus firing on cortical state dynamics and single-trial sensory processing. Proc Natl Acad Sci U S A *112*, 12834-12839.

Samuelsson, C., Hillered, L., Zetterling, M., Enblad, P., Hesselager, G., Ryttlefors, M., Kumlien, E., Lewen, A., Marklund, N., Nilsson, P.*, et al.* (2007). Cerebral glutamine and glutamate levels in relation to compromised energy metabolism: a microdialysis study in subarachnoid hemorrhage patients. J Cereb Blood Flow Metab *27*, 1309-1317.

Scheeringa, R., Fries, P., Petersson, K.M., Oostenveld, R., Grothe, I., Norris, D.G., Hagoort, P., and Bastiaansen, M.C. (2011). Neuronal dynamics underlying high- and low-frequency EEG oscillations contribute independently to the human BOLD signal. Neuron *69*, 572-583.

Schlichtherle-Cerny, H., Affolter, M., and Cerny, C. (2003). Hydrophilic interaction liquid chromatography coupled to electrospray mass spectrometry of small polar compounds in food analysis. Anal Chem *75*, 2349-2354.

Schmiedt, J.T., Maier, A., Fries, P., Saunders, R.C., Leopold, D.A., and Schmid, M.C. (2014). Beta oscillation dynamics in extrastriate cortex after removal of primary visual cortex. J Neurosci *34*, 11857-11864.

Schroeder, C.E., and Lakatos, P. (2009). Low-frequency neuronal oscillations as instruments of sensory selection. Trends Neurosci *32*, 9-18.

Schwarz, A.J., Gozzi, A., Reese, T., and Bifone, A. (2007). In vivo mapping of functional connectivity in neurotransmitter systems using pharmacological MRI. Neuroimage *34*, 1627-1636.

Seamans, J.K., Durstewitz, D., Christie, B.R., Stevens, C.F., and Sejnowski, T.J. (2001a). Dopamine D1/D5 receptor modulation of excitatory synaptic inputs to layer V prefrontal cortex neurons. Proc Natl Acad Sci U S A *98*, 301-306.

Seamans, J.K., Gorelova, N., Durstewitz, D., and Yang, C.R. (2001b). Bidirectional dopamine modulation of GABAergic inhibition in prefrontal cortical pyramidal neurons. J Neurosci *21*, 3628-3638.

Seamans, J.K., and Yang, C.R. (2004). The principal features and mechanisms of dopamine modulation in the prefrontal cortex. Prog Neurobiol *74*, 1-58.

Self, M.W., van Kerkoerle, T., Super, H., and Roelfsema, P.R. (2013). Distinct roles of the cortical layers of area V1 in figure-ground segregation. Curr Biol *23*, 2121-2129.

Sengupta, B., Laughlin, S.B., and Niven, J.E. (2014). Consequences of converting graded to action potentials upon neural information coding and energy efficiency. PLoS Comput Biol *10*, e1003439.

Serences, J.T. (2008). Value-based modulations in human visual cortex. Neuron *60*, 1169-1181.

Servan-Schreiber, D., Printz, H., and Cohen, J.D. (1990). A network model of catecholamine effects: gain, signal-to-noise ratio, and behavior. Science *249*, 892-895.

Shackman, H.M., Shou, M., Cellar, N.A., Watson, C.J., and Kennedy, R.T. (2007). Microdialysis coupled on-line to capillary liquid chromatography with tandem mass spectrometry for monitoring acetylcholine in vivo. J Neurosci Methods *159*, 86-92.

Shah, V.P., Midha, K.K., Dighe, S., Mcgilveray, I.J., Skelly, J.P., Yacobi, A., Layloff, T., Viswanathan, C.T., Cook, C.E., Mcdowall, R.D*., et al.* (1991). Analytical Methods Validation - Bioavailability, Bioequivalence and Pharmacokinetic Studies - Conference Report. Eur J Drug Metab Ph *16*, 249-255.

Shannon, C.E. (1948). A Mathematical Theory of Communication. At&T Tech J *27*, 379-423.

Sharpe, L.T., Stockman, A., Jagla, W., and Jagle, H. (2005). A luminous efficiency function, V*(lambda), for daylight adaptation. J Vis *5*, 948-968.

Shmuel, A., Augath, M., Oeltermann, A., and Logothetis, N.K. (2006). Negative functional MRI response correlates with decreases in neuronal activity in monkey visual area V1. Nat Neurosci *9*, 569-577.

Shuler, M.G., and Bear, M.F. (2006). Reward timing in the primary visual cortex. Science *311*, 1606-1609.

Sicard, K.M., and Duong, T.Q. (2005). Effects of hypoxia, hyperoxia, and hypercapnia on baseline and stimulus-evoked BOLD, CBF, and CMRO2 in spontaneously breathing animals. Neuroimage *25*, 850-858.

Siegel, M., Donner, T.H., and Engel, A.K. (2012). Spectral fingerprints of large-scale neuronal interactions. Nat Rev Neurosci *13*, 121-134.

Siegelbaum, S.A., and Tsien, R.W. (1983). Modulation of Gated Ion Channels as a Mode of Transmitter Action. Trends Neurosci *6*, 307-313.

Sirotin, Y.B., and Das, A. (2009). Anticipatory haemodynamic signals in sensory cortex not predicted by local neuronal activity. Nature *457*, 475-479.

Smith, E.W., Skelton, M.S., Kremer, D.E., Pascoe, D.D., and Gladden, L.B. (1997). Lactate distribution in the blood during progressive exercise. Med Sci Sports Exerc *29*, 654-660.

Smith, M.L., Gosselin, F., and Schyns, P.G. (2006). Perceptual moments of conscious visual experience inferred from oscillatory brain activity. PNAS *103*, 5626-5631.

Sokoloff, L. (1977). Relation between physiological function and energy metabolism in the central nervous system. J Neurochem *29*, 13-26.

Sokoloff, L., Reivich, M., Kennedy, C., Des Rosiers, M.H., Patlak, C.S., Pettigrew, K.D., Sakurada, O., and Shinohara, M. (1977). The [14C]deoxyglucose method for the measurement of local cerebral glucose utilization: theory, procedure, and normal values in the conscious and anesthetized albino rat. J Neurochem *28*, 897-916.

Spaak, E., Bonnefond, M., Maier, A., Leopold, D.A., and Jensen, O. (2012). Layer-specific entrainment of gamma-band neural activity by the alpha rhythm in monkey visual cortex. Curr Biol *22*, 2313-2318.

Sperling, R., Greve, D., Dale, A., Killiany, R., Holmes, J., Rosas, H.D., Cocchiarella, A., Firth, P., Rosen, B., Lake, S*., et al.* (2002). Functional MRI detection of pharmacologically induced memory impairment. PNAS *99*, 455-460.

Stanisor, L., van der Togt, C., Pennartz, C.M., and Roelfsema, P.R. (2013). A unified selection signal for attention and reward in primary visual cortex. PNAS *110*, 9136-9141.

Steriade, M., Dossi, R.C., Pare, D., and Oakson, G. (1991). Fast Oscillations (20-40 Hz) in Thalamocortical Systems and Their Potentiation by Mesopontine Cholinergic Nuclei in the Cat. P Natl Acad Sci USA *88*, 4396-4400.

Steriade, M., and Hobson, J. (1976). Neuronal activity during the sleep-waking cycle. Prog Neurobiol *6*, 155-376.

Stockman, A., Jagle, H., Pirzer, M., and Sharpe, L.T. (2008). The dependence of luminous efficiency on chromatic adaptation. J Vis *8*, 1 1-26.

Szymanski, F.D., Rabinowitz, N.C., Magri, C., Panzeri, S., and Schnupp, J.W. (2011). The laminar and temporal structure of stimulus information in the phase of field potentials of auditory cortex. J Neurosci *31*, 15787-15801.

Tombaugh, G.C., and Somjen, G.G. (1996). Effects of extracellular pH on voltage-gated Na+, K+ and Ca2+ currents in isolated rat CA1 neurons. J Physiol-London *493*, 719-732.

Tort, A.B., Komorowski, R., Eichenbaum, H., and Kopell, N. (2010). Measuring phase-amplitude coupling between neuronal oscillations of different frequencies. J Neurophysiol *104*, 1195-1210.

Traub, R.D., Whittington, M.A., Buhl, E.H., Jefferys, J.G., and Faulkner, H.J. (1999). On the mechanism of the gamma --> beta frequency shift in neuronal oscillations induced in rat hippocampal slices by tetanic stimulation. J Neurosci *19*, 1088-1105.

Treves, A., and Panzeri, S. (1995). The Upward Bias in Measures of Information Derived from Limited Data Samples. Neural Comp *7*, 399-407.

Trevino, M., Vivar, C., and Gutierrez, R. (2007). beta/gamma oscillatory activity in the CA3 hippocampal area is depressed by aberrant GABAergic transmission from the dentate gyrus after seizures. Journal of Neuroscience *27*, 251-259.

Tsai, T.R., Cham, T.M., Chen, K.C., Chen, C.F., and Tsai, T.H. (1996). Determination of acetylcholine by on-line microdialysis coupled with pre- and post-microbore column enzyme reactors with electrochemical detection. J Chromatogr B Biomed Appl *678*, 151-155.

Uhlhaas, P.J., and Singer, W. (2015). Oscillations and neuronal dynamics in schizophrenia: the search for basic symptoms and translational opportunities. Biol Psychiatry *77*, 1001-1009.

Uran, S., Landmark, K.E., Hjellum, G., and Skotland, T. (2007). Quantification of 13C pyruvate and 13C lactate in dog blood by reversed-phase liquid chromatography-electrospray ionization mass spectrometry after derivatization with 3-nitrophenylhydrazine. J Pharm Biomed Anal *44*, 947-954.

Uutela, P., Reinila, R., Piepponen, P., Ketola, R.A., and Kostiainen, R. (2005). Analysis of acetylcholine and choline in microdialysis samples by liquid chromatography/tandem mass spectrometry. Rapid Commun Mass Spectrom *19*, 2950-2956.

van Dam, J.C., Eman, M.R., Frank, J., Lange, H.C., van Dedem, G.W.K., and Heijnen, S.J. (2002). Analysis of glycolytic intermediates in Saccharomyces cerevisiae using anion exchange chromatography and electrospray ionization with tandem mass spectrometric detection. Analytica Chimica Acta *460*, 209-218.

van Kerkoerle, T., Self, M.W., Dagnino, B., Gariel-Mathis, M.A., Poort, J., van der Togt, C., and Roelfsema, P.R. (2014a). Alpha and gamma oscillations characterize feedback and feedforward processing in monkey visual cortex. PNAS *111*, 14332-14341.

van Kerkoerle, T., Self, M.W., Dagnino, B., Gariel-Mathis, M.A., Poort, J., van der Togt, C., and Roelfsema, P.R. (2014b). Alpha and gamma oscillations characterize feedback and feedforward processing in monkey visual cortex. Proc Natl Acad Sci U S A *111*, 14332-14341.

van Kerkoerle, T., Self, M.W., and Roelfsema, P.R. (2017). Layer-specificity in the effects of attention and working memory on activity in primary visual cortex. Nat Commun *8*, 13804.

Viklund, C., Ponten, E., Glad, B., Irgum, K., Horstedt, P., and Svec, F. (1997). ''Molded'' macroporous poly(glycidyl methacrylate-co-trimethylolpropane trimethacrylate) materials with fine controlled porous properties: Preparation of monoliths using photoinitiated polymerization. Chem Mater *9*, 463-471.

Vlassenko, A.G., Rundle, M.M., Raichle, M.E., and Mintun, M.A. (2006). Regulation of blood flow in activated human brain by cytosolic NADH/NAD+ ratio. PNAS *103*, 1964-1969.

von Pfostl, V., Li, J., Zaldivar, D., Goense, J., Zhang, X., Serr, N., Logothetis, N.K., and Rauch, A. (2012). Effects of lactate on the early visual cortex of non-human primates, investigated by pharmaco-MRI and neurochemical analysis. Neuroimage *61*, 98-105.

Voytko, M.L., and Tinkler, G.P. (2004). Cognitive function and its neural mechanisms in nonhuman primate models of aging, Alzheimer disease, and menopause. Front Biosci *9*, 1899-1914.

Weatherall, D. (2006). The Weatherall report on the use of non-human primates in research. London:The Royal Society.

Weis, T., Puschmann, S., Brechmann, A., and Thiel, C.M. (2012). Effects of L-dopa during auditory instrumental learning in humans. PLoS One *7*, e52504.

Whittingstall, K., and Logothetis, N.K. (2009). Frequency-band coupling in surface EEG reflects spiking activity in monkey visual cortex. Neuron *64*, 281-289.

Williamson, D.H., Lund, P., and Krebs, H.A. (1967). The redox state of free nicotinamide-adenine dinucleotide in the cytoplasm and mitochondria of rat liver. Biochem J *103*, 514-527.

Wójcik, D.K., and Leski, S. (2010). Current source density reconstruction from incomplete data. Neural Comp *22*, 48-60.

Wong, E.C., Buxton, R.B., and Frank, L.R. (1997). Implementation of quantitative perfusion imaging techniques for functional brain mapping using pulsed arterial spin labeling. NMR Biomed *10*, 237-249.

Wrobel, A. (2000). Beta activity: a carrier for visual attention. Acta Neurobiol Exp (Wars) *60*, 247-260.

Yang, T.T., Chang, C.K., Tsao, C.W., Hsu, Y.M., Hsu, C.T., and Cheng, J.T. (2009). Activation of muscarinic M-3 receptor may decrease glucose uptake and lipolysis in adipose tissue of rats. Neurosci Lett *451*, 57-59.

Yao, T., Yano, T., Nanjyo, Y., and Nishino, H. (2003). Simultaneous determination of glucose and L-lactate in rat brain by an electrochemical in vivo flow-injection system with an on-line microdialysis sampling. Anal Sci *19*, 61-65.

Yu, A.J., and Dayan, P. (2005). Uncertainty, neuromodulation, and attention. Neuron *46*, 681-692.

Yuste, R. (2015). From the neuron doctrine to neural networks. Nat Rev Neurosci *16*, 487-497.

Zaldivar, D., Logothetis, N.K., Rauch, A., and Goense, J. (2017). Pharmaco-Based fMRI and Neurophysiology in Non-Human Primates. In In Vivo Neuropharmacology and Neurophysiology, A. Philippu, ed. (New York, NY: Springer New York), pp. 37-66.

Zaldivar, D., Rauch, A., Whittingstall, K., Logothetis, N.K., and Goense, J. (2014). Dopamine-induced dissociation of BOLD and neural activity in macaque visual cortex. Curr Biol *24*, 2805-2811.

Zappe, A.C., Pfeuffer, J., Merkle, H., Logothetis, N.K., and Goense, J.B. (2008a). The effect of labeling parameters on perfusion-based fMRI in nonhuman primates. J Cereb Blood Flow Metab *28*, 640-652.

Zappe, A.C., Uludag, K., and Logothetis, N.K. (2008b). Direct measurement of oxygen extraction with fMRI using 6% CO2 inhalation. Magn Reson Imaging *26*, 961-967.

Zhang, X., Rauch, A., Lee, H., Xiao, H., Rainer, G., and Logothetis, N.K. (2007). Capillary hydrophilic interaction chromatography/mass spectrometry for simultaneous determination of multiple neurotransmitters in primate cerebral cortex. Rapid Commun Mass Spectrom *21*, 3621-3628.

Zhang, X., Rauch, A., Xiao, H., Rainer, G., and Logothetis, N.K. (2008). Mass spectrometry-based neurochemical analysis: perspectives for primate research. Expert Rev Proteomics *5*, 641-652.

Zhu, Y., Wong, P.S., Cregor, M., Gitzen, J.F., Coury, L.A., and Kissinger, P.T. (2000). In vivo microdialysis and reverse phase ion pair liquid chromatography/tandem mass spectrometry for the determination and identification of acetylcholine and related compounds in rat brain. Rapid Commun Mass Spectrom *14*, 1695-1700.

Zhu, Y., and Zhu, J.J. (2004). Rapid arrival and integration of ascending sensory information in layer 1 nonpyramidal neurons and tuft dendrites of layer 5 pyramidal neurons of the neocortex. J Neurosci *24*, 1272-1279.

Zonta, M., Angulo, M.C., Gobbo, S., Rosengarten, B., Hossmann, K.A., Pozzan, T., and Carmignoto, G. (2003). Neuron-to-astrocyte signaling is central to the dynamic control of brain microcirculation. Nat Neurosci *6*, 43-50.